Nano-Optics and Nanophotonics

Motoichi Ohtsu

Silicon Light-Emitting Diodes and Lasers

Photon Breeding Devices using Dressed Photons

Springer

Nano-Optics and Nanophotonics

The Springer Series in Nano-Optics and Nanophotonics provides an expanding selection of research monographs in the area of nano-optics and nanophotonics, science- and technology-based on optical interactions of matter in the nanoscale and related topics of contemporary interest. With this broad coverage of topics, the series is of use to all research scientists, engineers and graduate students who need up-to-date reference books. The editors encourage prospective authors to correspond with them in advance of submitting a manuscript. Submission of manuscripts should be made to the editor-in-chief, one of the editors or to Springer.

More information about this series at http://www.springer.com/series/8765

Motoichi Ohtsu

Silicon Light-Emitting Diodes and Lasers

Photon Breeding Devices using Dressed Photons

Springer

Motoichi Ohtsu
Graduate School of Engineering
The University of Tokyo
Tokyo
Japan

ISSN 2192-1970 ISSN 2192-1989 (electronic)
Nano-Optics and Nanophotonics
ISBN 978-3-319-42012-7 ISBN 978-3-319-42014-1 (eBook)
DOI 10.1007/978-3-319-42014-1

Library of Congress Control Number: 2016945786

Printed on acid-free paper

This Springer imprint is published by Springer Nature
The registered company is Springer International Publishing AG Switzerland

Preface

This book, entitled Silicon Light Emitting Diodes and Lasers, reviews the use of an indirect transition-type semiconductor to construct light emitting devices, which has not been possible with conventional methods employed in materials science and technology. Silicon (Si) and related crystals, which are typical popular indirect transition-type semiconductors, are considered here. The light emitting devices that are examined are light emitting diodes (LED) and diode lasers.

These devices can be fabricated using dressed photons (DPs) and dressed-photon–phonons (DPPs) via a novel method known as DPP-assisted annealing. Besides the fabrication step, DPs and DPPs are also used in the operation of the fabricated device. It should be pointed out that the fabricated devices exhibit a novel and unique property called "photon breeding", which originates from the DPs and DPPs. In photon breeding, the photon energy and photon spin of the light emitted from the device are identical to those of the light that irradiates the crystal during the DPP-assisted annealing. Due to this unique property, which is based on novel fabrication and operation principles, it would be appropriate to call this novel device "the third light source", after LEDs and lasers. More concretely, it should be called "a photon breeding device", as represented by the subtitle of this book, Photon Breeding Devices using Dressed Photons.

In order to review the fabrication and operation of photon breeding devices, Chap. 1 surveys the problems with conventional LEDs and lasers (the first and second light sources) and presents solutions that can be achieved by utilizing DPs and DPPs. After presenting definitions of the DP and the DPP, the photon breeding phenomenon is reviewed. Chapter 2 describes the fabrication and operation of a visible LED using Si crystal. Chapter 3 describes those of an infrared LED using Si crystal. In the same chapter, the spatial distribution of the dopant atoms is analyzed, and a description is given of how to control the polarization of the emitted light. Chapter 4 discusses the strength of the phonon coupling, the contribution of multimode coherent phonons, and how to control the light emission spectral profile. Chapter 5 reviews infrared lasers using Si crystal, demonstrating a low threshold current density and a high output power. Chapter 6 surveys LEDs fabricated using

SiC crystal, which is also an indirect transition-type semiconductor. Emission of visible, ultraviolet, and broad-spectrum light is also demonstrated. The first half of Chap. 7 is devoted to LEDs using GaP crystal, an indirect transition-type semiconductor, and the second half is devoted to LEDs using ZnO crystal. Finally, Chap. 8 reviews three examples of other novel photon breeding devices. The first is an optical and electrical relaxation oscillator, and the second is an infrared photodetector with optical amplification, which have been fabricated using Si crystal. The last is a novel optical polarization rotator, using ZnO crystal and also SiC crystal. Appendices A—E are devoted to reviewing details of the features of DPs and relevant phenomena.

Photon breeding devices using Si and other crystals are expected to bring about a major paradigm shift in the design, fabrication, and operation of photonic devices and their applications. This book will provide scientific and technical information on these devices to scientists, engineers, and students who are and will be engaged in this field.

The author thanks Drs. T. Kawazoe, T. Yatsui, N. Tate, W. Nomura, K. Kitamura (the University of Tokyo), and M. Naruse (National Institute of Information and Communications Technology) for their collaborations in research on dressed photons. The author's work on Silicon light emitting devices was partially supported by the JSPS Core-to-Core Program (A. Advanced Research Networks).

Several experimental results reviewed in this book were obtained through academia–industry collaborations under arrangements made by the Specified Nonprofit Corporation "Nanophotonics Engineering Organization". Finally, the author is grateful to Dr. C. Ascheron of Springer–Verlag for his guidance and suggestions throughout the preparation of this book.

Tokyo, Japan Motoichi Ohtsu

Contents

Chapter 1
Problems with Light Emitting Devices and Their Solutions

This book reviews how to use an indirect transition-type semiconductor to construct light emitting diodes (LEDs) and lasers, which has not been possible with conventional methods employed in materials science and technology. First, this chapter surveys the problems to be solved. Some strategies and principles achieve solutions are reviewed. Detailed discussions of the theoretical aspects are described in Appendices A–E.

1.1 Introduction

The wavelength of the light emitted from a conventional LED is governed by the bandgap energy E_g of the semiconductor material used. Although there is a Stokes wavelength shift [1], its magnitude is negligibly small. Therefore, the value of E_g must be adjusted for the desired light emission wavelength, and this has been achieved by exploring novel semiconductor materials. For this purpose, direct transition-type semiconductors have been used for conventional LEDs. Among these semiconductors, InGaAsP has been used for optical fiber communication systems because the wavelength of the emitted light is 1.00–1.70 μm (E_g = 0.73–1.24 eV) [2, 3]. When fabricating a highly efficient infrared LED or laser using InGaAsP, it is necessary to use a double heterostructure composed of an InGaAsP active layer and an InP carrier confinement layer. However, there are some problems with this approach, including the complexity of the structure and the high toxicity of As [4]. In addition, In is a rare metal. On the other hand, composite semiconductors that emit visible light, such as AlGaInP and InGaN, have extremely low emission efficiencies around the wavelength of 550 nm (=2.25 eV) [5], which is called the green gap problem. Although this efficiency has been increasing recently due to improvements in dopant materials and fabrication methods, there are still several technical problems because highly toxic or rare materials are required, which increases the cost of fabrication.

In order to solve the problems described above, several methods using silicon (Si) have been recently proposed. Although Si has been popularly used for

M. Ohtsu, *Silicon Light-Emitting Diodes and Lasers*,
Nano-Optics and Nanophotonics, DOI 10.1007/978-3-319-42014-1_1

electronic devices, there is a long-held belief in materials science and technology that Si is not suitable for use in LEDs and lasers because it is an indirect transition-type semiconductor, and thus, its light emitting efficiency is very low. The reason for this is that electrons have to transition from the conduction band to the valence band to spontaneously emit light by electron–hole recombination. However, in the case of an indirect transition-type semiconductor, the momentum (wave-number) of the electron at the bottom of the conduction band and that of the hole at the top of the valence band are different from each other. Therefore, for electron–hole recombination, a phonon is required in the process to satisfy the momentum conservation law. In other words, electron–phonon interaction is required. However, the probability of this interaction is low, resulting in a low interband transition probability.

In order to solve this problem, for example, porous Si [6], a super-lattice structure of Si and SiO_2 [7, 8], and Si nanoprecipitates in SiO_2 [9] have been used to emit visible light. To emit infrared light, Er-doped Si [10] and Si-Ge [11] have been employed. In these examples, the emission efficiency is very low since Si still works as an indirect transition-type semiconductor in these materials.

In contrast to these examples, as explained in this article, the use of dressed photons (DPs) and dressed-photon–phonons (DPPs) can realize highly efficient LEDs and lasers even when using Si bulk crystal.

1.2 Dressed Photons and Dressed-Photon–Phonons

First, as an introductory topic, the concept of elementary excitations is reviewed. Elementary excitations have been discussed for a long time in the field of solid state physics [12]. Excited states of a many-body system are regarded as a collection of certain fundamental excited states that has been called an elementary excitation, and also a quasi-particle. A phonon is a well-known example of a quasi-particle that represents the normal mode of crystal lattice vibration in a solid. Another example is a plasmon, which corresponds to the collective motion of electron density variations in an interacting electron gas. An exciton, another well-known example, represents a quasi-particle related to an electron–hole pair in a solid. The interaction between a photon and an exciton forms a new steady-state that also represents a quasi-particle called an exciton-polariton. Its dispersion relation, which is the relation between the wave-number k and energy E of the excition–polaritons in macroscopic space, is represented by curves A and B in Fig. 1.1. It should be noted that the quasi-particles described above also follow dispersion relations that are similar to these curves.

Second, in preparation for starting the main topic of this section, it should be pointed out that there is a vast space around the curves A and B in this figure, which is represented by the gray shaded rectangle. A quasi-particle is also created in this space. By referring to the large size of this space, unique features of this quasi-particle are as follows:

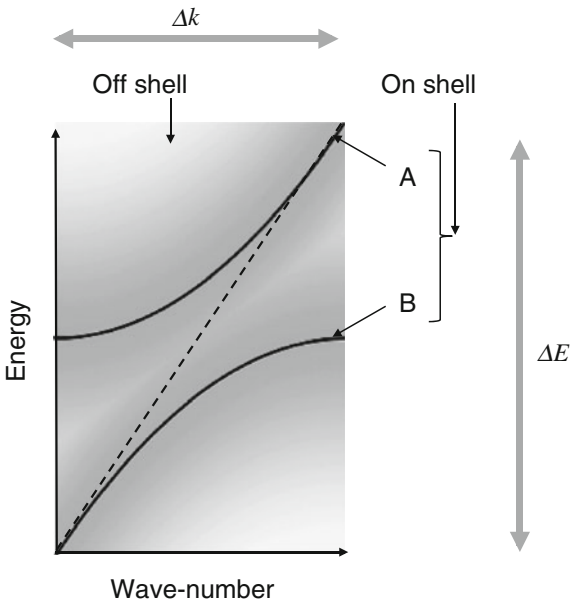

Fig. 1.1 Dispersion relation between the wave-number k and the energy E. The *curves* A and B represent the dispersion relation of the exciton-polariton. The *broken line* is that for light in free space. The *gray* shaded rectangle represents that for the dressed photons

(1) As represented by the horizontal double-pointed gray arrow, the wave-number, k, of this quasi-particle spans a wide range. This also means that its uncertainty, Δk, is large, which represents the non-conservation of the quasi-particle's momentum, $\hbar k$(where $\hbar = h/2\pi$, and h is Planck's constant). This large uncertainty, Δk, also means that the quasi-particle is composed of a large number of normal modes. Furthermore, it means that the uncertainty, Δx, of the quasi-particle's position, x, is small, due to Heisenberg uncertainty relation, $\Delta(\hbar k) \cdot \Delta x \geq \hbar$. This small uncertainty, Δx, means that the size of this quasi-particle is small.

(2) As is represented by the vertical double-pointed gray arrow, the energy E of this quasi-particle spans a wide range. This means that its uncertainty, ΔE, is large, which represents the non-conservation of the energy. The large uncertainty, ΔE, also means that the time uncertainty, Δt, is small, due to Heisenberg uncertainty relation $\Delta E \cdot \Delta t \geq \hbar$. This means that this quasi-particle is created and subsequently annihilated within a short duration. In other words, the energy of this quasi-particle is temporally modulated, generating a large number of spectral sidebands.

The first feature, that is, the small size, means that the quasi-particle is created in a nanomaterial, and a part of the field of this quasi-particle penetrates through the surface of the nanomaterial to the outside. This penetrated field has been called the optical near field [13]. The second feature, the short duration, means that the quasi-particle is a virtual photon. A dressed photons (DP) provides a physical picture that describes these two features consistently, including the large number of normal modes and the spectral sideband features of (1) and (2), respectively.

For comparison, the exciton-polariton, represented by the curves A and B in Fig. 1.1, is a quasi-particle in a macroscopic material where the size of this material is much larger than the wavelength of light. This quasi-particle propagates toward the far-field and has been called a real photon; its momentum and energy are conserved ($\Delta k = 0, \Delta E = 0$). The behavior and properties of this real photon have been studied in conventional optical science and technology for a long time.

The curves A and B in Fig. 1.1 correspond to a physical system, which has been called "on shell" in quantum field theory [14–16]. On the other hand, the shaded gray rectangle has been called "off shell". Whereas the real photon on shell conserves its momentum and energy, the virtual photon off shell does not. The probability of creating virtual photons diminishes depending on how far off shell they are. The value of this probability is represented by the gradation depth of the gray rectangle.

We now begin our discussion of the main topic, based on the first and second topics above. First, it is noted that the concept of a real photon on shell has been established in the conventional quantum theory of light [17]. The real photon corresponds to a quantum of the electromagnetic mode in a cavity defined in a macroscopic free space. Since the real photon is massless, it is difficult to express its wave function in a coordinate representation in order to draw a picture of the real photon as a spatially localized point-like particle, unlike an electron [18].

When describing the virtual photon off shell in a nanometric space, energy transfer between two nanomaterials and detection of the transferred energy are essential. They are formulated by assuming that the nanomaterials are arranged in close proximity to each other and illuminated by a real photon. Although the separation between the two nanomaterials is much shorter than the optical wavelength, it is sufficiently long to prevent electron tunneling. As a result, the energy is transferred not by a tunneled electron but by some sort of optical interactions between the two nanomaterials.

A serious problem, however, is that a cavity cannot be defined in a sub-wavelength–sized nanometric space, which differs from the approach taken in the conventional quantum theory of light. In order to solve this problem, an infinite number of electromagnetic modes and an infinite number of frequencies are assumed, corresponding to the large number of normal modes and spectral sidebands mentioned in (1) and (2) above, respectively. In parallel with this assumption, infinite numbers of energy levels must also be assumed in the electrons. Based on these assumptions, the dressed photons (DP) is defined as a virtual photon that dresses the electron energy (Appendix A) [19, 20]. The DP is modulated spatially and temporally due to features (1) and (2) above. The interaction between the two nanomaterials can be represented by energy transfer due to the annihilation of a DP from the first nanomaterial and its creation on the second nanomaterial.

Furthermore, since an actual nanometric system (composed of nanomaterials and DPs) is always surrounded by a macroscopic system (composed of macroscopic materials and real photons), energy transfer between the nanometric and macroscopic systems has to be considered when analyzing the interaction between the nanomaterials in the nanometric system. As a result, it is found that the magnitude of the transferred energy is represented by the Yukawa function (Appendix B). This analysis also elucidates an intrinsic feature of DPs, namely, the size-dependent

resonance; that is to say, the efficiency of the energy transfer between nanomaterials depends on the sizes of the nanomaterials that are interacting. It should be noted that this resonance is unrelated to diffraction of the real photon on shell, which governs the conventional wave-optical phenomena. Furthermore, since the DP is localized in nanometric space, the long-wavelength approximation, which is valid for conventional light–matter interactions, is not valid for DP-mediated interactions. As a result, an electric dipole-forbidden transition turns out to be allowed in the case of the DP-mediated interactions.

In actual materials, such as semiconductors, the contribution of the crystal lattice also needs to be included in the theoretical model of the DP. By doing so, it has been found that the DP interacts with phonons. Furthermore, in a nanomaterial, it is possible to generate multimode coherent phonons via a DP–phonon interaction. As a result of this interaction, a novel quasi-particle is generated. This quasi-particle is called a dressed-photon–phonon (DPP), which is a DP dressing the energy of the multimode coherent phonon (Appendix C). Furthermore, it is found that the DPP field is localized at the impurity sites in the crystal lattice of the nanomaterial with a spatial extent as short as the size of the impurity site. It is also localized at the end of the nanomaterial with a spatial extent as short as the size of this end.

The DPP energy can be transferred to the adjacent nanomaterial, where it induces a novel light–matter interaction. Here, since translational symmetry is broken due to the finite size of the nanomaterial, the momentum of the DPP has a large uncertainty and is non-conserved, as was the case of the DP itself. Also, since the DPP has an infinite number of spectral modulation sidebands as was the case of the DP, the electron dresses the energies of the photon and phonon, which means that the energy of the electron in the nanomaterial is also modulated.

When analyzing the conventional light scattering phenomenon in a macroscopic material, it has been sufficient to study one phonon. In contrast, the coherent phonon described above is composed of an infinite number of phonons. This coherent phonon assists in exciting the electron in the adjacent nanomaterial instead of merely increasing the material temperature, which enables DPP-assisted excitation of the electrons. Therefore, for analyzing the optical excitation of the nanomaterial, it is essential to represent the relevant quantum state of the nanomaterial by the direct product of the quantum states of the electron and the coherent phonon. This relevant quantum state means that an infinite number of energy levels has to be considered in the energy bandgap between the valence and conduction bands of an electron in the case of a semiconductor. This quasi-continuous energy distribution originates from the modulation of the eigenenergy of the electron as a result of the coupling between the DP and the coherent phonon. This DPP-assisted excitation and de-excitation can be exploited in the fabrication and operation of LEDs, lasers, and other devices using Si bulk crystals, which are reviewed in the following chapters.

1.3 Principles of Photon Emission

For spontaneous emission of light by DPPs, a single-step or a two-step de-excitation of an electron takes place depending on whether the emitted real photon energy is higher or lower than the energy difference between the excited and ground states of the electron, which is E_g in the case of a semiconductor material (Appendix D). Stimulated emission also takes places in the same way.

1.3.1 Single-Step De-Excitation

In Fig. 1.2a, b, since the electron strongly couples with the photon and phonon, the energy state is expressed as the direct product of the ket vectors of the electronic state and the phonon state. For example, $\left|E_g; el\right\rangle \otimes |E_{ex}; phonon\rangle$ includes

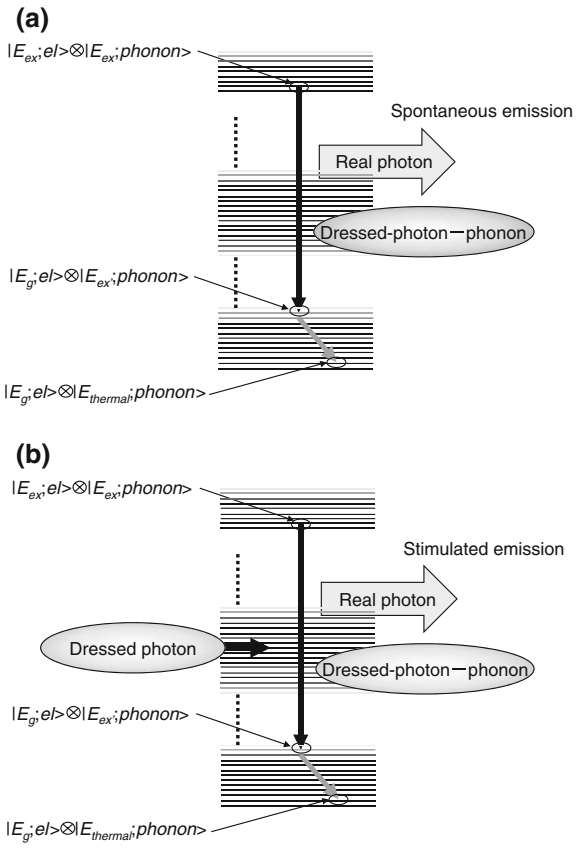

Fig. 1.2 Single-step photon emission processes via dressed-photon–phonon. **a** Spontaneous emission. **b** Stimulated emission

the ground state of the electron and the excited state of the phonon. The spontaneous emission of a DPP, as well as a real photon (Fig. 1.2a), is the result of the radiative transition from the excited state $|E_{ex}; el\rangle \otimes |E_{ex}; phonon\rangle$ to the ground state $\left|E_g; el\right\rangle \otimes |E_{ex'}; phonon\rangle$. Here, in the case of a semiconductor, the excited and ground states of the electron, ($|E_{ex}; el\rangle$ and $\left|E_g; el\right\rangle$), correspond to the states in the conduction and valence bands, respectively. After the transition, the phonon in the excited state relaxes to the thermal equilibrium state ($|E_{thermal}; phonon\rangle$) determined by the crystal lattice temperature, and finally the electron and phonon transition to the state $\left|E_g; el\right\rangle \otimes |E_{thermal}; phonon\rangle$.

The stimulated emission process (Fig. 1.2b) is explained as follows: When an electron in the excited state is irradiated with a DP, a transition from the initial state $|E_{ex}; el\rangle \otimes |E_{ex}; phonon\rangle$ to the ground state $\left|E_g; el\right\rangle \otimes |E_{ex'}; phonon\rangle$ takes place, resulting in photon emission. Like the spontaneous emission, the phonon then relaxes to a thermal equilibrium state determined by the crystal lattice temperature and finally the electron and phonon transition to the state $\left|E_g; el\right\rangle \otimes |E_{thermal}; phonon\rangle$.

1.3.2 Two-Step De-Excitation

Figure 1.3a schematically illustrates the two-step de-excitation for spontaneous emission (Appendix D).

First step The initial state is expressed by the direct product of the excited state of the electron and the excited state of the phonon, ($|E_{ex}; el\rangle \otimes |E_{ex}; phonon\rangle$). De-excitation takes place from this initial state to the ground state $\left|E_g; el\right\rangle$ of the electron. Since this de-excitation is an electric dipole-allowed transition, it generates not only a DPP but also a real photon. As a result, the system reaches the intermediate state $\left|E_g; el\right\rangle \otimes |E_{ex'}; phonon\rangle$. Here, the excited state $|E_{ex'}; phonon\rangle$ of the phonon after DPP emission (route 1 in Fig. 1.3a) has a much higher eigenenergy than that of the thermal equilibrium state $|E_{thermal} : phonon\rangle$. This is because the DP couples with the phonon, resulting in phonon excitation. On the other hand, the excited state $|E_{ex'}; phonon\rangle$ of the phonon after a real photon emission (route 2 in Fig. 1.3a) has an eigenenergy as low as that of $|E_{thermal} : phonon\rangle$. This is because the real photon does not couple with the phonon.

Second step This step is an electric dipole-forbidden transition because the electron stays in the ground state. Thus, only the DPP is generated by this emission process. As a result, the phonon is de-excited to the lower excited state $|E_{ex''}; phonon\rangle$, and the system is expressed as $\left|E_g; el\right\rangle \otimes |E_{ex''}; phonon\rangle$. After this transition, the phonon promptly relaxes to the thermal equilibrium state, and thus, the final state is expressed as $\left|E_g; el\right\rangle \otimes |E_{thermal}; phonon\rangle$. The de-excitation for the stimulated emission is explained by Fig. 1.3b, which is similar to Fig. 1.3a. The only difference is that the DP is incident on the electron in the excited state, triggering stimulated emission.

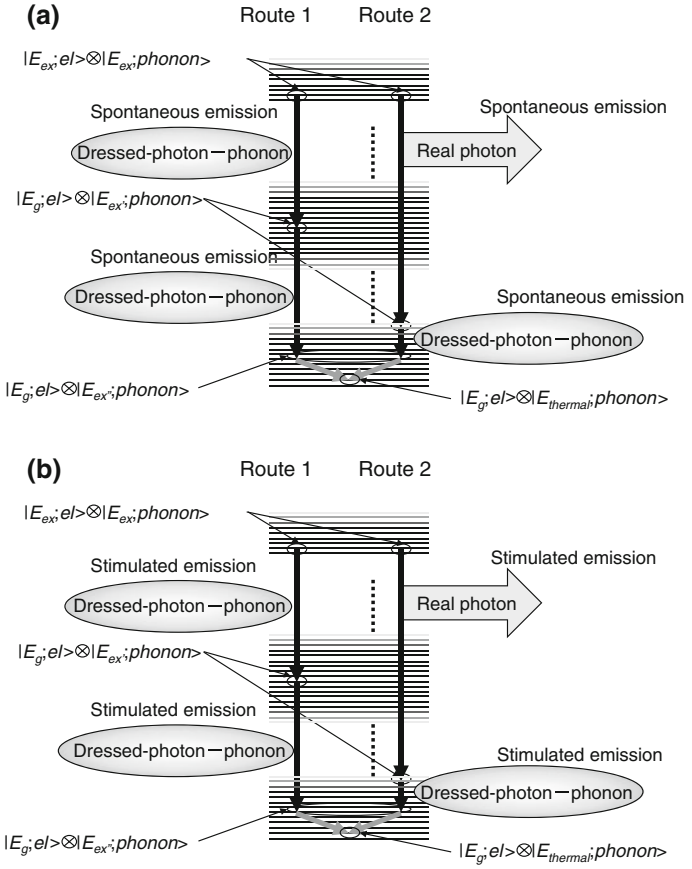

Fig. 1.3 Two-step photon emission processes via dressed-photon–phonon. **a** Spontaneous emission. **b** Stimulated emission

1.4 Photon Breeding

The following chapters review novel LEDs and lasers fabricated by using Si crystals and other relevant indirect transition-type semiconductor crystals. Prior to this review, it should be pointed out that the fabrication and operation principles of these devices are different from those of conventional LEDs and lasers fabricated by using direct transition-type semiconductors. This section describes these differences.

To realize a device by using Si crystal, dressed-photon–phonons (DPPs) are used two times: first for device fabrication, and second for device operation.

(1) For device fabrication, a p–n homojunction-structured Si crystal is annealed, via Joule-heat produced by current injection, in order to diffuse boron (B) atoms (the p-type dopant). During the annealing, the Si crystal surface is irradiated

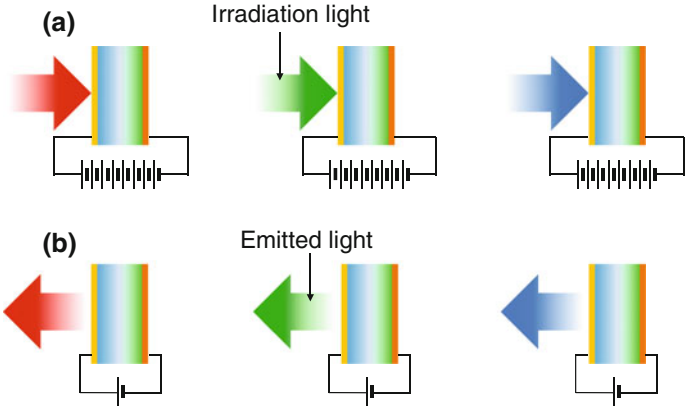

Fig. 1.4 Light emitting devices using Si. **a** Fabrication. **b** Operation

with light (a real photon) (Fig. 1.4a) to create DPPs on the B atom surface. Driven by the created DPPs, electron–hole recombination takes place, emitting light (a real photon). Since the energy of the emitted light dissipates from the Si crystal, the efficiency of the Joule-heating decreases. As a result, a unique spatial distribution of B atoms is realized, which depends on the created DPP energy. This novel annealing is called DPP-assisted annealing. In this spatial distribution, neighboring B atoms form a pair, and the resultant B atom pair orients in a specific direction to efficiently create localized phonons (Sects. 3.3 and 4.3.3).

(2) For the operation of the fabricated Si-LED, the light irradiation is not required any more; it is used only during the DPP-assisted annealing. Only forward current that is much lower than that used for annealing is injected, as is the case of the conventional LED operation. By this forward current, an electron is injected into the conduction band at the p–n homojunction and creates a photon by spontaneous emission even though its probability is very low. However, once this photon is created, it subsequently creates a DPP on the surface of the B atom at the p–n homojunction, and this DPP interacts with another electron in the conduction band to exchange momentum so that a secondary photon is created. By repeating these momentum exchange and photon creation processes, the emitted light intensity is amplified and reaches a stationary value within a short duration, so that light with a sufficiently high intensity is emitted from the p–n homojunction.

It should be noted that photon breeding occurs during device operation. As a result, the photon energy of the emitted light is equal to the photon energy $h\nu_{anneal}$ of the light irradiated during the annealing (Fig. 1.4b). This is in contrast to a conventional device, where the photon energy of the emitted light is determined by E_g. This is because the difference between $h\nu_{anneal}$ and E_g is compensated for by the energy of the created phonons. This means that the photon energy of the light

emitted from the device is identical to $h\nu_{anneal}$. This is because the spatial distribution of the B atoms has been controlled by the light irradiated during the DPP-assisted annealing, enabling most efficient stimulated emission and spontaneous emission of photons with identical photon energy. In other words, the light irradiated during the DPP-assisted annealing serves as a "breeder" that creates photons with an energy equivalent to $h\nu_{anneal}$. This is the reason why this novel phenomenon is named photon breeding with respect to photon energy. Photon breeding has been observed in the radiation energy dissipation process from relativistic jets in blazars [21, 22]. However, in this astrophysical phenomenon, a very-high-energy photon (X ray) is generated from a low-energy photon (infrared or visible light) by inverse Compton scattering with a charged particle. Therefore, the photon breeding discussed in this book, producing equal-energy photons by using a DPP in a nanometric-sized space in a material, is quite different from that described above. Due to this difference, the present photon breeding may have to be called "nano-photon breeding" in order to avoid confusion. However, this book uses the name "photon breeding" for conciseness.

Photon breeding has been observed not only for the photon energy but also for the photon spin (Sects. 3.4 and 6.3). For example, linearly polarized light is emitted from the LED if it was fabricated by irradiating linearly polarized light during the annealing step. (Remember that the light emitted from a conventional LED is not polarized.)

In summary, the principles, operation, and functions of the present devices are different from those of conventional LEDs and lasers because DPPs and electric dipole-forbidden transitions are involved. Furthermore, photon breeding occurs, so that the energy and spin of the emitted photons are identical to those of the light irradiated during the annealing. Due to this difference, it is appropriate to call this novel device "a third light source", or more concretely, "a photon breeding device".

1.5 Fabrication and Performance of Photon Breeding Devices

As the last topic of Chap. 1, this section summarizes the fabrication and performance of the photon breeding devices that will be reviewed in the following chapters.

1.5.1 Fabrication

(1.1) In DPP-assisted annealing, an electric current is injected into the sample while irradiating it with light (photon energy: $h\nu_{anneal}$). (Refer to Sects. 2.2 and 3.1.)

(1.2) DPP-assisted annealing is possible even when the value of $h\nu_{anneal}$ is lower than E_g (Refer to Sect. 3.1.)

(1.3) The optimum condition for effective DPP-assisted annealing is that the ratio of the electron injection rate to the photon irradiation rate be set to 1:1. (Refer to Sect. 7.1.)

(1.4) The sample's temperature during the DPP-assisted annealing can be as low as 400 K; in other words, an extremely high temperature is not required. (Refer to Sects. 2.2, 3.1, and 7.1.)

(1.5) Conventional thermal annealing, e.g., by heating the sample in an electric furnace, is not compatible with the fabrication of photon breeding devices. (Refer to Sect. 7.1.3.)

1.5.2 Spatial Distribution of the Dopant Atoms

(2.1) As a result of DPP-assisted annealing, p-type dopant atoms (B atoms in the case of a Si crystal) form pairs. The separation, d, between the dopant atoms in the pair is given by $d = na$, where a is the lattice constant of the crystal. The integer n satisfies the relation $h\nu_{anneal} = E_g - nE_{phonon}$, where E_{phonon} is the energy of the created phonon. (Refer to Sect. 3.3).

(2.2) The orientation of the pair of the dopant atoms is perpendicular to the propagation direction of the light irradiated during the DPP-assisted annealing. Furthermore, in the case where this light is linearly polarized, it is also perpendicular to the direction of polarization. (Refer to Sect. 3.4.)

1.5.3 Performance

(3.1) The fabricated devices exhibit electroluminescence by injecting an electric current. (Refer to Sects. 2.2 and 3.1.)

(3.2) The photon energy of the emitted light is identical to $h\nu_{anneal}$; i.e., photon breeding takes place with respect to the photon energy. (Refer to Sects. 2.2 and 3.1.)

(3.3) The polarization direction of the emitted light is identical to that of the light irradiated during the DPP-assisted annealing; i.e., the device exhibits photon breeding with respect to the photon spin. (Refer to Sects. 3.4 and 6.3.)

(3.4) When the device is fabricated under the condition described in (1.2) above, the photon energy of the emitted light is lower than E_g, as can be deduced from (3.2). Therefore, the emitted light is not absorbed by the crystal, enabling high efficiency and high output power. (Refer to Sects. 3.2, 5.3, 6.1–6.4, 7.1, and 7.2.)

Table 1.1 Family of photon breeding devices

Devices	Photon energy	Crystal	Chapters and sections to refer to
Light emitting diode	Visible	Si	Chap. 2
		SiC	Chap. 6
		GaP	Sect. 7.1
		ZnO[1]	Sect. 7.2
	Infrared	Si	Chap. 3
Laser	Infrared	Si	Chap. 5
Optical and electrical relaxation oscillator	Infrared	Si	Sect. 8.1
Photodiode[2]	Infrared	Si	Sect. 8.2
	Visible	Si	Sect. 8.2
Modulator[3]	Visible	ZnO[1]	Sect. 8.3
		SiC	Sect. 8.3

[1]Although ZnO is a direct transition-type semiconductor, a p-type semiconductor is difficult to fabricate by the conventional method
[2]Provided with optical amplification gain
[3]Light polarization rotator and light beam deflector

1.5.4 Family of Photon Breeding Devices

The photon breeding devices that have been fabricated are listed in Table 1.1.

References

1. F. Yang, M. Willkinson, E.J. Austin, K.P. O' Donnell, Phys. Rev. Lett. **70**, 323 (1993)
2. ZhI Alferov, Semiconductors **32**, 1 (1988)
3. R.A. Milano, P.D. Dapkus, G.E. Stillman, I.E.E.E. Tran, Electron Devices **29**, 266 (1982)
4. U.S. Department of Health and Human Services, Public Health Service, National Inst. Health, National toxicology program (ed.), *NTP Technical Report on the Toxicology and Carcinogenesis Studies of Indium Phosphide* (U.S. Department of Health and Human Services, Washington, DC., 2012) NTP TR 499
5. K.T. Delaney, P. Rinke, C.G. Van de Walle, Appl. Phys. Lett. **94**, 191109 (2009)
6. K.D. Hirschman, L. Tysbekov, S.P. Duttagupta, P.M. Fauchet, Nature **384**, 338 (1996)
7. Z.H. Lu, D.J. Lockwood, J.-M. Baribeau, Nature **378**, 258 (1995)
8. L. Dal Negro, R. Li, J. Warga, S.N. Beasu, Appl. Phys. Lett. **92**, 181105 (2008)
9. T. Komoda, Nucl. Instrum. Methods Phys. Res. Sect.B, Beam Interact. Mater. Atoms **96**, 387 (1995)
10. S. Yerci, R. Li, L. Dal Negro, Appl. Phys. Lett. **97**, 081109 (2010)
11. S.K. Ray, S. Das, R.K. Singha, S. Manna, A. Dhar, Nanoscale Res. Lett. **6**, 224 (2011)
12. D. Pines, *Elementary Excitation in Solids* (Perseus Books, Reading, 1999)
13. M. Ohtsu, K. Kobayashi, *Optical Near Fields (Perseus Books, Reading, Massachusetts, 1999)* (Springer, Berlin, 2004)
14. M. Thomson, *Modern Particle Physics* (Cambridge University Press, Cambridge, 2013)

15. R.P. Feynman, *The Theory of Fundamental Processes* (W.A. Benjamin, New York, 1962), pp. 95–100
16. M. Ohtsu, H. Hori, *Near-Field Nano-Optics* (Kluwer Academic/Plenum Publishers, New York, 1999), pp. 29–31
17. J.J. Sakurai, *Advanced Quantum Mechanics* (Addison-Wesley, Reading, 1967)
18. T.D. Newton, E.P. Wigner, Rev. Mod. Phys. **21**, 400 (1949)
19. M. Ohtsu, *Progress in Nanophotonics 1*, ed. by M. Ohtsu (Springer, Berlin, 2011), pp. 1–4
20. M. Ohtsu, *Dressed Photon* (Springer, Berlin, 2013), pp. 11–18
21. J. Poutanen, B.E. Stern, Mon. Not. R. Astron. Soc. **372**, 1217 (2006)
22. B.E. Stern, J. Poutanen, Mon. Not. R. Astron. Soc. **383**, 1695 (2008)

Chapter 2
Visible Light Emitting Diodes Using Silicon Crystal

This chapter reviews the fabrication and operation of a Si bulk p–n homojunction-structured LED [1]. Spontaneous emission of visible light takes places based on the principle described in Sect. 1.3.1 because the emitted photon energy is higher than E_g of Si.

2.1 Introduction

Since the DPP has a large uncertainty in its momentum due to its spatially modulated nature (refer to Sect. 1.2), it can provide momentum for electron de-excitation, i.e., for the recombination of an electron and hole. Although the lowest point of the conduction band (X-point) and the highest point of the valence band (Γ-point) correspond to different momenta, an electron in the conduction band efficiently relaxes to the valence band and emits a real photon thanks to the assistance of the phonon in the DPP. Furthermore, a radiative transition from a high-energy excited electron can also occur via the DPP. For example, due to the existence of the DPP at a high energy (e.g., level a in Fig. 2.1), an excited-state electron nearby can quickly couple with the coherent phonon and then directly relax to the ground state; thus, a radiative relaxation shown by the red downward arrows occurs, resulting in emission with a photon energy higher than E_g. Recall that, without the DPP, an electron in an excited state at high energy quickly transitions to the lowest point in the conduction band due to fast intraband relaxation; therefore, the probability of an interband transition from a high-energy excited state is extremely low in conventional methods.

In order to realize a visible Si-LED, the single-step spontaneous and stimulated emission processes described in Sect. 1.3.1 were used two times. The first is for fabrication of the device, more specifically, for self-organization of the spatial distribution of the dopant atoms to form a distribution that is suitable for the emission of high-energy photons. The second is for the operation of the device, to obtain spontaneously emitted photons. These are reviewed in the following sections.

M. Ohtsu, *Silicon Light-Emitting Diodes and Lasers*,
Nano-Optics and Nanophotonics, DOI 10.1007/978-3-319-42014-1_2

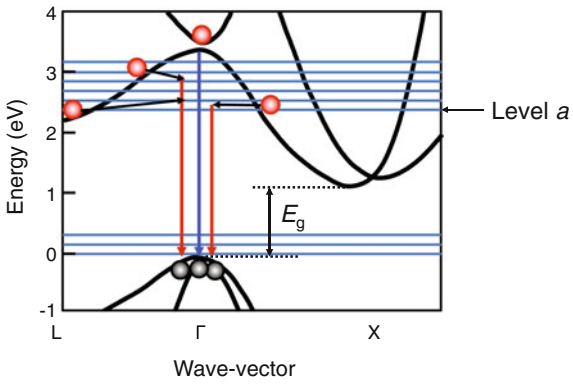

Fig. 2.1 Energy band structure of Si.*Blue horizontal lines* represent the phonon-coupled electronic states. *Red* and *blue downward arrows* show the radiative relaxation

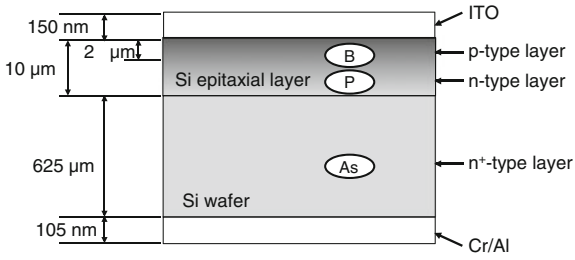

Fig. 2.2 Cross-sectional profiles of the layer structures of the device

2.2 Device Fabrication

The fabrication of the device can be divided into two steps. The first step is to prepare a Si p–n homojunction structure having a modifiable dopant distribution. The second step is to modify the shape of the dopant domains through DPP-assisted annealing.

In the first step, an epitaxial layer of phosphorus (P) was deposited on an n-type Si crystal with low arsenic (As) concentration. Subsequently, this Si crystal was doped with boron (B) atoms by ion implantation, with seven different accelerating energies, namely, 30, 70, 130, 215, 330, 480, and 700 keV, to form dopant domains with a dopant concentration of 10^{19} cm^{-3}. This doping formed a p-type region in the Si, and as a result, a p–n homojunction structure was constructed. The B distribution in the p–n homojunction was spatially inhomogeneous due to the high accelerating energy and high doping concentration; this was to increase the probability of producing a B distribution favorable for generating DPPs. The crystal was then diced. Then, an ITO film was deposited on the surface of the p-type layer, and a Cr/Al film was deposited on the back surface of the n-type Si for use as electrodes. The cross-sectional profile of the layer structure of the device is shown in Fig. 2.2.

In the second step, DPP-assisted annealing was performed by causing a forward-bias current to flow through the device while irradiating the p-type side of the device with a laser beam. The forward-bias current density used for the annealing was

1.44 A/cm^2. The optical power density of the laser beam was 3.33 W/cm^2, which was sufficiently high for inducing DPP-assisted annealing. The photon energy $h\nu_{anneal}$ of the laser light was 3.1 eV (400 nm wavelength), which was 2.8-times higher than E_g of Si (1.12 eV, or 1.11 μm wavelength) [2], and thus the light was absorbed in the Si bulk crystal by a direct transition. The forward-bias voltage was set to be higher than $h\nu_{anneal}/e$, where e represents the electron charge.

It was pointed out in Sect. 1.2 that the DPP is localized at the impurity sites in the nanomaterial with a spatial extent as short as the size of the impurity site. This suggests the possibility of generating and localizing DPPs at the B impurity sites by light irradiation, depending on the spatial distribution and concentration of B. During the DPP-assisted annealing process, B atom diffuses, and its spatial distribution in the p–n homojunction is continuously modified in a self-organized manner until reaching the desired shape.

The mechanism of this DPP-assisted annealing is explained as follows, by considering regions where DPPs are hardly generated and regions where DPPs are easily generated:

(1) Regions where DPPs are hardly generated: If the device is irradiated with light (a real photon) satisfying $h\nu_{anneal} > E_g$, as shown in Fig. 2.3a, when an electron in the valence band absorbs a photon, it is simultaneously scattered by a phonon (indicated by the upward blue arrow and the green wavy arrows, respectively). As a result, the electron is excited to the conduction band and then immediately relaxes to the bottom of the conduction band. After this relaxation, the electron cannot radiatively relax because of the different momenta between the bottom of the conduction band and the top of the valence band. Therefore, it eventually relaxes non-radiatively, as indicated by the green thick arrow. This non-radiative relaxation generates heat in the Si crystal, causing the B atom to diffuse, and thus changing the spatial distribution of the B atoms.
(2) Regions where DPPs are easily generated: When the B diffuses as in (1), the B concentration changes to a spatial distribution suitable for generating DPPs with a fairly high probability. Here, in the case where DPPs are generated at

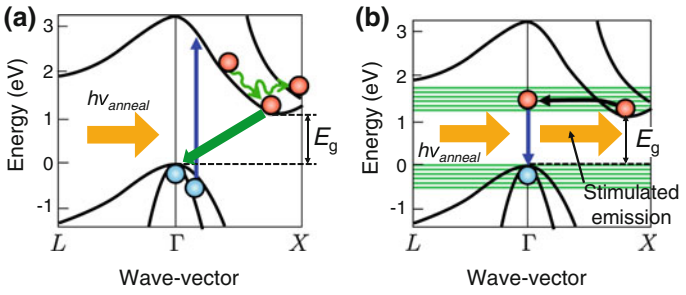

Fig. 2.3 Schematic explanation of the DPP-assisted annealing. **a** Regions where DPPs are hardly generated. **b** Regions where DPPs are easily generated

the B atoms, as shown in Fig. 2.3b, an electron injected by the forward current is de-excited via the DPP energy level (indicated by horizontal green parallel lines in this figure), producing a photon generated by stimulated emission. When the electron number densities of occupation in the excited state (the conduction band) and the ground state (the valence band), denoted by n_{ex} and n_g, satisfy the Bernard–Duraffourg inversion condition ($n_{ex} > n_g$) [3], the number of photons created by stimulated emission exceeds the number of photons annihilated by absorption. Since the photons generated by stimulated emission are radiated outside the device, part of the light energy that the device absorbs is dissipated outside the device in the form of propagating light energy, and therefore, the thermal diffusion rate of the B atom becomes smaller than in (1).

(3) Due to the difference in the thermal diffusion rates between (1) and (2), after the B atom has diffused throughout the entire device in a self-organized manner as annealing proceeds, it reaches an equilibrium state in which its spatial distribution has been modified, and the annealing process is thus completed. Since region (2) is in a state where stimulated emission with photon energy $h\nu_{anneal}$ is easily generated via the DPPs, and since the stimulated emission probability is proportional to the spontaneous emission probability [4], the DPP-assisted annealed device should become an LED that exhibits spontaneous emission with the photon energy $h\nu_{anneal}$ of the irradiation light. In other words, the irradiation light during the DPP-assisted annealing serves as a "breeder" that generates light with the same photon energy $h\nu_{anneal}$ in the LED; that is, a novel phenomenon that we call photon breeding takes place in this LED.

After one hour of annealing, fabrication of the Si-LED was completed. To confirm the stimulated emission, Fig. 2.4 shows the measured temporal evolution of the surface temperature difference between the irradiated area and the non-irradiated area. The Si crystal was continuously irradiated with light, and current injection was started after 7 min. At the beginning, when only the laser beam was radiated, the temperature increased to 75 °C, and the temperature difference dramatically increased due to the heat provided by light absorption. After a few minutes, the heat gradually

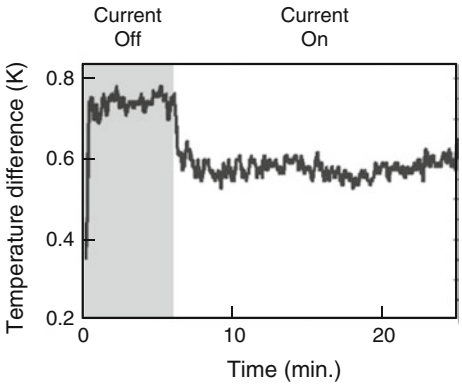

Fig. 2.4 Temporal evolution of the surface temperature difference between the irradiated area and the non-irradiated area

diffused into the whole device, and the temperature difference reached a stable value. This agreed with our hypothesis of how the annealing process advances with laser irradiation, which was described in (1) and (2). Next, after 7 min, a forward-bias current was injected to the device. This led to an obvious decrease in the temperature difference. This decrease was a result of stimulated emission in the area where DPPs were generated; that is, the irradiated light was not converted into heat but induced light emission due to the stimulated emission process. In other words, this decrease in temperature difference confirmed the occurrence of stimulated emission via DPPs.

2.3 Device Operation

Figure 2.5a–c show light emitted from the fabricated Si-LED (current density 2 A/cm^2) taken with a band-filtered visible CCD camera at room temperature. They clearly reveal that the light emission spectrum from the Si-LED contained all three primary colors: blue, green, and red, with photon energies of 3.1, 2.1 and 2.0 eV (wavelengths 400, 590 and 620 nm), respectively. This confirms that the fabricated Si-LED showed light emission in the visible region when a forward-bias voltage was applied.

Curves A and B in Fig. 2.6 are light emission spectra of the devices at room temperature before and after the DPP-assisted annealing, respectively. No light emission was observed before annealing. However, after the annealing, a broad emission spectrum was observed. Noticeably, there are three dominant peaks in this spectrum: the first one at 3.1 eV (400 nm wavelength), which corresponds to blue, and the other two close peaks at photon energies of 2.1 eV (590 nm wavelength) and 2.0 eV (620 nm wavelength), which correspond to green and red light, respectively.

The above light emission characteristics agree with the principle described in Sect. 1.3.1 and will be explained in detail here. Figure 2.7 shows the energy band structure of Si (black curves) and the phonon-coupled electronic levels $|E_{ex}; el\rangle \otimes$

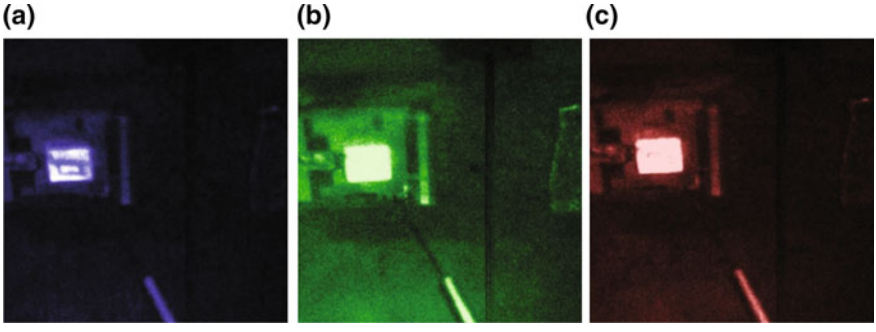

Fig. 2.5 Light emitted from the Si-LED. **a–c** are *blue*, *green*, and *red* light with photon energies of 3.1, 2.1 and 2.0 eV (wavelength; 400, 590 and 620 nm), respectively

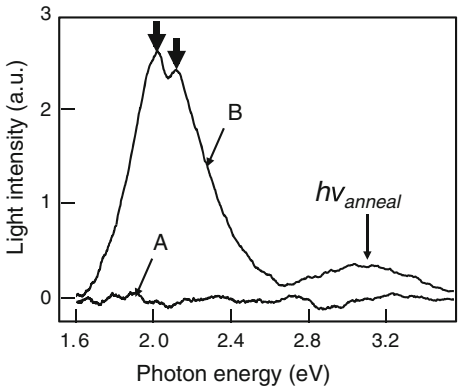

Fig. 2.6 Light emission spectra of the devices at room temperature. *Curves A* and *B* are the spectra taken before and after the DPP-assisted annealing, respectively. *Two downward arrows* represent the spectral peaks at 2.0 eV (620 nm-wavelength) and 2.1 eV (590 nm-wavelength)

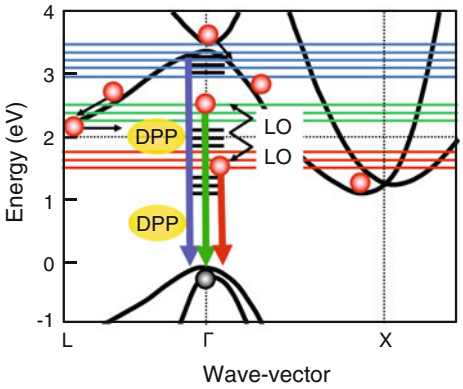

Fig. 2.7 Energy band structure of Si and the phonon-coupled electronic levels. The *blue*, *green*, and *red horizontal lines* represent phonon levels involved in the light emission in the visible region. *Three blue*, *green*, and *red downward arrows* represent the radiative relaxation processed of electron

$|E_{ex}; phonon\rangle$ (in particular, the blue, green, and red horizontal lines represent phonon levels involved in the light emission in the visible region). Since a DP strongly couples with phonons, a transition between the phonon-coupled electronic levels takes place if the generation probability of a DP that is resonant with the transition energy is sufficiently high. After the DPP-assisted annealing process, almost all of the B domains in the Si become suitable for generating DPPs whose photon energy corresponds to the light irradiated during annealing. Because the photon energy $h\nu_{anneal}$ of the annealing light was 3.1 eV (400 nm wavelength), high-energy excited electrons at the Γ-point of the conduction band relaxed to the ground state via 3.1 eV-photon emission (blue downward arrow in Fig. 2.7), resulting in the spectral peak at 3.1 eV in the light emission spectrum. This light emission is the result of photon breeding, as was described above.

Moreover, the injected electrons also tended to relax to the lower energy level via intra-band relaxation, i.e., to the L- and X-points in the conduction band. Therefore, the density of electrons at those points in the conduction band was considerably high. Because the emission intensity is also proportional to the number of electrons, the

radiative transition of electrons from the L-point resulted in light emission in the proximity of 2.0 eV.

The broad spectrum of the observed light emission is a result of the interaction of electrons with phonons. Since the probability of this interaction is inversely proportional to the number of phonons involved in phonon absorption or emission, the emission spectrum has two peaks at photon energies of 2.0 and 2.1 eV (two downward arrows on the curve B in Fig. 2.6). These photon energies are close to the energy level of the L-point, indicating the interaction with one longitudinal optical (LO)-mode phonon in the light emission process. Since there is a large difference in momentum between an electron at the L-point of the conduction band and a hole at the Γ-point of the valence band, the electron at the L-point needs to interact with a phonon in order to lose or gain the momentum for emitting a photon. As a result, photons are emitted from two separate energy levels (green and red downward arrows in Fig. 2.7). This explains the existence of two peaks in the vicinity of the L-point, at 2.1 and 2.0 eV. The energy difference between the two peaks is 100 meV, which is approximately equivalent to twice the LO-mode phonon energy [5]. The dip between the two peaks corresponds to the zero-phonon line. On the other hand, no similar peaks appeared in the spectrum at 3.1 eV. This is because the electrons directly relaxed to the valence band (the blue downward arrow in Fig. 2.7), and thus, the interactions with phonons were weaker.

As discussed above, the visible light emission is a result of the high-energy excited electrons, which are provided by the electrical power source. Therefore, it is necessary to study the dependence of the light emission performance of the Si-LED on the forward-bias voltage. Curves A and B in Fig. 2.8 show the dependences of the height of the peaks at 2.0 eV (red light) and at 3.1 eV (blue light) in Fig. 2.6 on the forward-bias voltage. The peak at 2.1 eV (green light) showed behavior similar to the peak at 2.0 eV and is therefore omitted here. Figure 2.8 shows that, at a voltage of 2.5 V, curve A starts rising with a higher slope. This corresponds to the threshold for red light emission. Furthermore, at a voltage of about 4.0 V, curve B changes its slope. This kink corresponds to the start of blue light emission. Interestingly, a kink in curve A is also observed in the curve B.

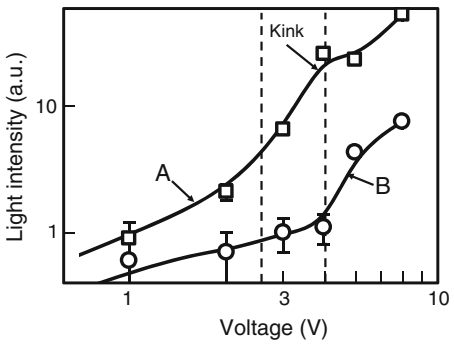

Fig. 2.8 Dependences of the height of the peaks on the forwarded-bias voltage. *Curves A* and *B* are at 2.0 eV (*red light*) and at 3.1 eV (*blue light*) in Fig. 2.6, respectively

This characteristic dependence of the emission intensity on the voltage is well explained by the emission mechanism discussed above: Since the voltage loss due to the Schottky barrier and parasitic circuit resistance is about 1.0 V, the highest energy of injected electrons is about 2.0 eV when a forward-bias voltage of 3.0 V is applied. Thus, the number density of electrons that have relaxed to the L-point in the conduction band (energy level of about 2.0 eV) starts increasing. Therefore, the emission with photon energies of 2.0 and 2.1 eV appears. This transition corresponds to the change in slope of curve A in Fig. 2.8. When a sufficiently high forward-bias voltage is applied, the energy of injected electrons becomes larger than 3.1 eV, and the number density of electrons at the Γ-point increases, resulting in the appearance of emission from a transition with a photon energy corresponding to blue light. This threshold voltage corresponds to the kink in the slope of curve B. Here, the appearance of a kink in curve A is evidence for the fact that some of the injected electrons recombine to cause blue light emission, and so the number density of electrons that have relaxed to the L-point becomes relatively lower and results in the decreased emission intensity of the red light.

2.4 Increasing the Light Extraction Efficiency

Although previous sections described the successful fabrication and operation of visible Si-LEDs, visible photons generated at a p–n homojunction in a Si substrate (2 μm down from the surface in the case of Fig. 2.2) are easily absorbed before they reach the surface because their photon energies are higher than E_g. This section reviews a novel lateral p–n homojunction structure, as shown in Fig. 2.9a [6]. Because it is formed on the surface of the Si substrate, the generated photons can be emitted without suffering from absorption, which is expected to increase the light extraction efficiency. This structure is formed by a novel laser doping method which does not need specialized expensive fabrication equipment, and which is thus suitable for mass production.

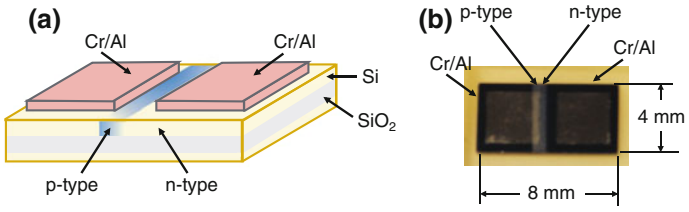

Fig. 2.9 Profile and photograph of the Si-LED with the lateral p–n homojunction. **a** Bird's eye view. **b** Photograph acquired after laser doping

The fabrication process, including the laser doping, is as follows:

(1) For use as electrodes, Cr/Pt films (total thickness 300 nm) were deposited on an n-type silicon-on-insulator (SOI) substrate in which the thickness of the device layer was 10 μm and the resistivity was 0.5 Ωcm. The areal sizes of the substrate and the electrode were 4 mm × 8 mm and 3 mm × 3 mm, respectively.
(2) A solution, in which B-doped Si nanocrystals were dispersed (B concentration 1×10^{20} cm^{-3}), was coated on half of the surface of the n-type Si substrate.
(3) For laser doping, the coated area was selectively irradiated with pulsed laser light having a photon energy of 2.35 eV (528 nm wavelength) and a fluence of 4.0 J/cm^2 to melt the Si nanocrystals, causing B atoms to diffuse into the Si substrate and transforming the n-type material to a p-type material. Figure 2.9b is a top-view photograph of the Si-LED acquired after the laser doping.

Figure 2.10a, b show the electrical and optical properties of the device measured after the laser doping (3), where Fig. 2.10a is the relation between the applied forward-bias voltage and injected current, and Fig. 2.10b is the weak light emission spectrum, representing the band-edge emission at E_g. Successful formation of the lateral p–n homojunction is confirmed by these figures.

After the processes (1)–(3) above, DPP-assisted annealing was conducted by applying a forward-bias voltage, V, of 15 V and irradiating the lateral p–n homojunction with CW laser light having a photon energy $h\nu_{anneal}$ of 3.1 eV (400 nm wavelength) and an intensity of 8.0 W/cm^2.

Figure 2.11 shows the light emission spectra of the fabricated Si-LED at V=15 V. Unlike the curve A in Fig. 2.6, the curve A in this figure represents the weak emission of visible light even before the DPP-assisted annealing. Detection of such low-intensity emission is made possible thanks to the increase in the light extraction efficiency by the lateral p–n homojunction. The spectral peak at 3.0 eV is attributed to the direct transition of electrons at the singular Γ-point in the energy band of Si. On the other hand, the peak at 1.9 eV is attributed to the radiative transition of electrons at the Γ-point via scattering by phonons, which is because electrons and phonons are weakly coupled even before the DPP-assisted annealing.

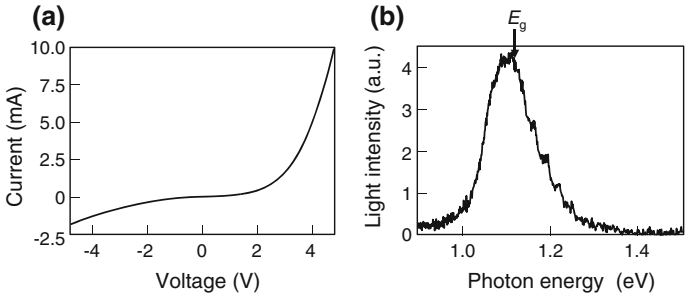

Fig. 2.10 Electrical and optical properties measured after the laser doping. **a** Relation between the forward-bias voltage and injection current. **b** Light emission spectrum

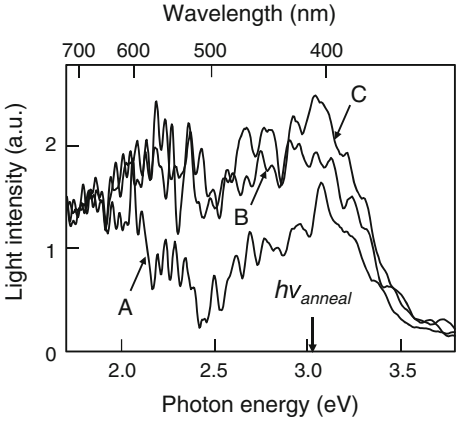

Fig. 2.11 Light emission spectra of the Si-LED. The applied forward-bias voltage was 15 V. Curve A is the spectrum acquired before the DPP-assisted annealing. *Curves B* and *C* are the spectra acquired after 30 and 90 min of DPP-assisted annealing, respectively

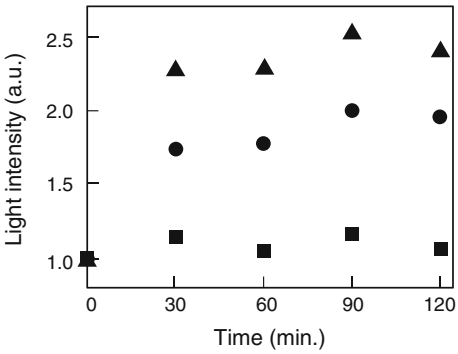

Fig. 2.12 Time evolution of the emitted light intensities. *Closed squares*, *triangles*, and *circles* represent the time evolution of the emitted light intensity of *red* (1.8–2.1 eV photon energy, 590–700 nm wavelength), *green* (2.1–2.5 eV photon energy, 490–590 nm wavelength), and *blue* (2.5–3.1 eV photon energy, 400–490 nm wavelength) colors in Fig. 2.11, respectively

Curves B and C in Fig. 2.11 are the spectra acquired after 30 and 90 min of DPP-assisted annealing, respectively. Compared with curve A, they show that the visible light emission is enhanced by the DPP-assisted annealing at photon energies between 2.0, and 3.3 eV, which are below $h\nu_{anneal}$. This selective enhancement originates from the coupling between an electron-hole pair and a phonon via DPPs.

Closed squares, triangles, and circles in Fig. 2.12 represent the time evolution of the emitted light intensity of red (1.8–2.1 eV photon energy, 590–700 nm wavelength), green (2.1–2.5 eV photon energy, 490–590 nm wavelength), and blue (2.5–3.1 eV photon energy, 400–490 nm wavelength) colors in Fig. 2.11, respectively, where the intensities were normalized to those before the DPP-assisted annealing.

This figure shows that the annealing time required for the increases in the emitted light intensities to saturate was about 90 min. It also shows that the enhancement of the green light intensity is larger than those of blue and red light, which is attributed to a radiative recombination involving phonon emission.

The increase in light extraction efficiency can be evaluated by noting the two peaks of the curves B and C in Fig. 2.11, at around 2 and 3 eV. Since the absorption at 2 eV is negligible as compared with that at 3 eV (the absorption coefficient of Si at 2 eV is two orders of magnitude smaller than that at 3 eV [7]), the emitted light intensity at 2 eV, I_{2eV}, can be used as a reference to compare the light extraction efficiency between the lateral and vertical p–n homojunctions. The light extraction efficiency is defined as $\eta_r = I_{3eV}/I_{2eV}$, where I_{3eV} is the emitted light intensity at 3 eV. As a result, the values of η_r for the lateral and the vertical p–n homojunctions (Sects. 2.2 and 2.3) were evaluated to be 1.10 and 0.14, respectively, from which it is confirmed that the lateral p–n homojunction had 7.8-times higher light extraction efficiency at a photon energy of 3 eV.

An advantage of the increased light extraction efficiency is the increase in the sensitivity of measuring the light emission spectrum, which enables detailed investigation of the emission process. The following part of this section reviews this investigation and confirms that the visible light emission originates from the coupling between an electron-hole pair and a phonon.

Curves A–E in Fig. 2.13a show the light emission spectra under several values of the forward-bias voltage V, which show that the emitted light intensity in a high-energy band around 3.0 eV increased with increasing V, resulting in a spectral blue-shift. This shift causes a large shift of the Commission Internationale de l'Eclairage (CIE) chromaticity coordinates, from (x, y)= (0.343, 0.359) at V= 8 V to (0.286, 0.288) at V=24 V, as is shown in Fig. 2.13b. This has never been observed in conventional LEDs fabricated using compound semiconductors with a direct transition-type

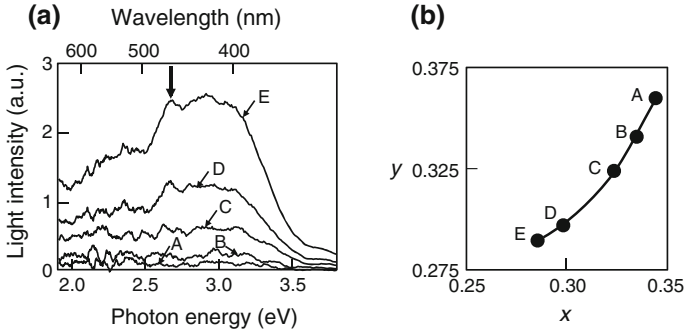

Fig. 2.13 Light emission spectra under several values of the forward-bias voltage, V. **a** Spectral profiles. *Curves A–E* are at V = 8, 12, 16, 20, and 24 V, respectively. **b** Relation between V and the textcolorredCommission Internationale de l'Eclairage (CIE) chromaticity coordinates (x, y). Closed *circles A–E* are at V = 8, 12, 16, 20, and 24 V, respectively

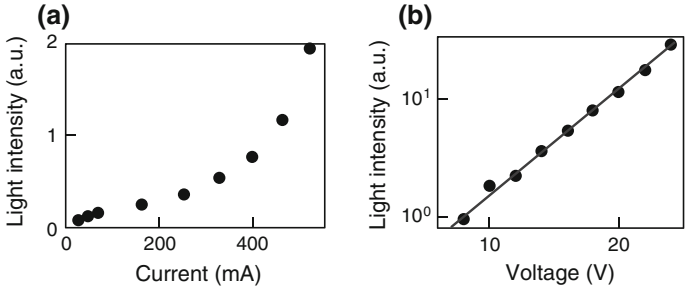

Fig. 2.14 Emitted light intensity. **a** Relation with the injection current. **b** Relation with the forward-bias voltage

structure. The closed circles in Fig. 2.14a show the measured relation between the injected current and the emitted light intensity, where the light intensity was derived by integrating the light emission spectra of Fig. 2.13a over the whole range of the photon energy. The nonlinear relation in this figure shows that the visible light emission originates from hot electrons with much higher energy than those at the bottom of the conduction band. Closed circles in Fig. 2.14b show the measured relation between V and the emitted light intensity, where the vertical axis is on a logarithmic scale. They are fitted by a line, confirming that the emitted light intensity exponentially increases with increasing V. Since the photon energy of the emitted light shown in Fig. 2.13a is much higher than E_g of Si (=1.12 eV), this exponential increase originates from high-energy electrons, because the emitted light intensity is proportional to the number density $n\,(E)$ of high-energy electrons and, furthermore, $n\,(E)$ is proportional to $\exp\,(eV/kT)$, where e, k, and T are the electron charge, Boltzmann's constant, and temperature, respectively.

In contrast to the two peaks at 1.9 and 3.0 eV in the curve A in Fig. 2.11, the curves in Fig. 2.13a have a peak at 2.7 eV, represented by a downward arrow. In order to find the origin of this peak, the upper-left and -right parts of Fig. 2.15 show the dispersion relation and the density of states (DOS) of phonons in Si [8], respectively. The DOS has a peak at 60 meV (indicated by a horizontal arrow), which corresponds to the wave vector between the Γ- and K-points, as indicated by the horizontal and vertical broken lines. The lower part of Fig. 2.15 shows the energy band structure of the electron [9], in which the horizontal and vertical broken lines represent that the electron, with the same wave-vector as that of the high-DOS phonon, has an energy of 2.7 eV. Due to the agreement between this electron energy and the energy of the peaks in Fig. 2.13a, it is concluded that the emission from the visible Si-LED originates from the coupling between an electron-hole pair and a phonon, as was illustrated in Fig. 2.7, which is consistent with the spectral properties of infrared Si-LEDs to be reviewed in Chap. 3.

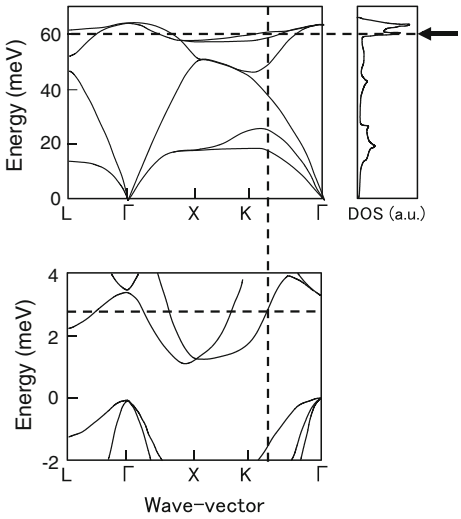

Fig. 2.15 Schematic explanation of the contribution of the coupling between the electron–hole pair and the phonon via DPPs. *Upper part* The dispersion relation and the density of states of phonons. *Lower part* The electronic energy band structure

References

1. M.A. Tran, T. Kawazoe, M. Ohtsu, Appl. Phys. A **115**, 105 (2014)
2. R.J. Van Overstraeten., P. Mertens, Sold-State Electron, **30**, 1077 (1987)
3. M.G. Bernald, G. Duraffourg, Phys. Status Solidi **1**, 699 (1961)
4. A. Einstein, P. Ehrenfest, Z. Phys. **19**, 301 (1923)
5. W. Goldammer, W. Ludwig, Z. Zierau, Phys. Rev. B **36**, 4624 (1987)
6. M. Yamaguchi, T. Kawazoe, T. Yatsui, M. Ohtsu, Appl. Phys. A **121**, 1389 (2015)
7. M. Green, M. Keevers, Progr. Photovoltaics Res. Appl. **3**, 189 (1995)
8. P. Giannozzi, S. de Gironcoli, Phys. Rev. B **43**, 7231 (1991)
9. K. Sieh, P. Smith, Phys. Status Solidi (b) **129**, 259 (1985)

Chapter 3
Infrared Light Emitting Diodes Using Silicon Crystal

This chapter reviews the fabrication and operation of a Si-LED that emits infrared light. In contrast to the single-step spontaneous and stimulated emission processes described in Sect. 1.3.1, those of infrared light emission are two-step processes (Sect. 1.3.2). This is because the emitted photon energy is lower than E_g.

3.1 Device Fabrication

As with the case described in Sect. 2.2, an n-type Si crystal with low As concentration was used [1]. By doping the crystal with B atoms, the Si crystal surface was transformed to p-type, forming a p–n homojunction. An ITO film and an Al film were deposited on opposite surfaces of the Si crystal for use as electrodes. A forward bias voltage of 16 V was applied to inject current (current density of 4.2 A/cm^2) in order to generate Joule-heat for performing annealing, causing the B atom to be diffused and varying the spatial distribution of its concentration. During the annealing, the Si crystal was irradiated, through the ITO electrode, with laser light (light power density, 10 W/cm^2) whose photon energy hv_{anneal} was 0.95 eV (1.30 μm wavelength). Since hv_{anneal} is lower than E_g of Si, the radiated light is not absorbed by the Si crystal. Therefore, in the regions where DPPs are hardly generated, B diffuses simply due to the Joule-heat of the applied electrical energy. However, in the regions where DPPs are easily generated, the thermal diffusion rate of the B atom becomes smaller via the following processes:

(1) Since the energy of the electrons driven by the forward-bias voltage (16 V) is higher than E_g, the difference $E_{Fc} - E_{Fv}$ between the quasi Fermi energies in the conduction band E_{Fc} and the valence band E_{Fv} is larger than E_g. Therefore, the Benard–Duraffourg inversion condition is satisfied. Furthermore, since

M. Ohtsu, *Silicon Light-Emitting Diodes and Lasers*,
Nano-Optics and Nanophotonics, DOI 10.1007/978-3-319-42014-1_3

$h\nu_{anneal} < E_g$, this light propagates through the Si crystal without absorption and reaches the p–n homojunction. As a result, it generates DPPs efficiently at B atoms. Since stimulated emission takes place via DPPs (Sect. 1.3.2), the electrons generate photons by the stimulated emission and are de-excited from the conduction band to the valence band via the phonon energy level.

(2) The annealing rate decreases because a part of the electrical energy for generating the Joule-heat is spent for the stimulated emission of photons. As a result, at the regions where the DPPs are easily generated, the B atoms become more difficult to change.

(3) Spontaneous emission occurs more efficiently at the regions in which the DPPs are easily generated because the probability of spontaneous emission is proportional to that of stimulated emission. Furthermore, with temporal evolution of process (2), the light from stimulated and spontaneous emission spreads through the whole Si crystal, and as a result, process (2) takes place in a self-organized manner throughout the entire volume of the Si crystal.

It is expected that this method of DPP-assisted annealing will form the optimum spatial distribution of the B concentration for efficient generation of DPPs, resulting in efficient device operation. Figure 3.1 shows the temporal evolution of the temperature of the device surface as annealing progressed. After the temperature rapidly rose to 154 °C, it fell and asymptotically approached a constant value (140 °C) after 6 min, at which time the temperature inside the device was estimated to be about 300 °C. The features of this temporal evolution are consistent with those of the principle of DPP-assisted annealing under light irradiation described above: The temperature rises due to the Joule-heat by the applied electrical energy. However, the temperature gradually falls because stimulated emission is induced by the DPPs generated at the domain boundary of the inhomogeneous distribution of the B atoms. Finally, the system reaches the stationary state.

This temporal decrease in the device temperature, and also the temporal increase in the emitted light intensity, have been theoretically reproduced by a stochastic model of the spatial distribution of B atoms, which was controlled by the DPPs [2].

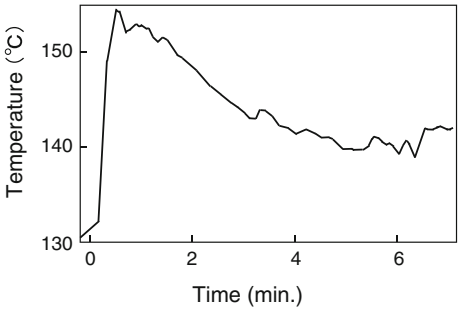

Fig. 3.1 Temporal evolution of the temperature of the device surface as annealing progresses

3.2 Device Operation

Figure 3.2a shows the relationship between the forward-bias voltage (V) applied to the device and the injection current (I) for a Si crystal with a surface area as large as 9 mm^2 and a thickness of 650 μm. This figure indicates negative resistance at $I > 50$ mA, and the breakover voltage V_b was 63 V [3]. This was due to the spatially inhomogeneous current density and the generation of filament currents, as shown in the inset of Fig. 3.2a. In other words, the B distribution had a domain boundary, and the current was concentrated in this boundary region. A center of localization where the electrical charge is easily bound was formed in this current concentration region, and a DPP was easily generated there. That is, the negative resistance is consistent with the principle of the device fabrication described in Sect. 3.1. The reason why V_b was higher than the built-in potential of the Si p–n homojunction is because of the high total resistance due to the thick Si crystal wafer and the large contact resistance between the electrodes and the Si crystal wafer. In addition, although the device surface temperature during annealing (Fig. 3.1) was too low for diffusing the B, localized heating occurred due to the filament currents described above, which made the temperature inside the device sufficiently high. From secondary ion-microprobe mass spectrometry, it was confirmed that the B penetration depth was increased to at least 300 nm by the annealing. For comparison, when the device had a size as small as 0.6 mm^2 in area and 120 μm in thickness, the $V - I$ characteristic did not exhibit such negative resistance but was identical to that of an ordinary LED using a direct transition-type semiconductor, as shown in Fig. 3.2b.

Figure 3.3a, b are photographs showing the device without and with current injection (current density, 4.2 A/cm^2), respectively, at room temperature, which were taken by an infrared CCD camera (photosensitive bandwidth: 1.73–1.38 eV, wavelength: 0.90–1.70 μm) under fluorescent lamp illumination. Figure 3.3b shows a bright spot

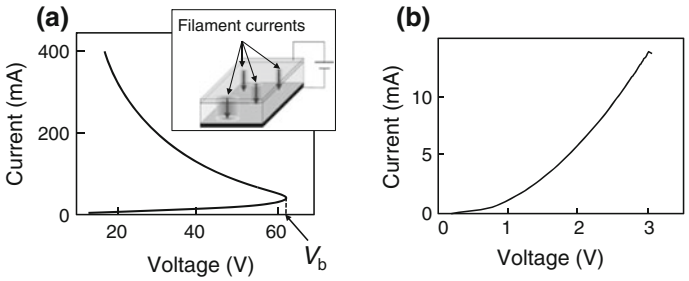

Fig. 3.2 Relationship between the forward-bias voltage (V) to the device and the injection current (I) for the Si crystal. **a** The surface area of the Si crystal is as large as 9 mm^2 and the thickness is 650 μm. The inset is a schematic explanation of the filament currents generated due to the spatially inhomogeneous current density. **b** The surface area is as small as 0.6 mm^2, and the thickness is 120 μm

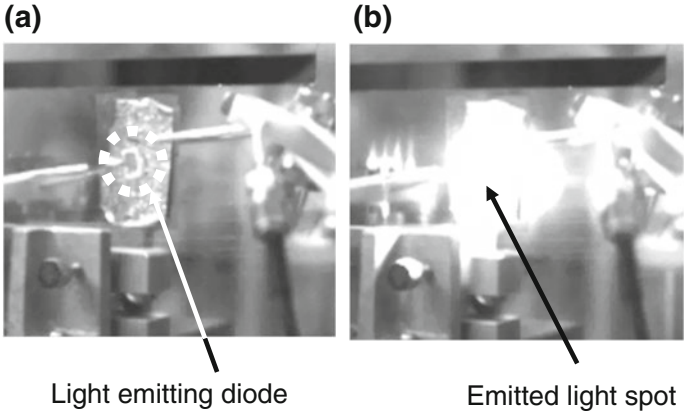

Fig. 3.3 Photographs of the device. **a** and **b** were taken without and with current injection, respectively, at room temperature

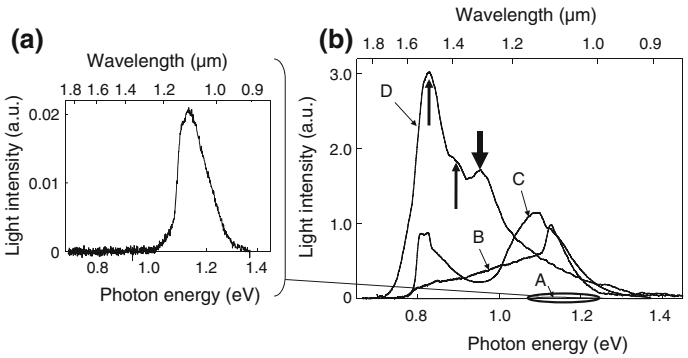

Fig. 3.4 Light emission spectra. **a** The spectrum of a commercial photodiode (Hamamatsu Photonics, L10823) at an injection current density of 0.2 A/cm^2. **b** *Curve A* is identical to the curve in (**a**). *Curves B–D* are the spectra of the devices fabricated by annealing for 1, 7, and 30 min, respectively

of light with an optical power as high as 1.1 W, which was emitted by applying 11 W of electrical power.

It should be pointed out that a conventional Si photodiode can emit light even though its efficiency is extremely low. Figure 3.4a shows the light emission spectrum of a commercial photodiode (Hamamatsu Photonics, L10823) at an injection current density of 0.2 A/cm^2. Higher current injection damaged the photodiode. The main part of the light emission spectrum in this figure is located at energies higher than E_g (=1.12 eV), as a result of the indirect transition caused by phonon scattering [4]. Figure 3.4b shows the light emission spectra of three devices at an injected current density of 1.5 A/cm^2, which were fabricated by the method described in the previous section. Curve A in this figure is identical to the curve in Fig. 3.4a, drawn for comparison. Curves B–D are the spectra of the devices fabricated by DPP-assisted

annealing for 1, 7, and 30 min, respectively. Their profiles considerably differ from that of curve A, and the spectra are located at lower energies than E_g. The light intensity values of the curves B–D appear low at energies lower than 0.8 eV, which is due to the low sensitivity of the photodetector used for the measurement. Although the light emission spectrum of the device fabricated using 1 min of annealing (curve B) still had a clear peak around E_g, the spectrum broadened and reached an energy of 0.75 eV (1.65 μm wavelength). That of the device annealed for 7 min (curve C) showed a new peak at around 0.83 eV (1.49 μm wavelength). In the case of the device annealed for 30 min (curve D), no peaks were seen around E_g; instead, a new peak appeared, identified by a downward thick arrow, at an energy that corresponds to the photon energy $h\nu_{anneal}$ (=0.95 eV, 1.30 μm wavelength) of the light radiated in the annealing process. This peak is evidence that DPPs were generated by the light irradiation and that the B diffusion was controlled. In other words, photon breeding took place also by the two-step de-excitation process (Sect. 1.3.2). The value of the emission intensity at the highest peak (identified by the left thin upward arrow) on curve D was 14-times and 3.4-times higher than those of the peaks on curves B and C, respectively.

Here, the separations between the energies identified by two upward thin arrows (0.83 and 0.89 eV), and by the downward thin arrow (0.95 eV) were 0.06 eV, which is equal to the energy of an optical phonon in Si. This means that the two upward thin arrows show that the DPP with an energy of 0.95 eV was converted to a real photon after emitting one and two optical phonon. This conversion process demonstrates that the light emission described here uses the phonon energy levels as an intermediate state.

The spectrum of curve D extended over the energies 0.73–1.24 eV (1.00–1.70 μm wavelength), which covers the wavelength band of optical fiber communication systems. The spectral width of curve D was 0.51 eV, which is more than 4-times greater than that (0.12 eV) of a conventional commercial InGaAs LED with a wavelength of 1.6 μm. For the device annealed for 30 min, the relation between the applied electric power and the emitted light power was measured at photon energies higher than 0.73 eV (1.70 μm wavelength). From this measurement, it was found that the evaluated external power conversion efficiency and the differential external power conversion efficiency reached as high as 1.3% and 5.0%, respectively, with an applied electric power of 11 W. This relation was also measured for emitted photon energies of 0.11–4.96 eV (0.25–11.0 μm wavelength), giving an external power conversion efficiency and a differential external power conversion efficiency as high as 10% and 25%, respectively.

In order to estimate the quantum efficiency, the relation between the injection current density J and the emitted light power density P_d at photon energies higher than 0.73 eV (1.70 μm wavelength) was measured for the device annealed for 30 min. From this measurement, it was found that P_d was proportional to J^2, which is due to the two-step spontaneous emission process; i.e., one electron is converted to two photons. For comparison, P_d is proportional to J in a conventional LED device. Furthermore, the external quantum efficiency was estimated to be 15% at J=4.0 A/cm^2, and the differential external quantum efficiency was estimated to be 40% at

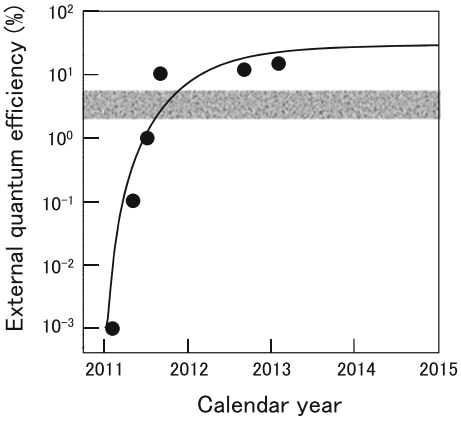

Fig. 3.5 Progress in external quantum efficiency. The *solid curve* is the logistic curve fitted to the experimental values. The *gray thick horizontal line* represents the value for a commercially available InGaAs near-infrared LED

$J = 3.0$–4.0 A/cm^2. From the measured relation between J and P_d at photon energies of 0.11–4.96 eV (0.25–11.0 μm wavelength), the external quantum efficiency at photon energies higher than 0.73 eV (1.70 μm wavelength) was as high as 150%. The reason why this value is higher than 100% is that the two-step spontaneous emission process converts one electron not to one photon but to two photons.

Figure 3.5 shows the progress made in increasing the external quantum efficiency in the wavelength range of 1.32 ± 0.15 μm. By early 2013, an efficiency of 15% had been reached. This value is already higher than those of commercially available 1.3 μm-wavelength LEDs using the direct transition-type semiconductor InGaAs, such as Hamamatsu Photonics L7866 and L10822 (external quantum efficiencies of 2% and 5%, respectively). The solid curve in this figure is the least-squares fitted logistic curve, which has been popularly used to represent population growth, technological progress, and increases in the number of articles on the market. This curve fits the experimental values well, showing the rapid, smooth progress of Si-LED technology.

The high optical power emitted from the fabricated Si-LED, as high as 1 W, offers a variety of novel application systems; several have been proposed, and their feasibilities have been confirmed by experiments [5]. One example is infrared imaging, as demonstrated in Fig. 3.6. Figure 3.6a shows one scene from a video of a dancing toy robot acquired by irradiating the robot with infrared light from the Si-LED. As a reference, Fig. 3.6b shows that from a conventional video acquired by irradiating the robot with visible light. Another example is demonstrated by Fig. 3.7. Figure 3.7a shows a piece of crumpled black plastic tape attached to a substrate. When it is irradiated with the focused infrared light beam from the Si-LED, it immediately ignites and gives of smoke, as shown in Fig. 3.7b, c, respectively. This burning experiment suggests novel applications of this technique to materials processing.

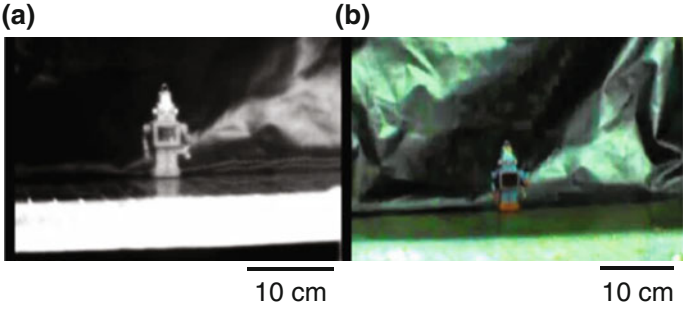

Fig. 3.6 Infrared imaging. **a** One scene from a *video* of a dancing toy robot acquired under infrared irradiation. **b** One scene from a conventional video acquired under visible light irradiation, shown for reference

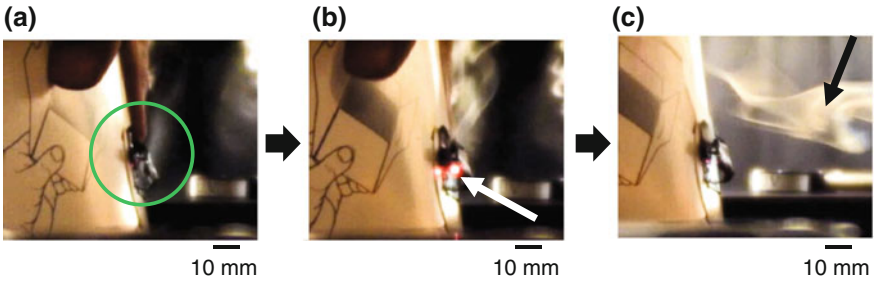

Fig. 3.7 Burning a piece of *black plastic tape*. **a** Image of the tape, which is crumpled and attached to a substrate, indicated by the *green circle*. **b** A flame ignited by infrared light irradiation, indicated by the *white arrow*. **c** *Smoke* pouring out after the burning, indicated by *black arrow*

3.3 Spatial Distribution of Boron

This section presents the analysis results of the three-dimensional spatial distribution of the doped B atoms [6]. Figure 3.8 shows the three-dimensional spatial distribution of B atoms at the p–n homojunction, which was measured by atom probe field ion microscopy with sub-nanometer resolution [7]. The black dots represent the positions of the individual B atoms. The distribution is projected onto the xy-, yz-, and zx-planes ((001), (100), and (010) planes), represented by green, blue, and red dots, respectively.

It should be noted that the Si crystal is composed of multiple cubic lattices with a lattice constant a of 0.54 nm [8], and its top surface lies in the xy-plane. The light irradiated during the DPP-assisted annealing is normally incident on this plane; i.e., the light propagation direction is parallel to the z-axis, which is parallel to the [001] orientation.

Some of the regularly arranged Si atoms are replaced by the doped B atoms in the DPP-assisted annealing. It has been pointed out that phonons can be localized at the

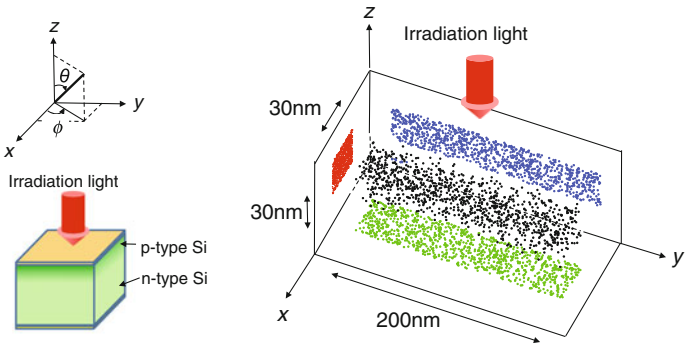

Fig. 3.8 Three-dimensional spatial distribution of B atoms, measured by the atom probe ion microscopy

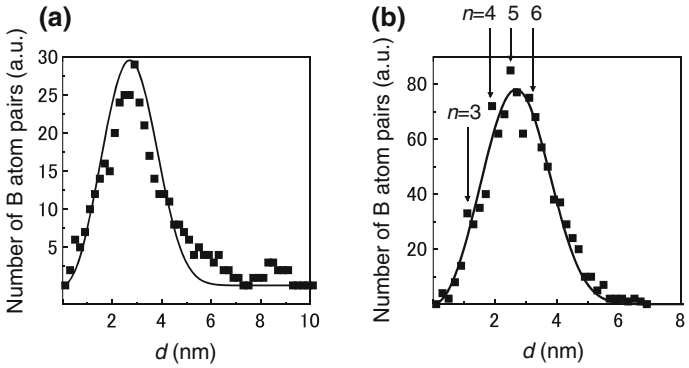

Fig. 3.9 Number of B atom pairs plotted as a function of the separation d between the B atoms in the pair. **a** The un-annealed Si crystal. **b** The DPP-assisted-annealed Si crystal

B atoms for creating a DPP under light irradiation because the B atoms are lighter than the Si atoms. However, for this localization, it has also been pointed out that two or more adjacent B atoms (in other words, two or more unit cells containing B atoms) are required (refer to Fig. C.1 in Appendix C). Since the doped B atom concentration is as low as 0.04% relative to the Si atom concentration, making it difficult for more than three B atoms to aggregate, the following discussion considers two closely spaced adjacent B atoms (a B atom pair), around which a phonon is localized for creating a DPP. That is, the pair of unit cells containing the B atoms serves as a phonon localization center.

Figure 3.9a, b show the numbers of B atom pairs plotted as a function of the separation, d, between the B atoms in the pair, which were derived from the measurement results in Fig. 3.8. Since the distribution of the number of B atom pairs is nearly random, it can be least-squares fitted by the Weibull distribution function (the solid curve in these figures), which is expressed as

$$p(d) = (3/\beta) \cdot (d/\beta)^2 \cdot \exp\left[-(d/\beta)^3\right], \tag{3.1}$$

where δ is the concentration of the B atoms, and $\beta = \sqrt[3]{3/4\pi\delta}$. In the un-annealed Si crystal (Fig. 3.9a), the measured number of B atoms pairs deviates from the solid curve in the range $d > 45$ nm. The deviation depends on the characteristics of the ion implantation.

In contrast, in the Si crystal after the DPP-assisted annealing (Fig. 3.9b), the deviation is much less than that in Fig. 3.9a, which means that the DPP-assisted annealing modified the spatial distribution and decreased the deviation induced by the ion implantation, making the distribution more random. However, at specific values of d ($= na$, where $n = 3, 4, 5, 6$; refer to the four downward arrows in this figure), the number of B atom pairs still deviates from the solid curve and is larger than that of the solid curve. This is explained as follows: The B atom pair with the shortest d (i.e., equal to the lattice constant a) can orient in a direction parallel to the [1,0,0], [0,1,0], or [0,0,1] orientation because the Si crystal is composed of multiple cubic lattices. As a result, the wave-vector (momentum) of the localized phonon points in this direction, which corresponds to the Γ-X direction in reciprocal lattice space (Fig. 3.10). Thus, a photon is efficiently created because this Γ-X direction is the same as the direction of the wave-vector of the phonon required for recombination between an electron at the bottom of the conduction band at the X-point and a hole at the top of the valence band at the Γ-point. Here, it should be noted that the absolute value of

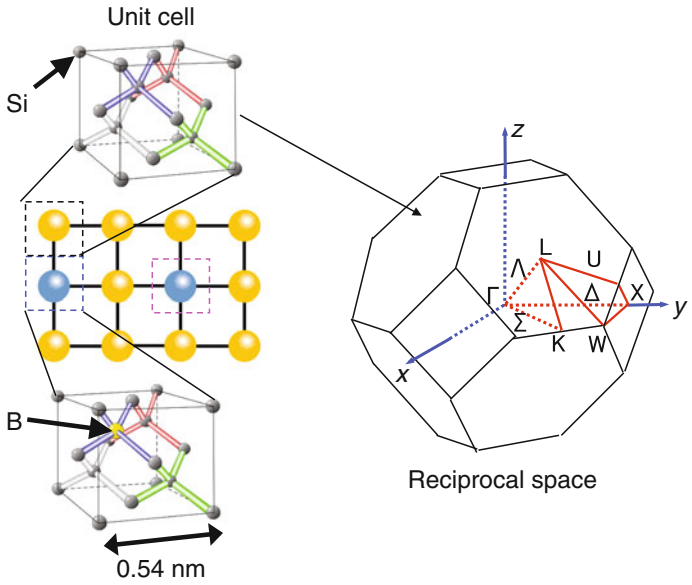

Fig. 3.10 A unit cell of the Si crystal in real lattice space and in reciprocal lattice space

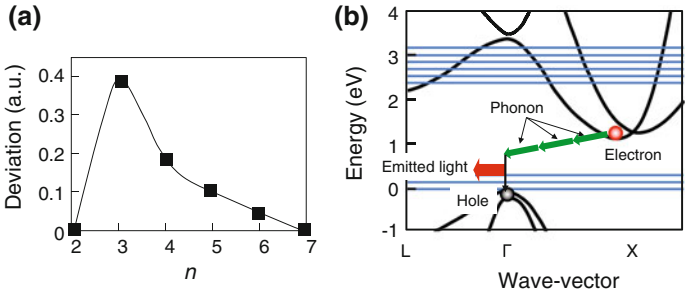

Fig. 3.11 Relation between n and the deviation. **a** Measured results. **b** The energy band structure of Si and schematic explanation of light emission

the wave-vector of the phonon has to be $1/a$ for this electron–hole recombination to take place. Furthermore, it should also be noted that, among the phonons localized at the B atom pair with separation d $(= na)$, the absolute value of the wave-vector of the lowest mode is $1/na$. By comparing these two absolute values, it is found that the DPP at this B atom pair has to create n phonons for recombination. Thus, it can be concluded that the four downward arrows in Fig. 3.9b indicate selective increases in the number of B atom pairs with separation $d = na$ due to the DPP-assisted annealing, and these pairs serve as phonon localization centers.

Figure 3.11a shows the relation between n and the measured deviation in Fig. 3.9b. This figure shows that the deviation takes the maximum value at $n = 3$, which means that B atom pairs most efficiently create three phonons for light emission, as is schematically shown in Fig. 3.11b. This phonon creation process is consistent with the discussion in Sect. 4.1, in which the magnitudes of the phonon sidebands in the light emission spectra were analyzed based on the density of states of phonons and the estimated value of the Huang–Rhys factor. As a result, the emitted photon energy $h\nu_{em}$ is expressed as $h\nu_{em} = E_g - 3E_{phonon}$. By substituting the values of E_g (= 1.12 eV) and the relevant optical mode phonon energy E_{phonon} (=65 meV [9]) into this equation, the value of $h\nu_{em}$ is derived to be 0.925 eV, which is identical to the photon energy $h\nu_{anneal}$ irradiated during the DPP-assisted annealing. This numerical relation confirms that photon breeding with respect to photon energy occurs.

Figure 3.9b indicates selective increases in the number of B atom pairs with separation $d = na$. This means that, since n is an integer, B atom pairs are apt to orient along a plane perpendicular or parallel to the top surface of the Si crystal (zenith angle $\theta = 0°$ or $90°$ in Fig. 3.8). Orientation along other directions in which n is not an integer ($\theta \neq 0°, 90°$) hardly occurs.

Figure 3.12 shows the relation between the zenith angle θ and the number of B atom pairs. It can be seen that this number takes the maximum value at $\theta = 90°$, which means that the B atom pairs are apt to stretch in a plane (xy-plane) which is parallel to the top surface of the Si crystal, i.e., perpendicular to the propagation direction ([00$\bar{1}$] orientation; z-axis) of the light irradiated during the DPP-assisted annealing. On the other hand, the number of B atom pairs takes the minimum value

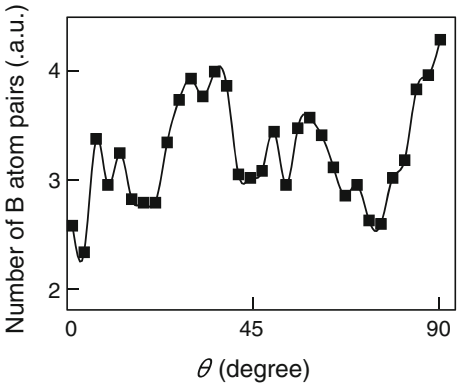

Fig. 3.12 Relation between the *zenith angle* θ and the number of B atom pairs

at $\theta = 0°$, which means that the B atom pairs hardly orient along the propagation direction (z-axis) of the light irradiated during the DPP-assisted annealing. This is because the phonons are hardly localized along this direction since their momenta (wave-vectors) are parallel to $\theta = 90°$ [10].

3.4 Polarization Control

It is expected that photon breeding takes place not only with respect to photon energy described above but also with respect to photon spin. That is, the light emitted from the LED can be polarized if it is fabricated by irradiating the Si crystal with polarized light during the DPP-assisted annealing.

The output light from conventional LEDs is not polarized, and several methods have been proposed for polarizing it, such as using the specific anisotropic optical properties of nonpolar GaInN quantum wells [11] and installing a complicated subwavelength-size metallic nanograting [12]. Instead of these approaches, the present section proposes a novel polarization control method for infrared Si-LEDs based on photon breeding with respect to photon spin [6].

The fabrication method is the same as that described in Sect. 3.1, except that the irradiated light is linearly polarized along the x-axis. Its photon energy, $h\nu_{anneal}$, and wavelength are 0.924 eV and 1.342 μm, respectively.

For evaluating the polarization characteristics of the fabricated Si-LED, the emitted light was decomposed into two linearly polarized components by using a linear polarizer, and their intensities ($I_{\parallel}$, $I_{\perp}$) were acquired. The polarization directions of these components are respectively parallel and perpendicular to that of the light irradiated during the DPP-assisted annealing.

Their light emission spectra at an injection current of 100 mA are represented by the curves A and B in Fig. 3.13, whose spectral peaks are close to $h\nu_{anneal}$ due to the photon breeding with respect to photon energy. It is seen that $I_{\parallel}$ is larger than

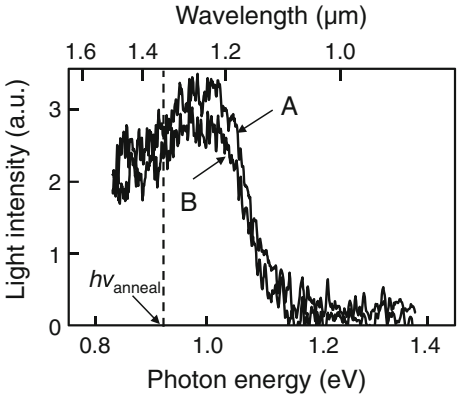

Fig. 3.13 Light emission spectra. *Curves A* and *B* are the linearly polarized components, which are respectively parallel and perpendicular to the direction of the linear polarization of the light irradiated during the DPP-assisted annealing. The annealing time was 180 min

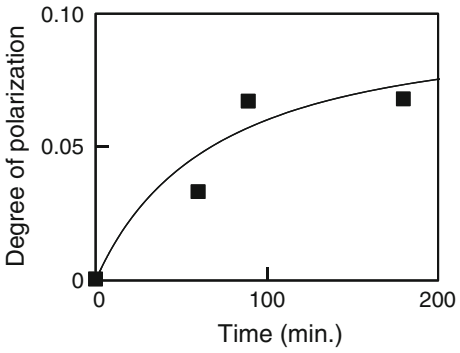

Fig. 3.14 Relation between the DPP-assisted annealing time and the degree of polarization P at the photon energy, $h\nu_{anneal}$. *Black squares* represent the measured values. The *solid curve* represents the theoretical values, which were fitted to the measured values

$I_\perp$ in a wide spectral range around $h\nu_{anneal}$. Since the linearly polarized light is the superposition of the two photons with up- and down-spins, this difference between $I_\parallel$ and $I_\perp$ in this figure also represents the successful results of polarization control, which is due to photon breeding with respect to photon spin.

The black squares in Fig. 3.14 represent the measured relation between the DPP-assisted annealing time and the degree of polarization

$$P = \left(I_\parallel - I_\perp\right) / \left(I_\parallel + I_\perp\right) \tag{3.2}$$

at the photon energy $h\nu_{anneal}$. The value of P in this figure is zero at zero annealing time because the Si crystal is optically isotropic. However, this value increases with increasing annealing time and asymptotically approaches a maximum value of 0.07. This increase is not due to the optical anisotropy induced by the Joule-heat because the applied Joule energy was too low to strain or deform the Si crystal. For reference, the surface temperature was maintained at as low as 154 °C in the DPP-assisted annealing (Fig. 3.1).

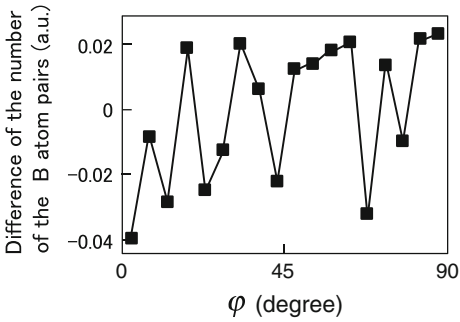

Fig. 3.15 Relation between the azimuthal angle φ and the difference in the numbers of B atom pairs after and before the DPP-assisted annealing

The measured values were fitted by the solid curve in Fig. 3.14. This curve represents the result of numerical calculation based on the two-level system model (refer to Appendix E).

Figure 3.15 shows the relation between the azimuthal angle φ and the number of the B atom pairs. This angle is defined in the xy-plane ($\theta = 90°$), and $\varphi = 0°$ corresponds to the polarization direction (x-axis) of the light irradiated during the annealing. The vertical axis in Fig. 3.15 represents the difference in the numbers of B atom pairs after and before the DPP-assisted annealing. The negative value of this difference at $\varphi = 0°$ means that the number of B atom pairs orienting to $\varphi = 0°$ decreases as a result of the DPP-assisted annealing. In the region $\varphi > 45°$, this difference becomes a positive value, which means that the number increased due to the DPP-assisted annealing. The number of B atom pairs takes the maximum value at $\varphi = 90°$. This angular dependence means that the diffusion of the B atoms was controlled by the linearly polarized light irradiated during the DPP-assisted annealing, with the result that the B atom pairs oriented to $\varphi = 90°$.

As a result, the light emitted from the fabricated LED was polarized, and the polarization direction was governed by that of the light irradiated during the DPP-assisted annealing. There are two possible origins of this induced polarization of the emitted light: (1) Since the oriented B atom pairs work as a kind of nano-wire grid in the xy-plane (the orientation of this grid is $\varphi = 90°$), the light emitted from the fabricated LED can be linearly polarized in the direction ($\varphi = 0°$) perpendicular to the direction of the grid. (2) First, when the LED is fabricated by the DPP-assisted annealing, transverse optical phonons are created at the B atom pairs and couple with the DPs. The vibration direction of these phonons is parallel to that of the electric field of the polarized light ($\varphi = 0°$) irradiated during the DPP-assisted annealing. Next, when the fabricated LED is operated, since these phonons are created again, the direction of the electric field vector of the emitted light becomes also parallel to the vibration direction of these phonons. Therefore, the polarization direction of the emitted light becomes identical to that of the light irradiated during the DPP-assisted annealing.

The number of B atom pairs at $\varphi \geq 45°$ in Fig. 3.15 is 8.6% of the total, which corresponds to a P value of 0.07 for the 180 min annealing time. This correspondence

supports the origins (1) and (2) presented above. It should be possible to increase P further by more precisely controlling the annealing parameters for orienting more B atom pairs along the direction $\varphi = 90°$ (and also $\theta = 90°$).

References

1. T. Kawazoe, M.A. Mueed, M. Ohtsu, Appl. Phys. B **104**, 747 (2011)
2. K. Takahashi, M. Katori, M. Naruse, T. Kawazoe, M. Ohtsu, Abstract of 2015 Autumn Meeting of the Physical Society of Japan, September 2015, Osaka, Japan, paper number 18aCR-3
3. E. Shl, *Nonequilibrium Phase Transitions in Semiconductors* (Springer, Berlin, 1987)
4. R.A. Milano, P.D. Dapkus, G.E. Stillman, IEEE Trans. Electron Device. **29**, 266 (1982)
5. M. Ohtsu, *Proceedins of the Northern Optics & Photonics* (Lappeenranta, 2015), p.18
6. T. Kawazoe, K. Nishioka, M. Ohtsu, Appl. Phys. A **9**, 1 (2015)
7. K. Hono, Prog. Mater. Sci. **47**, 621 (2001)
8. K. Godwod, R. Kowalczyk, Z. Szmid, Phys. Stat. Sol. (a) **21**, 227 (1974)
9. E. Anastassakis, A. Pinczuk, E. Burstein, F.H. Pollak, M. Cardona, Solid State Commun. **8**, 133 (1970)
10. Y. Shinohara, T. Otobe, J. Iwata, K. Yanaba, J. Phys. Soc. Jpn. **67**, 685 (2012)
11. M.F. Schubert, S. Chhajed, J.K. Kim, E.F. Schubert, Appl. Phys. Lett. **91**, 051117 (2007)
12. L. Zhang, J.H. Teng, S.J. Chua, E.A. Fitzgerald, Appl. Phys. Lett. **95**, 261110 (2009)

Chapter 4
Contribution and Control of Coherent Phonons

This chapter estimates the value of the Huang–Rhys factor, which is a parameter representing the coupling strength between electron–hole pairs and phonons. Furthermore, the origin of the sidebands described in Chaps. 2 and 3 is described. Finally, how to control the generation of these sidebands is demonstrated.

4.1 Strength of Phonon Coupling

The main features of the Si-LEDs reviewed in Chaps. 2 and 3 are that the emitted photon energy does not depend on E_g; instead, the emitted light has approximately the same photon energy as the photon energy $h\nu_{anneal}$ of the light radiated during annealing. In other words, photon breeding occurs. Also, phonon sidebands are found in the light emission spectrum, and these are caused by the creation of DPPs. The phonons constituting these DPPs have been theoretically shown to be multi-mode coherent phonons [1]. The parameter representing the coupling strength between electron–hole pairs and phonons is called the Huang–Rhys factor, S [2]. The value of S can be obtained experimentally from the intensities of the phonon sidebands [3, 4].

This section estimates the value of S in the fabricated Si-LEDs by comparing the measured emission intensities of the phonon sidebands found in its light emission spectrum and a simulation result of the light emission process [5]. In the case of the device used in this section, the photon energy of the light absorbed in the depletion layer is 1.2–3.0 eV, which was estimated based on the depletion layer depth and thickness obtained from the B doping conditions. There is no singular point in the Si band structure in this range of energies and especially in the range corresponding to the photon energy of the emitted light (1.4 eV). Thus, this range is suitable for evaluating the involvement of phonons in the light emission process. Therefore, the surface of the device was irradiated with light having a photon energy $h\nu_{anneal}$ of

M. Ohtsu, *Silicon Light-Emitting Diodes and Lasers*,
Nano-Optics and Nanophotonics, DOI 10.1007/978-3-319-42014-1_4

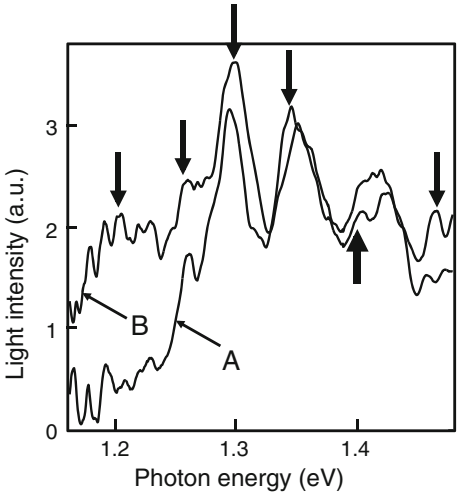

Fig. 4.1 Light emission spectra of the Si-LED. The *curves A* and *B* show the spectra obtained 1 and 3 h after starting annealing, respectively

1.4 eV during annealing. The principle of light emission and DPP-assisted annealing are the same as those described in Sects. 1.3.1 and 2.2, respectively.

Ion implantation was used to dope B into an n-type Si crystal in order to form a p-type layer, thus fabricating a p–n homojunction. The highest B ion implantation energy was 700 keV, the concentration was 1×10^{19} cm^{-3}, and the thickness of the p-type layer was 2 μm. After dicing this crystal, an ITO film and a Cr/Al film were respectively deposited on the surfaces of the p-type and n-type layers for use as electrodes. A forward-bias voltage of 2 V was applied to the device (current density 0.96 A/cm^2) while simultaneously irradiating it with laser light ($h\nu_{anneal} = 1.4$ eV) to perform DPP-assisted annealing for 3 h.

Figure 4.1 shows the light emission spectra measured when a forward current (current density 3.2 A/cm^2) was injected into the Si-LED. The curves A and B are the spectra obtained 1 and 3 h after starting annealing, respectively. By comparing these curves, it can be seen that the emission intensity showed almost no change at photon energies of 1.25 eV and above, whereas at photon energies below 1.25 eV, the emission intensity was considerably increased. A possible reason for this is that, in the regions where low-energy photons are easily generated, the energy dissipation level due to stimulated emission produced in those regions is small, like those discussed in (2) in Sect. 2.2. Thus, the thermal diffusion rate is similar to that in region (1) in Sect. 2.2, and therefore, annealing proceeds slowly. This phenomenon suggests the validity of the annealing principle discussed in Sect. 2.2. In Fig. 4.1, the photon energy $h\nu_{anneal}$(=1.4 eV) of the light irradiated during annealing is indicated by the upward arrow. From the curves A and B, it is found that this Si-LED emitted light with a photon energy approximately equal to $h\nu_{anneal}$; i.e., photon breeding took place. Furthermore, multiple sidebands are observed in the curve B (indicated by the downward arrows). The spacing between these downward and upward arrows are

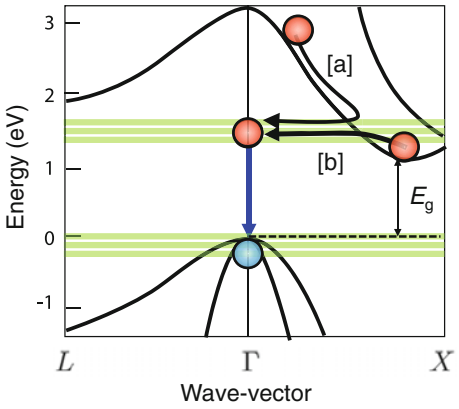

Fig. 4.2 Schematic explanation of the light emission process via DPP energy levels. [a] and [b] represent two possible relaxation processes

approximately constant at 60 meV, which agrees with the energy of optical phonons in Si [6], and therefore, these sidebands likely originate from phonons.

In the Si-LED fabricated here, since it involves a simple single-step transition, only one photon is emitted due to the radiative relaxation of a single electron. In addition, the emission lifetime of a Si-LED using DPPs is on the order of 1 ns (Sect. 8.1), which is considerably shorter than the lifetime of the weak light emission from a normal Si bulk crystal. However, it is three to four orders of magnitude larger than the intraband relaxation time of electrons in Si (0.1–1 ps) [7, 8]. Therefore, it is reasonable to assume that the injected electrons do not radiatively relax during the relaxation process (a) in Fig. 4.2, but instead radiatively relax by coupling with phonons after they have relaxed to the bottom of the conduction band, as shown by process (b). This indicates that the electron–hole pairs have an energy identical to E_g. Therefore, it can be concluded that the difference between the photon energy of the emitted light and E_g is the energy of the phonons that have coupled with the electron–hole pairs.

The light emission spectrum was obtained via simulation, and the coupling strength between electron–hole pairs and phonons was examined by comparing the simulation results with the measured spectrum. The following four assumptions were made in the simulation:

(1) The electron and hole are at the bottom of the conduction band and at the top of the valence band, respectively, and the momentum and energy of the phonon are imparted to this electron–hole pair. This assumption was made based on the fact that the electron and hole intraband relaxation time is shorter than the emission lifetime via the phonon level, as described above.
(2) The electron–hole pair couples with coherent phonons including all optical modes. This was assumed based on experimental results [9] and theoretical considerations [1] regarding DPPs.
(3) The probability distribution of the number of phonons that couple with an electron–hole pair follows a Poisson distribution. In other words, the proba-

bility of n phonons coupling with an electron–hole pair is proportional to $S^n/n!$. This means that coupling of electron–hole pairs and phonons via DPPs occurs randomly.

(4) Radiative relaxation occurs by following the momentum conservation law between the initial state and the final state.

The simulation procedure is as follows:

(I) Based on assumption (3), the number of phonons that couple with an electron–hole pair is determined.

(II) Based on assumption (2), from among all of the optical phonons, phonons whose number was determined in (I) are randomly selected. From this number and the dispersion relation of phonons in Si [10], the momentum and energy of the coupling phonons are determined.

(III) From among the electron energy levels between the Γ-point and the X-point, those at the bottom of the conduction band, having the lowest energy are selected. Then, their momenta and the momenta of the phonons selected in (II) are summed up. If this summed value and the value of the momentum at the Γ-point do not match, no light emission occurs, and the procedure returns to (I). On the other hand, if they do match, the light whose photon energy corresponds to the sum of the energies of the electron–hole pair and the phonons is emitted. Therefore the value of this photon energy can be calculated. Then the procedure returns to (I).

(IV) The number of individual photons, obtained by repeating (I)–(III) above, is determined, and the simulation ends.

Figure 4.3a shows the light emission spectrum obtained by performing the simulation using both longitudinal optical mode (LO-mode) and transverse optical mode (TO-mode) phonons as the phonons that couple with the electron–hole pair, where n is the number of phonons. Multiple peaks corresponding to each n are observed in this spectrum, similarly to the measured results (Fig. 4.1). For ease of viewing the spectral shape, the heights of all peaks are normalized to unity. By comparing the curve in this figure with the curve shown in Fig. 4.1, it can be concluded that the phonons that couple with the electron–hole pair are composed of both LO-mode and TO-mode phonons since the photon energies at the peaks match, and since the spectral shapes resemble each other. For the sake of comparison, Fig. 4.3b shows a light emission spectrum obtained by performing the simulation using only LO-mode phonons. The positions of the peaks on the curve in Fig. 4.3b differ from the positions of the peaks in Figs. 4.1 and 4.3a, from which it is confirmed that both LO-mode and TO-mode phonons are involved in the coupling with the electron–hole pair.

Next, to determine the value of the Huang–Rhys factor, S, the heights of the emission peaks were considered. As described in assumption (3) above, since the distribution of the number of phonons n follows a Poisson distribution that depends on the value of S, the height of each spectral peak in Fig. 4.3a also depends on the value of S. Hence, least squares fitting was carried out on the heights of each peak in Fig. 4.3a and each peak on the curve B in Fig. 4.1. As a result, the value of S was

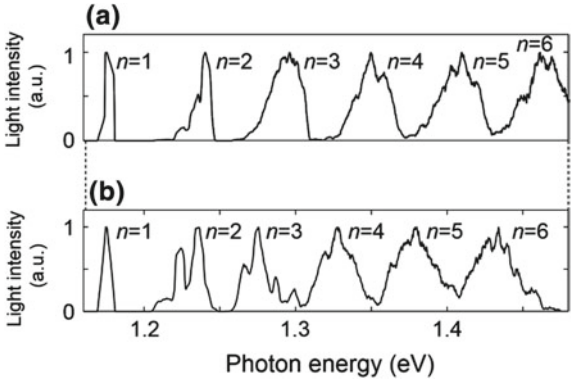

Fig. 4.3 Light emission spectra obtained by performing the simulation. The parameter n is the number of phonons that coupled with an electron–hole pair via a DPP. **a** The results obtained by using both longitudinal optical mode (LO-mode) and transverse optical mode (TO-mode) phonons as the phonons that couple with the electron–hole pair. **b** The result obtained by using only LO-mode phonons

found to be 4.08 ± 0.02. In a normal bulk Si crystal, on the other hand, S ranges from 0.001 to 0.01 [11], which means that the DPP-mediated coupling between the electron–hole pair and phonons is two to three orders of magnitude stronger. The peak widths in the light emission spectrum of the actual device were found to differ from those in the simulated spectrum. This is because coupling between the electron–hole pair and acoustic phonons was not taken into account in the simulation.

4.2 Contribution of the Multimode Coherent Phonons

Previous sections have revealed that DPs are accompanied by multimode coherent phonons, resulting in the creation of DPPs. High-resolution Raman spectroscopy [12] and Fourier transform infrared spectroscopy [13] have been used to study the spectral properties of phonons generated in a super-wavelength sized space in a macroscopic material. Furthermore, coherent phonons (CPs) have been generated by irradiating macroscopic materials with short optical pulses, and their spectral properties have been studied by measuring CP-induced temporal variations in macroscopic physical quantities of the materials, such as the optical reflectivity [14, 15]. Theoretical studies have also been carried out to explain several phenomena caused by these CPs [16]. In contrast to these conventionally studied CPs, the multimode coherent phonons are excited by the DPs in nanometric spaces. These multimode coherent phonons in the nanometric spaces (MCP-NSs) have large uncertainties in their momenta (wavenumbers) because of the sub-wavelength size of the nanometric spaces in which they are generated. In this section, the origin of the sidebands observed in the light emission

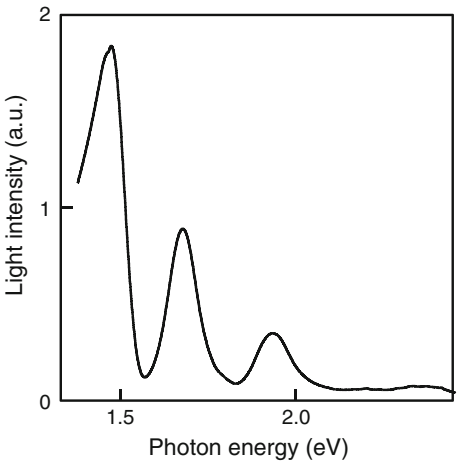

Fig. 4.4 Main part of the spectrum of the light emitted from the Si-LED with an injection current of 450 mA

spectrum of a visible Si-LED is reviewed based on the results of measurement of optical phonons in the MCP-NSs by using pump–probe spectroscopy [17].

A Si-LED was fabricated by applying a forward-bias voltage of 3.5 V (injection current: 240 mA) while irradiating the Si crystal with pulsed laser light for 1 h. The laser light had a photon energy $h\nu_{anneal}$ of 3.1 eV (400 nm wavelength), a pulse width of 100 fs, a repetition frequency of 80 MHz, a pulse energy density of 5×10^{-8} J/cm^2, and an average power density of 4 W/cm^2. The principles of light emission and DPP-assisted annealing are the same as those of Sects. 1.3.1 and 2.2, respectively. The reason for using a pulsed laser, not a CW laser, is to maintain a sufficiently high peak power for efficient annealing by light absorption.

Figure 4.4 shows the main part of the spectrum of the light emitted from the fabricated Si-LED with an injection current of 450 mA. The curve in this figure clearly shows three peaks in the visible region. The spectral component at 3.1 eV ($=h\nu_{anneal}$), which originated from the light irradiated in the annealing process (i.e., photon breeding), is not displayed due to the low efficiency of the diffraction grating in the monochromator used for the spectral measurement. The separations between adjacent peaks are about 250 meV (60 THz), from which these peaks can be identified as phonon sidebands originating from the strong coupling between DPs and MCP-NSs in the Si crystal, as will be discussed in the following.

In order to generate and evaluate the MCP-NSs for studying the origin of the sidebands in Fig. 4.4, pump–probe laser spectroscopy was employed based on the principle of impulsive stimulated Raman scattering (ISRS) [18]. If the spectral width of the optical pulse (carrier frequency ν) from the light source is wider than the eigen-frequency of the phonon, ν_p, the intensity of the frequency components $\nu - \nu_p$ in the optical pulse can be maintained sufficiently high for generating the MCP-NSs efficiently.

Since the generated MCP-NSs temporally modulate the Coulomb potential of the interaction with electrons, the energy band structure of the electrons is modulated,

resulting in modulation of the optical reflectivity of the Si crystal [15, 19]. Among the coherent and incoherent phonons, this modulation enables selective detection of the MCP-NSs because the thermally excited incoherent phonons do not induce any variations in the optical reflectivity.

The temporal variation of the optical reflectivity can be acquired by plotting the reflected probe beam intensity as a function of the time difference, t, between the arrival times of the incident probe and pump optical beams at the Si crystal surface. A Ti:sapphire laser was used as a light source. The center wavelength was 780–805 nm (photon energy, 1.54–1.59 eV), and the pulse width was 15 fs. The temporal variation of the optical reflectivity was measured by lock-in detection of the probe beam intensity reflected from the Si crystal surface.

Figure 4.5a shows a normalized fractional variation of the optical reflectivity measured as a function of the time difference defined above. The curve in this figure represents a rapidly oscillating, amplitude-modulated optical interference signal between the pump and probe beams. Figure 4.5b shows the spectrum obtained by Fourier transforming the fractional variation of the optical reflectivity when the average powers of the pump and probe beams were 120 and 20 mW, respectively. Their beam spot diameters were 1 mm. As represented by the four downward arrows, the spectral curve shows several sidebands on both sides of the high spectral peak of the optical interference signal at 385 THz. These sidebands originate from the amplitude and phase modulations of the reflected probe beam intensity, i.e., the modulation of the optical reflectivity of the Si crystal. These results suggest that there is strong coupling between the MCP-NSs and the pump-beam photons.

In order to evaluate the spectral properties in Fig. 4.5b more quantitatively, the average power of the probe beam was increased to 120 mW to increase the measurement sensitivity. Figure 4.6 shows the measured Fourier-transformed spectrum. In this curve, the interference signal peak at 385 THz is much higher than the maximum

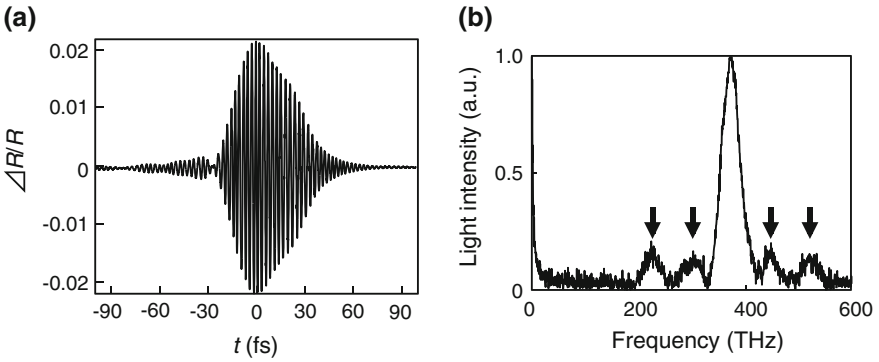

Fig. 4.5 Measured optical reflectivity. **a** Normalized fractional variation of the optical reflectivity measured as a function of the time difference t between the arrival times of the incident probe and pump optical beams at the Si crystal surface. **b** The spectrum obtained by Fourier transforming the fractional variation of the optical reflectivity

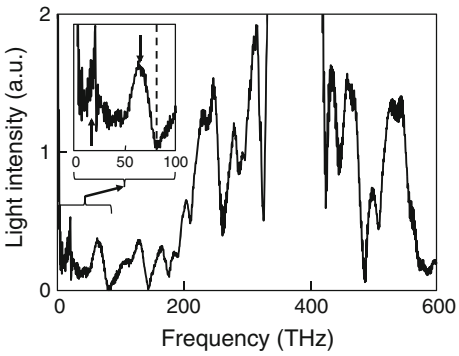

Fig. 4.6 Measured Fourier-transformed spectrum. The *inset* represents the magnified spectral curve of the signals originating from the MCP-NSs

on the vertical axis. On both sides of this over-scaled peak, many more sidebands are seen, as compared with Fig. 4.5b. In addition to the optical interference signal and the sidebands in Figs. 4.5b and 4.6 also reveals the unique signals originating from the MCP-NSs. The spectral curve of these signals is magnified and shown in the inset of Fig. 4.6. These signals are manifested by spectral peaks at frequencies lower than 80 THz, as represented by the two arrows. The high-frequency cut-off, which is governed by the value $\nu - \nu_p$, was confirmed to be 80 THz because the spectral intensity of the curve in the inset decreased to zero at 80 THz (represented by a vertical broken line in the inset). The curve in the region higher than 80 THz represents tails of the sidebands of the optical interference signal.

The spectral peaks shown by the two arrows on the curve in the inset are at the frequencies of 18 and 64 THz (74 and 265 meV). It is easily seen that the spectral intensity at 64 THz, which is defined by the area under the bell-shaped spectral curve, is larger than that at 18 THz. As a result of the comparison between the spectral intensities, it was found that the sidebands with a separation of about 60 THz in Fig. 4.4 originated from the spectral peak at 64 THz in this magnified curve.

For a more detailed evaluation of the curve in the inset, it was fitted by the superposition of the Lorentzian spectral curves of the fundamentals and harmonics of the LO-mode phonons with the center frequency $n\nu_p$, which can contribute to forming the MCP-NSs. The integer n represents the order of the harmonics, where $n = 1$ represents the fundamental. The center frequency ν_p was set to 15.6 THz for the LO-mode phonons by referring to previous experimental and theoretical studies. (From a study of the LO-mode CPs in a Si crystal, the eigen-frequency of the LO-mode phonon has been measured to be 15.6 THz [14, 15].) Since TO-mode phonons can also contribute to forming the MCP-NSs, these could also be measured; however, with pump–probe spectroscopy, only phonons with a wave-number of 0 (the Γ-point in wave-number space) are measured and, since the frequencies of the LO-mode phonons and TO-mode phonons at the Γ-point are approximately equal [20], it is not possible to distinguish between them. The full-width at half maximum of the Lorentzian spectral curve was fixed at 10 THz (41 meV) by referring to the average

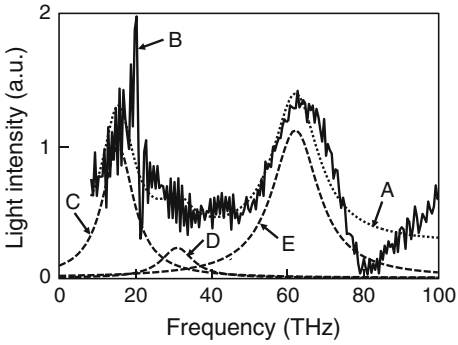

Fig. 4.7 Result of the curve fitting. *Curve A* is the result of fitting. *Curve B* is a copy of the curve in the inset of Fig. 4.6. *Curves C–E* represent the Lorentzian spectral curves of the fundamental and the second- and fourth-order harmonics of the LO-mode phonons, respectively

phonon energy (30 meV) and additional scattering by incoherent phonons at room temperature [14, 21].

The curve A in Fig. 4.7 represents the result of the fitting, whereas the curve B is a copy of the curve in the inset of Fig. 4.6. The curves C–E represent the Lorentzian spectral curves of the fundamental, and the second- and fourth-order harmonics of the LO-mode phonons, respectively, whose superposition yields the curve A. The contribution from the third-order harmonics was negligibly small. As a result of this accurate fitting of the curve A to the curve B, the spectral peak at 64 THz in the inset of Fig. 4.6 was found to be composed of the fourth-order harmonic of the LO-mode phonons. The spectral peak at 18 THz is composed of the fundamental of the LO-mode phonons. The second- and third-order harmonics of the LO-mode phonons contribute to the lower signal. Since the spectral intensity of the 64 THz peak was the largest, it was found that the fourth-order harmonic of the LO-mode phonons couple most strongly with the pump-beam photons and are the origin of the sidebands in the emission spectrum in Fig. 4.4.

From the discussion above, the fundamental and harmonics of the LO-mode phonons were revealed to be the constituent components of the multimode coherent phonons generated in the nanometric spaces around the domain boundaries of B in the Si-LED.

4.3 Control of Light Emission Spectral Profile

4.3.1 Principle of Control

Since a DPP is a state in which a DP is coupled with a phonon in the material, the light emission spectrum of the Si-LED described above has a large number of sidebands that are regularly arranged with a spacing corresponding to the optical phonon energy, centered on the photon energy of the light used in the DPP-assisted annealing. These sidebands are caused by coherent phonons (CPs) contributing to light emission. In

typical light emitting devices, such sidebands originating from phonons (phonon sidebands) are observed in the photoluminescence spectrum, but are not observed in the electroluminescent spectrum. The observation of such sidebands in the spectrum, as described above, is a phenomenon unique to LEDs (photon breeding devices) fabricated using DPPs. By using this phenomenon, it is possible to control the shape of the light emission spectrum of a Si-LED by controlling the number of CPs created during the DPP-assisted annealing. This section reviews how to control the creation of CPs by using a pair of pulses during the DPP-assisted annealing, allowing us to control the shape of the light emission spectrum of a Si-LED [22].

The mechanism of sideband creation will be explained. Figure 4.8a is an energy level diagram showing electronic states in a Si-LED fabricated by DPP-assisted annealing. The state $\left|E_g;\, el\right\rangle \otimes |E_{ex};\, phonon\rangle$ in the figure is a state represented by the direct product of the ground state $\left|E_g;\, el\right\rangle$ of the electron and the excited phonon state $|E_{ex};\, phonon\rangle$. Transitions to this state $\left|E_g;\, el\right\rangle \otimes |E_{ex};\, phonon\rangle$ have been shown to occur only due to absorption or emission of photons via DPPs [9]. When this is illustrated in the electronic energy band structure, it is a localized state in which DPP-mediated excitation can take place, and therefore, it is indicated by a constant-energy straight line (horizontal solid or broken line), as shown in Fig. 4.8b, due to wavenumber uncertainty. Although an adequate explanation of the conventional light emission process in Si-LEDs has been possible until now with only Fig. 4.8a, b is also presented to emphasize the significance of phonons. In the light emission process of Si-LEDs, since electrons are excited to the state $|E_{ex};\, el\rangle$ by current injection, the initial state $|E_{ex};\, el\rangle \otimes |E_{thermal};\, phonon\rangle$ in the light emission process exists close to the X-point in the conduction band in Fig. 4.8b. Here, $|E_{thermal};\, phonon\rangle$ is the thermally excited state of the phonon. Similarly, since the final state $\left|E_g;\, el\right\rangle \otimes |E_{thermal};\, phonon\rangle$, reached after the light emission, corresponds to the energy state of holes created by the injection current, the state $\left|E_g;\, el\right\rangle$ concentrates in the vicinity of the Γ-point at the top of the valence band. The state $|E_{thermal};\, phonon\rangle$ is limited to phonons that can exist at room temperature, according to Bose statistics. In other words, the states $|E_{ex};\, el\rangle \otimes |E_{therrmal};\, phonon\rangle$ and $\left|E_g;\, el\right\rangle \otimes |E_{thermal};\, phonon\rangle$ are the initial state and the final state in the usual indirect transition.

Next, the processes (0), (0'), (1), and ($1^{\dagger}$) in Fig. 4.8 will be explained. As the first-step, process (0) occurs. Processes (0'), (1), and ($1^{\dagger}$) occur as the second step. These processes involve externally observable transitions, in other words, photon emission. Processes (0) and (0') are transitions that do not require a phonon, whereas processes (1) and ($1^{\dagger}$) require an optical phonon. Similarly, (n) and ($n^{\dagger}$) are transitions involving n optical phonons ($n = 2,\ 3,\ 4, \ldots$).

Process (0) is the first-step transition from the initial state $|E_{ex};\, el\rangle \otimes |E_{thermal};\, phonon\rangle$ of electrons injected near the X-point by the current to the intermediate state $\left|E_g;\, el\right\rangle \otimes |E_{ex};\, phonon\rangle$, which can be reached via a DPP-mediated transition. It corresponds to the energy relaxation from the bottom of the conduction band E_g(=1.14 eV) to the state $\left|E_g;\, el\right\rangle \otimes |E_{ex};\, phonon\rangle$ (the energy of this state was experimentally determined to be 0.94 eV). This transition is allowable via emission of a large number of phonons or via the emission of infrared light. However, the probability of the transition via phonon emission is small because the simultaneous

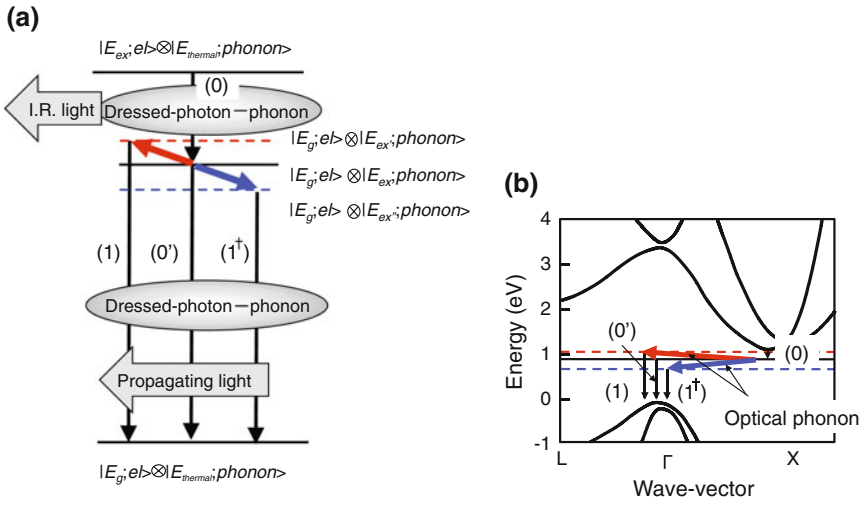

Fig. 4.8 Diagram for explaining DPP-mediated transitions. **a** Energy levels. **b** Levels that can be reached via DPP-mediated transitions in electronic energy band structure of Si crystal

emission of about 10 phonons is required at room temperature (thermal energy 25 meV). On the other hand, in the transition via infrared light emission, since the electronic state changes from $|E_{ex};\, el\rangle$ to $\left|E_g;\, el\right\rangle$, the selection rule required for photon emission is fulfilled. In addition, this transition is a direct transition in wave-number space, as shown in Fig. 4.8b. Therefore, the probability of this transition is higher than the probability of a transition via phonon emission. In real space, this process is a transition from the state $|E_{ex};\, el\rangle \otimes |E_{thermal};\, phonon\rangle$, which is broadened to the extent of the electron coherence length, to the localized state $\left|E_g;\, el\right\rangle \otimes |E_{ex};\, phonon\rangle$. The reason why infrared light can be emitted in this transition is that part of the electron energy can be dissipated as infrared light via a DPP having an energy that is resonant with this infrared light.

Process (0') is the second-step transition from the intermediate state $\left|E_g;\, el\right\rangle \otimes |E_{ex};\, phonon\rangle$ to $\left|E_g;\, el\right\rangle \otimes |E_{thermal};\, phonon\rangle$. The photon energy emitted during this process is equal to $h\nu_{anneal}$. Since this is a transition between the same electronic states $\left|E_g;\, el\right\rangle$, the selection rule required for photon emission is governed by a phonon, and the state $\left|E_g;\, el\right\rangle \otimes |E_{ex};\, phonon\rangle$ is also a state that can be reached via a DPP-meditated transition. The Si-LED fabricated by DPP-assisted annealing has a high probability of conversion from a DPP to propagating light, and almost all of the electrons in the state $\left|E_g;\, el\right\rangle \otimes |E_{ex};\, phonon\rangle$ relax by emitting photons with energy $h\nu_{anneal}$.

Process (1) is the second-step transition from the intermediate state $\left|E_g;\, el\right\rangle \otimes |E_{ex};\, phonon\rangle$ to the final state $\left|E_g;\, el\right\rangle \otimes |E_{thermal};\, phonon\rangle$ by absorption of an optical phonon. Since the first-step transition due to process (0) is an infrared light emission process, optical phonons are created via the Raman scattering process.

If the electrons in the state $\left|E_g; el\right\rangle \otimes |E_{ex}; phonon\rangle$ are scattered to the Γ-point by absorbing optical phonons, the second-step transition from the state $\left|E_g; el\right\rangle \otimes |E_{ex'}; phonon\rangle$ to the state $\left|E_g; el\right\rangle \otimes |E_{thermal}; phonon\rangle$ becomes possible, resulting in photon emission, as in the case of a direct transition-type semiconductor. This is process (1) shown in Fig. 4.8b. Here, $|E_{ex}; phonon\rangle$ and $|E_{ex'}; phonon\rangle$ are the excited states that the phonon reached before and after absorbing optical phonons. The energy of the emitted photons is $h\nu_{anneal} + h\nu_p$, where $h\nu_p$ is the energy of the optical phonon.

Process $(1^{\dagger})$ represents the second-step transition from the intermediate state $\left|E_g; el\right\rangle \otimes |E_{ex}; phonon\rangle$ to the final state $\left|E_g; el\right\rangle \otimes |E_{thermal}; phonon\rangle$, which occurs via emission of an optical phonon. Thus, it is conjugate to process (1). In this process, $|E_{ex''}; phonon\rangle$ in Fig. 4.8 shows the phonon excited state after the emission of the optical phonon. The emitted photon energy is $h\nu_{anneal} - h\nu_p$.

Similarly, processes (n) and $(n^{\dagger})$ are transitions in which n optical phonons are absorbed or emitted. Since, in practice, the processes (n) and $(n^{\dagger})$ occur simultaneously, sidebands with photon energies $h\nu_{anneal} - nh\nu_p$ and $h\nu_{anneal} + nh\nu_p$ appear in the light emission spectrum. The relationship between the nth order sideband energy and the photon energy $h\nu_{anneal}$ is the same as that of an nth order Raman scattering process with respect to the zero-phonon line. As is well-known, in Raman scattering, when a large number of phonons are excited, the electrons absorb them, emitting light. On the other hand, when a small number of phonons are excited, the electrons emit phonons, emitting light [23]. Thus, the intensity of these sidebands changes according to the number of phonons. This suggests that the intensity of the sidebands can be controlled by controlling the number of phonons.

The number of created phonons can be controlled by a method involving multi-photon absorption or CP excitation using pulsed light. Since the Si crystal is heated by DPP-assisted annealing, resonant absorption to a specific exciton state for creation of coherent phonons is not possible by using a high-power CW-laser optical source. This is because the high-power CW laser excitation changes not only the phonon structures but also DP state. Therefore, phonons are selectively created here via CP excitation using ultrashort pulsed light. The principle of the CP excitation in this case can be understood as an impulsive stimulated Raman scattering (ISRS) process of Sect. 4.2. The duration and the repletion rate of the used pulsed light was 17 fs and 80MHz, respectively. Therefore, its duty ratio was 1.3×10^{-6}. The Raman scattering process based on the third order optical nonlinearity. Therefore, the enough laser power for the control of CP creation using the ultrashort pulsed light is 2.3×10^{-18} times lower than that using the CW laser. Thus, the adverse effect was reduced to the negligible small coming from the DP generation by the additional laser excitation for the CP control.

In ISRS, the frequency component of the pulsed light irradiating the crystal includes coherent frequency components ν and $\nu - \nu_p$ with sufficiently high intensity. Therefore, when the crystal is irradiated with pulsed light, the electrons absorb light with energy $h\nu$ and exhibit stimulated emission of light with energy $h\nu - h\nu_p$. At this time, it is possible to create CPs having an energy $h\nu_p$. Since these CPs are coherent, it is possible to control the creation of CPs by a single pulse or multiple pulses of

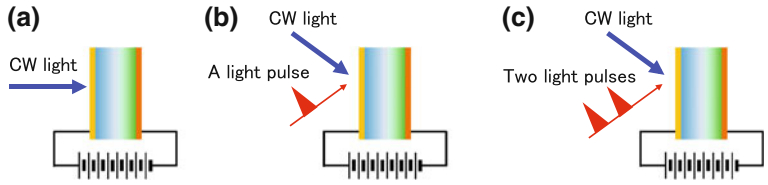

Fig. 4.9 Illustration of DPP-assisted annealing. **a** Using CW light. **b** Using CW light and a light pulse. **c** Using CW light and two light pulses

light and causing them to interfere. In other words, unlike conventional DPP-assisted annealing in which the Si crystal is irradiated with CW light, CP creation is controlled by irradiating the Si crystal with pulsed light in addition to CW light. Therefore, it is possible to control the intensities of the sidebands in the light emission spectrum. In the following, two cases are reviewed; one is the case where the Si-LED is irradiated with a single pulse of light during the DPP-assisted annealing, and the other is the case where the Si-LED is irradiated with a pair of light pulses.

(1) Irradiation with a single light pulse: In the conventional DPP-assisted annealing, as shown in Fig. 4.9a, the CW light plays the role of decreasing the thermal diffusion rate by means of stimulated emission. In the present case, as shown in Fig. 4.9b, a light pulse is also radiated, together with the CW light. Since the light pulse excites multimode CPs via ISRS, the coupling probability of electron–hole pairs, photons, and CPs increases. As a result, the probability of electrons absorbing phonons and emitting light increases because the number of excited phonons increases as the light emission intensity increases. Therefore, the intensity of the sidebands having energy $h\nu_{anneal} + nh\nu_p$ increases, and the intensity of sidebands having energy $h\nu_{anneal} - nh\nu_p$ decreases. Thus, compared with an Si-LED fabricated by irradiation with only CW light, it is expected that the light emission spectral shape of the Si-LED will show a higher light emission intensity at energies higher than $h\nu_{anneal}$, and conversely a lower light emission intensity at energies lower than $h\nu_{anneal}$.

(2) Irradiation with two light pulses (light pulse pair): Since the CPs created by ISRS are coherent and thus have the ability to interfere, as described above, let us consider the case where a Si crystal is sequentially irradiated with two coherent light pulses having an arrival time difference Δt. If the value of Δt is a half-integer multiple of the vibration period, $1/\nu_p$, of the phonons ($n/2\nu_p$; $n = 1, 3, 5, \ldots$), as shown in Fig. 4.9c, it is known that the excited CPs destructively interfere [15]. On the other hand, they constructively interfere when Δt is an integer multiple of the vibration period (n/ν_p; $n = 1, 2, 3, \ldots$). That is to say, by radiating a pair of light pulses, it is possible to control the creation of CPs so as to be suppressed or enhanced. Thus, by adjusting the value of Δt, it is possible to perform various types of sideband control as compared with (1) above.

As an example, in the case of $\Delta t = 1/2\nu_p$, methods of control the CP creation and the light emission spectrum are explained. The value $\Delta t = 1/2\nu_p$ corresponds to one

period of vibration of a phonon with frequency $2\nu_p$. Therefore, by radiating a pair of pulses having this value Δt, the number of phonons of frequency ν_p decreases, whereas the number of phonons of frequency $2\nu_p$ increases. Thus, the probability of process ($1^{\dagger}$) increases, by which electrons emit phonons of frequency ν_p and emit light, resulting in a higher probability of electrons absorbing phonons of frequency $2\nu_p$ and emitting light. In other words, as a result of the reduction in the number of phonons with frequency ν_p, the intensity of the sideband at energy $h\nu_{anneal} - h\nu_p$ becomes higher than that of the sideband at energy $h\nu_{anneal} + h\nu_p$. At the same time, as a result of the increase in the number of phonons with frequency $2\nu_p$, the intensity of the sideband at energy $h\nu_{anneal} - 2h\nu_p$ becomes lower than that of the sideband at energy $h\nu_{anneal} + 2h\nu_p$. The above discussion can also be extended to an explanation of the case where the sideband intensity at energy $h\nu_{anneal} - (2n-1)\,h\nu_p$ increases, and that at energy $h\nu_{anneal} + (2n-1)\,h\nu_p$ decreases. It can be also extended to the case where the sideband intensity at energy $h\nu_{anneal} - 2nh\nu_p$ decreases, and that at energy $h\nu_{anneal} + 2nh\nu_p$ increases. For controlling the number of phonons during the DPP-assisted annealing, two light pulses were used with delay times of $\Delta t = 1/\nu_{p,\mathrm{exp}}$(=64.1 fs), $1/2\nu_{p,\mathrm{exp}}$(=32.1 fs), and $1/4\nu_{p,\mathrm{exp}}$(=16.0 fs).

4.3.2 Evaluation of Light Emission Spectrum

The device fabrication conditions were the same as those of Chap. 3. In DPP-assisted annealing, a CW laser light was used ($h\nu_{anneal} = 0.94$ eV, wavelength 1.3 μm) as the light source for creating DPs. As the pulsed light source for creating CPs, a mode-locked laser was used (a photon energy 1.55 eV, wavelength 0.8 μm, a pulse width 17 fs, and a repetition frequency 80 MHz). To verify the DPP-assisted annealing method, the following four samples were employed.

(a) Sample 1 Sample 1 was irradiated with pulsed light (average power 100 mW, spot diameter 150 μm) and CW light ($h\nu_{anneal} = 0.94$ eV, power 1 W, spot diameter 3 mm). It was annealed with a voltage of 20 V and a current of 145 mA for 1 h (Fig. 4.9b).

(b) Samples 2–4 Of the CPs created by pulsed light irradiation, optical phonons with the highest creation probability [10] ($h\nu_p = 65$ meV ($\nu_p = 15.6$ Hz); indicated as $h\nu_{p,\mathrm{exp}}$ below) were selected as the phonons to be controlled. The samples were irradiated with CW light and a pair of light pulses with $\Delta t = 1/\nu_{p,\mathrm{exp}}$ (=64.1 fs), $1/2\nu_{p,\mathrm{exp}}$ (=32.1 fs), and $1/4\nu_{p,\mathrm{exp}}$ (=16.0 fs). They were annealed with a voltage of 25 V and a current of 120 mA for 1 h (Fig. 4.9c). The other experimental conditions were the same as those used for Sample 1 above. In the following, samples for $\Delta t = 1/\nu_{p,\mathrm{exp}}$, $1/2\nu_{p,\mathrm{exp}}$, and $1/4\nu_{p,\mathrm{exp}}$, are referred to as Samples 2, 3, and 4, respectively.

To eliminate the contributions of variations in the sizes and shapes of the electrode and the substrate to the experimental results, the CW light was radiated onto the entire surface of the sample, and the pulsed light was radiated only at the center of the region

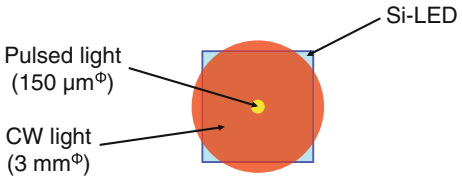

Fig. 4.10 Irradiation spots of CW light and pulsed light on sample surface during DPP-assisted annealing

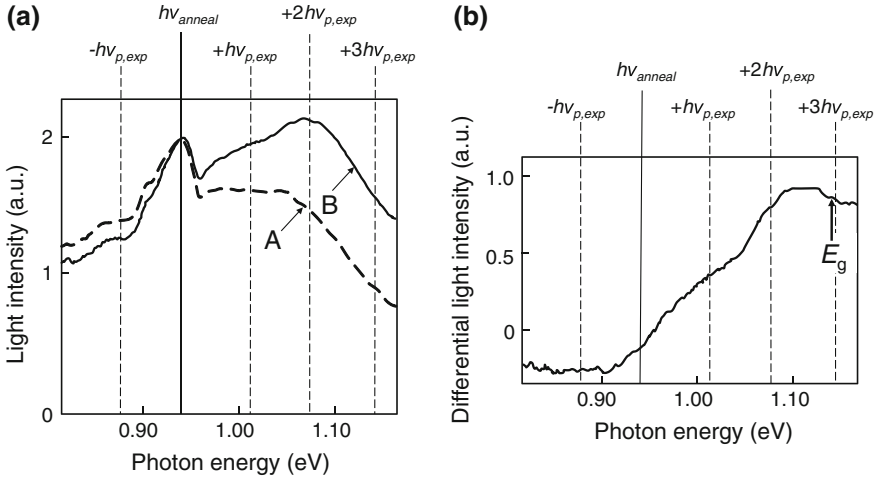

Fig. 4.11 Light emission spectra. **a** Sample 1. *Curve A* area irradiated only with CW light. *Curve B* area irradiated with CW light and pulsed light. **b** Differential light emission spectrum

irradiated with the CW light, as shown by the red and yellow circles, respectively, in Fig. 4.10. With the samples prepared with this method, the light emission spectral shapes in these two circles were different. By taking this difference between the intensities of these light emission spectra, it was possible to eliminate the contributions above and to examine the details of the changes in the light emission spectra depending on the presence/absence of the pulsed light irradiation. Experimental results are reviewed below.

(a) Sample 1 Figure 4.11a shows, for Sample 1, the light emission spectrum of the part irradiated with only the CW light (curve A: L_{CW}) and the light emission spectrum of the part irradiated with the CW light and the pulsed light (curve B: $L_{CW+pulse}$). Figure 4.11b shows the difference between their intensities ($L_{CW+pulse} - L_{CW}$; differential light emission spectrum). By irradiating the sample with the pulsed light, the emitted light intensity at higher energies increased, and the intensity of the +1 and +2 order sidebands of the optical phonons (energy $h\nu_{p,\mathrm{exp}} = 65$ meV) increased. In the differential light emission spectrum, band-edge light emission and an increase in the intensity of the +3 order sideband were

also confirmed. However, since mode selection was not performed by using a pair of pulses, the spectra of the sidebands were extremely broad. The increase in intensity of these sidebands is explained by the creation of a large number of CPs by ISRS, using the pulsed light, as explained in Sect. 4.2. In other words, since a large number of CPs are created, the process in which CPs are absorbed becomes dominant, resulting in light emission. In addition, the increase in light emission at the band edge is considered to be a consequence of the increased number of phonons due to CP creation causing an increased probability of a direct transition between electronic bands. On the other hand, in the sideband corresponding to the -1 order optical phonons, the emitted light intensity is decreased by the incident pulsed light during DPP-assisted annealing. This is because process ($1^{\dagger}$), in which optical phonons and light are emitted, is suppressed due to CPs created by the pulsed light.

(b) Samples 2 Figure 4.12a shows the differential light emission spectrum for Sample 2. In this sample, small bumps (arrows A, B, and C) are observed at the positions of the $+1$ to $+3$ order optical phonon sidebands ($h\nu_{p,\mathrm{exp}} = 65$ meV). They are due to the selective creation of optical phonons $nh\nu_{p,\mathrm{exp}}$ ($n = 1, 2, 3, \ldots$), which were mode-selected by irradiating this sample with a pair of pulses with $\Delta t = 1/\nu_{p,\mathrm{exp}}$. On the other hand, a region with reduced light emission, like that seen in Fig. 4.11b, was not observed in the region whose energy is lower than $h\nu_{anneal}$ (arrow D). The reason for this is that the number of created optical phonons is half or less of that in the case of Sample 1 because ISRS is a second-order nonlinear process, and the energy of the pulses irradiating this sample is one-half of the energy of the pulses irradiating Sample 1. This is due to the suppression of process ($1^{\dagger}$), in which light emission occurs while phonons are emitted.

(c) Samples 3 Figure 4.12b shows the differential light emission spectrum for Sample 3. In this sample, the intensity of the -1 order sideband increased (arrow A). The reason for this is that, with $\Delta t = 1/2\nu_{p,\mathrm{exp}}$, the number of odd-numbered harmonic components was decreased, and the number of even-numbered harmonic components was increased. In other words, since the electrons had an increased probability of emitting the $+1$ order phonons, process ($1^{\dagger}$) was dominant, and the intensity of the -1 order sideband increased. On the other hand, process (1), in which light emission occurs while phonons are absorbed, is suppressed. Therefore, since the high-order modes are also suppressed, a region exhibiting reduced optical phonon sidebands is observed at energies higher than $h\nu_{anneal}$, which is the opposite to what is shown in Fig. 4.11b.

(d) Samples 4 Figure 4.12c shows the differential light emission spectrum for Sample 4. The intensities of the $+1$ order and $+2$ order sidebands (arrows A and B, respectively) were decreased, and those of the $+4$ order and $+5$ order sidebands (arrows C and D, respectively) were increased. A reason for this is that, with $\Delta t = 1/4\nu_{p,\mathrm{exp}}$, the number of $+2$ order harmonic phonons was decreased, and that the number of $+4$ order harmonic phonons was increased. The reason for the increase in the number of optical phonons in the $+5$ order is considered to be because the values of $1/4\nu_{p,\mathrm{exp}}$ and $1/5\nu_{p,\mathrm{exp}}$ are close. As a result, the intensity

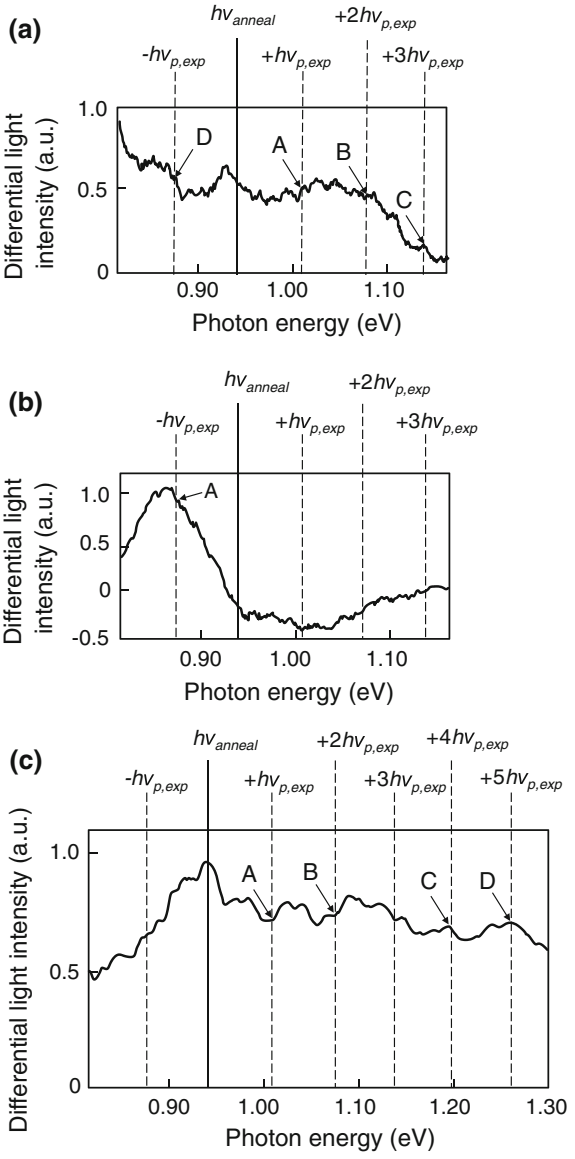

Fig. 4.12 Differential light emission spectra. **a** Sample 2. **b** Sample 3. **c** Sample 4

of the +1 order sideband is decreased. In other words, this is because the +1 order optical phonons are absorbed for creating the +4 order and +5 order harmonic phonons. The reason why the generation of the +5 order sideband dominates over generation of the +1 order sideband is that the energy of the +5 order sideband is higher than the bandgap energy, E_g, of Si, and this is a phonon scattering process that is resonant with the electronic level. As a result, process (1) is suppressed, and the intensity of the +1 order sideband is decreased. On the other hand, since the overall number of optical phonons is increased, process ($1^{\dagger}$) is suppressed, as in the case of Fig. 4.11b. As a result, a region with reduced light emission, similar to that seen in Fig. 4.11b, is observed in the region at energy $h\nu_{anneal} - nh\nu_{p,\exp}$.

The curves A and B in Fig. 4.13 show the light emission spectra of the regions irradiated with the light pulses for Samples 2 and 3, respectively. In Sample 2, the numbers of phonons of the fundamental ($h\nu_{p,\exp}$) and the harmonics ($nh\nu_{p,\exp}$; $n = 2, 3, \ldots$) were all increased, and therefore, the phonon absorption probability of the electrons increased, resulting in higher light emission at higher energies. In Sample 3, on the other hand, due to the interference of CPs, the number of odd-order harmonic components of the phonons was decreased, and the number of even-order harmonic components was increased; therefore, the absorption probability of phonons of odd-order harmonic components was decreased, resulting in relatively higher light emission at lower energies. The above results indicate that the light emission spectral shape of the Si-LED was successfully controlled by changing the conditions of the pair of light pulses radiated during DPP-assisted annealing. That is, the intensity at energies higher than $h\nu_{anneal}$ is increased, and that at lower energies is decreased. Furthermore, conversely, the intensity at energies lower than $h\nu_{anneal}$ is increased, and that at higher energies is decreased.

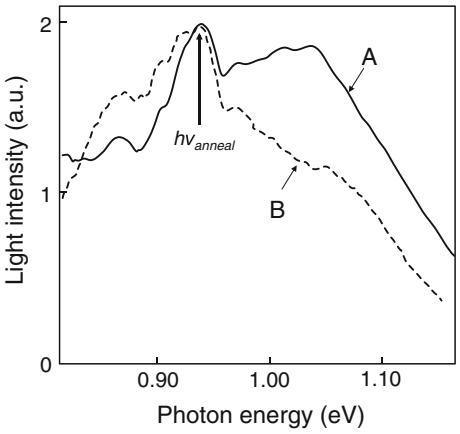

Fig. 4.13 Light emission spectra after annealing. *Curves A* and *B* are for Samples 2 and 3, respectively

In DPP-assisted annealing without using a pulsed light source, the broadening (half width at half maximum, HWHM) towards lower energies was 250 meV or greater, and the broadening (HWHM) towards higher energies was 50 meV. In contrast, in the light emission spectrum of the Si-LED fabricated using a pulsed light source for creating phonons, the light emission spectrum was broadened towards higher energies by 200 meV or greater (HWHM), and the broadening towards lower energies was reduced to 120 meV (HWHM).

In DPP-assisted annealing, the spectral shape of a Si LED was successfully controlled by radiating a pair of light pulses for creating CPs. In the light emission spectrum, the intensity of sidebands due to phonons could be controlled by the number of phonons during DPP-assisted annealing. The peak wavelength in the light emission spectrum was determined by the wavelength of the light source used in DPP-assisted annealing. In order to broaden the light emission spectrum toward higher energy, a pair of light pulses having $\Delta t = 1/4\nu_{p,\exp}$ was radiated. Conversely, to broaden the light emission spectrum towards lower energies, a pair of light pulses having $\Delta t = 1/2\nu_{p,\exp}$ was radiated. As a result, the light emission spectrum was broadened towards higher energies by 200 meV or greater (HWHM), and the broadening towards lower energies was reduced to 120 meV (HWHM).

4.3.3 Control of Spatial Distribution of Boron

This subsection describes the three-dimensional spatial distribution of boron (B) atoms, which was formed by simultaneously irradiating a Si crystal with a pair of light pulses and CW light for the DPP-assisted annealing [24]. Figure 4.14a shows the number of B atom pairs plotted as a function of the separation of the B atoms in the pair, which was derived from the measured spatial distribution of B atoms, as was the case in Sect. 3.3. When comparing the plotted results with the solid curve (Weibull distribution function), the measured values do not show any deviations, unlike the ones indicated by the four downward arrows in Fig. 3.9b. This means that the B atom pair orients not along a specific orientation [1,0,0], [0,1,1], or [0,0,1] but along the direction schematically explained by Fig. 4.14b.

To realize the orientation shown in Fig. 4.14b, diffusion of B atoms is controlled by the following DPP creation mechanism: First, DPPs are created by the CW light irradiation, exciting multimode CPs. Simultaneous irradiation of the pair of light pulses selects the CP modes. In the case where only the CW light is radiated, Sect. 3.3 described that the wave-vector of the phonon for creating the DPP is parallel to the direction of propagation of the light radiated for the DPP-assisted annealing ($\theta = 0°$ in Fig. 3.8), i.e., parallel to the Γ-X direction in reciprocal lattice space. However, the present case suppresses the creation of phonons with a wave-vector parallel to the Γ-X direction. Since other phonons are not suppressed, the separation d becomes random and takes continuous values, by which the solid curve was fitted precisely to the measured values in Fig. 4.14a. Due to this suppression of phonon creation, the

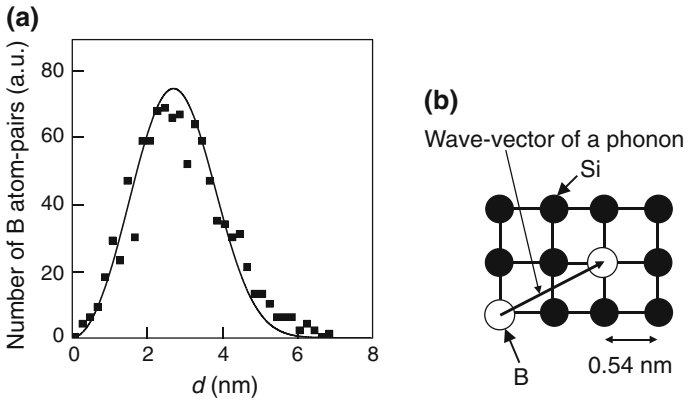

Fig. 4.14 Spatial distribution of B atoms. **a** Number of B atom pairs plotted as a function of the separation between the B atoms in the pair. **b** B atom pair in the Si crystal

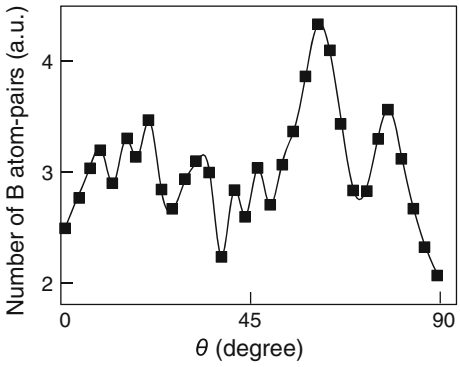

Fig. 4.15 Relation between θ and the number of B atom pairs

magnitude of the phonon sidebands in the light emission spectra decreased, as was described in Sect. 4.3.2.

Figure 4.15 shows the relation between the zenith angle θ and the number of B atom pairs. In contrast to Fig. 3.12, the number of B atom pairs does not take the maximum value at $\theta = 90°$, due to the above-mentioned suppression of the phonon creation. However, it should be noted that the number of B atom pairs take the minimum value at $\theta = 0°$, as was the case in Fig. 3.12.

References

1. Y. Tanaka, K. Kobayashi, J. Microsc. **229**, 228 (2008)
2. K. Huang, A. Rhys, Proc. R. Soc. Lond. A. **204**, 406 (1950)
3. H. Zhao, H. Kalt, Phys. Rev. B **68**, 125309 (2003)
4. T.W. Hagler, K. Pakbaz, K.F. Voss, A.J. Heeger, Phys. Rev. B **44**, 8652 (1991)

5. M. Yamaguchi, T. Kawazoe, M. Ohtsu, Appl. Phys. A **115**, 119 (2014)
6. H. Palevsky, D.J. Hughes, W. Kley, E. Tunkelo, Phys. Rev. Lett. **2**, 258 (1959)
7. J.R. Goldman, J.A. Prybyla, Phys. Rev. Lett. **72**, 1364 (1994)
8. A.J. Sabbah, D.M. Riffe, Phys. Rev. B **66**, 165217 (2002)
9. T. Kawazoe, K. Kobayashi, S. Takubo, M. Ohtsu, J. Chem. Phys. **122**, 024715 (2005)
10. P. Giannozzi, S. Gironcoli, P. Pavone, S. Baroni, Phys. Rev. B **43**, 7231 (1991)
11. S. Nomura, T. Kobayashi, Phys. Rev. B **45**, 1305 (1992)
12. D. Bermejo, M. Cardona, J. Non-Cryst, Solids **32**, 405 (1979)
13. T. Prokofyeva, M. Seon, J. Vanbuskirk, M. Holtz, S.A. Nikishin, N.N. Faleev, H. Temkin, S. Zollner, Phys. Rev. B, Rev. B **63**, 125313 (2001)
14. D.M. Riffe, A.J. Sabbah, Phys. Rev. B **76**, 085207 (2007)
15. M. Hase, M. Katsuragawa, A.M. Constantinescu, H. Petek, Nat. Photonics Lett. **6**, 243 (2012)
16. A.V. Kuznetsov, C.J. Stanton, Phys. Rev. Lett. **73**, 3243 (1994)
17. N. Wada, M.-A. Tran, T. Kawazoe, M. Ohtsu, Appl. Phys. A **115**, 113 (2014)
18. Y.-X. Yan, E.B. Gamble Jr., K.A. Nelson, J. Chem. Phys. **83**, 5391 (1985)
19. S.I. Kudryashov, M. Kandyla, C.A.D. Roeser, E. Mazur, Phys. Rev. B **75**, 085207 (2007)
20. T. Soma, Phys. Stat. Sol. (b) **99**, 701 (1980)
21. T.R. Hart, R.L. Aggarwal, B. Lax, Phys. Rev. B **1**, 638 (1970)
22. T. Kawazoe, N. Wada, M. Ohtsu, Adv. Opt. Technol. **2014**, Article ID 958327 (2014)
23. S.K. Arora, A.J. Kothari, R.G. Patel, K.M. Chauhan, B.N. Chudasama, J. Phys. **28**, 48 (2006)
24. T. Kawazoe, K. Nishioka, M. Ohtsu, Appl. Phys. A **121**, 1409 (2015)

Chapter 5
Infrared Lasers Using Silicon Crystal

This chapter reviews infrared Si lasers fabricated by using DPPs and capable of continuous-wave operation at room temperature. After describing basic devices that have been experimentally demonstrated, devices having an ultralow threshold current density are reviewed. In addition, the values of optical amplification quantities are estimated accurately for achieving further improvements in lasing performance. Finally, novel devices that emit high output optical power are demonstrated.

5.1 Basic Devices

Si has been the subject of extensive research for use in fabricating lasers since it shows excellent compatibility with electronic devices [1]. For example, there have been several reports of basic devices that have been demonstrated, including Raman lasers [2] and lasers utilizing quantum size effects in Si [3]. However, parameters such as the operating temperature, efficiency, wavelength, optical power and so forth are still not adequate for practical adoption of these lasers. This chapter reviews an infrared Si laser designed to solve these problems, fabricated by using DPPs and capable of continuous-wave operation at room temperature [4, 5].

Optical amplification gain occurs when the Bernard–Duraffourg inversion condition is satisfied. Furthermore, if the fabricated devices have an optical cavity structure for confining the emission energy, and if the optical amplification gain is larger than the cavity loss, there is a possibility of laser oscillation occurring as a result of stimulated emission.

This section reviews the fabrication and operation of basic Si laser devices. An As-doped n-type Si crystal was used as a device substrate, whose electrical resistivity and thickness were $10\,\Omega\,\mathrm{cm}$ and $625\,\mu\mathrm{m}$, respectively. A part of this crystal was further doped with B atoms by ion implantation to form a p-type layer. The B concentration was $1 \times 10^{19}\,\mathrm{cm}^{-3}$. After forming a p-n homojunction, an ITO film was deposited on

M. Ohtsu, *Silicon Light-Emitting Diodes and Lasers*,
Nano-Optics and Nanophotonics, DOI 10.1007/978-3-319-42014-1_5

the p-layer side of the Si substrate, and an Al film was deposited on the n-substrate side for use as electrodes. Next, the Si crystal was diced to form the device. For DPP-assisted annealing (refer to Sect. 3.1), the substrate was irradiated with infrared laser light having a photon energy, $h\nu_{anneal}$, of 0.94 eV (1.32 μm wavelength) and a power density of 200 mW/cm^2 during which annealing was performed by applying a forward-bias current of 1.2 A to generate Joule-heat, causing the B atom to diffuse. With this method, the spatial distribution of the B atom changes, forming domain boundaries in a self-organized manner, which have shapes and distributions suitable for efficiently inducing the DPP-assisted process.

Next, the ITO electrode and the Al electrode were removed by etching. Then, a ridge waveguide was fabricated by using conventional photolithography: An SiO_2 film, used as a mask in wet chemical etching of Si by KOH, was deposited by means of tetraethyl orthosilicate chemical vapor deposition (TEOS-CVD). After transferring the mask pattern (10 μm linewidth) to the SiO_2, KOH etching was conducted to fabricate a ridge waveguide. Then, an SiO_2 film for isolating the Si wafer and the electrode was deposited by TEOS-CVD, and a contact window was formed on top of the ridge waveguide.

After that, an Al electrode was deposited by DC sputtering. The substrate was then polished to a thickness of 100 μm, and Al was deposited on the reverse side of the Si substrate. The sample was cleaved to various cavity lengths, and the cleaved facets served as cavity mirrors.

Several Si laser devices were fabricated with the above method. All of the experiments described below were conducted at room temperature (15–25 °C). Figure 5.1a illustrates the device structure. Secondary ion mass spectrometry measurements confirmed that the active layer formed in the p-n homojunction was located at a depth of 1.5–2.5 μm from the surface of the Si substrate. This corresponds to the bottom of the ridge waveguide. Figure 5.1b shows an SEM image of a fabricated Si laser. The width and thickness of the ridge waveguide constituting the cavity were confirmed to be 10 and 2 μm, respectively. Several Si lasers were fabricated, whose cavity lengths were 250–1000 μm.

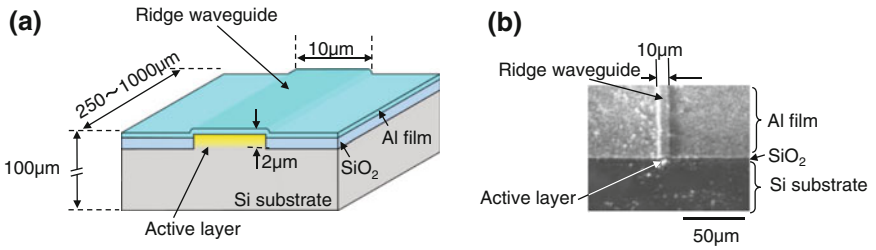

Fig. 5.1 The device structure of a Si laser. **a** Schematic illustration of the structure. **b** An SEM image of a fabricated Si laser

Figure 5.2 shows a numerically calculated cross-sectional light intensity profile for the device in Fig. 5.1. This figure shows that a portion of the lasing light leaked from the active layer. From this calculated result, the estimated optical confinement factor, Γ, was as low as 4.7×10^{-4}.

Due to such weak optical confinement, the guiding loss in the ridge waveguide was expected to be as large as 90% or more. However, because the DPP-assisted annealing forms an active layer that efficiently creates DPPs, the effective refractive index of the active layer can become higher than the refractive index of the surrounding area. As a result, the sum of the guiding loss and the optical scattering loss at the cleaved facets was 70% for the TE-polarization component, which was smaller than the value expected above.

From the measurement of the relation between the injection current density and the optical amplification gain at a wavelength of 1.32 μm, the transparent current density, J_{tr}, was estimated to be 26.3 A/cm^2. This value is about 1/10-times that for a conventional laser device made using a direct transition-type semiconductor [6], demonstrating that this ridge waveguide with the p-n homojunction structure has adequate performance for use as a laser.

For the laser with a waveguide length of 750 μm, the far-field and near-field images of the optical radiation pattern are shown in Fig. 5.3a, b, respectively. There is a ridge waveguide with a width of 10 μm at the center of the white broken circle in Fig. 5.3b. At an injection current of 50 mA and above, the optical radiation pattern was concentrated inside the ridge waveguide, and the optical power increased. This concentration indicates that the directivity of the optical radiation pattern was high

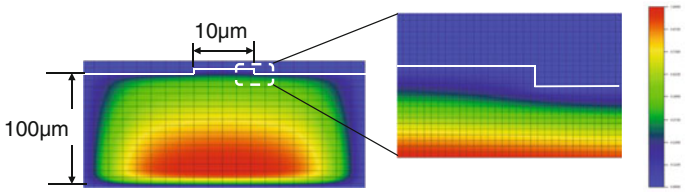

Fig. 5.2 Numerically calculated cross-sectional light intensity profiles for the device of Fig. 5.1

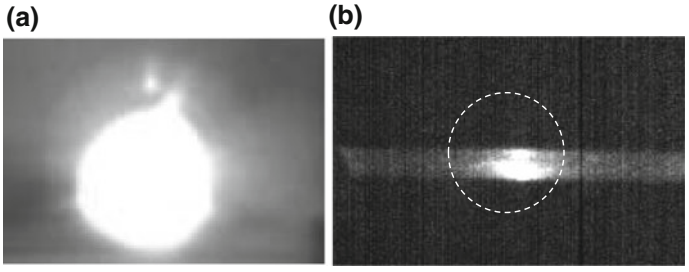

Fig. 5.3 Optical radiation patterns from the Si laser. **a** Far-field image. **b** Near-field image

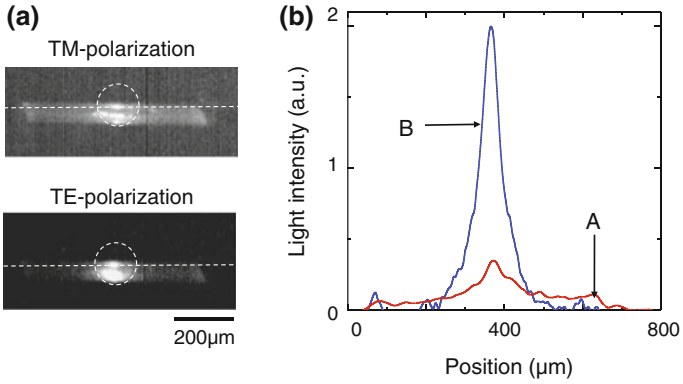

Fig. 5.4 TM- and TE-polarization polarization components. **a** Near-field images. **b** The cross-sectional light intensity profiles along the *white broken lines* in (**a**). The *curves A* and *B* are the profiles for the TM- and TE-polarization components, respectively

due to the laser oscillation. At an injection current below 50 mA, on the other hand, the directivity was low. This is because the main components of the optical radiation pattern are spontaneous emission and amplified spontaneous emission (ASE).

Figure 5.4a shows images of the TM- and TE-polarization components of the near-field image in Fig. 5.3b. Figure 5.4b is their cross-sectional light intensity profiles taken along the white broken lines in Fig. 5.4a. These figures show that the TM-polarization component spread over the entire device, whereas the TE-polarization component was concentrated in the ridge waveguide. The intensity ratio of the TE-polarization and the TM-polarization was 8:1. On the other hand, in a conventional semiconductor laser, this ratio is 100:1 or greater [7]. The reason for the difference between these ratios is the absence of the optical confinement structure in the thickness direction of the ridge waveguide in the present device, in contrast to the case of conventional semiconductor lasers, where it has been formed by providing a double-heterojunction structure. Another possible reason is that the spectral wavelength bands of the spontaneous emission and ASE are extremely wide.

Curves A–D in Fig. 5.5 show the light emission spectral profiles of the Si laser with several injection currents. In these measurements, another device with a shorter waveguide length (250 μm) was used in order to separately observe each longitudinal mode. A sharp peak was observed at a wavelength of 1.356 μm (the position indicated by the downward arrow on curve D), which shows laser oscillation at an injection current of 60 mA. The tip of the peak went off the top edge of the graph due to saturation of the sensitivity of the photodetector in the measurement equipment. This sharp peak is evidence of laser oscillation due to photon breeding, as was described in the previous chapters. Figure 5.5 also shows a magnified view of the vicinity of the oscillation spectral peak (curve D) during laser oscillation, where several longitudinal modes (positions indicated by the upward arrows) are observed at a wavelength spacing of 1.0 nm, determined by the waveguide length (250 μm).

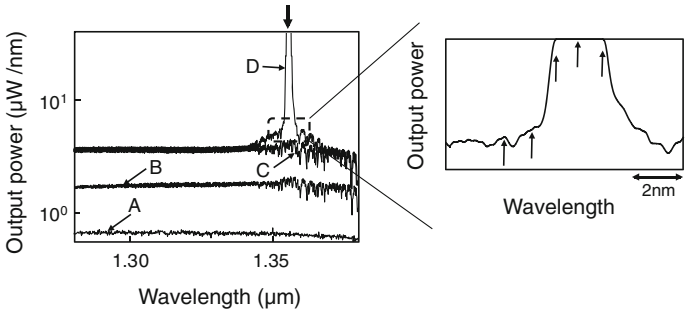

Fig. 5.5 Light emission spectral profiles of the Si laser with a short waveguide length (250 μm). *Curves A–D* are for injection currents of 20, 33, 53, and 60 mA, respectively

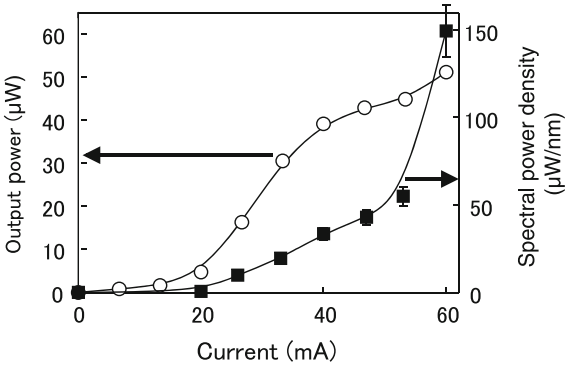

Fig. 5.6 Current dependency of the output optical power. The *open circles* are values obtained by integrating the optical power with respect to wavelength in the wavelength range 1.220–1.380 μm. The *closed squares* are values of the spectral power density at a wavelength of 1.356 μm

Figure 5.6 shows the current dependency of the output optical power. The open circles are values obtained by integrating the optical power with respect to wavelength in the range 1.220–1.380 μm. At an injection current of 60 mA, the output optical power was 50 μW, and the external differential quantum efficiency was 1%. This value is as high as that reported for a conventional 1.3 μm-wavelength double heterojunction-structured laser using InGaAsP/InP, which is a direct transition-type semiconductor [8]. The closed squares are values of the spectral power density at a wavelength of 1.356 μm. At the injection current of 60 mA, the spectral power density was 150 μW/nm. Because this device had a wide emission wavelength band, the optical powers of the spontaneous emission and ASE also increase as the current increases. Therefore, the measurement results indicated by the open circles do not show a sudden increase in the output optical power of laser oscillation. The closed squares, on the other hand, do show this, and the threshold current for laser oscillation was found to be 50 mA, giving a threshold current density, J_{th}, of 2.0 kA/cm^2.

Light emission spectral profiles were measured also for the Si laser with the longer waveguide length (500 μm). The results are shown in Fig. 5.7. At a current of 56 mA, a sharp laser oscillation spectrum was observed, as shown in Fig. 5.7a, with a center wavelength of 1.271 μm, which is also evidence of photon breeding. The full

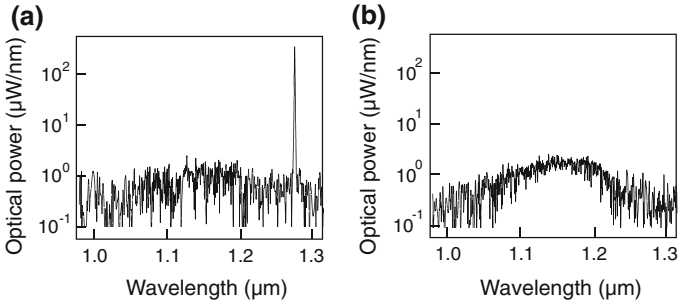

Fig. 5.7 Light emission spectral profiles of the Si laser with the long waveguide length (550 μm). **a** Above the threshold. **b** Below the threshold

width at half maximum was 0.9 nm or less, which is limited by the resolution of the measurement equipment. At an injection current of 55 mA (Fig. 5.7b), only a wide emission spectrum that originated from the spontaneous emission was measured. From these measured results, the threshold current density, J_{th}, for laser oscillation was found to be 1.1 kA/cm^2.

5.2 Decreasing the Threshold Current Density

This section reviews the design and fabrication of an improved device with a higher optical confinement factor, for achieving a further reduction in the threshold current density, J_{th} [5]. First, the value of the transparent current density, J_{tr}, is estimated for this design. It should be noted that, as shown by Fig. 5.2, a part of the lasing light leaked out from the active layer. Since this leaked light does not contribute to the optical amplification, only the light in the active layer has to be used to estimate J_{tr}. For this estimation, an infrared Si photodetector with optical amplification (to be described in Sect. 8.2) was used, and its photocurrent was measured by irradiating it with light having a wavelength of 1.32 μm. This measurement was possible because all of the irradiated light contributes to J_{tr} for the photodetection process. As a result, the transparent current density, J_{tr}, was estimated to be 5.0 A/cm^2. Through this estimation, the differential gain coefficient, g, was also estimated to be 38.4 cm/A.

Next, by using these estimated values, the threshold current density, J_{th}, of the laser is derived from

$$\Gamma g(J_{th} - J_{tr}) = \alpha_{\text{int}} + \frac{1}{2L} \ln\left(\frac{1}{R_f R_b}\right), \tag{5.1}$$

where Γ, α_{int}, and L are the optical confinement factor, the internal loss coefficient, and the waveguide length, respectively [9]. Furthermore, R_f and R_b are the reflectivities of the front and back facets of the waveguide, respectively, which are

used as cavity mirrors. The values of these parameters for the device in Fig. 5.1 are $J_{tr} = 5.0\,\mathrm{A/cm^2}$, $g = 38.4\,\mathrm{cm/A}$, $\alpha_{\mathrm{int}} = 1.6 \times 10^{-5}\,\mathrm{cm^{-1}}$, $\Gamma = 4.7 \times 10^{-4}$, $L = 250\,\mu\mathrm{m}$, and $R_f = R_b = 0.31$. By substituting these into (5.1), the threshold current density, J_{th}, is estimated to be $2.6\,\mathrm{kA/cm^2}$, which is close to the measured value given in Sect. 5.1.

Since the optical confinement factor, Γ, for the device in Fig. 5.1 was very low (4.7×10^{-4}), a further decrease in the threshold current density, J_{th}, is expected by increasing Γ. For this decrease, the dependence of J_{th} on Γ was derived by using (5.1) and the numerical values listed above, where $500\,\mu\mathrm{m}$ was used as the value of L. The derived relation is shown in Fig. 5.8, which suggests that J_{th} decreases to less than 1/100-times that of the device in Fig. 5.1, i.e., to $8.8\,\mathrm{A/cm^2}$, by increasing Γ to 0.16.

By following this suggestion, an improved device with a larger Γ was designed in order to decrease J_{th} to $8.8\,\mathrm{A/cm^2}$. Its cross-sectional profile is schematically shown in Fig. 5.9. The device layer is $15\,\mu\mathrm{m}$ thick, which was realized by using a silicon-on-insulator (SOI) substrate. The thickness and width of the ridge waveguide are 2 and $8\,\mu\mathrm{m}$, respectively. Figure 5.10 shows the numerically calculated cross-sectional

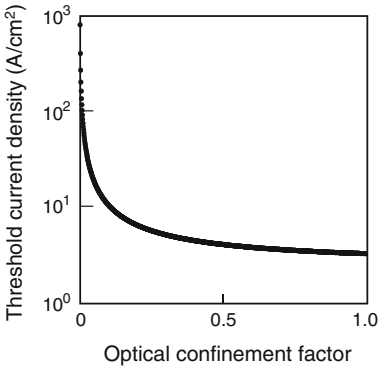

Fig. 5.8 Calculated relation between the optical confinement factor and the threshold current density

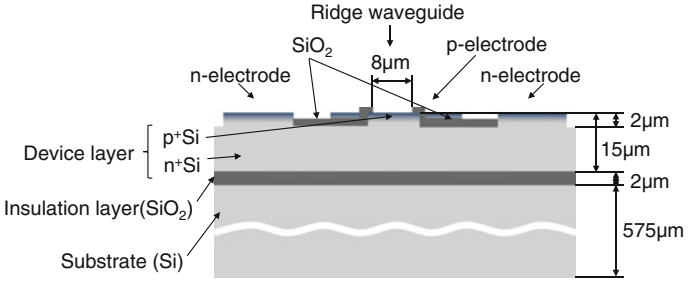

Fig. 5.9 A cross-sectional profile of the improved device

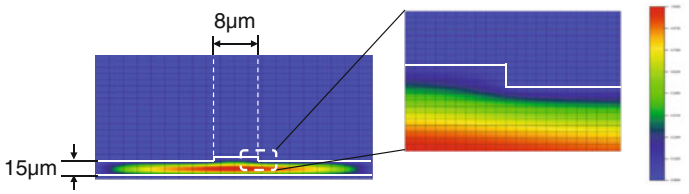

Fig. 5.10 Numerically calculated cross-sectional light intensity profiles for the device in Fig. 5.9

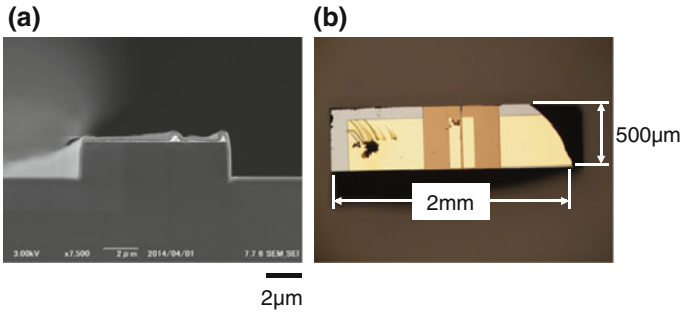

Fig. 5.11 Images of the fabricated device. **a** An SEM image of the end facet of the waveguide. **b** An optical microscopic image of the device

light intensity profiles for the device in Fig. 5.9. A comparison between Figs. 5.2 and 5.10 confirms a higher optical confinement factor, Γ, in the device in Fig. 5.9. However, it should be noted that this figure still shows that a portion of the lasing light leaks and spreads over a wide area of the device layer, even in the improved device of Fig. 5.9, because of its p-n homojunction structure.

The SOI substrate consists of a device layer, an insulating layer made of SiO_2, and a Si support substrate. The device layer is P-doped n-type Si with a resistivity of 2.0×10^{-2} to $3.4 \times 10^{-2}\,\Omega$cm. The thicknesses of the insulation layer and the Si support substrate are 2 and 575 μm, respectively.

Some of the fabrication steps were modified from the process described in Sect. 5.1: (1) B atoms were doped into the device layer by ion implantation to form a p-type layer. Numerical calculations estimated that a p-n homojunction was located at a depth of 1.5–2.5 μm from the surface of the SOI substrate. (2) A Cr/Pt film was deposited on the surface of the SOI substrate. (3) An electron-beam (EB) resist was coated on the Cr/Pt film layer and a stripe (8 μm wide) was formed by EB lithography. (4) A Cr/Pt stripe was formed by ICP-RIE etching. (5) The device layer was etched with CF_4 gas to fabricate a ridge waveguide. (6) An SiO_2 film was deposited on the surface of the waveguide to serve as an insulating film. (7) The insulating film on the waveguide and on a part of the device layer surface was removed. (8) The SiO_2 was etched to expose the top side of the waveguide and part of the device layer surface. (9) A Cr/Pt/Au film was deposited for use as an electrode. (Figure 5.11a shows an SEM image of the end facet of one of the waveguides, which were formed in parallel

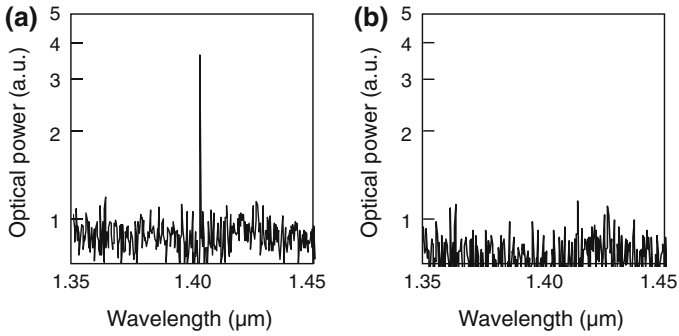

Fig. 5.12 Light emission spectral profiles of the output light. **a** Above the threshold. **b** Below the threshold

on the SOI substrate.) (10) The SOI substrate was diced to separate each waveguide to form solitary laser devices. (Figure 5.11b shows an optical microscopic image of the waveguide.)

DPP-assisted annealing was adopted by injecting a current pulse (1 kHz repetition frequency, 100 μs pulse width, 77.5 A/cm^2 peak current density, 3.2 V peak voltage). The substrate was irradiated with an infrared laser light (1.31 μm wavelength, 1 mW power) during this current injection. The annealing time was 1.5 h.

Figure 5.12 shows the light emission spectral profiles for the fabricated device, acquired at room temperature (25 °C). The vertical axis of this graph is a logarithmic scale. Figure 5.12a shows the profile above the threshold for lasing (current density $J = 42$ A/cm^2, $J/J_{th} = 1.05$). Here, the threshold current density, J_{th}, is 40 A/cm^2, as will be presented below. The sharp spectral peak at a wavelength of 1.40 μm wavelength represents the CW laser oscillation with a single longitudinal mode, even though the waveguide is as long as 500 μm. The origin of this single mode oscillation is that the low infrared absorption by the Si provides a low threshold for the principal longitudinal mode at the optical amplification gain spectral peak and, as a result, the gains for other modes are depleted by this principal mode due to nonlinear mode competition [10, 11]. Figure 5.12b shows the spectral profile below the threshold (current density, $J = 38$ A/cm^2, $J/J_{th} = 0.95$), in which no ASE spectra are seen, which is also because of the gain depletion due to the mode competition described above.

For accurate estimation of the threshold current density, J_{th}, an extremely small current drop in the relation between the applied voltage and the injected current density, due to electrical energy being immediately converted to photon energy when the current density reached the threshold [12], was measured. Figure 5.13 shows the measured relation. An upward arrow in this figure indicates the above-mentioned current drop at 3 V. From the current value at the instant this drop occurred, J_{th} was found to be 40 A/cm^2, which is 1/28 times that of the device in Fig. 5.1.

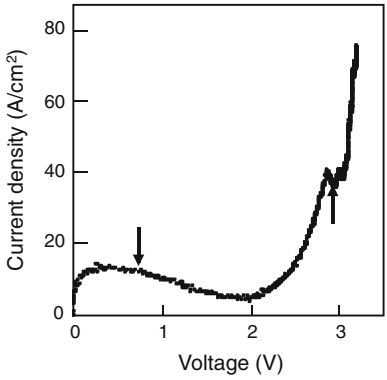

Fig. 5.13 Relation between the applied voltage and current density. The *upward arrow* represents the position of the lasing threshold. The *downward arrow* represents the negative resistance, which originated from the floating capacitance associated with the electrical circuit used for driving this device

A possible reason why this value of J_{th} is still higher than the designed value (8.8 A/cm^2) is that the actual internal loss coefficient is still higher than the value (1.6×10^{-5} cm^{-1}) used for the device design. It should be possible to reduce this coefficient further by improving the fabrication process so that J_{th} approaches the value suggested in Fig. 5.8.

5.3 Evaluation of Optical Amplification Quantities

Section 5.2 demonstrated a laser having an optical waveguide with a large optical confinement factor achieved a remarkably low threshold current density of 40 A/cm^2. Furthermore, its optical amplification quantities, such as the transparent current density J_{tr} and the differential gain coefficient g, were evaluated by using an infrared Si photodetector with optical amplification.

To achieve further improvements in lasing performance, this section evaluates these optical amplification quantities more accurately [13] by using a different method, which has been employed for a conventional infrared laser of a direct transition-type semiconductor [14]. Specifically, the output optical power, P_{out}, of the light emitted from the output facet of the waveguide is measured by irradiating the input facet of the waveguide with laser light (input optical power, P_{in}).

For this evaluation, a wide ridge waveguide was fabricated by using a SOI substrate in order to increase the optical confinement factor. This increase enables improved optical alignment accuracy when irradiating the input facet with the light for exciting a guided mode in the waveguide, resulting in higher accuracy when measuring the value of P_{out}.

As shown in Fig. 5.14a, the width of the ridge waveguide was increased to 750 μm. The thickness and length, L, of the waveguide were 2 and 2000 μm, respectively. The overall dimensions of the device were 1.5 mm × 2.0 mm. The device layer in the SOI substrate was P-doped n-type Si (resistivity 0.020–0.034 Ω cm) with a thickness of 15 μm. The thickness of the SiO_2 insulation layer was 2 μm, and the thickness

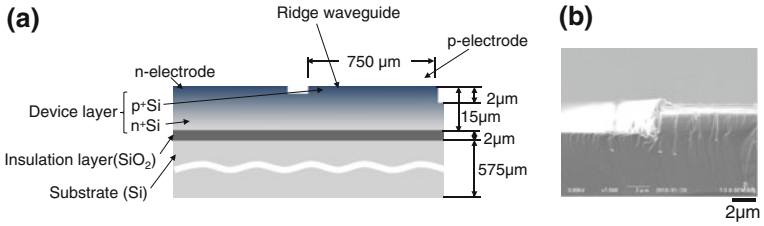

Fig. 5.14 Structure of the optical waveguide used for evaluation. **a** Schematic explanation of the optical waveguide. **b** SEM image of the input facet of waveguide

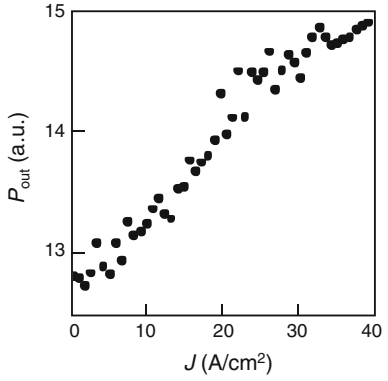

Fig. 5.15 Measured relation between the injection current density, J, and the output optical power, P_{out}. The input optical power, P_{in}, was fixed at 11 mW

of the Si support substrate was 575 μm. The concentration of B doped in the device layer was $1 \times 10^{19}\,\mathrm{cm}^{-3}$. By numerical calculations, the p-n homojunction interface was found to be at a depth of 1.5–2.5 μm from the surface of the SOI substrate. Figure 5.14b is an SEM image of the input facet of the waveguides, which confirms that the thickness of the waveguide is 2 μm.

DPP-assisted annealing was performed for 1 h by injecting a triangular-wave current (current density 0–40 A/cm^2, voltage 0–3 V, frequency 1 Hz) to bring about Joule-heating, while simultaneously irradiating the device with laser light having a photon energy of $h\nu_{anneal} = 0.95\,\mathrm{eV}$ (1.31 μm wavelength) and a power of 40 mW through the input facet of the waveguide. As a result, an infrared Si optical waveguide that can be used for accurate evaluation of the optical amplification quantities was fabricated.

These quantities were evaluated at the photon energy of $h\nu_{anneal} = 0.95\,\mathrm{eV}$ since the Si laser exhibits photon breeding with respect to photon energy. Figure 5.15 shows the relation between the injection current density, J, and the output optical power, P_{out}, which was measured at $P_{in} = 11\,\mathrm{mW}$. From these measured values of P_{out}, the relation between J and the net optical amplification gain G was derived from the equation $G = (1/L)\ln\left(P_{out}(J)/P_{out}(0)\right) - \alpha$, where $\alpha\ (= 2.7 \times 10^{-5}\,\mathrm{cm}^{-1})$ is the absorption loss at the photon energy of 0.95 eV [15]. Figure 5.16 shows the

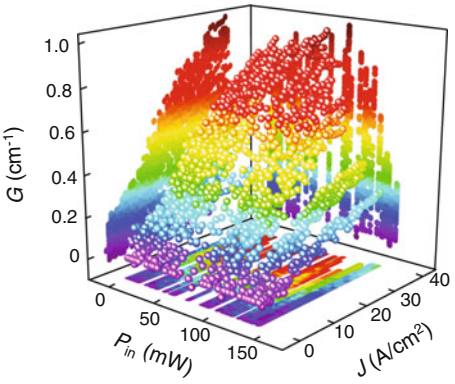

Fig. 5.16 Measured dependence of the net optical amplification gain G on the injection current density J and the input optical power P_{in}

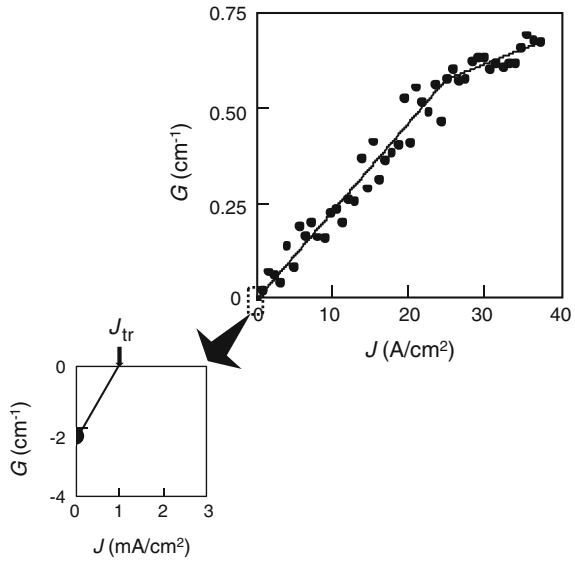

Fig. 5.17 Relation between the injection current density J and the net optical amplification gain G. The input optical power, P_{in}, was fixed at 11 mW. Closed circles are the measured values, to which lines are fitted

measured dependence of G on J and P_{in}, from which the relation between J and G was derived and is represented by closed circles in Fig. 5.17. At $J < 25\,\mathrm{A/cm^2}$, the closed circles are fitted by a line. The value of J_{tr} was evaluated to be $1\,\mathrm{mA/cm^2}$ from the intersection of this line with the horizontal axis, as is represented in the magnified graph at $J < 3\,\mathrm{mA/cm^2}$ in this figure. In the region $J > 25\,\mathrm{A/cm^2}$ of Fig. 5.17, saturation in the increase of G can be seen, as is represented by the fitted line with a smaller slope, which is due to the current leakage. As a reference, this value of J_{tr} is 2×10^{-4}-times that ($5.0\,\mathrm{A/cm^2}$) derived in Sect. 5.2. This is because the mode volume in the waveguide was 1×10^4-times that of the Si photodetector used in Sect. 5.2 (i.e., the value of L of the present device is 1×10^3-times the thickness of the active layer of an infrared Si photodetector, and the spot size of the light incident

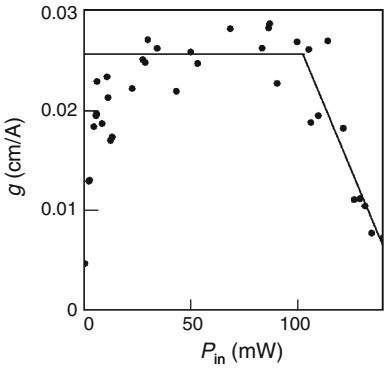

Fig. 5.18 Relation between the differential gain coefficient, g, and the input optical power, P_{in}. *Closed circles* are the measured values, to which *two lines* are fitted

on the input facet of the waveguide is 10-times larger), which corresponds to the inverse of the value 2×10^{-4}. That is, the whole mode volume of the waveguide was fully used for evaluation, by which it is confirmed that the present evaluation result is more accurate than that in Sect. 5.2.

Closed circles in Fig. 5.18 represent the measured relation between P_{in} and the differential gain coefficient g, derived from Fig. 5.16 and the equation $g = (1/JL) \ln (P_{out}(J) / P_{out}(0))$, which were fitted by two lines. It is found from this figure that, at $P_{in} < 40\,\text{mW}$, the value of g decreases as P_{in} decreases. This is because spatially diverging spontaneously emitted light is the main component of the output light. Therefore, a part of the emitted light does not reach the photodetector used for evaluation. However, at $P_{in} > 40\,\text{mW}$, g is independent of P_{in} and takes the value $2.6 \times 10^{-2}\,\text{cm/A}$. This is because high-directivity stimulated emission light is the main component, enabling efficient collection and detection of the emitted light by the photodetector.

Furthermore, at $P_{in} > 100\,\text{mW}$, the value of g decreases as P_{in} increases, which represents the gain saturation. From the line fitted in this region of P_{in}, the saturation power P_{sat} and the saturation power density p_{sat} were evaluated to be 120 mW and $30\,\text{kW/cm}^2$, respectively.

5.4 Novel Devices with High Output Optical Power

Section 5.2 demonstrated that low threshold current density can be achieved, which suggests the capability to realize high output optical power operation with a fairly low injection current. Based on this suggestion, novel devices were designed and fabricated by referring to the values of physical quantities evaluated in Sect. 5.3. Here, for ensuring a large total optical amplification gain, a Si crystal with a large cross-section and long length, and without a waveguide structure, was employed as a laser medium. Employing such a large Si crystal can be more advantageous than

increasing the optical confinement factor of a small waveguide because, due to the p-n homojunction-structure in the Si crystal, an extremely high optical confinement cannot be expected even by further modifying the waveguide structure described in Sect. 5.2.

Figure 5.19 shows the cross-sectional structure of the Si crystal used as the laser medium (1 mm width, 150 μm thickness) [16]. The length of the crystal was 15 mm, as seen in the photograph in Fig. 5.20a. The output facets were cleaved for use as laser cavity mirrors. An As-doped n-type epitaxial Si film (10 μm thickness, 10 Ω cm resistivity) was grown on a Sb-doped n-type Si crystal substrate (15 mΩ cm resistivity). A part of this film was further doped with B atoms by ion implantation to form a p-type layer. The B concentration was 1×10^{19} cm^{-3}. The thickness of the B-doped p-type layer was 1.2 μm. After depositing Cr/Pt/Au films for use as electrodes, the device was installed in a heat sink made of copper plates, as shown in Fig. 5.20b. For DPP-assisted annealing, one of the output facets was irradiated with infrared laser light having a photon energy, $h\nu_{anneal}$, of 0.95 eV (1.31 μm wavelength) and a power of 200 mW, during which annealing was performed by applying a forward-bias current of 5 A to generate Joule-heat, causing the B atoms to diffuse.

Figure 5.21 shows the light emission spectral profile above the lasing threshold of the fabricated device under continuous-wave operation at room temperature [17]. In contrast to those in Figs. 5.7a and 5.12a, it has three spectral peaks A, B, and C. This

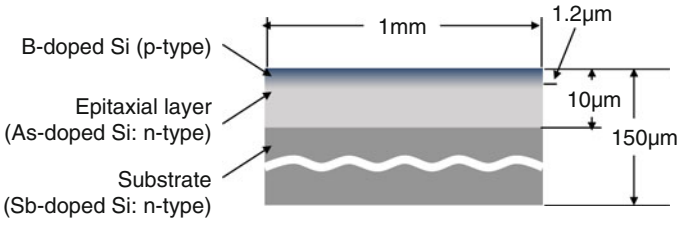

Fig. 5.19 Cross-sectional profile of the Si crystal used as a laser medium and the laser cavity

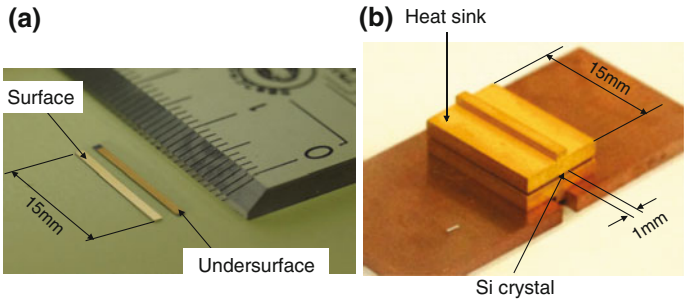

Fig. 5.20 Photograph of the laser. **a** The Si crystal. **b** A heat sink, in which the Si crystal is installed

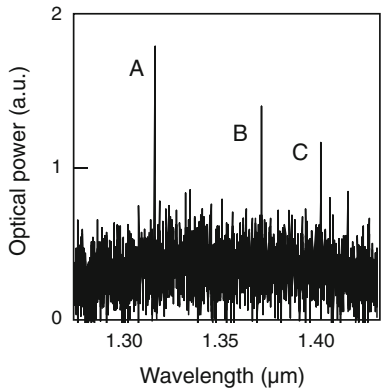

Fig. 5.21 Light emission spectral profile of the output light

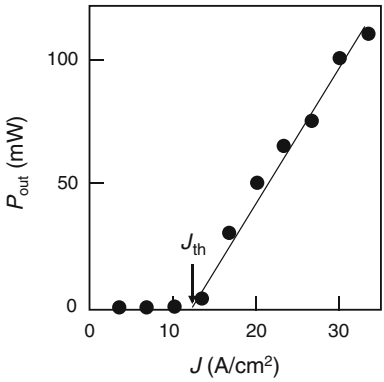

Fig. 5.22 Measured relation between the injection current density, J, and the output optical power, P_{out}, emitted from one output facet of the Si crystal

multi-wavelength operation is attributed to the multiple transverse and longitudinal modes, which are allowed to exist in the present large laser cavity.

The spectral peak A is located at a wavelength of 1.31 μm. This is identical to the wavelength of the light used for the DPP-assisted annealing, which is direct evidence for photon breeding. The spectral peak B at a wavelength of 1.37 μm is a phonon sideband, which is generated after emitting an LO-mode phonon with an energy of 40 meV at the X-point in the energy band diagram in Fig. 3.11b. The spectral peak C is also a phonon sideband, which is generated after emitting a TO-mode phonon with an energy of 60 meV at the X-point.

Closed circles in Fig. 5.22 represent the measured relation between the injection current density, J, and the output optical power, P_{out}, emitted from one output facet of the fabricated device. The value of P_{out} takes a maximum value of 110 mW at $J = 33$ A/cm^2 (5 A injection current). This value is more than 10-times higher than that of a conventional double heterojunction-structured InGaAsP/InP laser (10 mW at 1.3 μm wavelength: SLT1130 series manufactured by Sumitomo Electric). By taking the output optical power from the other output facet into account, the maximum total

output optical power is 220 mW. Further increases in P_{out} are expected by increasing J because the values of P_{out} in this figure are linearly proportional to J and do not saturate.

Figure 5.22 also shows that the threshold current density, J_{th}, is 12 A/cm^2, which is lower than that described in Sect. 5.2 (40 A/cm^2). The origin of such a low J_{th} in the present device is attributed to the large total optical gain due to a large laser medium.

The slope of the line fitted to the closed circles in this figure indicates that the external differential quantum efficiency is 9.0% in the case where the total output optical power is radiated from the two output facets. This is higher than the efficiency of a conventional double heterojunction-structured InGaAsP/InP laser (7% at 1.3 μm wavelength: SLT1130 series manufactured by Sumitomo Electric).

Figure 5.23a shows a dazzling infrared radiation pattern from the output facet, acquired by an infrared camera, which demonstrates the high output optical power. Figure 5.23b is an image of the light scattered from the surface of a screen installed at a position 20 cm away from the laser. The image is spatially modulated, i.e., speckles are clearly seen, which demonstrates a high spatial coherence of the output infrared light beam. Figures 5.21, 5.22 and 5.23 demonstrate that the high output optical power and low threshold current density were simultaneously realized by the present device. These originated from the large optical amplification gain and also from the very low infrared absorption loss.

Since a Si bulk crystal without a waveguide structure was used, the structure of the present device is more similar to those of solid-state and gas lasers than those of conventional double heterojunction-structured semiconductor lasers [18, 19]. Further similarities with solid-state and gas lasers can be found by referring to the magnitude of absorption loss: In the case of solid-state and gas lasers, electronic transitions in the electronically isolated ions, atoms, and molecules are used for lasing. Therefore, even though direct electric current injection to these laser media is difficult, the absorption loss per unit volume is very low. Thus, a high output optical power can be

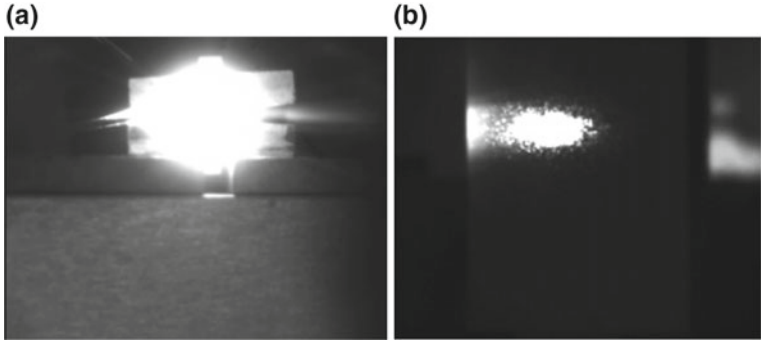

Fig. 5.23 Images of the output infrared light. **a** Radiation pattern of the infrared light emitted from the output facet. **b** The speckles in the light pattern scattered from the screen surface

obtained by increasing the size of the laser medium even though the photon density of the lasing light is low.

On the other hand, in the case of conventional semiconductor lasers, coupled electrons and holes in the conduction and valence bands, respectively, have been used for lasing. Therefore, direct electric current injection to the laser medium is easy. An additional advantage is that the laser medium can be very small. However, the problem is that the absorption loss per unit volume is large, making it impossible to achieve high output optical power and low threshold current density even though the photon density of the lasing light is high.

Considering the discussions above, the present Si laser is found to be similar to solid-state and gas lasers because electronically isolated DPPs are used, which keeps the absorption loss per unit volume very low. Thus, the threshold current density can be decreased. Furthermore, the output optical power can be greatly increased by increasing the size of the laser medium even though the photon density of the lasing light is low. An additional advantage is that electrons can be easily supplied by direct electric current injection, due to a low recombination loss in the Si crystal.

Finally, it should be pointed out that, early in the study of semiconductor lasers, it was found that the absorption loss in indirect transition-type semiconductors was low at low temperature, which was advantageous for inverting the electron population for lasing [20]. However, the disadvantage was that the magnitude of the population inversion was not sufficiently large for ensuring a large optical amplification gain. Since this finding, it has been believed for a long time that indirect transition-type semiconductors are not appropriate for use as laser media. Instead, direct transition-type semiconductors have been popularly used up to now [21].

Now, thanks to the advent of dressed photon technology, DPPs have resulted in the manifestation of large optical amplification gain in indirect transition-type semiconductors, which is the secret to the dramatically high output optical power and low threshold current density realized by the present device made of Si crystal.

References

1. D. Liang, J.E. Bowers, Nat. Photonics **4**, 511 (2010)
2. H. Rong, R. Jones, A. Liu, O. Cohen, D. Hak, A. Fang, M. Paniccia, Nature **433**, 725 (2005)
3. S. Saito, Y. Suwa, H. Arimoto, N. Sakuma, D. Hisamoto, H. Uchiyama, J. Yamamoto, T. Sakamizu, T. Mine, S. Kimura, T. Sugawara, M. Aoki, Appl. Phys. Lett. **95**, 241101 (2009)
4. T. Kawazoe, M. Ohtsu, K. Akahane, N. Yamamoto, Appl. Phys. B **107**, 659 (2012)
5. H. Tanaka, T. Kawazoe, M. Ohtsu, K. Akahane, Fluoresc. Mater. **1**, 1 (2015)
6. W.J. Choi, P.D. Dapkus, J.J. Jewell, I.E.E.E. Photon, Tech. Lett. **11**, 1572 (1999)
7. T. Tanbun-Ek, N.A. Olsson, R.A. Logan, K.W. Wecht, A.M. Sergent, I.E.E.E. Photon, Tech. Lett. **3**, 103 (1991)
8. ZhI Alferov, Semiconductors **32**, 1 (1998)
9. Z.-I. Kazi, T. Egawa, T. Jimbo, M. Umeno, IEEE Photonics Technol. Lett. **11**, 1563 (1999)
10. M. Ohtsu, Y. Teramachi, T. Miyazaki, IEEE J. Quantum Electron. **24**, 716 (1988)
11. M. Ohtsu, Y. Teramachi, T. Miyazaki, IEEE J. Quantum Electron. **25**, 31 (1988)
12. G.P. Agrawal, N.K. Dutta, *Semiconductor Lasers*, 2nd edn. (Van Nostrand Reinhold, New York, 1993)

13. H. Tanaka, T. Kawazoe, M. Ohtsu, K. Akahane, N. Yamamoto, Appl. Phys. A **121**, 1377 (2015)
14. Z.I. Kazi, T. Egawa, T. Jimbo, M. Umeno, IEEE Photonics Technol. Lett. **11**, 1563 (1999)
15. M.A. Green, M.J. Keevers, Prog. Photovolt. **3**, 189 (1995)
16. H. Tanaka, T. Kawazoe, M. Ohtsu, Abstract of the 63st JSAP Spring Meeting (2016, Tokyo, Japan), paper number 19a-S622-8
17. H. Tanaka, T. Kawazoe, M. Ohtsu, K. Akahane, N. Yamamoto, Abstract of the 76th JSAP Autumn Meeting (2015, Nagoya, Japan), paper number 16p-2G-8
18. M. Ohtsu, *Coherent Quanatum Optics and Technology* (KTK Scientific and Kluwer Academic, Tokyo, 1992)
19. M. Ohtsu, *Highly Coherent Semiconductor Lasers* (Artech House, Boston, 1992)
20. J.R. Singer (ed.), *Advances in Quantum Electronics* (Columbia University Press, New York, 1961), pp. 456–506
21. W.P. Dumke, Phys. Rev. **177**, 1559 (1962)

Chapter 6
Light Emitting Diodes Using Silicon Carbide Crystal

A silicon carbide (SiC) is an indirect transition-type semiconductors, as is the case of Si. This section reviews the use of a DPP-assisted process in a bulk crystal SiC for fabricating and operating green, ultraviolet, and broad-spectral width light emitting diodes.

6.1 Basic Light Emitting Diodes

Silicon carbide (SiC) has been considered to be a suitable material for use in high-electrical-power devices because of its high electrical breakdown strength, thermal conductivity, and heat tolerance [1]. Although SiC is an indirect transition-type semiconductor, research has been conducted for realizing blue LEDs using this crystal. However, the external quantum efficiency of the light emission is low, at 0.1% or less, and it has not been easy to fabricate practical devices [2, 3]. This section reviews the use of a DPP-assisted process in a bulk crystal SiC.

Since the bandgap energy E_g of SiC corresponds to ultraviolet to blue wavelengths, visible to ultraviolet SiC-LEDs fabricated via the DPP-assisted process can avoid a decrease in efficiency due to light absorption by 4H-SiC [4]. To achieve light emission from 4H-SiC, the two-step de-excitation process was used, as was described in Sects. 1.3.2 and 3.2. A 500 nm-thick n-type buffer layer (dopant density 1×10^{18} cm^{-3}) was deposited on an n-type 4H-SiC crystal with a thickness of 360 μm, a diameter of 100 mm, a resistivity of 25 m Ω cm, and a surface orientation of (0001), after which a 10 μm-thick n-type epitaxial layer (dopant density 1×10^{16} cm^{-3}) was deposited. The 4H-SiC crystal was then implanted with a p-type dopant (Al) atoms by ion implantation. During this process, the implantation energy was changed in multiple steps in the range 30–700 keV, and the ion dose was adjusted in the range 3.0×10^{13} cm^{-2} to 2.5×10^{14} cm^{-2} for each implantation energy. As a result, the dopant density was modulated between 2.2×10^{19} cm^{-3} and 1.8×10^{19} cm^{-3} in

M. Ohtsu, *Silicon Light-Emitting Diodes and Lasers*,
Nano-Optics and Nanophotonics, DOI 10.1007/978-3-319-42014-1_6

seven periods in the depth direction. After this, thermal annealing was performed for 5 min at 1800 °C to activate the Al ions, forming a p–n homojunction. An ITO film and a Cr/Pt/Au film were deposited on the front and back surfaces, respectively, for use as electrodes. After this, the 4H-SiC crystal was diced to form a device with an area of 500 μm × 500 μm.

A forward bias voltage of 12 V (current density 45 A/cm^2) was applied to the device to bring about annealing due to Joule-heat, which caused the Al to diffuse, modifying the spatial distribution of the dopant concentration. During this process, the device was irradiated from the ITO electrode side with laser light (optical power density 2 W/cm^2) having a photon energy $h\nu_{anneal}$(=2.33 eV, 532 nm wavelength) smaller than E_g of the 4H-SiC (=3.26 eV) [5]. This induced the DPP-assisted process, which modified the Al diffusion due to annealing, leading to the self-organized formation of unique minute inhomogeneous domain boundaries of Al.

Curves A–G in Fig. 6.1a show the measured light emission spectra from the SiC-LED acquired during DPP-assisted annealing. They were measured at 0.01, 0.25, 0.5, 1.0, 3.0, 8.0, and 24.0 hr, respectively, after starting the DPP-assisted annealing. The surface temperature during annealing was 120–150 °C. In order to demonstrate photon breeding, the wavelength (the photon energy $h\nu_{anneal}$) of the light irradiated onto the device during annealing is indicated by the long downward arrow in the figure. These curves show that the total emission power (the area surrounded by the curves and horizontal axis in Fig. 6.1a) increases approximately in proportion to the logarithm of the annealing time because the dopant diffusion rate due to annealing has an extremely large distribution, as has been described for two-level systems [6]. After 8 h of annealing (curve F in Fig. 6.1a), the total emission power was five-times greater than the value immediately after starting annealing (curve A). The total emission power saturated when annealing was conducted for 8 h or more. As shown in

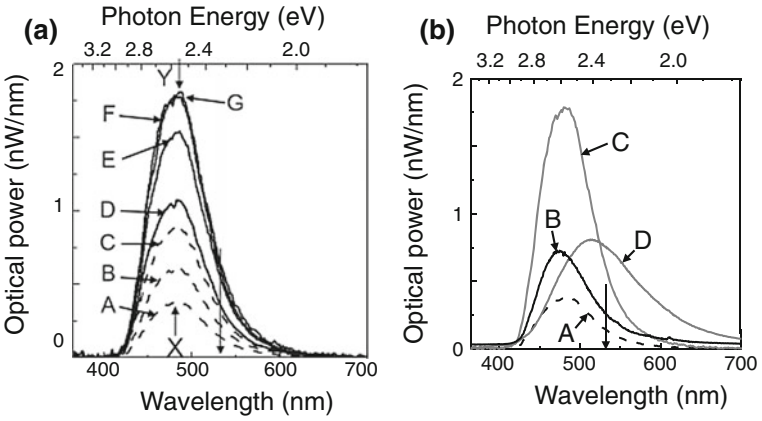

Fig. 6.1 Light emission spectra of the SiC-LED. **a** The spectra acquired during DPP-assisted annealing. *Curves A–G* were acquired at 0.01, 0.25, 0.5, 1.0, 3.0, 8.0, and 24.0 h, respectively, after starting the DPP-assisted annealing. **b** Relationship between the light emission spectral profiles and irradiation intensity during DPP-assisted annealing. The *curve A* was acquired immediately after starting annealing. The *curve B* is the result of annealing without irradiating light. The *curves C* and *D* are the results of annealing with irradiation intensities of 2 and 10 W/cm^2, respectively

Fig. 6.1a, the peak emission wavelength was red-shifted from 480 nm (upward arrow X) to 490 nm (downward arrow Y). Curves A–D in Fig. 6.1b show light emission spectra observed after 8 h of annealing. As shown by the curve D, when the irradiation intensity during annealing was 10 W/cm^2, the wavelength had red-shifted to 515 nm after annealing. It is also shown that the total emission power of the curve D was reduced to about half that in the case of the curve C (irradiation intensity of 2 W/cm^2 during annealing). This was because the progress of the DPP-assisted annealing was not sufficiently controlled by the light irradiation since the 4H-SiC crystal absorbed 532 nm-wavelength light for generating heat. Compared with the curve C, the greater red-shift and also the lower total emission power in the case of the curve D was because the intrinsic energy of the DPP level was close to the photon energy $h\nu_{anneal}$ of the light irradiated during annealing, which counteracted the heat generation due to absorption. On the other hand, when annealing was performed using only current, without irradiating any light (curve B in Fig. 6.1b; current density 45 A/cm^2), the electrodes were degraded due to heat generation in about 1 h, and the emission power decreased.

Figure 6.2 shows the measured relations between the injection current and the light emission power. The SiC-LED was driven with both direct current (closed circles) and pulsed current (closed squares). The images of the output optical beams from the SiC-LED shown in the insets were taken under fluorescent room lights. From the measured relationship between the forward bias voltage and the injection current, it was found that a Schottky barrier effect at the electrodes reduced the light emission efficiency. However, this can be eliminated by applying a voltage sufficiently higher than the potential gap of the Schottky barrier. To achieve this, first, the injection direct current was increased, which caused the voltage applied to the device to rise. In this case, as shown by the closed circles and the solid curve in the figure, the emission power increased nonlinearly due to the two-step de-excitation, and at injection currents of 0.3 mA or higher, it saturated. The major cause of this saturation is probably heat generation due to the injection current. Therefore, to avoid this heat generation, second, a pulsed current was injected with a pulse width of 50 μs

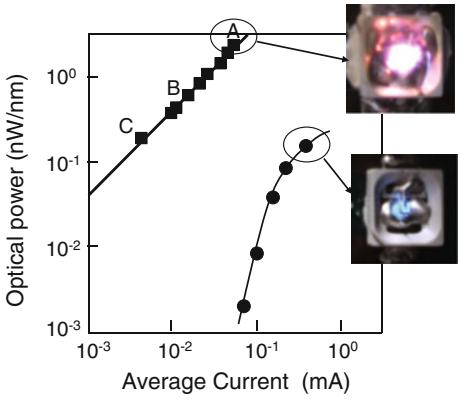

Fig. 6.2 Injection current dependency of the light emission power. The SiC-LED was driven with both direct current (*closed circles*) and pulsed current (*closed squares*). The *insets* show the images of output optical beams from the SiC-LED

and a repetition frequency of 100 Hz. In this case, an instantaneous current of 780–1300 mA flowed in the SiC-LED, and the instantaneous voltage was 23.0–23.6 V. As a result, the emission power was observed to increase linearly and did not saturate, as shown by the closed squares and the solid line in the figure. The reasons for this linear increase are as follows: (1) The driving voltage was sufficiently high, making the number of carriers, which nonradiatively recombine at the Schottky barrier at the electrode, negligibly small. (2) For the injection pulsed current density as high as 320–520 A/cm^2, the Al concentration was not high enough to cause efficient two-step de-excitation. As a result, electrons and holes accumulated at the bottom of the conduction band and the top of the valence band, respectively, where they formed DPPs. Therefore, the one-step transition due to phonon scattering was dominant.

Reason (1) above is well-known in electronic devices having a normal Schottky barrier. The basis for reason (2) is described as follows: Fig. 6.3a–c show measurement results of the light emission spectra of the SiC-LED, driven by pulsed current, which correspond to closed squares A, B, and C on the solid line in Fig. 6.2, respectively. When the pulsed current was small (Fig. 6.3c), the temperature of the device was low, and a separate phonon level was observed (the peak at the wavelength of 390 nm in the figure: downward arrow). This peak appeared for the first time due to pulsed current operation, but the photon energy of this peak is lower than E_g of 4H-SiC by an amount corresponding to the energy of LO-mode phonons (95 meV) or the energy of TO-mode phonons (110 meV) [7]. From a comparison of Fig. 6.3a–c, it

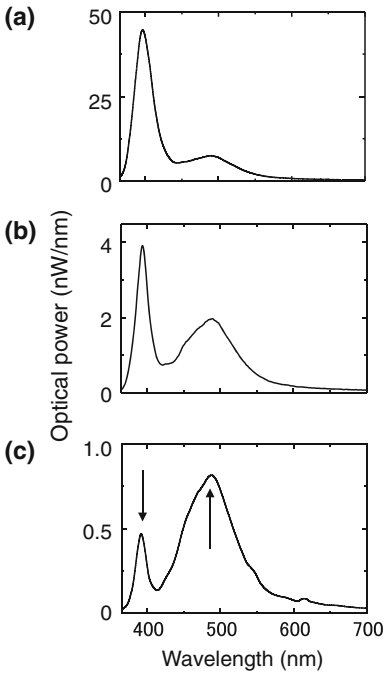

Fig. 6.3 Light emission spectra of the SiC-LED, driven by pulsed current. **a–c** correspond to squares A, B, and C on the *solid line* in Fig. 6.2, respectively

is clear that the intensity of this emission peak governs the emission intensity while driving the device with pulsed current. Since the energy of this emission level is close to E_g, recombination luminescence is possible via a one-step transition involving only phonon emission. Of course, an emission peak corresponding to the DPP level also exists (upward arrow in Fig. 6.3c) even under direct-current injection to the SiC-LED. However, comparing Fig. 6.3a–c, the height of the emission peak is saturated. Therefore, when the SiC-LED was driven by a pulsed current, it is likely that the one-step transition was dominant, resulting in a linear increase in the emission power with increasing current.

The gradient of the solid line in Fig. 6.2 corresponds to an external quantum efficiency of 1%. From the light extraction efficiency (<30%) and the light absorption (>70%), the internal quantum efficiency was estimated to be 10%. This value is as large as the efficiency of conventional LEDs using direct transition-type semiconductors. It is expected that this efficiency will be increased by carrying out more precise adjustments of the thickness and dopant density.

6.2 Green Light Emitting Diodes

This section reviews the fabrication and operation of a SiC-LED, which emits green light [8]. An N-doped 6H-SiC bulk crystal (n-type) was used, and the crystal was doped with Al atoms to convert the it from n-type to p-type for forming a p–n homojunction. The size of the fabricated SiC-LED was 3 mm × 3 mm (Fig. 6.4).

ITO and Cr/Al films were used as electrodes. The device surface was irradiated with green laser light with a wavelength of 532 nm for the DPP-assisted annealing.

The light emission spectra of the fabricated SiC-LED (Fig. 6.5) show that the emitted light intensity at the wavelength of 550 nm increases remarkably with increasing annealing time. Two upward arrows represent the peak wavelengths of the emission spectra acquired at 10 and 50 min after starting annealing, showing that the peak wavelength shifted toward the wavelength (532 nm) of the light irradiated during the annealing. The magnitude of this blue-shift observed during this 40 min-period was 15 nm.

The downward arrow represents the spectral peak at a wavelength of 448 nm (2.77 eV photon energy) which appeared 10 min after starting annealing. This peak origi-

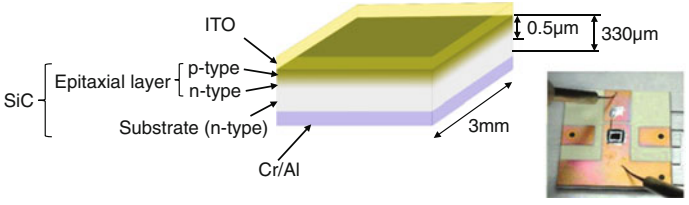

Fig. 6.4 Structure and photograph of the SiC-LED

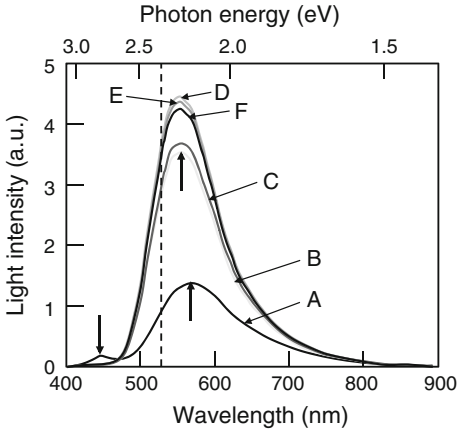

Fig. 6.5 Light emission spectra. *Curves A–F* are the results acquired at 10, 50, 60, 90, 120, and 150 min after starting the DPP-assisted annealing, respectively. The injection current density was 10 A/cm^2

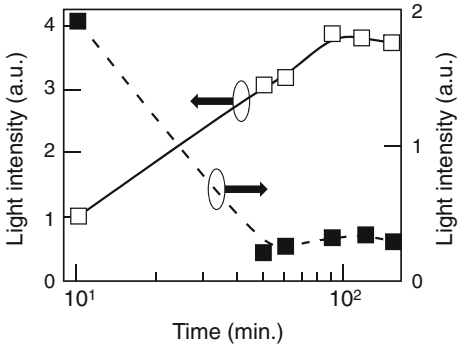

Fig. 6.6 Relation between the DPP-assisted annealing time and the emitted light intensity. Closed and open *squares* represent the light intensity at wavelengths of 448 ± 0.5 and 532 ± 0.5 nm, respectively

nated from an intra-band transition whose transition energy is lower than that of the band-edge transition for emitting light with a wavelength of 410 nm (3.02 eV photon energy) [9]. The difference is 250 meV, which corresponds to the difference between the bandgap energy E_g(=3.26 eV) of the SiC crystal and the emitted photon energy. This photon emission comes from a donor-acceptor recombination or a free-to-bound electron recombination. Closed squares in Fig. 6.6 represent the emitted light intensity at a wavelength of 448 ± 0.5 nm, indicated by the downward arrow in Fig. 6.5. It decreases with increasing annealing time, which is due to the following reasons: Soon after the annealing starts, the SiC crystal temperature increases, so that a large number of incoherent non-localized phonons are created. These phonons trigger the electron-hole recombination, increasing the spontaneous emission probability. However, as the annealing advances, the stimulated emission probability increases, decreasing the crystal temperature. As a result, the spontaneous emission probability and also the emitted light intensity decrease.

Open squares in Fig. 6.6 represent the emitted green light intensity at a wavelength of 532 ± 0.5 nm, which takes the maximum value at 90 min and slightly decreases subsequently. These temporal variations originate from the variation of the spatial

distribution of the Al atoms and can be described by a two-level system model (refer to Appendix E) [10]: Since the time evolution of the spatial distribution of Al atoms correlates with that of the emitted light intensity and can be represented by the two-level system model, the temporal variation of the emitted light intensity is given by (E.5) of Appendix E. The solid curve in Fig. 6.7 represents (E.5), which was least-squares fitted to the experimental results (open squares, which are identical to those in Fig. 6.6). The agreement between this curve and the open squares confirms the validity of applying the two-level system model.

The emitted light intensity (open squares in Figs. 6.6 and 6.7) decreased after 90 min, which is due to the deterioration of the electrical characteristics of the electrodes and electrical wires caused by the heat generated during the annealing. In order to avoid this decrease, the device structure was improved by employing more-reliable assembly technologies, including wire-bonding, which have been popularly used for conventional commercial LEDs. Figure 6.8 shows the improved device structure with an areal size of 500 μm × 500 μm. An ITO film was used for the front electrode, a part of which was replaced with a Ni/Au film. A Cr/Pt/Au film was used for the back electrode. Figure 6.9 represents the light emission spectra. Comparing the curves A and B in this figure, it is confirmed that the emitted light intensity increased at a

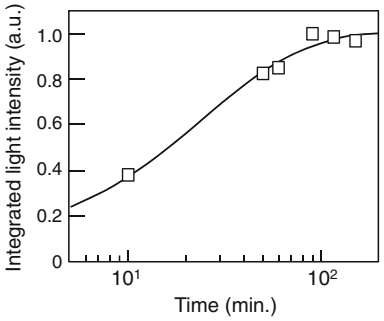

Fig. 6.7 Temporal evolution of the emitted light intensity. Open *squares* are the experimental results, which are identical to those in Fig. 6.6. The *solid curve* represents (E.5), which was least-squares fitted to the open *squares*

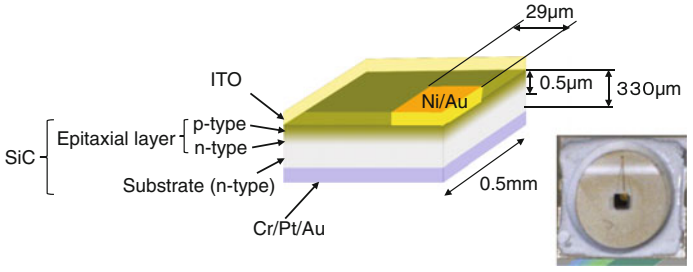

Fig. 6.8 Structure and photograph of the improved SiC-LED device

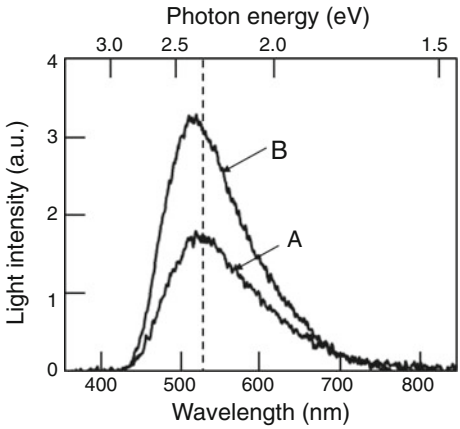

Fig. 6.9 Light emission spectra. *Curve A* is the result for the un-annealed device. *Curve B* is the result for the DPP-assisted annealed device. Their annealing time is 230 min

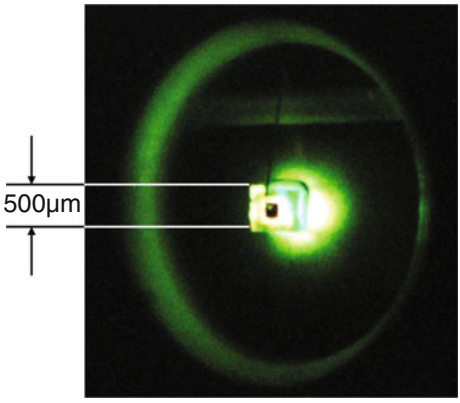

Fig. 6.10 *Green light* emitted from the improved SiC-LED device

wavelength of 532 nm after the DPP-assisted annealing. Since the injection current for annealing could be maintained low, the two curves do not have a peak at a wavelength of 448 nm, which confirms that the reproducibility and reliability of the device performance improved.

As shown by Fig. 6.10, the emitted green light intensity localizes around the Ni/Au film. This is because the injection current is concentrated under this film, as is demonstrated by the result of numerical calculations shown in Fig. 6.11. The light intensity around the ITO film is lower, because the injection current is lower at the p–n homojunction (Fig. 6.11). This is also because of the low light extraction efficiency due to total reflection at the air–SiC interface. This efficiency can be increased by adopting a cap layer, a window layer, and a patterned electrode.

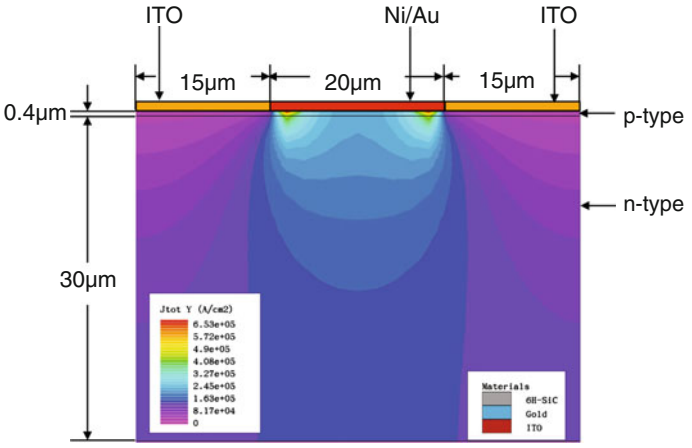

Fig. 6.11 Cross-sectional profile of the injection current density derived by numerical calculations

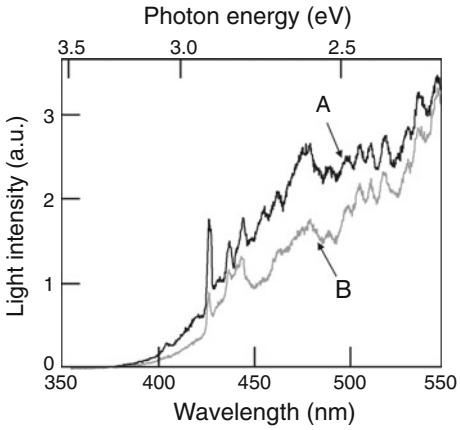

Fig. 6.12 Photoluminescence spectra. *Curves A* and *B* are the results acquired at temperatures of 7 and 100 K, respectively

6.3 Ultraviolet Light Emitting Diodes

This section reviews the fabrication and operation of a SiC-LED, which emits ultraviolet light whose photon energy is higher than E_g [11]. An N-doped 4H-SiC bulk crystal (n-type) was used, and the crystal was doped with Al atoms in order to convert the n-type material to p-type for forming a p–n homojunction.

Figure 6.12 shows the photoluminescence spectra emitted from an un-annealed device acquired by using a 325 nm-wavelength He-Cd laser as an excitation light source. The two curves have several spectral peaks, which suggest the existence of impurities in the SiC crystal. Absorption spectra were also acquired and are shown in Fig. 6.13. The two curves in this figure have a spectral peak at a wavelength of 470 nm, which originated from the doped N atoms.

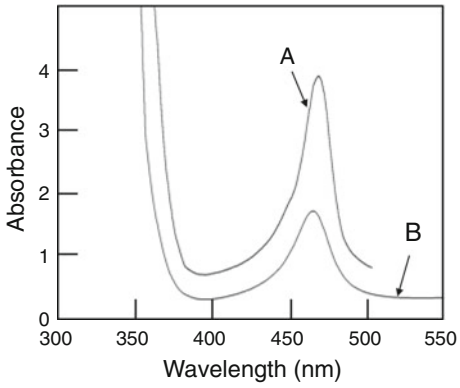

Fig. 6.13 Absorption spectra. *Curves A* and *B* are the results for the SiC crystals with and without doping N atoms, respectively

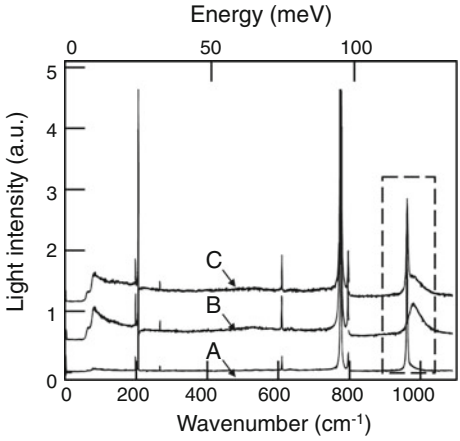

Fig. 6.14 Raman scattering spectra. *Curves A–C* are the results acquired in the epitaxial layer, the n-layer, and the p-layer, respectively

Raman scattering spectra were acquired for finding the defects in the SiC crystal and evaluating the crystalline quality after doping with the Al atoms. Back-scattered light from the (0001)-surface was collected by using a laser (wavelength 488 nm and power 20 mW) as an excitation light source. Figure 6.14 shows the acquired Raman scattering spectra. Sharp spectral peaks in the wavenumber region of 200–800 cm^{-1} originated from the Raman-active folded phonon modes, which are created since the dispersion curve of the phonon modes (propagating along the c-direction in the crystal) are approximated by folded curves in the basic Brillouin zone [12]. In the area surrounded by the broken-line square, spectral peaks originated from the LO-mode phonon-plasmon coupled mode [13], which indicates that a thin intrinsic layer exists between the p- and n-layers. A broader spectral component at the tail of the curve C in this broken-line square indicates that the p-type carriers are activated.

Figure 6.15 shows the experimental setup for the DPP-assisted annealing. Since the short-wavelength light, irradiated during the annealing, is strongly absorbed by the SiC crystal due to its higher photon energy than E_g, this light was irradiated not from the top surface of the device but from the side surface in order to carry out the DPP-assisted annealing effectively by decreasing the magnitude of absorption. DPP-assisted annealing was carried out using both a single light source and two light sources.

(1) Using a single light source

Curve A in Fig. 6.16a shows the light emission spectrum of the un-annealed device, which exhibits a low emitted light intensity in the region around E_g (refer to the inset). Curves B–D show the light emission spectra acquired after the DPP-assisted annealing by irradiating the device with light from a single light source (wavelength 325 nm, photon energy 3.81 eV). The curves in the inset show that the emitted light intensity around 3.13 eV increased with increasing annealing time. This emitted photon energy is nearly equal to or higher than E_g, which falls in the UV region. On the other hand, the intensities for photon energies

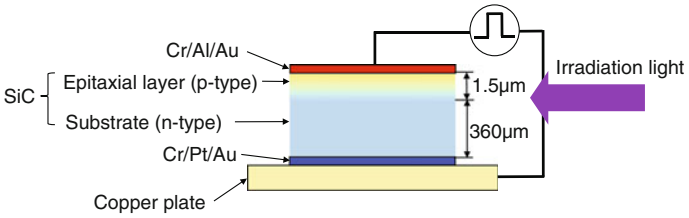

Fig. 6.15 Experimental setup for the DPP-assisted annealing

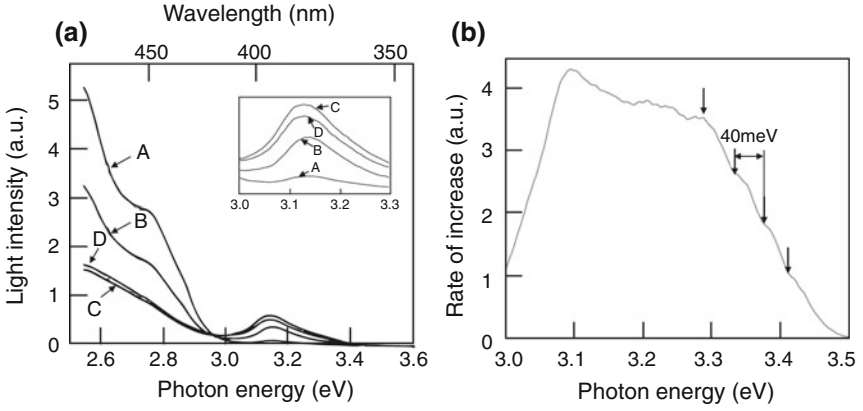

Fig. 6.16 Light emission spectra. **a** *Curve A* is the result for the un-annealed device. *Curves B–D* are those for the DPP-assisted annealed device. Their annealing times are 68, 324, and 410 min, respectively. **b** Rate of increase, i.e., the spectral intensity of the *curve D*, which is divided by that of the *curve A*

lower than 3.0 eV decreased, as represented by the main part in Fig. 6.16a. The above-described dependencies of the emitted light intensities on the annealing time are explained as follows: Although a DPP with an energy of 3.81 eV is created at the doped Al atoms by irradiating the device with 3.81 eV-photon energy light during the annealing, the created DPP does not trigger stimulated emission because the energy of the excited electron in the conduction band is lower than the created DPP energy. However, after creating a multimode coherent phonon by the DPP-assisted annealing, the DPP can trigger stimulated emission since the DPP energy decreases and approaches the excited electron energy. Furthermore, since the wave-number of this phonon is equal to the difference between those of the electrons at the Γ–point and the M-point, the requirement for the momentum conservation law is met, and a photon is emitted. As a result, the light intensity emitted from the annealed device increases around 3.13 eV. In contrast, the light intensity at longer wavelengths decreases because the injected electrons are spent for emitting photons around 3.13 eV. Figure 6.16b shows the rate of increase of the emitted light intensity, i.e., the intensity from the annealed device, which was divided by that from the un-annealed device. The curve in this figure has a spectral peak at 3.10 eV, which is 130 meV lower than the photon energy (3.23 eV) emitted by the interband transition. Since the value of this energy difference corresponds to the phonon energy of the LO-mode, it is confirmed that the annealed device created an LO-mode phonon in the electron-hole recombination process. This curve has an oscillatory profile with a period of 40 meV (indicated by the downward arrows) in the energy region higher than E_g, which indicates that the phonons of the optically active acoustic mode are also involved in the electron-hole recombination process.

(2) Using two light sources

Two light sources were used for more effective DPP-assisted annealing. In more detail, in addition to 325 nm-wavelength light, 473 nm-wavelength light was simultaneously irradiated during the annealing. Curves A and B in Fig. 6.17 show

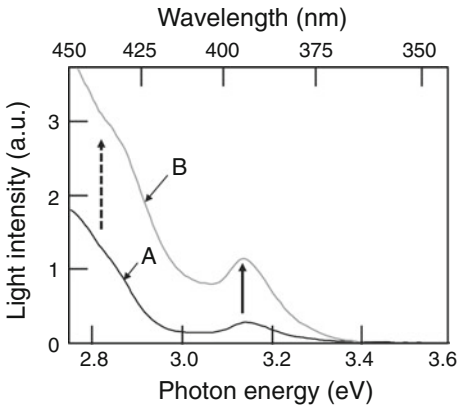

Fig. 6.17 The light mission spectra. *Curve A* is the result for the un-annealed device. *Curve B* is the result for the DPP-assisted annealed device with an annealing time of 190 min

the light emission spectra from the un-annealed and annealed devices, respectively, from which it is confirmed that the DPP-assisted annealing increased the emission intensity not only in the UV region but also in the blue region, as indicated by the upward solid and broken arrows, respectively. In order to compare the results of the DPP-assisted annealing by using a single light source and two light sources, Fig. 6.18 shows the rate of increase of the emitted light intensity. The curve A is identical to the curve in Fig. 6.16b. The curve B was derived from the two curves in Fig. 6.17. It is confirmed from these curves that the use of two light sources resulted in two effects in the SiC-LED. One effect is to broaden the spectral width, which is because both kinds of light, with higher and lower photon energies, efficiently contributed to the DPP-assisted annealing, thus increasing the emitted light intensity at corresponding photon energies due to photon breeding. As a superposition of these light emission spectra, the curve B is broader than the curve A. The photon energy at the peak of the curve B is 100 meV lower than that of the curve A, which is due to irradiation of the device with the 473 nm-wavelength light. The other effect is acceleration of the DPP-assisted annealing. Although the values of the rate of increase between these curves are almost equal, the annealing time required to attain these values was as short as 190 min in the case of the curve B, whereas it was 324 min in the case of the curve A. The reason for this difference, i.e., the acceleration of the DPP-assisted annealing, can be explained by using the two-level system model (refer to Appendix E): Among the two kinds of light, the photon energy of the 325 nm-wavelength light is higher than E_g, resulting in excitation of the Al atoms, causing them to transition to the excited state. As a result, Al atoms drift in a wide range of the configuration coordinate space since the energy at the local minimum of the potential energy of Al atom is low in this space. On the other hand, since the photon energy of the 473 nm-wavelength light is lower than E_g, this light decreases the drift range by triggering stimulated emission so that the Al atoms promptly reach a specific position and are stabilized. After this stabilization, the Al atoms are de-excited to the ground state. This prompt stabilization accelerates the DPP-assisted annealing.

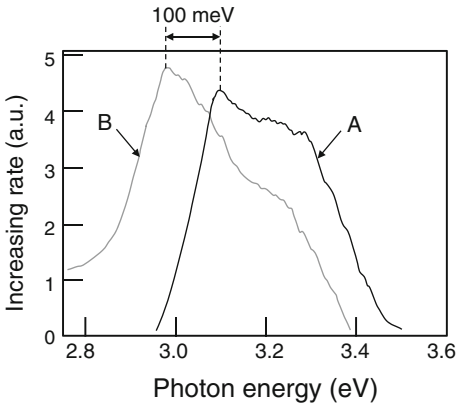

Fig. 6.18 Rate of increase. *Curve A* is identical to the curve in Fig. 6.16b. *Curve B* is the magnitude of the *curve B* in Fig. 6.17, which is divided by that of the *curve A*

As the last topic of this section, a novel polarization control method is reviewed. Since a SiC-LED emits visible light, controlling its polarization could be advantageous in reducing power consumption in backlight systems for displays and imaging systems. As was the case of the Si-LED described in Sect. 3.4, it is expected that photon breeding with respect to photon spin occurs also in a SiC-LED. That is, the light emitted from the SiC-LED is polarized if it is fabricated by irradiating the SiC crystal with polarized light during the DPP-assisted annealing. The remaining part of this section reviews a novel polarization control method for SiC-LEDs (4H-type SiC crystal) based on photon breeding with respect to photon spin [14]. The fabrication method is the same as those described in the previous sections, except that the irradiated light is linearly polarized. Its photon energy, $h\nu_{anneal}$, and wavelength are 2.62 eV and 473 nm, respectively.

For evaluating the polarization characteristics of the fabricated SiC-LED, the emitted light was decomposed into two linearly polarized components by using a linear polarizer, and their intensities ($I_{\parallel}$, $I_{\perp}$) were acquired. The polarization directions of these components are respectively parallel and perpendicular to that of the light irradiated during the DPP-assisted annealing. Their light emission spectra at an injection current of 100 mA are represented by the curves A and B in Fig. 6.19, whose spectral peak energy $h\nu_{peak}$ (=2.58 eV, 480 nm-wavelength) is close to $h\nu_{anneal}$ due to the photon breeding with respect to photon energy. It is seen that $I_{\parallel}$ is larger than $I_{\perp}$ in a wide spectral range, which represents photon breeding with respect to photon spin.

The black squares and white circles in Fig. 6.20 represent the measured relation between the DPP-assisted annealing time and the degree of polarization P ((3.2) of Sect. 3.4) at the photon energies $h\nu_{peak}$ and $h\nu_{anneal}$, respectively. The value of P in this figure increases with increasing annealing time and reaches a maximum value of 0.12. The measured values were fitted by the curves A and B. These curves represent the result of numerical calculation based on the two-level system

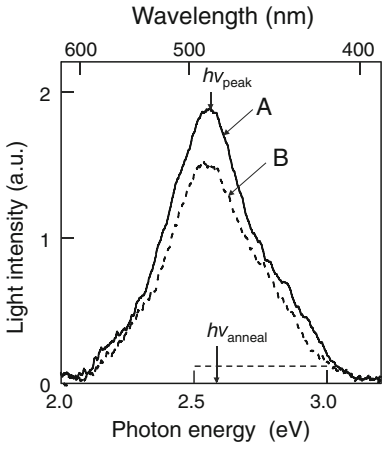

Fig. 6.19 Light emission spectra. *Curves A* and *B* are the linearly polarized components, which are respectively parallel and perpendicular to the direction of the linear polarization of the light irradiated during the annealing

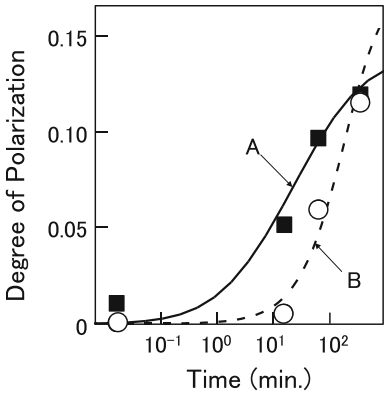

Fig. 6.20 Relation between the DPP-assisted annealing time and the degree of polarization. The *black squares* and white circles represent the measured values at the photon energies $h\nu_{peak}$ and $h\nu_{anneal}$, respectively. The *curves A* and *B* represent the theoretical values, which were fitted to the measured values

model ((E.5) of Appendix E). The agreement between this curve and the measured values suggests that the polarization was controlled by the linearly polarized light irradiated during the DPP-assisted annealing. The origin of the induced polarization in the emitted light is the spatial distribution of Al atoms, which was controlled by the linearly polarized light irradiated during the DPP-assisted annealing (refer to Sect. 3.3). The slope of the curve B is larger than that of the curve A, which means that a larger value of P is expected at the photon energy $h\nu_{anneal}$ by further increasing the annealing time and by more precisely adjusting the annealing parameters.

6.4 Broad-Spectral-Width Light Emitting Diodes

This section reviews broadening of the spectral width of the light emitted from a SiC-LED by using a Xe lamp for the DPP-assisted annealing [15]. An epitaxial film was grown on n-type 4H-SiC, and the crystal was doped with Al atoms for forming the p-type layer. The areal size of the device was 500 μm × 500 μm (Fig. 6.21). An ITO film and a Cr/Al film were used as electrodes.

(1) Using two lasers

As a preliminary broadening experiment, two kinds of light with wavelengths of 325 and 532 nm were simultaneously radiated during the annealing (refer to Sect. 6.3). Curve A in Fig. 6.22 shows the light emission spectrum of the un-annealed device. This emission is caused by electron-hole recombination from a defect energy level [16], especially via the energy levels of the Z1 centers created by the saw-tooth transition and also via the energy levels of the doped Al atoms [17]. Curves B and C are the spectra acquired at 370 min and 17 h after starting annealing, respectively, which show that the emitted light intensity increases with increasing annealing time. They also show the red-shift of the spectral peak and

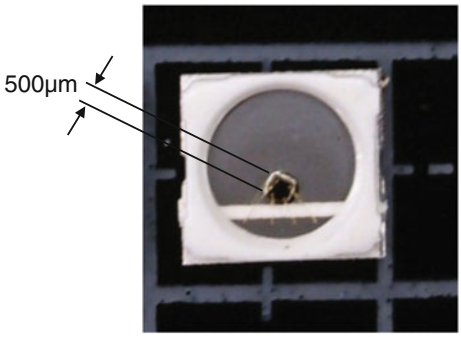

Fig. 6.21 Photograph of a broad-spectral-width SiC-LED

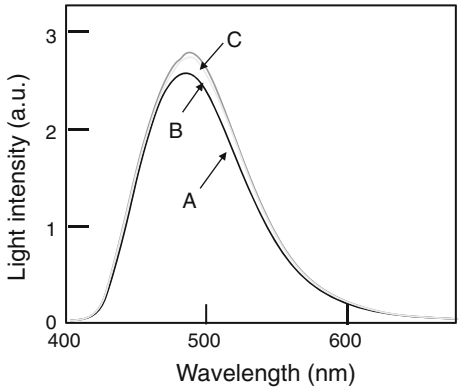

Fig. 6.22 Light emission spectra. *Curve A* is the result for the un-annealed device. *Curves B* and *C* are those for the DPP-assisted annealed devices with annealing times of 370 min and 17 h, respectively

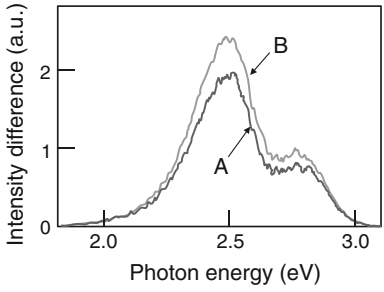

Fig. 6.23 Difference in the emitted light intensities between the annealed and un-annealed devices. *Curve A* is the difference between the *curves B* and *A* in Fig. 6.22. *Curve B* is the difference between the *curves C* and *A* in Fig. 6.22

the increases of the spectral half width. Their magnitudes are 2.2 and 1.4 nm, respectively. In order to investigate the origin of these variations of the spectral profiles, the curve A in Fig. 6.23 shows the difference in the emitted light intensities between the annealed and un-annealed devices (i.e., between the curves B and A in Fig. 6.22). Curve B is the difference between the curves C and A in Fig. 6.22. The curves A and B show that the emitted light intensities increase in the photon energy region of 2.47–2.81 eV. However, it should be noted that these photon

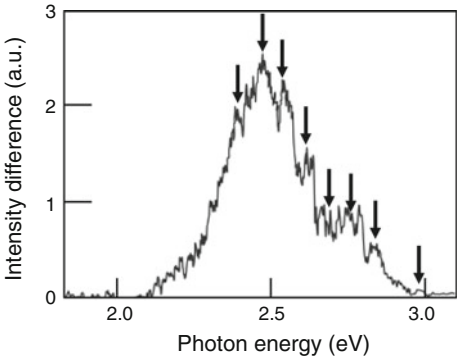

Fig. 6.24 Difference in the emitted light intensities between the annealed devices, i.e., the difference between the *curves C* and *B* in Fig. 6.22

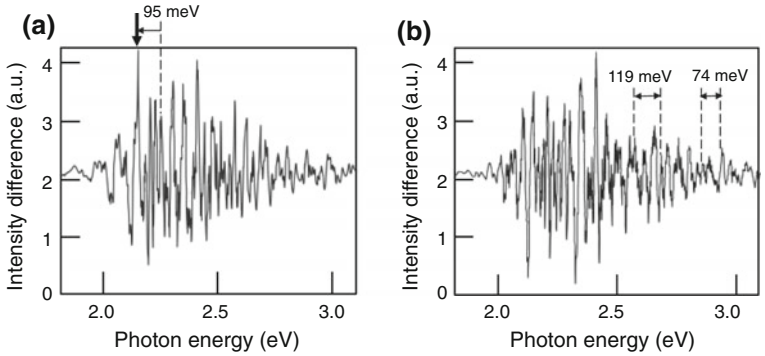

Fig. 6.25 High Fourier-frequency filtered components of the intensity differences. **a**, **b** are those extracted from the *curves A* and *B* in Fig. 6.23, respectively

energies are not equal to those of the two kinds of light irradiated during the annealing (3.81 and 2.33 eV, respectively, for wavelengths of 325 and 532 nm). For a more detailed investigation, Fig. 6.24 shows the difference in the emitted light intensities between the annealed devices, i.e., the difference between the curves C and B in Fig. 6.22. The curve in this figure exhibits multiple spectral peaks, as identified by downward arrows. The separation between the adjacent peaks is 74 meV, from which these spectral peaks are identified as phonon sidebands and the spectral peaks in Figs. 6.22 and 6.23 are attributed to the emission from the 2.33 eV-energy level via absorption of an LA-mode phonon [18]. For analyzing these sidebands, Fig. 6.25a, b show high Fourier-frequency components, extracted from curves A and B in Fig. 6.23, respectively. The curve in Fig. 6.25a has a high, sharp spectral component (indicated by a downward arrow) at 95 meV lower than the photon energy of 2.33 eV. This peak indicates that phonons of the TO-mode are created. On the other hand, the curve in Fig. 6.25b has a more

complicated oscillatory profile in the energy region higher than 2.33 eV because it has two intervals (74 and 119 meV), which indicates that phonons of the LA- and LO-modes are created. By referring to Fig. 6.25a, b, the sideband generation in Fig. 6.24 is discussed in detail as follows: Because the density of states of the TO-mode is sufficiently high to maintain the large probability of the interaction with a DP having an energy of 2.33 eV, the spatial distribution of Al atoms is optimized for this interaction within a short annealing time, resulting in sideband generation due to the phonons of the TO-mode. On the other hand, since the phonons of the LA- and LO-modes weakly interact with the 2.33 eV-energy DP, a longer annealing time is required for generating the phonon sidebands. Because the spatial distribution of Al atoms varies as annealing proceeds, the sidebands due to the TO-mode gradually disappear and, as a result, the sidebands due only to the LA- and LO-modes survive, forming the oscillatory profile in Fig. 6.25b.

(2) Using a Xe lamp

For further increasing the light emission spectral width, the two light sources described in (1) above were replaced with a broad-spectral-width Xe lamp. One purpose for this replacement is to demonstrate the possibility of realizing DPP-assisted annealing even when using incoherent light. Curve A in Fig. 6.26 shows the light emission spectrum of the un-annealed device, whereas the curves B–D were acquired after the DPP-assisted annealing by using the Xe lamp. By comparing the curves A–D, it is found that the emitted light intensity increased with increasing annealing time. However, it temporarily decreased between 30 and 60 min of annealing time. This decrease is because the sufficiently high diffusion rate of the Al atoms was maintained for up to 60 min since the Joule-heating caused by current injection was more dominant than cooling caused by the stimulated emission of light. After 60 min, however, the stimulated emission probability increased, reducing the heat generation, and finally, the spatial distribution of Al atoms approached a specific profile for increasing the intensity of the emitted light, whose spectral profile depends on the spectral profile of the light from the Xe lamp (curve E).

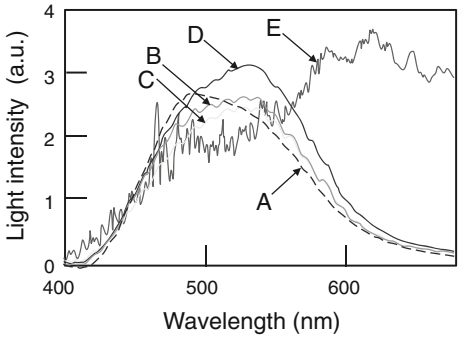

Fig. 6.26 Light emission spectra of the SiC-LED, annealed by using a Xe lamp. *Curve A* is the result for the un-annealed device. *Curves B–D* are those for the DPP-assisted annealed devices. Their annealing times are 30, 60, and 120 min, respectively. *Curve E* is the light emission spectrum from the Xe lamp

Comparing the curves B–D revealed a red-shift of the spectrum, whose magnitude increased with increasing annealing time. The magnitude of the red-shift of the curve D with respect to the curve A is as large as 10 nm. It is also found that the increase in the spectral width of the curve D is as large as 0.6 nm, which suggests the possibility of an asymptotic approach to the spectral width of the light from the Xe lamp by carefully adjusting the DPP-assisted annealing parameters.

References

1. M. Bhatnagar, B.J. Baliga, IEEE Trans. Electron Devices **40**, 645 (1993)
2. G. Ziegler, P. Lanig, D. Theis, C. Weyrich, IEEE Trans. Electron Devices **30**, 277 (1983)
3. J.A. Edmond, H.-S. Kong, C.H. Carter Jr., Phys. B **185**, 453 (1993)
4. T. Kawazoe, M. Ohtsu, Appl. Phys. A **115**, 127 (2014)
5. C. Persson, U. Lindefelt, Phys. Rev. B **54**, 10257 (1996)
6. W. Breinl, J. Friedrich, D. Haarer, Chem. Phys. Lett. **106**, 487 (1984)
7. H. Nienhaus, T.U. Kampen, W. Monch, Surf. Sci. **324**, L328 (1995)
8. K. Suzuki, K. Chieda, T. Kawazoe, T. Yatsui, M. Ohtsu, Abstract of the 61st JSAP Spring Meeting, March 2014, Sagamihara, Japan, Paper number 18a-F12-11
9. W.J. Choyke, L. Patrick, Phys. Rev. **127**, 1868 (1962)
10. R. Jankowiak, R. Richert, H. Bassler, J. Phys. Chem. **89**, 4569 (1985)
11. Q.H. Vo, T. Kawazoe, M. Ohtsu, Abstract of the 61st JSAP Spring Meeting, March 2014, Sagamihara, Japan, Paper number 18a-F12-10
12. S. Nakashima, H. Harima, Phys. Status Solidi (a) **162**, 39 (1997)
13. T. Yuasa, S. Naritsaka, M. Mannoh, K. Shinozaki, K. Yamanaka, Y. Nomura, M. Mihara, M. Ishii, Phys. Rev. B **33**, 1222 (1986)
14. T. Kawazoe, K. Nishioka, M. Ohtsu, Abstract of the International Display Workshop 2014, (Niigata, Japan, 2014) Paper number PRJ1-1
15. K. Chieda, Thesis Paper, the University Tokyo (2014)
16. A. Galecks et al., Appl. Phys. Lett. **81**, 883 (2002)
17. A.A. Lebedev, Semiconductor **33**, 107 (1999)
18. M. Hofmann, A. Zywiets, K. Karch, F. Bechstedt, Phys. Rev. B **50**, 13401 (1994)

Chapter 7
Light Emitting Diodes Fabricated Using Other Crystals

This chapter reviews LEDs using semiconductor materials other than Si. The first example is gallium phosphide (GaP), which is indirect transition-type semiconductors, as is the case of Si. The second one is zinc oxide (zinc oxide). Although it is a direct transition-type semiconductor, it has been difficult to form a p-type crystal in this material for highly efficient LEDs by conventional technologies.

7.1 Using a Gallium Phosphor Crystal

A gallium phosphor (GaP) ($E_g = 2.26$ eV; wavelength, 548 nm) is a low-cost material that can be readily used to grow single crystals and research into light emitting devices using GaP has been conducted for a long time, since as early as the 1960s [1, 2]. However, GaP is an indirect transition-type semiconductor, and the light emission efficiency is known to be extremely low. A widely known technique for increasing the efficiency is to introduce isoelectronic impurities such as N atoms, and devices based on this approach are commercially available [3]. Isoelectronic impurities capture and localize electrons due to differences in electronegativity with respect to the component atoms of the host crystal. As a result, according to the Heisenberg uncertainty principle, the wave function of the electrons in wave-number space becomes broader, making radiative recombination possible at yellow and green wavelengths. In addition, GaP-LEDs that emit red light by the addition of Zn and O have also been reported [4]. However, the light emission efficiency is low because of energy loss due to internal relaxation to the isoelectronic impurity levels. Furthermore, only photons with energies lower than E_g are emitted, since light emission occurs via localized levels in the forbidden band. On the other hand, if it were possible to effectively utilize the large E_g of GaP, it would be possible to develop a method that overcomes the environment-related problems and technical difficulties mentioned above, as well as to expand the color coverage of GaP-LEDs.

M. Ohtsu, *Silicon Light-Emitting Diodes and Lasers*,
Nano-Optics and Nanophotonics, DOI 10.1007/978-3-319-42014-1_7

7.1.1 Fabrication and Operation

The fabrication and operation of the GaP-LED are reviewed in this subsection through demonstrating strong enhancement of light emission in the 520–540 nm wavelength band by subjecting a GaP crystal to DPP-assisted annealing [5]. It also demonstrates that the photon energy of this radiative recombination changes by an amount equal to the energies of multimode coherent phonons involved, and therefore, the photon energy of emitted light can be higher than E_g.

An n-type (dopant: S) GaP single-crystal wafer (a thickness of 500 μm and a diameter of 50 mm) was used. The orientation was (111), and the dopant concentration was 2×10^{17}–4×10^{17} /cm^3 (resistivity, 0.05 Ωcm). This wafer was subjected to ion implantation to implant acceptors (Zn atoms; an implantation energy of 300 keV and a dose of 1.7×10^{14} /cm^2) to fabricate a p–n homojunction structure. An Au/Zn/Ni film (150 nm) was deposited on the front surface (p-type side) of the substrate (Fig. 7.1). The electrodes were formed in the shape of a mesh so as to facilitate light irradiation and light emission during DPP-assisted annealing and device driving, respectively. An Au/Ge/Ni film (300 nm) and a Pt film (50 nm) were sequentially deposited on the rear surface (n-type side) to serve as a negative electrode. Then, the wafer was diced into a 600 μm × 600 μm chip and was fixed to a printed circuit board (PCB).

To make the device emit light in the green band (wavelengths around 530 nm), an injection current (9.9 A/cm^2-current density) was injected into the device while irradiating it with 532 nm-wavelength laser light ($h\nu_{anneal} = 2.32$ eV, 0.4 W-power, 35.4 W/cm^2-power density). During the DPP-assisted annealing, the surface temperature of the device reached 40°C, while the PCB had been cooled to 26°C.

Figure 7.2a shows the results of measuring the light emission spectra of the device during DPP-assisted annealing. This figure shows that the emitted light intensity in the range 1.75–2.26 eV was became more intense as the annealing time was increased. Possible explanations for this include light emission from Zn-O pairs formed from Zn atoms and impurity O atoms which occupy the closely spaced Ga site and P site, respectively [6], and light emission originating from radiative recombination of electrons trapped at the donors (S) and free holes [7]. In particular, it has been reported that formation of Zn-O pairs can be explained by diffusion of Zn from the p

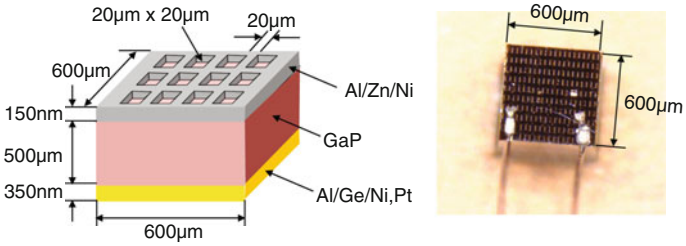

Fig. 7.1 Structure and photograph of the GaP-LED

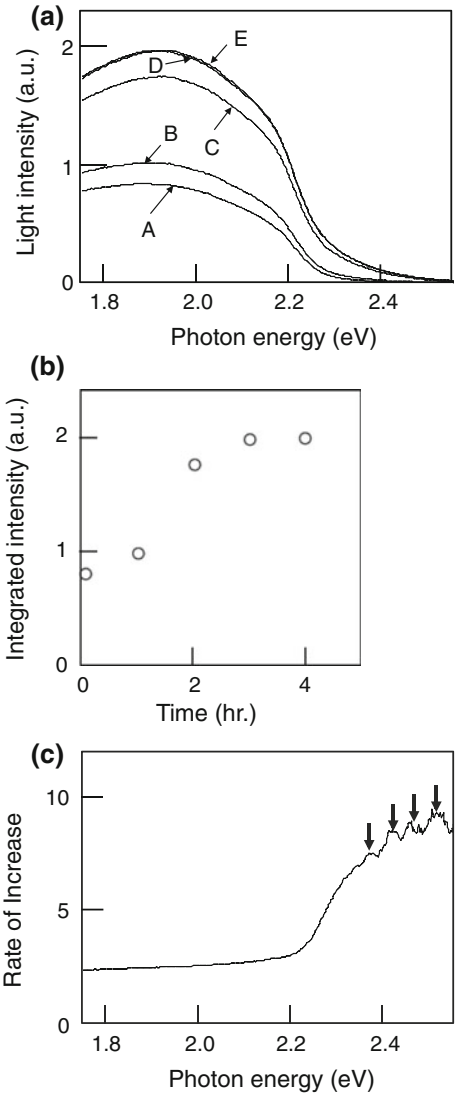

Fig. 7.2 Temporal variations of the light emission spectra. **a** Spectral profile. *Curve A* is for the un-annealed device. *Curves B–E* are acquired after the DPP-assisted annealing of 1, 2, 3, and 4 h, respectively. **b** Temporal variation of the total light emission intensity. **c** Rate of increase

side to the n side of the p–n homojunction [8]. In other words, the high emitted light intensity in this region as DPP-assisted annealing progressed is considered evidence that Zn diffusion took place. In addition, light emission was observed from levels above E_g. This is a result of the DPP-assisted annealing. The increase in emitted light intensity from these high energy levels is also a result of the DPP-assisted annealing.

Figure 7.2b shows the dependence of the integrated intensity (the areas enclosed by the curves and the horizontal axis in Fig. 7.2a) on the DPP-assisted annealing

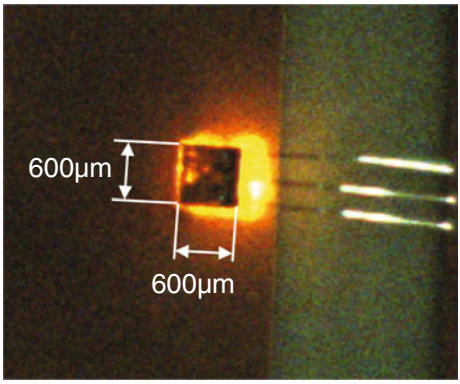

Fig. 7.3 Image of the emitted light

time. The emitted light intensity saturated after about 3 h of annealing, reaching the value three-times higher than the initial intensity. Figure 7.2c shows the rate of increase $R\ (= P_{4hr}\ (E)\ /\ P_{0hr}\ (E))$. Here, $P_{4hr}\ (E)$ is the emitted light intensity P at the photon energy E after 4 h of DPP-assisted annealing, and $P_{0hr}\ (E)$ is that from the un-annealed device. In this figure, at photon energies below 2.20 eV ($< E_g$), R was 2.50–3.50, whereas at photon energies higher than $h\nu_{anneal}$, R was 6.50 or greater. In addition, in this figure, periodic peaks (indicated by downward arrows) are observed at positions away from $h\nu_{anneal}$. These peaks were 50 meV apart, which corresponds to the energy of LO-mode phonons in GaP. In other words, phonon sidebands appeared in the emitted light in the high-energy region, as reviewed in Sects. 4.1 and 4.2, confirming that the light emission was due to multimode coherent phonons.

Figure 7.3 shows the image of the light emitted from the device. Although the value of R was large at energies higher than $h\nu_{anneal}$, the emission component originating from impurities or Zn-O centers [6, 7] was strong, making the emitted light appear orange. Usually, GaP contains defects or impurities such as oxygen, and these form emission centers. In other words, photons with a wide range of energies are generated inside the crystal during DPP-assisted annealing, and stimulated emission is also made possible triggered by these generated photons.

To confirm the effect of this light emission, the crystal was annealed without laser irradiation. The curve A in Fig. 7.4a represents the acquired light emission spectra. The curve A in Fig. 7.4b is the rate of increase R (the curve B is identical to the curve in Fig. 7.2c). First, the values of the curve A at the low energy side were close to the values of the curve B. However, above E_g, they are considerably different between each other. This feature can be explained as follows: In the 1.7–2.2 eV energy band, the photon number density with the corresponding energy is the same, regardless of whether or not laser irradiation is performed, and therefore, no change occurs in the DPP-assisted annealing process. In addition, the light emission from Zn-O or defects does not change compared with the case where laser irradiation is performed, and therefore, the rate of increase is the same. In the case of the high-energy band, there

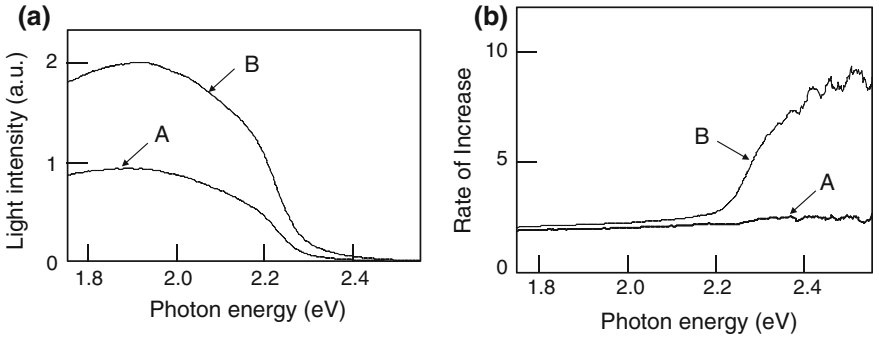

Fig. 7.4 Light emission spectra of device annealed without light irradiation. **a** Light emission spectral profiles. *Curve A* is for the un-annealed device. *Curve B* is for the device annealed for 4 h. **b** Rate of increase. *Curve A* is for the device annealed without light irradiation. *Curve B* is the one with light irradiation (identical to the curve in Fig. 7.2c)

is a difference between progression and suppression of dopant diffusion depending on whether or not laser irradiation is performed. In other words, if the high intensity light is made incident, stimulated emission from an energy level corresponding to the photon energy of that monochromatic light becomes more pronounced. Therefore, this demonstrates the effectiveness of DPP-assisted annealing, in terms of the ability to control the photon energy of the light emission from the device by the photon energy $h\nu_{anneal}$ rather than E_g (the photon breeding effect).

In general, lattice defects occur in crystals due to impurity doping by ion implantation. In particular, with high-energy ion implantation, there is also a risk of the crystal becoming amorphous. The crystallinity was examined by a Raman scattering method. The sample was preliminarily annealed at 800 °C for 30 min prior to DPP-assisted annealing, after ion implantation. Figure 7.5 shows the measured Raman scattering spectra (incident light wavelength: 488 nm) of the substrate before ion implantation (blue circles), the substrate after ion implantation (red diamonds), and the substrate after preliminary annealing carried out in a furnace (green triangles). In the spectrum for the substrate before ion implantation, sharp peaks appeared, which indicate the high crystal quality. However, after ion implantation, these peaks were not observed, which means that the surface changed to an amorphous structure. In the spectrum for the substrate after preliminary annealing, peaks appeared again. To confirm the effect of the amorphous surface on light emission, the substrate whose surface crystallinity was restored by preliminary annealing was formed into a device and was subjected to DPP-assisted annealing. The results are shown in Fig. 7.6a and b. As can be understood from these figures, the same spectral change as shown in Fig. 7.2a and c was observed.

The results shown in Figs. 7.5 and 7.6 can be explained as follows: By implanting Zn into GaP with a high acceleration energy (300 keV), the surface of the GaP crystal became amorphous. However, via the DPP-assisted process, the light emission occurs at the domain boundaries formed by the dopant (Zn) inside the crystal, and

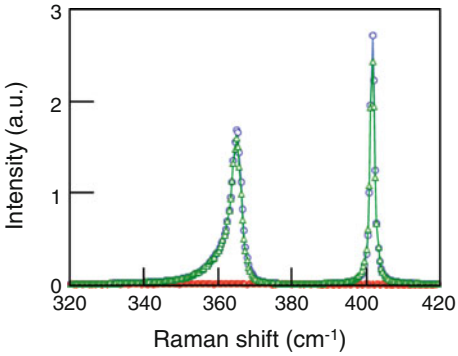

Fig. 7.5 Raman scattering spectra. *Blue circles* substrate before ion implantation, for comparison. *Red diamonds* substrate after ion implantation. *Green triangles* substrate subjected to preliminary annealing after ion implantation

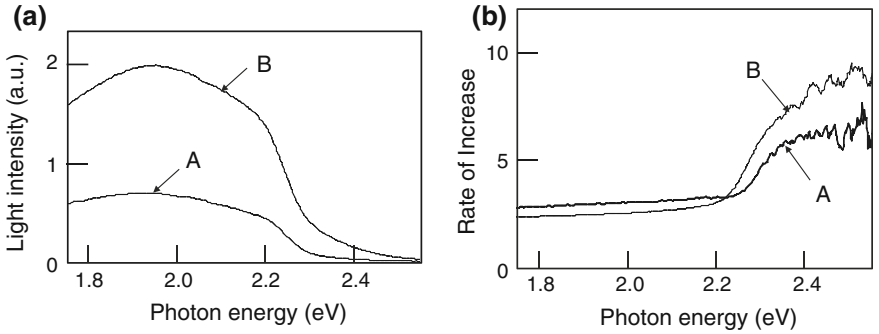

Fig. 7.6 Results of DPP-assisted annealing of sample subjected to preliminary annealing after ion implantation. **a** Light emission spectral profiles. *Curve A* the un-annealed device. *Curve B* acquired after the DPP-assisted annealing of 4 h. **b** Rate of increase (*Curve A*). For comparison, the *curve B* is the value which was acquired without preliminary annealing (identical to the curve in Fig. 7.2c)

does not rely on the amorphization of the crystal surface. Thus, the same results are obtained regardless of whether or not preliminary annealing is performed to recover the crystallinity.

7.1.2 Changing the Barrier Height with an Applied External Field

In this subsection, a two-level system model is used in order to discuss the change in the spatial distribution of doped Zn atoms due to the DPP-assisted annealing. This discussion enables evaluation of the barrier height in this model, which is decreased

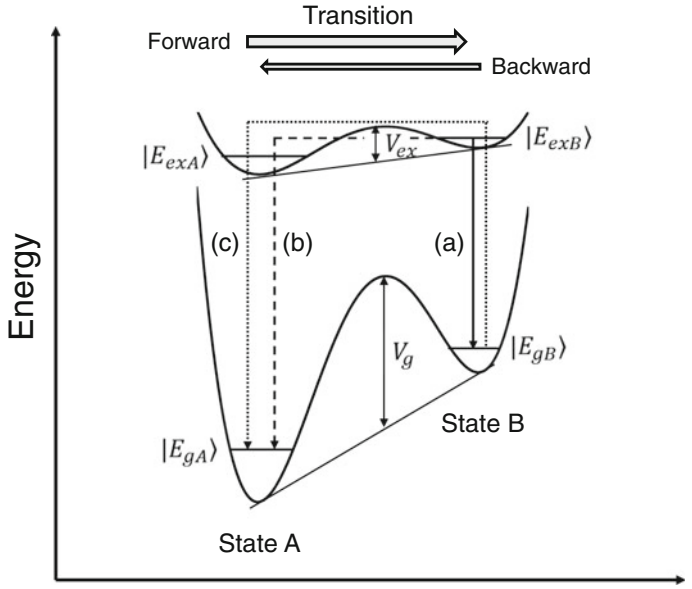

Fig. 7.7 Energy level diagram of the two-level system model. *Solid*, *broken*, and *dotted arrows* (*a*)–(*c*) represent the paths of de-excitation, excitation, and backward transition via photon emission and absorption (Refer to Sect. 7.1.3.)

by applying an external field [9]. For reference, the details of the two-level system model are reviewed in Appendix E [10, 11].

Figure 7.7 shows the energy level diagram of the two-level system model [11]. The horizontal axis does not represent any specific physical quantity, whereas the vertical axis is the electron energy. The states A and B represent the electron states before and after the DPP-assisted annealing, respectively. They are composed of two energy levels, i.e., the ground state ($|E_{gA}\rangle$, $|E_{gB}\rangle$) and excited state ($|E_{exA}\rangle$, $|E_{exB}\rangle$), which respectively correspond to the valence and conduction bands in a semiconductor. The DPP-assisted annealing forces a forward transition from state A to state B. The possibility of a backward transition from state B to state A is reviewed in Sect. 7.1.3. The initial and final states of this transition are $|E_{gA}\rangle$ and $|E_{gB}\rangle$, respectively. Since the potential barrier V_g in the ground state is generally high, the transition takes places through the lower potential barrier V_{ex} in the excited state after excitation from $|E_{gA}\rangle$ to $|E_{exA}\rangle$. De-excitation from $|E_{exB}\rangle$ to the final state $|E_{gB}\rangle$ takes place after the transition.

The two-level system model can describe the DPP-assisted annealing rate, depending on which state the electron is in:

(1) When the electron is in state A: State A corresponds to the region in the GaP crystal where the spatial distribution of Zn atoms is not suitable for generating DPPs. Therefore, the electron in $|E_{exA}\rangle$ generates Joule-heat due to scattering processes. On the other hand, the electron in $|E_{gA}\rangle$ is excited by absorbing the

irradiated light, and, as a result, Joule-heat is also generated. Because of the Joule-heat generated in these cases, the annealing rate is higher in state A.

(2) When the electron is in state B: State B corresponds to the region in the GaP crystal where the spatial distribution of Zn atoms is suitable for generating DPPs. Since electron–hole pairs can radiatively recombine in this case, the light irradiated during the DPP-assisted annealing triggers stimulated emission. As a result, the annealing rate is lower in state B because the stimulated emission optical energy dissipates from inside the GaP crystal to the outside.

Due to the difference in the annealing rates in (1) and (2), the spatial distribution of Zn atoms changes in a self-organized manner. When it reaches that of state B, the DPP-assisted annealing is completed, and the GaP-LED is thus fabricated.

The value of V_{ex} can be evaluated by noting that the net forward transition rate is given by [11]

$$\gamma_T \propto \exp\left(-\frac{V_{ex}}{kT}\right), \tag{7.1}$$

Here, k is Boltzmann's constant, and T is temperature. Figure 7.8 shows the measured relation between the DPP-assisted annealing time and the emitted light intensity. Open and closed circles are the results obtained at $T_1 = 320$ K and $T_2 = 310$ K, respectively, which were fitted by lines. The slopes γ_1 and γ_2 of these lines are proportional to γ_T in (7.1). A notable feature of these slopes is that the ratio γ_1/γ_2 is as large as 1.8 even though the relative temperature difference, $(T_1 - T_2)/T_1$, is only 0.03. By using this ratio, V_{ex} can be derived from (7.1) and is expressed as

$$V_{ex} = k\frac{T_1 T_2}{T_1 - T_2}\ln\frac{\gamma_1}{\gamma_2}. \tag{7.2}$$

The value of V_{ex} is evaluated to be 0.48 eV by substituting the numerical values given above into this equation. It should be noted that this evaluation was carried out during the DPP-assisted annealing, during which external electric and optical fields

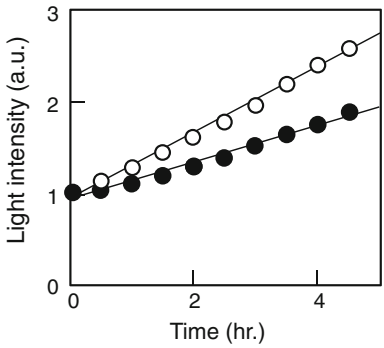

Fig. 7.8 Relation between the DPP-assisted annealing time and the emitted light intensity. *Open* and *closed circles* are the results obtained at $T_1 = 320$ K and $T_2 = 310$ K, respectively, which were fitted by the *solid lines*

were applied to the GaP crystal. The applied DC bias voltage was 22 V (injected current 25 mA), and the irradiation light power was 0.2 W (beam diameter 0.55 mm), respectively. On the other hand, in the previous work [12], the barrier height was evaluated to be 0.61 eV in the absence of external fields. In that report, too, the barrier height, which is the energy required to replace a Ga atom by a dopant atom via the kick-out mechanism, was evaluated to be 1.64 eV. These values are larger than the value of 0.48 eV above, which means that the applied external electric and optical fields decreased the value of V_{ex}. This decrease is the reason why the spatial distribution of Zn atoms was efficiently changed by the DPP-assisted annealing even at low temperature, such as T_1 and T_2 given above. In other words, the outstanding technical advantage of the DPP-assisted annealing is that it does not require any high-temperature electric furnaces, which have been needed for conventional thermal annealing.

7.1.3 Optimum Condition for DPP-Assisted Annealing

In this subsection, the optimum condition for DPP-assisted annealing, i.e., the optimum ratio between the electron injection rate and light irradiation rate for DPP-assisted annealing [9], is presented. First, the electron is assumed to be in the excited or ground state of state B ($|E_{exB}\rangle$ or $|E_{gB}\rangle$) as a result of DPP-assisted annealing, i.e., as a result of the forward transition from state A to state B. Next, the solid, broken and dotted arrows a–c in Fig. 7.7 represent the possible paths of the electron for de-excitation, excitation, and backward transition via photon emission and absorption, which may subsequently occur by continuing the DPP-assisted annealing.

Path (a): The electron in $|E_{exB}\rangle$ can emit a photon via spontaneous or stimulated emission. Thus, it de-excites to $|E_{gB}\rangle$ without a transition back to state A.

Path (b): If the electron in $|E_{exB}\rangle$ does not emit a photon, it transitions back to $|E_{exA}\rangle$ in state A, and subsequently de-excites to $|E_{gA}\rangle$ via nonradiative relaxation.

Path (c): The electron in $|E_{gB}\rangle$ is excited to $|E_{exB}\rangle$ by absorbing a photon. It subsequently transitions back to $|E_{exA}\rangle$ in state A and de-excites to $|E_{gA}\rangle$ via nonradiative relaxation, as in path (b).

In the case of path (a), the spatial distribution of Zn atoms is kept unchanged even though DPP-assisted annealing proceeds, because both the initial and final states ($|E_{exB}\rangle$ and $|E_{gB}\rangle$) are in state B. However, in the case of paths (b) and (c), the final state $|E_{gA}\rangle$ is in state A, and this spatial distribution easily changes as DPP-assisted annealing proceeds. Thus, to confine the electrons in state B, paths (b) and (c) must be blocked to prevent the backward transition.

Noting that a photon causes an electron to emit another photon via stimulated emission, a promising method for blocking the paths is to set the ratio of the electron injection rate and the photon irradiation rate to 1:1, which corresponds to the optimum condition for the DPP-assisted annealing. If the electron injection rate is higher than the photon irradiation rate, the excess electrons do not emit photons via stimulated

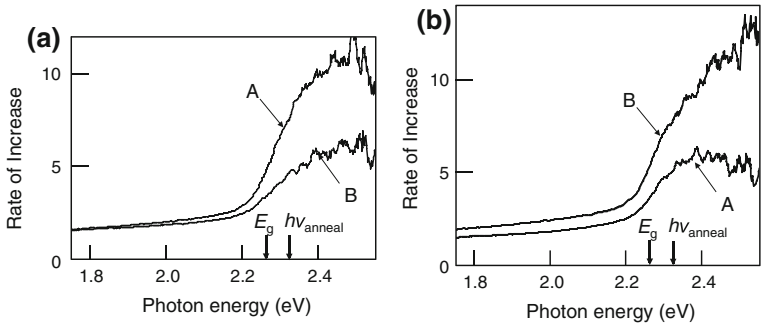

Fig. 7.9 Relation between the photon energy and the rate of increase, R. **a** and **b** show the values of R measured when the irradiation light powers during DPP-assisted annealing were 180 and 260 mW, respectively. *Curves A* and *B* represent the measured values for the injection currents of 20 and 30 mA, respectively

emission but escape through path (b). On the other hand, if the photon irradiation rate is higher than the electron injection rate, the excess photons do not cause electrons to emit photons via stimulated emission but allow the electrons to escape through path (c).

Experiments were carried out to confirm this optimum condition. As was the case of curve A in Fig. 7.6b, Fig. 7.9a and b show the rate of increase, R, defined in Sect. 7.1.1. It was measured when the irradiation light powers during DPP-assisted annealing were 180 and 260 mW, respectively. Curves A and B represent the results for injection currents of 20 and 30 mA, respectively. In Fig. 7.9a, the values of $R\left(E > E_g\right)$ were higher for the injection current of 20 mA than for the injection current of 30 mA. On the contrary, in Fig. 7.9b, they were lower.

Figure 7.10 shows measured values of R ($h\nu_{anneal}$) for various values of injection current and irradiation light power, including the values derived from Fig. 7.9. In this figure, the horizontal axis is the ratio of the numbers of photons and electrons irradiated and injected per unit time, respectively. This figure shows that R takes the maximum value when the ratio between the photon number and the electron number is 1.3:1, which is approximately 1:1. This clearly shows the optimum condition claimed above. This optimum condition has been theoretically reproduced by a stochastic model of the spatial distribution of B atoms, which was controlled by the DPPs [13].

This optimum condition suggests that conventional thermal annealing, i.e., by heating the sample in an electric furnace, is not compatible with fabricating photon breeding devices even if the furnace temperature can be increased to much higher than the values of T_1 and T_2 given in Sect. 7.1.2. DPP-assisted annealing is the only suitable fabrication method. Furthermore, it should be pointed out that the present discussion on the optimum condition is valid not only for GaP-LEDs but also for all of the photon breeding devices reviewed in this book.

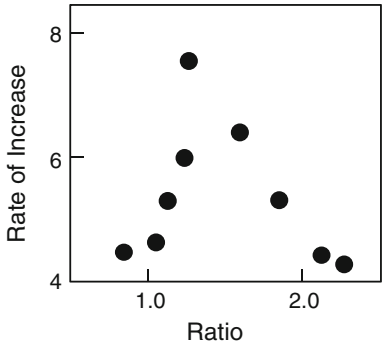

Fig. 7.10 Dependency of the measured values of $R\,(h\nu_{anneal})$ on the ratio of the numbers of photons and electrons irradiated and injected per second

7.2 Using a Zinc Oxide Crystal

ZnO is a direct transition-type, wide bandgap semiconductor and is expected to be used as a material for fabricating optical devices such as UV LEDs and laser diodes [14]. However, it is difficult to form a p-type crystal because the acceptors are compensated due to the numerous oxygen vacancies and interstitial zinc in the ZnO crystal [15]. Therefore, despite the numerous efforts that have been made [16–21], there have been very few reports of electroluminescence at room temperature [19, 20]. Because the radius of N ions is approximately the same as that of O ions, they are promising candidates to serve as p-type dopants in ZnO [14], and N doping by ion implantation has been examined [22]. However, the large number of lattice defects generated in normal ion implantation cannot be removed even with thermal annealing, and therefore, no p-type crystals of sufficient quality for fabricating devices have been obtained [22]. This section reviews a p–n homojunction-structured LED that emits visible light at room temperature by applying DPP-assisted annealing to a direct transition-type bulk ZnO crystal [23].

An n-type ZnO single crystal was used, which was grown by the hydrothermal growth method [24]. The crystal axis direction was (0001), the thickness was 500 μm, and the electrical resistivity was 50–150 Ωcm. N^{2+} ions were implanted into the crystal at an energy of 600 keV and an ion dose density of 1.0×10^{15} cm^{-2}. The implantation depth was confirmed to be about 3 μm by secondary ion mass spectrometry. This allowed the N dopant to be distributed in the vicinity of the crystal surface, forming a p-type ZnO layer. As a result, a p–n homojunction structure was realized. A 150 nm-thick ITO film was deposited on the surface of the p-type ZnO layer, and a 105 nm-thick Cr/Al film was deposited on the surface of the n-type ZnO layer to serve as electrodes. Then, the crystal was diced to form a device with an area of 9 mm^2.

As described in Chaps. 2 and 3, when a bulk Si crystal was implanted with B serving as a p-type dopant, the B atom was readily activated to form acceptors, thus creating a p–n homojunction. In the present case, however, the N atom was not readily activated [15]. Therefore, first, Joule-heat caused by an injection current was used

to anneal the crystal for activating the N atom. An overview of this principle is as follows: If an injection current is applied directly after implanting the N atom, the N atom is not activated sufficiently. Therefore, only electrons, which are majority carriers, carry the electrical current. Also, because no holes exist, recombination emission does not take place either. Therefore, the p–n homojunction remains highly resistive, and when a constant current is injected, the voltage applied across the p–n junction is high. As a result, a high level of Joule-heat occurs, diffusing the N atom and considerably changing the concentration distribution, causing the N atom to be activated. Therefore, since holes also become current carriers, the resistance decreases. Because ZnO is a direct transition-type semiconductor, the electrical energy is converted to spontaneously emitted optical energy through recombination of electrons and holes, and this is radiated from the crystal to the outside. The Joule-heat drops due to this energy dissipation and the decrease in resistance mentioned above, and therefore, the concentration distribution of the N atom eventually reaches a steady state. This completes the N atom activation process.

Second, DPP-assisted annealing was used simultaneously with the activation described above. The process can be explained as follows: A p–n homojunction is formed in the ZnO crystal by implanting N^{2+} ions. However, because this structure is simple, the electrons and holes both exhibit wide spatial distributions. Therefore, their recombination probability is low, and the emitted light intensity is also low. The DPP-assisted annealing is used to increase the emitted light intensity. Specifically, while applying an injection current during the annealing, the crystal surface is irradiated with light having a small photon energy $h\nu_{anneal}$ compared with E_g of ZnO. The mechanism of the DPP-assisted annealing of the ZnO crystal is equivalent to that described in Sect. 3.1. As a result, an N atom concentration distribution that is suitable for inducing the DPP-assisted annealing with high efficiency is formed in a self-organized manner.

The following two types of devices were fabricated.

Device 1 A device fabricated by annealing with an injection current alone, without light irradiation, to activate the N atom.

Device 2 A device fabricated by DPP-assisted annealing. To do so, during annealing with the injection current, the device was irradiated with laser light having a photon energy $h\nu_{anneal}$ (=3.05 eV, 407 nm wavelength), which is smaller than E_g (=3.4 eV) of ZnO.

The injection current density for annealing both devices was 0.22 A/cm^2. For Device 2, the irradiation power density was 2.2 W/cm^2. Figure 7.11a shows the change in surface temperature with time at the center of Device 2. The surface temperature rose to 100 °C when annealing commenced, and then dropped, reaching a constant temperature of 74 °C after about 60 min. This temperature drop was caused by the generation of DPPs as annealing progressed, bringing about stimulated emission, and by part of the electrical energy added to produce Joule-heat being dissipated in the form of optical energy. To confirm this stimulated emission effect, Fig. 7.11b shows the results of measuring the change in surface temperature with time for another identical sample of Device 2, when the irradiated light power was

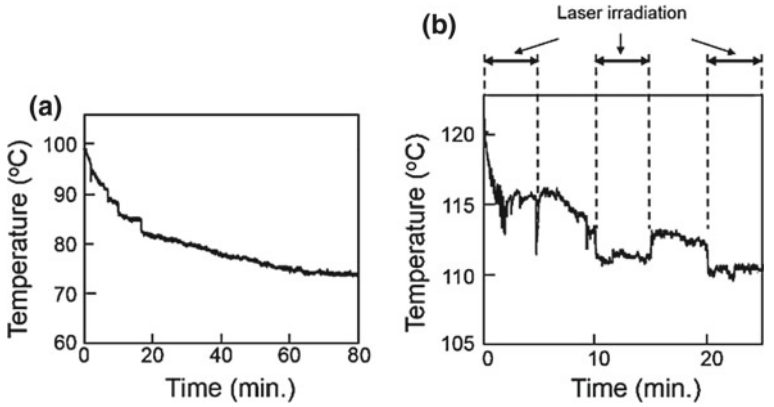

Fig. 7.11 Change in surface temperature with time at the center of Device 2. **a** The change in the surface temperature in the process of annealing with light irradiation. **b** The change in surface temperature for another identical sample of Device 2, when the irradiated light power was turned on and off every 5 min

turned on and off every 5 min. The temperature dropped during light irradiation, confirming the stimulated emission effect.

As for the device operation, first, the curves A–C in Fig. 7.12 are light emission spectra of Device 1 at room temperature with injection currents of 10, 15, and 20 mA, respectively. These spectra are composed of a high-intensity, narrow-band emission component in the ultraviolet region close to a wavelength of 382 nm and a low-intensity, wide-band emission component in the visible region above 490 nm. The former is attributed to the band edge transition in ZnO, and the latter is attributed to emission from defect levels [25]. The emission from the defect levels is not related to the DPP-assisted annealing in the case of Device 2, described below, and depends on the crystal quality. In other words, from these spectra, the emission from Device 1 was confirmed to be mainly due to the band edge transition. The $V - I$ characteristic of this device showed the same rectifying properties as an ordinary diode, confirming that a suitable p–n homojunction was formed by the annealing.

Next, light emission spectra of Device 2 at room temperature are shown by the three curves A, B, and C in Fig. 7.13a. Curves A, B, and C show the results obtained with injection currents of 10, 15, and 20 mA, respectively. The emission peak wavelength of curve A was 393 nm, which is attributed to the band edge transition, similar to the case of Device 1 (Fig. 7.12). Comparing curves B and C with curve A, the spectral centroid of the emission spectrum exhibits a red-shift as the injection current was increased. However, this shift was not attributed to a change in E_g induced by Joule-heat [26], because the emission peak attributed to the band edge transition in Device 1 did not show this kind of shift. Furthermore, as shown in the inset of this figure, the weak emission (arrow C_1), attributed to the band edge transition, was also found in curve C. Therefore, the red-shift of the emission spectra, which is attributed to Joule-heat at injection currents in the range of 10–20 mA, can be neglected. The

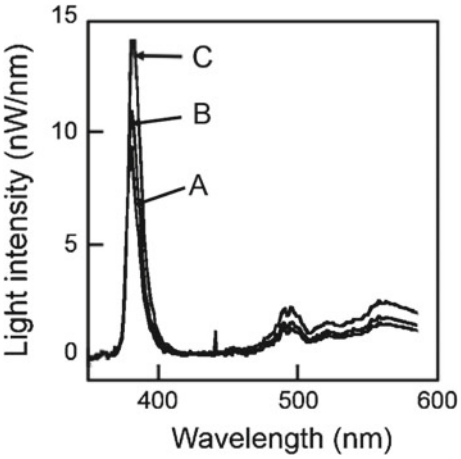

Fig. 7.12 Light emission spectra of Device 1. The *curves A–C* show the results obtained with injection currents of 10, 15, and 20 mA, respectively

reason why this red-shift is attributed to stimulated emission driven by DPPs, not Joule-heat, is as follows.

Light emission during LED operation, like the stimulated emission process during DPP-assisted annealing, is attributed to a two-step transition, as was described in Sect. 1.3.2. This transition is illustrated in Fig. 7.13b in the present case, i.e., from $|E_{ex}; el\rangle \otimes |E_{ex}; phonon\rangle$ to $\left|E_g; el\right\rangle \otimes |E_{ex}; phonon\rangle$ (the pink arrow at ② in Fig. 7.13b) and from $\left|E_g; el\right\rangle \otimes |E_{ex}; phonon\rangle$ to $\left|E_g; el\right\rangle \otimes |E_{ex'}; phonon\rangle$ (the green arrow at ② in Fig. 7.13b). Because the second-step transition is an electric dipole-forbidden transition, only DPPs are emitted, and these DPPs are scattered by the inhomogeneously distributed N dopant and are converted to propagating light. The photon energy of the emitted light is determined by the photon energy $h\nu_{anneal}$ of the light radiated during annealing, i.e., photon breeding takes place. This is because the N dopant concentration distribution is formed in a self-organized manner by the DPP-assisted annealing, with the result that a transition via the intermediate phonon level corresponding to $h\nu_{anneal}$ easily occurs in Device 2. Therefore, in curve B in Fig. 7.13a, the peak photon energy of 3.03 eV (409 nm wavelength, arrow B_1) is almost equal to $h\nu_{anneal}$.

On the other hand, the photon energy of light generated in the first-step transition is given by the energy difference between $|E_{ex}; el\rangle \otimes |E_{ex}; phonon\rangle$ and $\left|E_g; el\right\rangle \otimes |E_{ex}; phonon\rangle$. Comparing the blue arrow at ① and the green arrow at ② in Fig. 7.13b, this difference is 0.20 eV. (The blue arrow at ① represents the band edge transition of ZnO, whose energy is 3.25 eV (382 nm wavelength) according to Fig. 7.12.) This first-step transition is an electric dipole-allowed transition. However, because the occupation probability of such high-energy phonons is low, propagating light is not emitted, and only DPPs are generated. In addition, when the stimulated emission driven by the DPPs emitted in the first-step transition is repeated one or two more times, new intermediate phonon levels $\left|E_g; el\right\rangle \otimes |E_{ex''}; phonon\rangle$ and $\left|E_g; el\right\rangle \otimes |E_{ex'''}; phonon\rangle$ whose energies are lower by amounts corresponding to

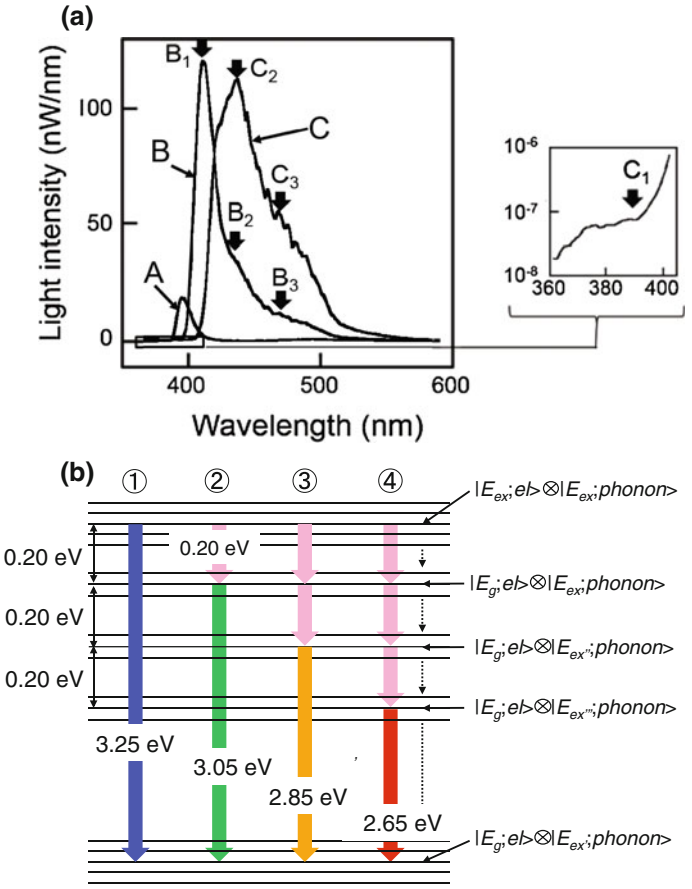

Fig. 7.13 Light emission characteristics of Device 2. **a** Light emission spectra at room temperature. The *curves A–C* show the spectra measured with injection currents of 10, 15, and 20 mA, respectively. **b** Schematic explanation of the two-step light emission during LED operation

the energy of the DPPs are formed. Thus, the energies of the photons emitted via these new intermediate phonon levels are lower by amounts corresponding to the energy of the DPPs emitted in the first-step transition (0.20 eV). In the case of ③ and ④ in Fig. 7.13b, these energies are 2.85 eV (435 nm) and 2.65 eV (468 nm), respectively, as shown by the yellow arrow and the red arrow. These are similar to the emission peaks measured in the conventional optical transition of bulk ZnO crystal, which are an integer multiple of the LO-mode phonon energy (72 meV) [25]. However, unlike the conventional electric dipole-allowed transition, in the transition driven by DPPs, the exchanged energy is an integer multiple of the energy determined by DPPs among the multiple phonon modes involved, rather than a material-specific phonon mode. The slope of curve B in Fig. 7.13a shows two bumps (arrows B_2 and B_3), whose positions were found to be 2.84 eV (436 nm) and 2.64 eV (470 nm), respectively,

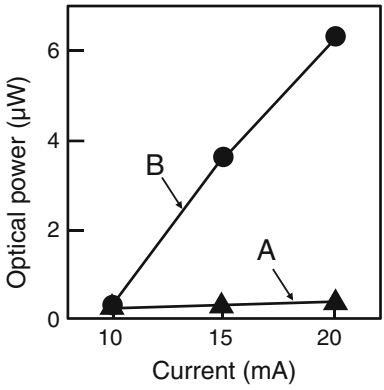

Fig. 7.14 The dependency of the output optical power of the two devices on the injection current. The *curves A* and *B* are for Devices 1 and 2, respectively

by the curve fitting based on the second-derivative spectroscopy method [27]. These agree well with the photon energies indicated by the yellow and red arrows at ③ and ④ in Fig. 7.13b. In addition, curve C also shows a peak (arrow C_2) and one bump (arrow C_3) at 2.84 eV (436 nm) and 2.63 eV (471 nm), respectively. These also agree well with the photon energies indicated by the yellow and red arrows at ③ and ④ in Fig. 7.13b.

Light emission via the intermediate phonon levels occurs not only due to two-step stimulated emission of ③ and ④ in Fig. 7.13b but also due to stimulated emission involving three or more steps. Therefore, when the injection current is increased, the emitted light intensity at the low-energy side also increases, which explains the red-shift in Fig. 7.13a. Note that the emitted light intensity due to the interband transition in curve B is small; this is attributed to the fact that the transition ② involving stimulated emission is faster than the transition ① involving only spontaneous emission, because electrons in the conduction band for stimulated emission relax to the intermediate phonon level.

To compare the performance of Devices 1 and 2, curves A and B in Fig. 7.14 respectively show the dependency of the output optical power of the two devices on the injection current. These output optical powers were obtained by integrating the curves in Figs. 7.12 and 7.13 in the wavelength range 350–600 nm. For curve B, at the injection current of 20 mA (current density 0.22 A/cm^2), the optical output power from Device 2 was 6.2 μW, which was about 15-times higher than that from Device 1, shown in curve A.

References

1. M. Gershenzon, R.M. Mikulyak, Solid-State Electron. **5**, 313 (1962)
2. D.G. Thomas, M. Gershenzon, F.A. Trumbore, Phys. Rev. **133**, A269 (1964)
3. R. Logan, H. White, W. Wiegmann, Solid-State Electron. **14**, 55 (1971)
4. J. Jayson, R. Bachrach, P. Dapkus, N. Schumaker, Phys. Rev. B **6**, 2357 (1972)

5. J.-H. Kim, T. Kawazoe, M. Ohtsu, Adv. Opt. Technol. **2015**, 236014 (2015)
6. K. Lohnert, E. Kubalek, Physica Status Solidi (a) **80**, 173 (1983)
7. T. Kawabata, S. Koike, Appl. Phys. Lett. **43**, 490 (1983)
8. K. Zdansky, J. Zavadil, D. Nohavica, S. Kugler, J. Appl. Phys. **83**, 7678 (1998)
9. J.H. Kim, T. Kawazoe, M. Ohtsu, Appl. Phys. A **121**, 1395 (2015)
10. R. Jankowiak, R. Richert, H. Bassler, J. Phys. Chem. **89**, 4569 (1985)
11. W. Kohler, J. Meiler, J. Friedrich, Phys. Rev. B **35**, 4031 (1987)
12. A. Hoglund, C. Castleton, S. Mirbt, Phys. Rev. B **77**, 113201 (2008)
13. K. Takahashi, M. Katori, M. Naruse, T. Kawazoe, M. Ohtsu, Abstract of 2015 autumn meeting of the physical society of Japan, September 2015, Osaka, Japan, Paper number 18aCR-3
14. Y.-S. Choi, J.-W. Kang, D.-K. Hwang, S.-J. Park, IEEE Trans. Electron Devices **57**, 26 (2010)
15. D. Seghier, H.P. Gislason, J. Mater. Sci. Mater. Electron **19**, 687 (2008)
16. A. Tsukazaki, A. Ohtomo, T. Onuma, M. Ohtsni, T. Makino, M. Sumiya, K. Ohtani, S.F. Chichibu, S. Fuku, Y. Segawa, H. Ohno, H. Koinuma, M. Kawasaki, Nat. Mater. **4**, 42 (2005)
17. W.Z. Xu, Z.Z. Ye, Y.J. Zeng, L.P. Zhu, B.H. Zhao, L. Jiang, J.G. Lu, H.P. He, S.B. Zhang, Appl. Phys. Lett. **88**, 173506 (2006)
18. Z.P. Wei, Y.M. Lu, D.Z. Shen, Z.Z. Zhang, B. Yao, B.H. Li, J.Y. Zhang, D.X. Zhao, X.W. Fan, Z.K. Tang, Appl. Phys. Lett. **90**, 042113 (2007)
19. J. Kong, S. Chu, M. Olmedo, L. Li, Z. Yang, J. Liu, Appl. Phys. Lett. **93**, 132113 (2008)
20. A. Nakagawa, T. Abe, S. Chiba, H. Endo, M. Meguro, Y. Kashiwaba, T. Ojima, K. Aota, I. Niikura, Y. Kashiwaba, T. Fujiwara, Phys. Status Solidi C **6**, S119 (2009)
21. F. Sun, C.X. Shan, B.H. Li, Z.Z. Zhang, D.Z. Shen, Z.Y. Zhang, D. Fan, Opt. Lett. **36**, 499 (2011)
22. Z.Q. Chen, T. Sekiguchi, X.L. Yuan, M. Maekawa, A. Kawasuso, J. Phys.: Condens. Matter **16**, S293 (2004)
23. K. Kitamura, T. Kawazoe, M. Ohtsu, Appl. Phys. B **107**, 293 (2012)
24. T. Sekiguchi, S. Miyashita, K. Obara, T. Shishido, N. Sakagami, J. Cryst. Growth **214/215**, 72 (2000)
25. Ü. Özgur, Y.I. Alivov, C. Liu, A. Teke, M.A. Reshchikov, S. Doğan, V. Avrutin, S.-J. Cho, H. Morkoç, J. Appl. Phys. **98**, 041301 (2005)
26. M.S. Kim, K.G. Yim, J.Y. Leem, D.Y. Lee, J.S. Kim, J.S. Kim, J. Phys. Soc. **58**, 821 (2011)
27. H. Mach, C.R. Middaugh, Anal. Biochem. **222**, 323 (1994)

Chapter 8
Other Devices

This chapter reviews applications in which DPs and DPPs can be used not only for LEDs and lasers but also for other optical devices. First example is an optical and electrical relaxation oscillator, the second one is an infrared photodetector with optical amplification, and the last one is a polarization rotator.

8.1 Optical and Electrical Relaxation Oscillator

Optical pulse oscillators have been widely used in the fields of optical communication, optical data storage, optical fabrication, spectroscopy, and so on. Mode-locked lasers and semiconductor lasers driven by pulsed current are popular examples of such devices [1]. The former are large in size and have high power consumption because they consist of numerous electronic parts and optical elements. Although the latter are compact, they need to be driven by an electrical trigger and thus require complicated electrical driving circuits.

This section reviews a novel optical and electrical relaxation oscillator by using the Si-LED described in Chap. 3 [2]. Because the device is operated by connecting it only to a DC power supply, and no optical elements are required, it is expected to solve the problems described above. For this purpose, two Si-LEDs were fabricated by the DPP-assisted annealing described in Sect. 3.1. They are:

Si-LED1 Fabricated by applying a voltage of about 10 V and an injection current of about 420 mA for 30 min under laser light irradiation (power: 500 mW).

Si-LED2 Fabricated by applying a voltage of about 7.2 V and an injection current of about 700 mA for 30 min under laser light irradiation (power: 200 mW).

Si-LED1 was mainly used for simulation and measurement of the spontaneous emission lifetime, whereas Si-LED2 was used for quantitative characterization of the oscillation. These Si-LEDs emit infrared light whose emission spectrum has a peak that corresponds to the photon energy $h\nu_{anneal}$ (=0.95 eV, 1.30 μm wavelength) of the irradiated laser light, which is evidence of photon breeding. In addition, because

M. Ohtsu, *Silicon Light-Emitting Diodes and Lasers*,
Nano-Optics and Nanophotonics, DOI 10.1007/978-3-319-42014-1_8

of the considerably inhomogeneous spatial distribution of the B concentration in the Si-LED, the current density also becomes inhomogeneous when the device has a size as large as 9 mm^2 in area and 650 μm in thickness. As a result, the $V-I$ characteristic curve is S-shaped, showing a breakover voltage V_b, as was the case with Fig. 3.2a. In the following, the S-shaped characteristic is expressed as $I = f(V)$. This S-shaped characteristic, i.e., a negative resistance characteristic, was utilized to realize an optical and electrical relaxation oscillator.

The curves A and B in Fig. 8.1 show the measured results of the temporal profiles of the optical power and the voltage of the Si-LED2, acquired at room temperature. Comparing the two curves, they varied synchronously, and the oscillation frequency was 10 kHz. The amplitudes of the curves A and B were 2.5 mW$_{p-p}$ and 47 V$_{p-p}$, respectively. The optical energy integrated over one period of oscillation was 0.14 μJ.

The S-shaped $V-I$ characteristic is shown in Fig. 8.2a. The Si-LED can be treated as an electrical circuit in which the Si-LED is connected in parallel with a capacitor and a constant-current source, as shown in Fig. 8.2b, where the capacitor can be regarded as the stray capacitance of the Si-LED and/or the circuit wiring. Here, C is the capacitance of the capacitor, I_1 and I_2 are the currents that flow through the Si-LED and the capacitor, respectively, V_1 and V_2 are the voltages applied to them, and I_0 is the current from the constant-current source. By setting $I_0 > f(V_b)$ and $V_1 = V_2 = 0$ as the initial conditions, it is expected that the optical power and voltage will exhibit periodic and oscillatory temporal behaviors due to sequential processes 1–4 described below and schematically explained in Fig. 8.2a.

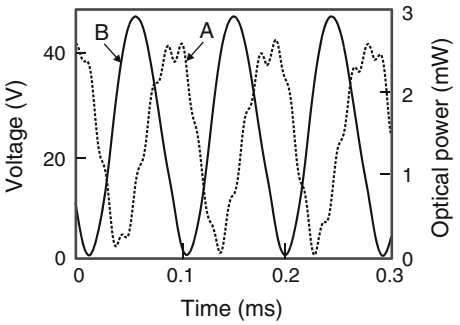

Fig. 8.1 Measured temporal profiles of the output signals from the Si-LED2. The *curves A* and *B* are the optical power and the voltage, respectively

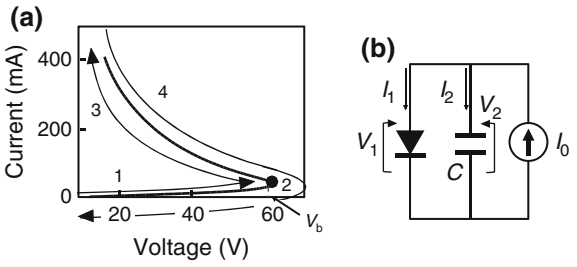

Fig. 8.2 S-shaped $V-I$ characteristic (**a**) and an equivalent electrical circuit (**b**)

1. V_1 increases as electric charges flow into C, and the current flows into the Si-LED simultaneously.
2. At the moment V_1 reaches V_b, V_2 increases because the current $I_0 - f(V_b)$ flows into C. However, because V_1 cannot exceed V_b, the difference between V_1 and V_2 increases.
3. I_1 increases and, as a result, V_1 decreases because the electric charge is released from C due to the voltage difference between V_1 and V_2. This accelerates the release of the charge and, as a result, the optical output power increases rapidly.
4. The values of V_1 and V_2 return to the initial state due to the decrease of the electric charge in C. Then, process 1 starts again.

The temporal behavior of the optical power exhibits a pulse-like profile due to the rapid increase of I_1 occurring right after the electric discharge. On the other hand, that of V_1 exhibits a sawtooth-like profile due to the instantaneous electric discharge. Because of a slight time difference between the electric discharge and the increase of I_1, there is a phase delay in the periodic pulse profile of the optical power with respect to the peak value of the voltage V_1. Since these temporal profiles are due to optical and electrical power dissipation based on the difference between V_1 and V_2, this circuit is regarded as a nonequilibrium open system. Thus, the temporal behavior of the voltage and optical power described above is called relaxation oscillation [3].

Figure 8.3 shows a simplified equivalent circuit of a Si-LED [4, 5], which is composed of a p-type layer, an n-type layer, and a depletion layer. For simplicity, carriers are assumed to recombine only in the depletion layer. C_e is the equivalent capacitance representing the capability of storing electric charge Q in the Si-LED, R_e is the resistance at the p-type layer, I_0 is the current from the constant-current source, I is the current injected into the depletion layer, V_v is the difference in the voltage between the anode-side and the cathode-side of the depletion layer, and V_t is the total voltage applied to the Si-LED.

The temporal variations in the number of carriers n in the Si-LED and the number of photons p in the depletion layer are represented by the following rate equations [6]:

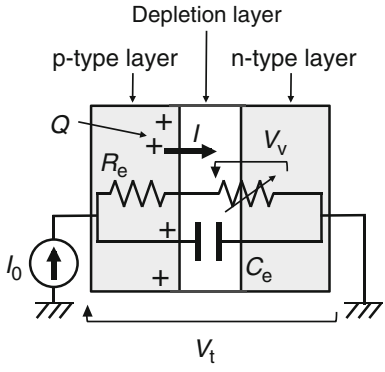

Fig. 8.3 Simplified equivalent circuit of a Si-LED

$$\frac{dn}{dt} = \frac{f(V)}{q} - \frac{n}{\tau} - G(n - n_{th})\, p, \tag{8.1}$$

and

$$\frac{dp}{dt} = \frac{n}{\tau} + BG(n - n_{th})\, p - Ap. \tag{8.2}$$

The first, second, and third terms on the right side of (8.1) represent electron injection, spontaneous emission, and stimulated emission, respectively. Those in (8.2) represent spontaneous emission, stimulated emission, and light emission from the Si-LED, respectively. Here, e is the electron charge, τ is the spontaneous emission lifetime, G is the stimulated emission coefficient, n_{th} is the transparency carrier number in the depletion layer, B is the coefficient of electron confinement, and A is the rate of photon dissipation from the depletion layer to the outside. For simplicity, the carrier injection efficiency is assumed to be unity.

The simulation was performed using (8.1), (8.2), and circuit equations for the equivalent circuit shown in Fig. 8.3. The values of n and p were derived iteratively with the time increment dt by the following steps:

1. Process that is rate-limited by charging of C_e: In the processes 1 and 2 shown in Fig. 8.2a, the charge Q at time $t + dt$ was derived using $Q(t + dt) = Q(t) + (I_0 - I)dt$. Then, V_t, V_v, and I were derived by $V_t = Q/C_e$, $V_v = V_t - R_e I$, $I = f(V_t)$. After substituting $f(V_t)$ into (7.1), (7.1) and (7.2) were approximated as difference equations to derive the values of n and p at time $t + dt$.
2. Process that is rate-limited by discharging of C_e:

2-1. If $V_1 > V_b$ in process 1, the capacitor C_e started discharging. Thus, V_t, V_v, and I were set to $V_t = V_v = V_b$ and $I = I_0$. Then, n and p at time $t + dt$ were derived using (7.1) and (7.2).

2-2. If the discharging of C_e continued, V_t and V_v were derived using $V_t = f^{-1}(I)$ and $V_\nu = Q/C_e$. Then, $Q(t+dt)$ and $I(t+dt)$ were derived using $Q(t + dt) = Q(t)(V_t - V_\nu)\, dt/R_e$ and $I(t + dt) = I_0(V_t - V_\nu)/R_e$. This calculation continued until $V_2 > V_b$ or $I < 0$ was satisfied.

The values of physical quantities R_e, C_e, $f(V)$, τ, G, n_{th}, B, and A have to be determined to perform the simulation. Among them, known values were employed for R_e, C_e, n_{th}, B, and A, as will be shown later. The curve in Fig. 3.2a was used for $f(V)$. However, the spontaneous emission lifetime τ must be found through measurements because electroluminescence from an indirect transition-type semiconductor has never been observed, and hence the value of τ for a bulk Si crystal is unknown.

The Si-LED1 was used for the direct measurement of τ, and the non-annealed Si wafer was also used as a reference specimen. As an excitation light source, the second-harmonic pulsed light from a Ti-sapphire mode-locked laser (2 ps pulse width, 80 MHz pulse repetition rate, 454 nm wavelength, 30 mW power) was used. The light passed through a longpass filter with a cut-off wavelength of 850 nm or

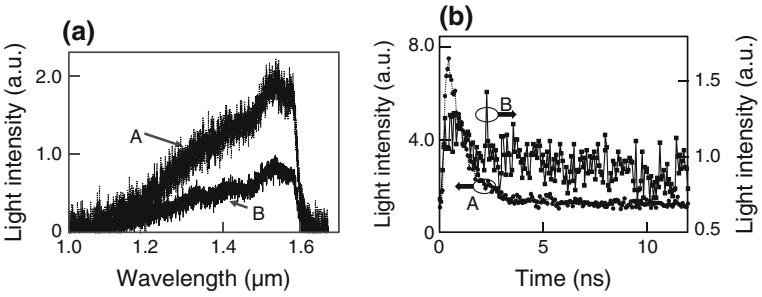

Fig. 8.4 Measured photoluminescence spectral profiles of the Si-LED (**a**) and temporal decreases in intensity (**b**). *Curves A* and *B* are for the Si-LED1 and the non-annealed Si wafer, respectively

1000 nm before reaching the Si-LED and the non-annealed Si wafer. The specimens were placed in a vacuum chamber and cooled down to about 6 K.

Curves A and B in Fig. 8.4a represent the acquired spectral profiles of the Si-LED1 and the non-annealed Si wafer, respectively. Neither curve clearly shows band-edge emission at wavelengths around 1.11 μm, which corresponds to E_g of Si. On the contrary, the spectra were broadened and extended to the longer-wavelength region, due to a multi-step de-excitation inherent to the DPP-assisted process. Temporal decreases in the photoluminescence intensity were measured for the Si-LED1 and the non-annealed Si wafer after optical pulse irradiation, as shown by the curves A and B in Fig. 8.4b. An exponential function was used for least squares fitting to the measured values:

$$y(t) = y_0 + y_1 \exp(-t/\tau) . \tag{8.3}$$

As a result, the value $\tau = 0.90 \pm 0.02$ ns was obtained from the curve A. This value was used for the simulation. In the case of curve B, on the other hand, the spontaneous emission probability was very low since the non-annealed Si wafer remained an indirect transition-type semiconductor. As a result, the values of curve B were very small, which made it difficult to estimate the value of τ. Comparing the curves A and B, the remarkable increase in the spontaneous emission probability enabled the first successful estimation of τ by this method. The value of τ derived above is as short as that of direct transition-type semiconductors [7–9].

The values of the other physical quantities used for the simulations were: $R_e = 5\,\Omega$, $C_e = 1.5 \times 10^{-10}$ F, $n_{th} = 7.0 \times 10^{13}$, and $B = 0.1$. For A, an equation $A = 1 - r^{1/t_0 \mathrm{s}^{-1}}$ was used, where $r = 2 \times 10^{-4}$ is the Fresnel reflection coefficient at the boundary of the depletion layer and the p-type/n-type layer, and $t_0 = 31$ fs is the time for the light to traverse the depletion layer. The value of G was used as a fitting parameter for the simulation.

The results of the simulation are shown by curves A and B in Fig. 8.5a. The photon number and voltage varied synchronously, and the temporal behavior of the photon number (curve A) exhibited a pulse-like profile, whereas that of the voltage

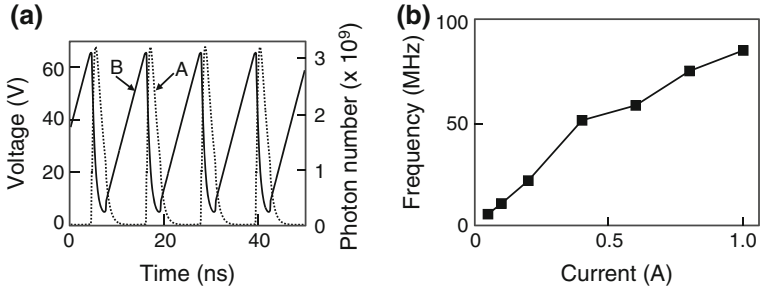

Fig. 8.5 Results of the simulation. **a** *Curves A* and *B* represent the photon number and voltage, respectively. **b** The relation between the injection current and oscillation frequency

(curve B) was sawtooth-like. The pulse width of curve A for the optical power depended on the spontaneous emission lifetime τ. The amplitude of the curve A decreased and exhibited relaxation oscillation with increasing G. As shown by Fig. 8.5b, the oscillation frequency increased with increasing injection current I_0, and the rate of increase was 80 MHz/A.

When the current was injected into Si-LED1 without connecting any external capacitor, the oscillation was caused by stray parasitic capacitance in the circuit and/or the Si-LED. The maximum oscillation frequency was 34 kHz. Comparing the two curves in Fig. 8.5a, the optical power and voltage oscillated synchronously, and the optical power took the maximum value at a time slightly after the voltage took the maximum value. This agrees with the measured result shown in Fig. 8.1. The reason why the two curves in Fig. 8.1 change more slowly than those of Fig. 8.5a is due to stray capacitance, stray inductance, and parasitic resistance of the circuit.

8.2 Infrared Photodetector with Optical Amplification

Si photodetectors (Si-PDs) are widely used photoelectric conversion devices. However, the long-wavelength cut-off (1.11 μm) of their photosensitivity is limited by E_g of Si [10]. Because of this, materials such as Ge [11], InGaAsP [12], and InGaAs [13] that have a smaller E_g than Si have been used in optical fiber communications. However, Ge photodetectors have a large dark current, and cooling is required in many cases. In addition, InGaAs photodetectors suffer from problems such as the use of highly toxic metal-organic materials in their fabrication, high cost, and so forth. Recently, depletion of resources, such as In, has also been a problem. If the photosensitivity limit of Si-PDs could be extended into the infrared region at 1.3 μm and above, these problems could be solved. An additional benefit of Si-PDs is their high compatibility with electronic devices. For this reason, photoelectric conversion devices exploiting effects such as mid-bandgap absorption [14–16], surface-state absorption [17, 18], internal photoemission absorption [19, 20], and two-photon

absorption [21, 22] in Si have been reported. However, in the case of mid-bandgap absorption, for example, the photosensitivity at a wavelength of 1.3 μm is limited to only 50 mA/W [14].

This section reviews a novel Si-PD with increased photosensitivity with optical amplification [23]. Specifically, the DPP-assisted annealing is performed to control the spatial distribution of the B concentration in a Si crystal in a self-organized manner to efficiently generate DPPs. The photocurrent of the novel Si-PD fabricated by this method is varied by a stimulated emission process driven by the incident light. Because this stimulated emission process causes optical amplification, the photosensitivity of this Si-PD remarkably increases.

The operating principle of the fabricated Si-PD is based on a DPP-assisted process. By using DPPs, it is possible to create an electron via a two-step excitation even with photons having an energy smaller than E_g of Si. Therefore, the Si-PD can exhibit photosensitivity even for infrared light with a photon energy smaller than E_g.

Electrons in the Si-PD experience a two-step excitation described below.

First step The electron is excited from the initial ground state $\left|E_g; el\right\rangle \otimes |E_{thermal}; phonon\rangle$ to intermediate state $\left|E_g; el\right\rangle \otimes |E_{ex}; phonon\rangle$. Here, $\left|E_g; el\right\rangle$ represents the ground state (valence band) of the electron, and $|E_{thermal}; phonon\rangle$ and $|E_{ex}; phonon\rangle$ respectively represent the thermal equilibrium state of the phonon determined by the crystal lattice temperature and the excited state of the phonon. Because this is an electric dipole-forbidden transition, a DPP is essential for the excitation.

Second step The electron is excited from the intermediate state $\left|E_g; el\right\rangle \otimes |E_{ex}; phonon\rangle$ to the final state $|E_{ex}; el\rangle \otimes |E_{ex}; phonon\rangle$. Here, $|E_{ex}; el\rangle$ represents the excited state (conduction band) of the electron, and $|E_{ex}; phonon\rangle$ represents the excited state of the phonon. Because this is an electric dipole-allowed transition, the electron is excited not only by the DPP but also by propagating light. After this excitation, the phonon in the excited state relaxes to a thermal equilibrium state having an occupation probability determined by the crystal lattice temperature, which completes excitation to the electron excited state $|E_{ex}; el\rangle \otimes |E_{thermal}; phonon\rangle$.

When light having a photon energy smaller than E_g is incident on the Si-PD, electrons are excited by the two-step excitation described above, generating a photocurrent. Photosensitivity to this incident light is manifested by means of the above process. Note that injecting a forward current to the Si-PD causes the two-step stimulated emission described in Sect. 1.3.2. Here, if the electron number densities occupying the state $|E_{ex}; el\rangle \otimes |E_{thermal}; phonon\rangle$ and the state $\left|E_g; el\right\rangle \otimes |E_{ex}; phonon\rangle$, satisfy the Bernard–Duraffourg inversion condition, the number of photons created by stimulated emission exceeds the number of photons annihilated by absorption. In other words, optical amplification occurs. Because the amplified light brings about the two-step stimulated emission again via DPPs, the photosensitivity of the Si-PD far exceeds the photosensitivity based on only the two-step excitation process.

To realize the optical amplification described above, it is essential to efficiently generate DPPs in the p–n homojunction of the Si-PD. To do so, the fabrication method

of Sect. 3.1 was adopted. First, an n-type Si crystal with an electrical resistivity of 10 Ω cm and a thickness of 625 μm, doped with As atoms, was used. This crystal was doped with B atoms via ion implantation to form a p-type layer. For the B doping, the implantation energy was 700 keV, and the ion dose density was $5 \times 10^{13}\,\mathrm{cm}^{-2}$. After forming a p–n homojunction in this way, an ITO film and a Cr/Al film were deposited for use as electrodes. Then, the Si crystal was diced to form a device.

Second, DPP-assisted annealing was performed by injecting a forward current to the Si-PD to generate Joule-heat, causing the B atom to diffuse and changing the spatial distribution of the B atoms. During annealing, the device was irradiated, from the ITO electrode side, with laser light having a photon energy $h\nu_{anneal}$ (=0.94 eV, 1.32 μm wavelength) smaller than E_g of Si.

This method is the same as the method in Sect. 3.1. Here, however, in order to make use of the stimulated emission process for the Si-PD to be fabricated, it is necessary to make the probability of stimulated emission larger than the probability of spontaneous emission. To do so, the forward current density for annealing was kept smaller than that of the two-step stimulated emission, namely, 1.3 A/cm^2. As a result, the number of injected electrons per unit time and per unit area was determined to be $8.1 \times 10^{18}\,\mathrm{s}^{-1} \cdot \mathrm{cm}^{-2}$, which corresponds to the probability of spontaneous emission. On the other hand, the probability of stimulated emission corresponds to the number of photons per unit time and per unit area, which is $3.9 \times 10^{19}\,\mathrm{s}^{-1} \cdot \mathrm{cm}^{-2}$ in the case of the laser power of 120 mW used here. Comparing this with the number of injected electrons confirms that the probability of stimulated emission is sufficiently large.

The fabricated Si-PD was evaluated by analyzing its optical and electrical properties, which are described as follows.

(1) The spectral photosensitivity was measured without injecting a forward current to the device. The results are shown by curves A–C in Fig. 8.6.

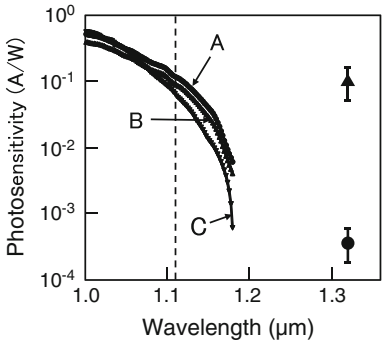

Fig. 8.6 Measured spectral photosensitivities. *Curves A* and *B* show the values obtained with a Si-PD fabricated with and without the DPP-assisted annealing, respectively. *Curve C* shows the values obtained with a Si-PIN photodiode (Hamamatsu Photonics, S3590) used as a reference. The *closed circle* and the *closed triangle* are the measured values for cases where the forward current densities of the fabricated Si-PD are 60 mA/cm^2 and 9 A/cm^2, respectively

Curve A shows the values obtained with a Si-PD fabricated by the DPP-assisted annealing. For comparison, curve B shows values obtained with a Si-PD fabricated without annealing. Curve C shows the values obtained with a Si-PIN photodiode (Hamamatsu Photonics, S3590) used as a reference. In the wavelength region longer than the cut-off wavelength (1.11 μm), curve A shows more gentle reduction of the photosensitivity, and its value is about three-times higher than that of curve C at wavelengths above 1.16 μm. In addition, the photosensitivity for curve A is larger than that for curve B. This is due to the spatial distribution of the B atoms being controlled in a self-organized manner by the DPP-assisted annealing so that DPPs are efficiently generated. Also, higher photosensitivity for curve B compared with that for curve C indicates that DPPs are readily generated inside the Si-PD compared with the case of curve C, as a result of implantation of a high concentration of B atoms. Because DPP-assisted annealing was performed while radiating 1.32 μm-wavelength light, it is expected that the photosensitivity will be selectively increased when light having the same wavelength (1.32 μm) is incident on the device. This wavelength-selective photosensitivity increase corresponds to photon breeding in the case of the LED and laser in the previous chapters. For reference, this increase has already been observed in the case of organic photovoltaic devices that have been developed using the DPP-assisted process [24]. In the following, the photosensitivity of the Si-PD for incident light with a wavelength of 1.32 μm in particular is discussed: A constant forward current was injected into the device, and the photosensitivity was evaluated when the wavelength of the incident light was 1.32 μm. Photoelectric conversion in this case involves not only the two-step excitation, but also the two-step stimulated emission process. Here, the contribution of the latter is sufficiently large. A semiconductor laser was used as the light source, and the output beam was made incident on the Si-PD after being intensity-modulated with a chopper. The current variation $\Delta I = V/R$ was obtained by the measured voltage variation V due to this incident light, where R is the resistance of the Si-PD. Then, it was divided by the incident light power P to obtain the photosensitivity $\Delta I/P$. The results are indicated by the closed circle and the closed triangle in Fig. 8.6. They are the measured values for cases where the forward current densities of the fabricated Si-PD are 60 mA/cm^2 and 9 A/cm^2, respectively. The photosensitivity for the current density of 9 A/cm^2 is 0.10 A/W. This is as much as two-times higher than the case using mid-bandgap absorption described above, demonstrating the increased photosensitivity. This value is about 300-times higher than the 60 mA/cm^2 case, and is as large as the value of curve C at a wavelength of 1.09 μm. This photosensitivity is sufficiently high for use in long-distance optical fiber communication systems [25]. The increase in photosensitivity with increasing forward current at a wavelength of 1.32 μm is due to the higher stimulated emission gain, as well as the higher number of recombining electrons.

(2) The V–I characteristics were evaluated for cases where the Si-PD was irradiated and not irradiated with 1.32 μm-wavelength, 120 mW-power laser light. The measurement results are shown by curves A and B in Fig. 8.7. Both curves show

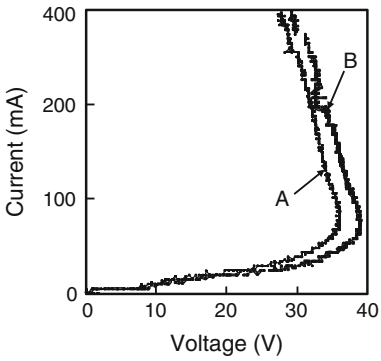

Fig. 8.7 Measured V–I characteristics. The *curves A* and *B* are for cases where the Si-PD was irradiated and not irradiated with light, respectively

negative-resistance characteristics at forward currents of 80 mA and higher, similarly to the case of the large-area infrared Si-LED used for the optical and electrical relaxation oscillator reviewed in the previous section (see Fig. 3.2a). Also, curve A was shifted toward lower voltages compared with curve B. This shift was particularly remarkable when the forward current was 30 mA and higher. The reason for this is that the electron number density in the conduction band is reduced because a population inversion occurs around a forward current of 30 mA, and electrons are consumed for stimulated emission. As a result, the voltage required for injecting the same number of electrons is decreased. On the other hand, when the forward current is increased further, the amount of shift is reduced. This is because the probability of stimulated emission recombination driven by spontaneous emission is increased as the forward current increases, and as a result, the voltage drop due to stimulated emission recombination becomes relatively small.

(3) For evaluating optical amplification characteristics, the relationship between the incident light power P and the current variation ΔI was measured. In a conventional Si-PD, only light absorption is used for photoelectric conversion. In the present Si-PD, however, because stimulated emission is also used, the current variation ΔI depends on the number of electron–hole pairs and varies due to stimulated emission, which is expressed as

$$\Delta I = (eP/h\nu)\,(G-1)\,. \tag{8.4}$$

Here, e is the electron charge, $h\nu$ is the photon energy, and G is the stimulated emission gain. Figure 8.8 shows the relationship between the incident light power at 1.32 μm-wavelength and the current variation ΔI. Similarly to Fig. 8.6, the closed circles and closed triangles show the measurement results for forward current densities of 60 mA/cm^2 and 9 A/cm^2, respectively. For the forward current density of 60 mA/cm^2, ΔI saturates as the incident light power increases; whereas for the forward current density of 9 A/cm^2, ΔI does not saturate but increases linearly. The curves A and B show calculation results fitted to the

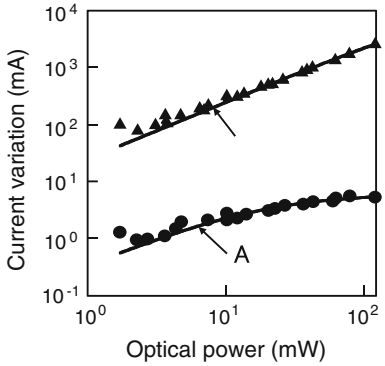

Fig. 8.8 Relationship between the incident light power at a wavelength of 1.32 μm and the current variation. The *closed circles* and *closed triangles* are for forward current densities of 60 mA/cm^2 and 9 A/cm^2, respectively. The *curves A* and *B* show calculated curves fitted to the experimental values

experimental results using (8.4). The stimulated emission gain G depends on the incident light power as $\exp[g/(1 + P/P_s)]$ [26], where g is the small-signal gain coefficient, and P_s is the saturation power. For the fitted results, these values are $g = 3.2 \times 10^{-4}$ and $P_s = 17$ mW in the case of curve A, and $g = 2.2 \times 10^{-2}$ and $P_s = 7.1 \times 10^2$ mW in the case of curve B. The increases in g and P_s as the forward current increases are due to the increasing number of electrons recombining with holes. The experimental values and calculated values show good agreement, confirming that the remarkable increase in photosensitivity shown by the closed circle and closed triangle in Fig. 8.6 is due to optical amplification as a result of stimulated emission.

(4) The photosensitivity was measured when a reverse-bias voltage V_r was applied, while keeping the incident light power fixed. The purpose of this measurement was to verify that the remarkable increases in photosensitivity were due to optical amplification based on stimulated emission under forward current injection. From the measurement results of the relationship between the reverse-bias voltage and the photosensitivity, the maximum photosensitivity was found to be about 3×10^{-4} A/W, which is about 1/300 of the value (0.10 A/W) indicated by the closed triangle in Fig. 8.6. When $V_r = 0$, the photosensitivity was too low to be measured. When V_r was low, for example, $V_r = -1$ V, the photosensitivity was about 2.5×10^{-5} A/W, and therefore, the value of 0.10 A/W above shows that the photosensitivity at $V_r = 0$ was amplified by a factor of at least 4000. Because the photosensitivity saturated as V_r increased, no electron avalanche effect [27] occurred. This means that there is no contribution from an avalanche effect in the remarkable increase in photosensitivity observed when a forward current was injected. Therefore, it was confirmed that the remarkable increase in photosensitivity in the fabricated Si-PD was due to optical amplification based on stimulated emission.

8.3 Polarization Rotator

This section reviews novel polarization rotators fabricated by using ZnO and SiC crystals. They can achieve a gigantic polarization rotation of the incident light due to the interactions among the electrons, the DPs, and the magnetic field generated by current injection.

8.3.1 Devices Using ZnO Crystal

Figure 8.9a and b show the cross-sectional structure of the reflection-type polarization rotator and a photograph taken from above, respectively. Although the structure of this device is almost the same as that of the ZnO-LED fabricated by DPP-assisted annealing, described in Sect. 7.2, Cr/Ni/Au films with a thickness of 200 nm were deposited on a transparent ITO film on the top surface in order to serve as electrodes for injecting an in-plane current for device operation [28]. As shown in Fig. 8.10, the current was injected into the ITO film via the electrodes. Linearly-polarized 405 nm-wavelength light was normally incident on the top surface of the device and was reflected at the Cr/Al film on the rear surface. During propagation through the device, the polarization of the incident light was rotated, and the resulting polarization

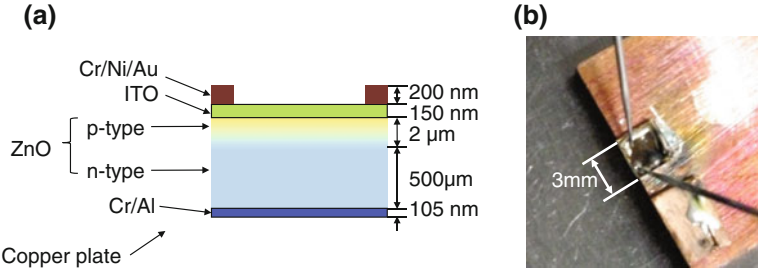

Fig. 8.9 Cross-sectional profile (**a**) and photograph (**b**) of reflection-type polarization rotator using ZnO crystal

Fig. 8.10 Device operation

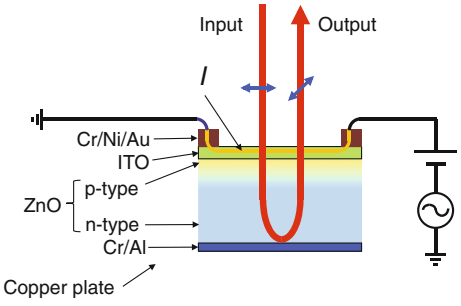

rotation was observed as an intensity variation of the reflected light after transmission through a Glan-Thompson prism.

Figure 8.11a shows images of the temporally varying reflected light spot. The brightness difference between the upper and lower images in this figure corresponds to a variation of $\pi/2$ radians in the polarization rotation angle. Curve A in Fig. 8.11b shows the measured temporal variation of the light intensity. Curve B shows that the frequency and amplitude of the sinusoidal voltage, applied to the device for current injection, were 0.1 Hz and 18 V, respectively. This figure shows that the polarization was rotated by more than 6 π radians by increasing the applied voltage to 18 V.

The measured relation between the injection current I and the polarization rotation angle θ_{rot} is shown in Fig. 8.12, which shows that the value of θ_{rot} was as large as 20 π radians at I = 100 mA. Such a gigantic polarization rotation is induced by the magnetic field generated by the current injected to the ITO film, and thus, it did not require any external strong magnetic field, unlike the polarization rotation using the conventional magneto-optical effect. Also, it did not require a long propagation length of the incident light. The effective propagation length for the modulation was less than 5 μm.

A transmission-type device has been also developed [29]. Its cross-sectional structure is shown in Fig. 8.13a. Although the structure is basically the same as that of the reflection-type device, an aperture was formed at the center of the Cr/Al film on the rear surface to allow the light transmission through the device. Figure 8.13b is a photograph of a two-dimensional array in which four devices are arranged. The closed circles in Fig. 8.14 show the measured temporal variation of the light

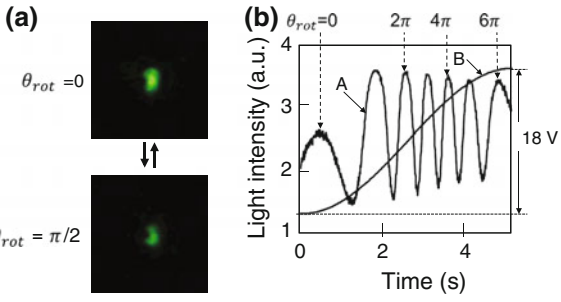

Fig. 8.11 Experimental results. **a** Images of the reflected light, projected on a screen after passing through a Glan-Thompson prism. θ_{rot} represents the polarization rotation angle. **b** Temporal variation of the output light intensity (*curve A*) and applied voltage (*curve B*)

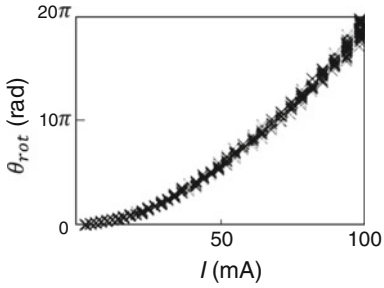

Fig. 8.12 Measured relation between the injection current I and the polarization rotation angle θ_{rot}

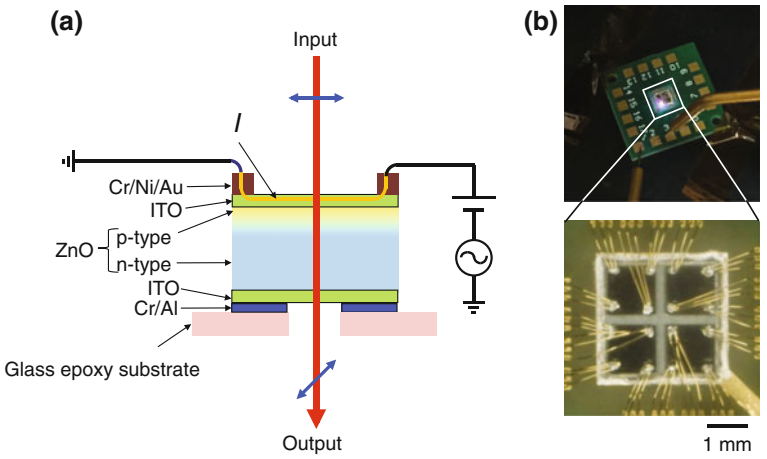

Fig. 8.13 Cross-sectional profile (**a**) and photograph (**b**) of the transmission-type polarization rotator formed of a two-dimensional array of four devices

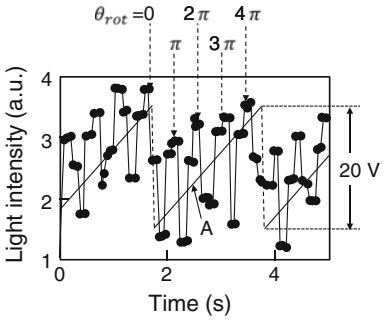

Fig. 8.14 Temporal variation of the transmitted light intensity (*closed circles*) and applied voltage (*line A*)

intensity transmitted through one of the devices in the array and subsequently through the Glan-Thompson prism. Here, as shown by line A, the frequency and amplitude of the applied sawtooth voltage were 1 Hz and 10 V, respectively. This figure shows that the value of θ_{rot} was changed by as much as 4 π radians by varying the applied voltage from -10 to $+10$ V.

An additional novel phenomenon is shown in Fig. 8.15a; here, a noticeable variation was observed in the light spot patterns during application of a voltage with a frequency of 5 Hz. This was due to the induced modulation of the focal position of the transmitted light. The equivalent refractive index change of the ZnO crystal for this modulation was evaluated and is shown in Fig. 8.15b. The refractive index change, as evaluated from this figure, was as large as 15% by applying a voltage of 20 V. This novel refractive index change has been used for high-speed reduction of laser-speckle noise for application to laser displays and related systems [29].

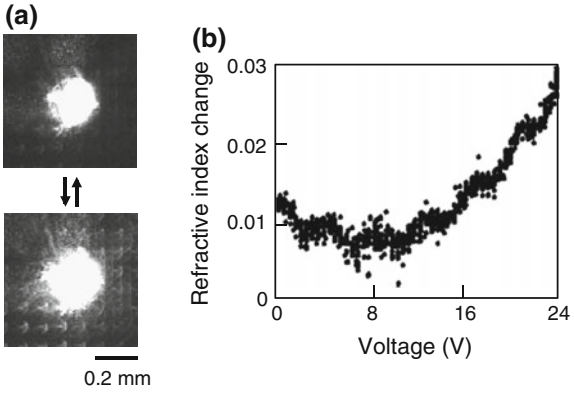

Fig. 8.15 Refractive index change. **a** Transmitted light spot patterns. The *upper* and *lower patterns* were obtained at applied voltages of 0 V and 20 V, respectively. **b** Relation between the applied voltage and the refractive index change

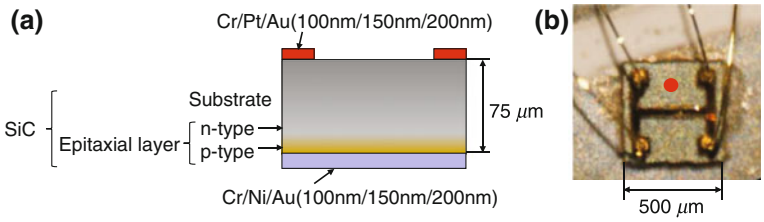

Fig. 8.16 Cross-sectional profile (**a**) and photograph (**b**) of the reflection-type polarization rotator using SiC crystal. The *red circle* in (**b**) represents a spot of normally incident light

8.3.2 Devices Using SiC Crystal

Figure 8.16a and b show the cross-sectional structure of a reflection-type polarization rotator using SiC crystal [30] and photograph of the device taken from above, respectively. Although the structure is almost the same as that of the SiC-LED described in Sect. 6.2, it is inverted, resulting in the SiC substrate being the top layer. Furthermore, an H-shaped electrode formed of a Cr/Pt/Au stripe film was deposited on the top surface, as shown in Fig. 8.16b. The ITO film was not used here, unlike the ZnO device in Sect. 8.3.1. By irradiating the device with light having a wavelength of 405 nm and a power of 20 mW, DPP-assisted annealing was carried out to fabricate the device.

For the device operation, a current was injected to the H-shaped electrode to inject electrons and generate a magnetic field. The spatial distribution of the magnetic flux density $\boldsymbol{B}_{\perp}$ (the upward blue arrow in Fig. 8.17a) normal to the top surface, was evaluated by numerical simulation. Figure 8.17b shows the result, where the injection current was 30 mA.

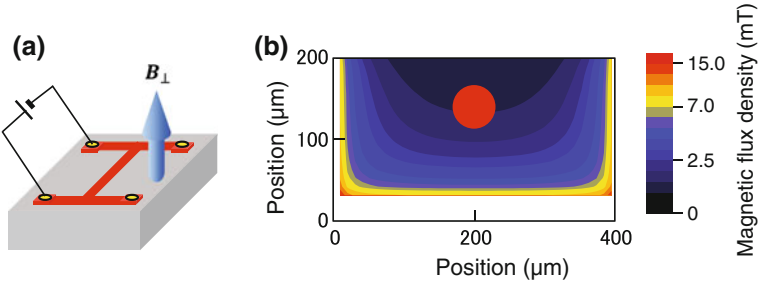

Fig. 8.17 Magnetic flux density generated by the current injected into the H-shaped electrode. **a** Schematic illustration of the profile of the H-shaped electrode formed of a Cr/Pt/Au stripe film on the top surface. The *upward arrow* represents the normal component $\boldsymbol{B}_\perp$ of the generated magnetic flux density. **b** Calculated spatial distribution of $\boldsymbol{B}_\perp$, where the injection current was 30 mA. The *red circle* represents a spot of normally incident light

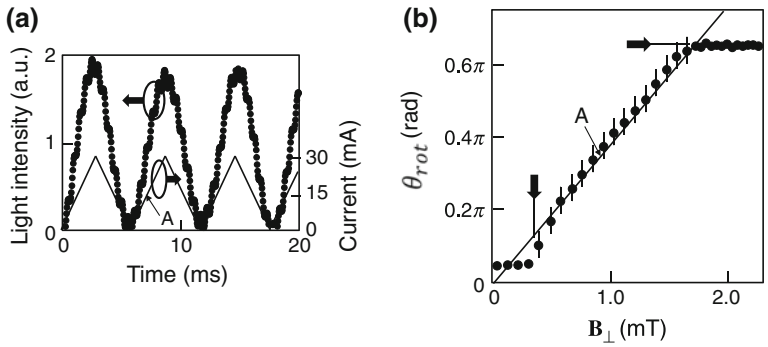

Fig. 8.18 Measured temporal variation of the light intensity and the estimated values of the polarization rotation angle θ_{rot}. **a** *Closed circles* represent the measured reflected light intensity transmitted through the Glan-Thompson prism. The *line A* is the waveform of the triangular current injected into the device. Its frequency and amplitude were 166 Hz and 30 mA, respectively. **b** The relation between $\boldsymbol{B}_\perp$ and θ_{rot}

In order to measure the polarization rotation angle θ_{rot}, linearly polarized 405 nm-wavelength light was made normally incident on the top surface of this device. The red circles in Figs. 8.16b and 8.17b represent the incident light beam spot. The value of $\boldsymbol{B}_\perp$ at this spot was evaluated to be 1.8 mT from Fig. 8.17b. The light reflected from the Cr/Ni/Au film on the rear surface was transmitted through a Glan-Thompson prism in order to measure the temporal variation of the light intensity. Closed circles in Fig. 8.18a represent the results of these measurements. Here, as shown by line A, the frequency and amplitude of the triangular current injected into the device were 166 Hz and 30 mA, respectively. The measured relation between $\boldsymbol{B}_\perp$ and θ_{rot} is derived from this variation and is represented by the closed circles in Fig. 8.18b. The solid line A in this figure was fitted to these circles. From the slope of the line A, the change of the polarization rotation angle per unit change of the injection current was evaluated to be 600 deg/A, which is 10^5–10^6 times larger than the Verdet constants

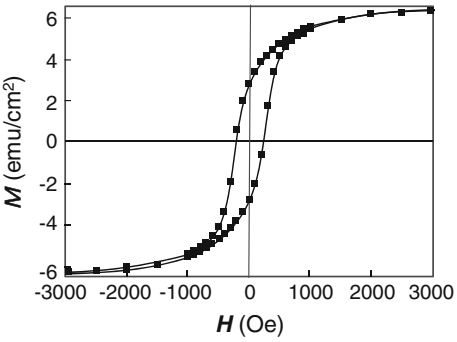

Fig. 8.19 Magnetization curve, measured at 27 °C

of conventional paramagnetic materials that are transparent in the visible region [31, 32].

The right-pointing arrow in Fig. 8.18b indicates that θ_{rot} saturated as $\boldsymbol{B}_{\perp}$ increased, as has been widely observed in conventional ferromagnetic materials. The saturated value corresponds to the Faraday rotation angle, which is as large as 7800 deg/cm. Furthermore, the downward arrow indicates the threshold value of $\boldsymbol{B}_{\perp}$, which is 0.36 mT. This threshold corresponds to the remanent magnetization in the conventional ferromagnetic material. As was the case in Sect. 8.3.1, it is also possible to fabricate a transmission-type device.

The magnetic properties of the device in Fig. 8.16 were evaluated in order to find the origin of the novel ferromagnetic properties. Figure 8.19 shows the magnetization curve measured at 27 °C [30]. Here, the applied magnetic field $\boldsymbol{H}$ (Oe) is proportional to the current injected to the device. The solid squares represent the measured values of the induced magnetization per unit volume, $\boldsymbol{M}$ (emu/cm^2), which were acquired by the SQUID at room temperature. The solid curves were fitted to them. These results clearly exhibit a hysteresis characteristic which is inherent to the ferromagnetic materials.

The existence of this characteristic proves that the semiconductor SiC crystal behaves as a ferromagnetic material as a result of the DPP-assisted annealing. This behavior originates from the formation of the Al atom pairs (Al dimers), as was the case in forming the B atom pairs in a Si crystal described in Sect. 3.3. This origin can be understood by referring to the following two research findings: (1) It has been found that the triplet state of the electron orbital in the Al atom pair is more stable than the singlet state [33]; and (2) two electrons with parallel spins in the triplet state induce the ferromagnetic characteristic [34].

References

1. O. Svelto, *Principles of Lasers*, 2nd edn. (Plenum Press, New York, 1982)
2. N. Wada, T. Kawazoe, M. Ohtsu, Appl. Phys. B **108**, 25 (2012)
3. E. Shl, *Nonequilibrium Phase Transitions in Semiconductors* (Springer, Berlin, 1987)
4. M. Meier, S. Karg, W. Riess, J. Appl. Phys. **82**, 1961 (1997)

5. J. Katz, S. Margalit, C. Harder, D. Wilt, A. Yariv, J. Quantum Electron. **17**, 4 (1981)
6. G. Bjork, Yamamoto. J. Quantum Electron. **27**, 2386 (1991)
7. E. Finkman, M.D. Sturge, R. Bhat, J. Lumin. **35**, 235 (1986)
8. V. Zwiller, T. Aichele, W. Seifert, J. Persson, O. Benson, Appl. Phys. Lett. **82**, 1509 (2003)
9. K. Okamoto, I. Niki, A. Scherer, Y. Narukawa, T. Mukai, Y. Kawakami, Appl. Phys. Lett. **87**, 071102 (2005)
10. M.E. Levinshtein, S.L. Rumyantsev, M. Shur, *Handbook Series on Semiconductor Parameters 1* (World Scientific Publishing, Singapore, 1996)
11. A. Loudon, P.A. Hiskett, G.S. Buller, Opt. Lett. **27**, 219 (2002)
12. C. Cremer, N. Emeis, M. Schier, G. Heise, G. Ebbinghaus, L. Stoll, I.E.E.E. Photon, Tech. Lett. **4**, 108 (1992)
13. A.F. Phillips, S.J. Sweeney, A.R. Adams, P.J.A. Thijs, I.E.E.E.J. Sel, Top. Quantum Electron **5**, 401 (1999)
14. J.E. Carey, C.H. Crouch, M. Shen, E. Mazur, Opt. Lett. **30**, 1773 (2005)
15. M.W. Geis, S.J. Spector, M.E. Grein, R.T. Schulein, J.U. Yoon, D.M. Lennon, C.M. Wynn, S.T. Palmacci, F. Gan, F.X. Kartner, T.M. Lyszczarz, Opt. Express **15**, 16886 (2007)
16. M.W. Geis, S.J. Spector, M.E. Grein, R.T. Schulein, J.U. Yoon, D.M. Lennon, F. Gan, F.X. Kartner, T.M. Lyszczarz, I, IEEE Photon. Technol. Lett. **19**, 152 (2007)
17. T. Baehr-Jones, M. Hochberg, A. Scherer, Opt. Express **16**, 1659 (2008)
18. H. Chen, X. Luo, A.W. Poon, Appl. Phys. Lett. **95**, 171111 (2009)
19. M. Lee, C. Chu, Y. Wang, Opt. Lett. **26**, 160 (2001)
20. M. Cassalino, L. Sirleto, L. Moretti, M. Gioffre, G. Coppola, Appl. Phys. Lett. **92**, 251104 (2008)
21. T. Tanabe, K. Nishiguchi, E. Kuramochi, M. Notomi, Appl. Lett. **96**, 101103 (2010)
22. B. Shi, X. Liu, Z. Chen, G. Jia, K. Cao, Y. Zhang, S. WWang, C. Ren. J. Zhao Appl. Phys. B **93**, 873 (2008)
23. H. Tanaka, T. Kawazoe, M. Ohtsu, Appl. Phys. B **108**, 51 (2012)
24. S. Yukutake, T. Kawazoe, T. Yatsui, W. Nomura, K. Kitamura, M. Ohtsu, Appl. Phys. B **99**, 415 (2010)
25. J.D. Schaub, J. Lightwave Technol. **19**, 272 (2001)
26. T. Saitoh, T. Mukai, IEEE J. Quantum Electron. **23**, 1010 (1987)
27. R.J. McIntyre, I.E.E.E. Trans, Electron Devices **13**, 164 (1966)
28. N. Tate, T. Kawazoe, W. Nomura, M. Ohtsu, Sci. Reports **5**, 12762 (2015)
29. N. Tate, T. Kawazoe, S. Nakashima, W. Nomura, M. Ohtsu, IDW 15, Otsu, Japan, December 9-11, (2015)
30. T. Kawazoe, N. Tate, and M. Ohtsu, IDW 15, Otsu, Japan, December 9-11 (2015)
31. Ed. by National Astronomical Observatory, *Chronological Scientific Tables 2005* (Maruzen Co., Tokyo, 2005) p.447
32. B.E.A. Saleh, M.C. Teich, *Fundamentals of Photonics* (Wiley, New York, 1991)
33. T.H. Upton, J. Phys. Chem. **90**, 754 (1986)
34. A. Pajca, Chem. Rev. **94**, 871 (1994)

Appendix A
Physical Picture of Dressed Photons

In order to understand the properties of dressed photons (DPs), this appendix investigates the interactions between photons and electrons in a nanometric space by taking the properties of photons reviewed in Sect. 1.2 into account. For this investigation, multiple nanomaterials, arranged in close proximity to each other and illuminated by a real photon, are considered. By considering the case of two nanomaterials for simplicity, the energy transfer between them and detection of this energy transfer are formulated. The present discussion deals with the case where the separation between the two nanomaterials is much shorter than the optical wavelength but sufficiently long to prevent electron tunneling. Therefore, the energy is transferred not by electron tunneling but by the electromagnetic interaction. This appendix describes the physical picture of photons that mediate this interaction and energy transfer [1].

It should be noted that the two nanomaterials and the light cannot be treated independently. This is because the nanomaterials emit or absorb virtual photons driven by fluctuations in the electromagnetic field, e.g., zero-point fluctuations of the vacuum. These absorption and emission processes, which have been called virtual processes, violate the energy conservation law; however, they are consistent with the Heisenberg uncertainty principle. As a result of these virtual processes, nanomaterials are covered with a cloud of virtual photons, and the clouds of virtual photons on the two nanomaterials spatially overlap each other.

When the nanomaterials are in excited states, conventional theories such as perturbation theories cannot be employed for describing the interaction because real photons (propagating light) are emitted in addition to the virtual photons. Although several theoretical attempts have been made to describe this interaction, no sufficiently accurate theory, including a proper description of the relaxation process, has been established. This appendix presents a novel theory for virtual photons around nanomaterials, even in the excited states. An advantage of this theory is that the energy transfer between the nanomaterials can be described by the emission or absorption of DPs, as will be described later.

In the following parts of this appendix, several properties of photons created around nanomaterials will be discussed by analyzing the interactions between pho-

M. Ohtsu, *Silicon Light-Emitting Diodes and Lasers*,
Nano-Optics and Nanophotonics, DOI 10.1007/978-3-319-42014-1

tons, electrons, and positive holes in the nanomaterials. A serious problem, however, is that a cavity cannot be defined in a sub-wavelength sized nanometric space, unlike the conventional quantum theory of light. In order to solve this problem, an infinite number of electromagnetic modes, with infinite frequencies, polarization states, and energies, must be assumed. Due to this assumption, an infinite number of energy states must be also assumed for the electrons and holes.

Under illumination with a real photon having photon energy $\hbar\omega_0$, the interaction between a photon and an electron-hole pair in nanometric space can be described by a multipolar Hamiltonian

$$\hat{H} = \sum_{\boldsymbol{k}\lambda} \hbar\omega_{\boldsymbol{k}} \hat{a}^{\dagger}_{\boldsymbol{k}\lambda} \hat{a}_{\boldsymbol{k}\lambda} + \sum_{\alpha>F,\beta<F} \left(E_\alpha - E_\beta\right) \hat{b}^{\dagger}_{\alpha\beta} \hat{b}_{\alpha\beta} + \hat{H}_{\text{int}}. \tag{A.1}$$

The first term represents the photon energy generated in the nanometric space, which is given by the sum of the infinite number of photon modes with angular frequency $\omega_{\boldsymbol{k}}$, polarization state λ, and energy $\hbar\omega_{\boldsymbol{k}}$. Here, the subscript $\boldsymbol{k}$ represents the wave-vector, and $\hat{a}_{\boldsymbol{k}\lambda}$ and $\hat{a}^{\dagger}_{\boldsymbol{k}\lambda}$ are its annihilation and creation operators, respectively, which satisfy a commutation relation

$$\left[\hat{a}_{\boldsymbol{k}\lambda}, \hat{a}^{\dagger}_{\boldsymbol{k}'\lambda'}\right] = \delta_{\boldsymbol{k}\boldsymbol{k}'}\delta_{\lambda\lambda'}, \tag{A.2}$$

where $\delta_{\boldsymbol{k}\boldsymbol{k}'}$ and $\delta_{\lambda\lambda'}$ are Kronecker deltas.

The second term represents the energy of the electron–hole pair, which is also given by the sum of the energies of the electron–hole pairs of the infinite number of energy states, identified by the subscripts α and β. The energy difference $E_\alpha - E_\beta$ represents the bandgap energy in the case of a semiconductor, and F represents the Fermi energy level. The operators

$$\hat{b}_{\alpha\beta} = S\hat{e}_\alpha \hat{h}_\beta \tag{A.3a}$$

$$\hat{b}^{\dagger}_{\alpha\beta} = S^* \hat{e}^{\dagger}_\alpha \hat{h}^{\dagger}_\beta \tag{A.3b}$$

respectively represent the simultaneous annihilation and creation of the electron and hole; i.e., they represent the annihilation and creation operators of the electron–hole pair. Here, S and S^* are complex numbers for representing the time inversion symmetry and its complex conjugate, respectively. Their absolute values are unity. $\hat{e}_\alpha$ and $\hat{e}^{\dagger}_\alpha$ are the annihilation and creation operators of the electron in the energy level α. $\hat{h}_\beta$ and $\hat{h}^{\dagger}_\beta$, on the other hand, are those of the hole in the energy level β. Since the electron–hole pair is a boson, its operators $\hat{b}_{\alpha\beta}$ and $\hat{b}^{\dagger}_{\alpha\beta}$ satisfy the commutation relation

$$\left[\hat{b}_{\alpha\beta}, \hat{b}^{\dagger}_{\alpha'\beta'}\right] = \delta_{\alpha\alpha'}\delta_{\beta\beta'} \tag{A.3c}$$

The third term of (A.1) represents the energy of the interaction between the photon and the electron–hole pair, which is given by

$$\hat{H}_{\text{int}} = -\int \hat{\psi}^{\dagger}(\boldsymbol{r})\,\boldsymbol{p}(\boldsymbol{r})\,\hat{\psi}(\boldsymbol{r})\cdot\hat{\boldsymbol{D}}^{\perp}(\boldsymbol{r})\,dv, \tag{A.4}$$

where $\boldsymbol{p}(\boldsymbol{r})$ is an electric dipole moment. $\hat{\psi}(\boldsymbol{r})$ is an annihilation operator for the field of the electron–hole pair, which is expressed as

$$\hat{\psi}(\boldsymbol{r}) = \sum_{\alpha>F}\varphi_{e\alpha}(\boldsymbol{r})\,\hat{e}_{\alpha} + \sum_{\beta<F}\varphi_{h\beta}(\boldsymbol{r})\,\hat{h}_{\beta}, \tag{A.5}$$

by using the state functions $\varphi_{e\alpha}(\boldsymbol{r})$ and $\varphi_{h\beta}(\boldsymbol{r})$ of the electron and hole. The field creation operator $\hat{\psi}^{\dagger}(\boldsymbol{r})$ is the Hermitian conjugate of (A.5). When these field operators are inserted into (A.4), only the operators of simultaneous annihilation, $\hat{e}_{\alpha}\hat{h}_{\beta}$, or creation, $\hat{e}^{\dagger}_{\alpha}\hat{h}^{\dagger}_{\beta}$, of the electron and hole are retained, and (A.3a)–(A.3c) are used. $\hat{\boldsymbol{D}}^{\perp}(\boldsymbol{r})$ is the transverse component of the electric displacement operator of the incident real photon, which is perpendicular to the wave-vector $\boldsymbol{k}$. This operator is expressed as

$$\hat{\boldsymbol{D}}^{\perp}(\boldsymbol{r}) = i\sum_{\boldsymbol{k}}\sum_{\lambda=1}^{2} N_{\boldsymbol{k}}\boldsymbol{e}_{\boldsymbol{k}\lambda}(\boldsymbol{k})\left\{\hat{a}_{\boldsymbol{k}\lambda}(\boldsymbol{k})\,e^{i\boldsymbol{k}\cdot\boldsymbol{r}} - \hat{a}^{\dagger}_{\boldsymbol{k}\lambda}(\boldsymbol{k})\,e^{-i\boldsymbol{k}\cdot\boldsymbol{r}}\right\}, \tag{A.6}$$

where plane waves were used for the mode functions. Here, $N_{\boldsymbol{k}}$ and $\boldsymbol{e}_{\boldsymbol{k}\lambda}(\boldsymbol{k})$ are a proportionality constant and the unit vector along the direction of polarization, respectively. Inserting (A.5) and (A.6) into (A.4) yields the interaction Hamiltonian

$$\begin{aligned}
\hat{H}_{\text{int}} &= -i\sum_{\boldsymbol{k}\lambda} N_{\boldsymbol{k}} \sum_{\alpha>F,\beta<F}\int \left(\varphi^{*}{}_{h\beta}\varphi_{e\alpha}\left(\boldsymbol{p}\cdot\boldsymbol{e}_{\boldsymbol{k}\lambda}(\boldsymbol{k})\right)\hat{b}_{\alpha\beta}\right.\\
&\quad\left.+\varphi^{*}{}_{e\alpha}\varphi_{h\beta}\left(\boldsymbol{p}\cdot\boldsymbol{e}_{\boldsymbol{k}\lambda}(\boldsymbol{k})\right)\hat{b}^{\dagger}_{\alpha\beta}\right)\left[\hat{a}_{\boldsymbol{k}\lambda}e^{i\boldsymbol{k}\cdot\boldsymbol{r}} - \hat{a}^{\dagger}_{\boldsymbol{k}\lambda}e^{-i\boldsymbol{k}\cdot\boldsymbol{r}}\right]dv\\
&= -i\sum_{\boldsymbol{k}\lambda} N_{\boldsymbol{k}} \sum_{\alpha>F,\beta<F}\left\{\int \varphi^{*}{}_{h\beta}\varphi_{e\alpha}e^{i\boldsymbol{k}\cdot\boldsymbol{r}}\left(\boldsymbol{p}\cdot\boldsymbol{e}_{\boldsymbol{k}\lambda}(\boldsymbol{k})\right)\hat{b}_{\alpha\beta}\hat{a}_{\boldsymbol{k}\lambda}\right.\\
&\quad+\int \varphi^{*}{}_{e\alpha}\varphi_{h\beta}e^{i\boldsymbol{k}\cdot\boldsymbol{r}}\left(\boldsymbol{p}\cdot\boldsymbol{e}_{\boldsymbol{k}\lambda}(\boldsymbol{k})\right)\hat{b}^{\dagger}_{\alpha\beta}\hat{a}_{\boldsymbol{k}\lambda}\\
&\quad-\int \varphi^{*}{}_{h\beta}\varphi_{e\alpha}e^{-i\boldsymbol{k}\cdot\boldsymbol{r}}\left(\boldsymbol{p}\cdot\boldsymbol{e}_{\boldsymbol{k}\lambda}(\boldsymbol{k})\right)\hat{b}_{\alpha\beta}\hat{a}^{\dagger}_{\boldsymbol{k}\lambda}\\
&\quad\left.-\int \varphi^{*}{}_{e\alpha}\varphi_{h\beta}e^{-i\boldsymbol{k}\cdot\boldsymbol{r}}\left(\boldsymbol{p}\cdot\boldsymbol{e}_{\boldsymbol{k}\lambda}(\boldsymbol{k})\right)\hat{b}^{\dagger}_{\alpha\beta}\hat{a}^{\dagger}_{\boldsymbol{k}\lambda}\right\}dv.
\end{aligned} \tag{A.7}$$

By representing the spatial Fourier transform of the electric dipole moment as

$$\rho_{\beta\alpha\lambda}(\boldsymbol{k}) = \int \varphi^*{}_{h\beta}(\boldsymbol{r})\,\varphi_{e\alpha}(\boldsymbol{r})\,(\boldsymbol{p}(\boldsymbol{r})\cdot\boldsymbol{e}_{\boldsymbol{k}\lambda}(\boldsymbol{k}))\,e^{i\boldsymbol{k}\cdot\boldsymbol{r}}dv, \tag{A.8}$$

$$\rho_{\alpha\beta\lambda}(\boldsymbol{k}) = \int \varphi^*{}_{e\alpha}(\boldsymbol{r})\,\varphi_{h\beta}(\boldsymbol{r})\,(\boldsymbol{p}(\boldsymbol{r})\cdot\boldsymbol{e}_{\boldsymbol{k}\lambda}(\boldsymbol{r}))\,e^{i\boldsymbol{k}\cdot\boldsymbol{r}}dv, \tag{A.9}$$

(A.7) is transformed to

$$\begin{aligned}\hat{H}_{\text{int}} &= -i\sum_{\boldsymbol{k}\lambda} N_{\boldsymbol{k}} \sum_{\alpha>F,\beta<F} \{\rho_{\beta\alpha\gamma}(\boldsymbol{k})\hat{b}_{\alpha\beta}\hat{a}_{\boldsymbol{k}\lambda} + \rho_{\alpha\beta\lambda}(\boldsymbol{k})\,\hat{b}^{\dagger}_{\alpha\beta}\hat{a}_{\boldsymbol{k}\lambda} \\ &\qquad -\rho^*{}_{\alpha\beta\lambda}(\boldsymbol{k})\,\hat{b}_{\alpha\beta}\hat{a}^{\dagger}_{\boldsymbol{k}\lambda} - \rho^*{}_{\beta\alpha\lambda}(\boldsymbol{k})\,\hat{b}^{\dagger}_{\alpha\beta}\hat{a}^{\dagger}_{\boldsymbol{k}\lambda}\} \\ &= -i\sum_{\boldsymbol{k}\lambda} N_{\boldsymbol{k}} \sum_{\alpha>F,\beta<F} \Big\{ \left[\rho_{\beta\alpha\gamma}(\boldsymbol{k})\,\hat{b}_{\alpha\beta} + \rho_{\alpha\beta\lambda}(\boldsymbol{k})\,\hat{b}^{\dagger}{}_{\alpha\beta}{}^{\dagger}\right]\hat{a}_{\boldsymbol{k}\lambda} \\ &\qquad -\left[\rho^*{}_{\alpha\beta\lambda}(\boldsymbol{k})\,\hat{b}_{\alpha\beta} + \rho^*{}_{\beta\alpha\lambda}(\boldsymbol{k})\,\hat{b}^{\dagger}{}_{\alpha\beta}{}^{\dagger}\right]\hat{a}^{\dagger}_{\boldsymbol{k}\lambda}\Big\}. \end{aligned} \tag{A.10}$$

Furthermore, by using

$$\hat{\gamma}_{\alpha\beta\lambda}(\boldsymbol{k}) = \rho^*{}_{\alpha\beta\lambda}(\boldsymbol{k})\,\hat{b}_{\alpha\beta} + \rho^*{}_{\beta\alpha\lambda}(\boldsymbol{k})\,\hat{b}^{\dagger}_{\alpha\beta}, \tag{A.11}$$

$$\hat{\gamma}^{\dagger}_{\alpha\beta\lambda}(\boldsymbol{k}) = \rho_{\alpha\beta\lambda}(\boldsymbol{k})\,\hat{b}^{\dagger}_{\alpha\beta} + \rho_{\beta\alpha\lambda}(\boldsymbol{k})\,\hat{b}_{\alpha\beta}, \tag{A.12}$$

(A.10) is simply expressed as

$$\hat{H}_{\text{int}} = -i\sum_{\boldsymbol{k}\lambda} N_{\boldsymbol{k}} \sum_{\alpha>F,\beta<F} \left(\hat{\gamma}^{\dagger}_{\alpha\beta\lambda}(k)\hat{a}_{\boldsymbol{k}\lambda} - \hat{\gamma}_{\alpha\beta\lambda}(k)\hat{a}^{\dagger}_{\boldsymbol{k}\lambda}\right). \tag{A.13}$$

After inserting (A.13) into (A.1), a unitary transform operator

$$\hat{U} = e^{\hat{S}} \tag{A.14a}$$

is used for diagonalizing the total Hamiltonian $\hat{H}$. Here, the relation

$$\hat{U}^{\dagger} = \hat{U}^{-1} \tag{A.14b}$$

holds, and $\hat{S}$ is an anti-Hermitian operator, which is defined by

$$\hat{S} = -i\sum_{\boldsymbol{k}\lambda} N_{\boldsymbol{k}} \sum_{\alpha>F,\beta<F} \left(\hat{\gamma}^{\dagger}_{\alpha\beta\lambda}(\boldsymbol{k})\,\hat{a}_{\boldsymbol{k}\lambda} + \hat{\gamma}_{\alpha\beta\lambda}(\boldsymbol{k})\,\hat{a}^{\dagger}_{\boldsymbol{k}\lambda}\right) \tag{A.15}$$

satisfying the relation $\hat{S} = -\hat{S}^{\dagger}$. Applying (A.14a) to $\hat{H}$ in (A.1) yields the diagonalized Hamiltonian

$$\tilde{H} = \hat{U}^{-1}\hat{H}\hat{U} = \sum_{\boldsymbol{k}\lambda}\sum_{\alpha>F,\beta<F}\left[\hbar\omega_{\boldsymbol{k}}^{'}\tilde{a}_{\boldsymbol{k}\lambda}^{\dagger}\tilde{a}_{\boldsymbol{k}\lambda} + \left(E_{\alpha}^{'} - E_{\beta}^{'}\right)\tilde{b}_{\alpha\beta}^{\dagger}\tilde{b}_{\alpha\beta}\right]. \tag{A.16}$$

This equation means that new normal vibrations with angular frequencies $\omega_{\boldsymbol{k}}^{'}$ and $\left(E_{\alpha}^{'} - E_{\beta}^{'}\right)/\hbar$ are created as a result of the coupling of the two harmonic oscillators in (A.1), which have the angular frequencies $\omega_{\boldsymbol{k}}$ and $\left(E_{\alpha} - E_{\beta}\right)/\hbar$. In the first term of (A.16), $\hbar\omega_{\boldsymbol{k}}^{'}$, $\tilde{a}_{\boldsymbol{k}\lambda}$, and $\tilde{a}_{\boldsymbol{k}\lambda}^{\dagger}$ represent the eigenenergy, annihilation operator, and creation operator of a new quantum, respectively. In the second term, $E_{\alpha}^{'} - E_{\beta}^{'}$, $\tilde{b}_{\alpha\beta}$, and $\tilde{b}_{\alpha\beta}^{\dagger}$ represent those of another new quantum. The annihilation operator $\tilde{a}_{\boldsymbol{k}\lambda}$ in the first term can be derived by using the formula

$$\tilde{a}_{\boldsymbol{k}\lambda} = \hat{U}^{-1}\hat{a}_{\boldsymbol{k}\lambda}\hat{U} = \hat{a}_{\boldsymbol{k}\lambda} + \left[\hat{a}_{\boldsymbol{k}\lambda}, \hat{S}\right] + \frac{1}{2!}\left[\left[\hat{a}_{\boldsymbol{k}\lambda}, \hat{S}\right], \hat{S}\right] + \cdots. \tag{A.17}$$

Since the relation

$$\begin{aligned}\left[\hat{a}_{\boldsymbol{k}\lambda}, \hat{S}\right] &= \left[\hat{a}_{\boldsymbol{k}\lambda}, -i\sum_{\boldsymbol{k}\lambda}N_{\boldsymbol{k}}\sum_{\alpha>F,\beta<F}\left(\hat{\gamma}_{\alpha\beta\lambda}(\boldsymbol{k})\,\hat{a}_{\boldsymbol{k}\lambda}^{\dagger}\right)\right] \\ &= -iN_{\boldsymbol{k}}\sum_{\alpha>F,\beta<F}\hat{\gamma}_{\alpha\beta\gamma}(\boldsymbol{k}) \\ &= -iN_{\boldsymbol{k}}\sum_{\alpha>F,\beta<F}\left(\rho^{*}{}_{\alpha\beta\lambda}(\boldsymbol{k})\,\hat{b}_{\alpha\beta} + \rho^{*}{}_{\beta\alpha\lambda}(\boldsymbol{k})\,\hat{b}_{\alpha\beta}^{\dagger}\right)\end{aligned} \tag{A.18}$$

is derived by using the commutation relation of (A.2), inserting (A.18) into (A.17) and retaining the term of the lowest order of $\hat{S}$ gives

$$\tilde{a}_{\boldsymbol{k}\lambda} = \hat{a}_{\boldsymbol{k}\lambda} - iN_{\boldsymbol{k}}\sum_{\alpha>F,\beta<F}\left(\rho^{*}{}_{\alpha\beta\lambda}(\boldsymbol{k})\,\hat{b}_{\alpha\beta} + \rho^{*}{}_{\beta\alpha\lambda}(\boldsymbol{k})\,\hat{b}_{\alpha\beta}^{\dagger}\right). \tag{A.19}$$

Similarly,

$$\tilde{a}_{\boldsymbol{k}\lambda}^{\dagger} = \hat{U}^{-1}\hat{a}_{\boldsymbol{k}\lambda}^{\dagger}\hat{U} = \hat{a}_{\boldsymbol{k}\lambda}^{\dagger} + \left[\hat{a}_{\boldsymbol{k}\lambda}^{\dagger}, \hat{S}\right] + \frac{1}{2!}\left[\left[\hat{a}^{\dagger}{}_{\boldsymbol{k}\lambda}, \hat{S}\right], \hat{S}\right] + \cdots, \tag{A.20}$$

giving

$$\tilde{a}_{\boldsymbol{k}\lambda}^{\dagger} = \hat{a}_{\boldsymbol{k}\lambda}^{\dagger} + iN_{\boldsymbol{k}}\sum_{\alpha>F,\beta<F}\left(\rho_{\alpha\beta\lambda}(\boldsymbol{k})\,\hat{b}_{\alpha\beta}^{\dagger} + \rho_{\beta\alpha\lambda}(\boldsymbol{k})\,\hat{b}_{\alpha\beta}\right). \tag{A.21}$$

The right-hand side of (A.19) indicates that the operator $\hat{b}_{\alpha\beta}$ of the electron–hole pair is added to the photon operator $\hat{a}_{\boldsymbol{k}\lambda}$. This means that the field represented by the operator $\tilde{a}_{\boldsymbol{k}\lambda}$ on the left-hand side is not the real photon but the photon dressing the

material energy, i.e., the energy of the electron–hole pair. Finally, annihilation and creation operators of the dressed photon (DP) are obtained by summing $\tilde{a}_{\boldsymbol{k}\lambda}$ and $\tilde{a}^{\dagger}_{\boldsymbol{k}\lambda}$ with respect to $\boldsymbol{k}$ and λ, i.e.,

$$\tilde{a} = \sum_{\boldsymbol{k}\lambda} \tilde{a}_{\boldsymbol{k}\lambda} \tag{A.22a}$$

and

$$\tilde{a}^{\dagger} = \sum_{\boldsymbol{k}\lambda} \tilde{a}^{\dagger}_{\boldsymbol{k}\lambda}. \tag{A.22b}$$

The quantities $\rho_{\alpha\beta\lambda}(\boldsymbol{k})$, ${\rho^*}_{\alpha\beta\lambda}(\boldsymbol{k})$, $\rho_{\beta\alpha\lambda}(\boldsymbol{k})$, ${\rho^*}_{\beta\alpha\lambda}(\boldsymbol{k})$, and ${\rho^*}_{\beta\alpha\lambda}(\boldsymbol{k})$ in the second and third terms of (A.19) and (A.21) indicate that the DP is created as a result of the interaction between the photon and the electron–hole pair. Also, the extent of the interaction range is given by the spatial distributions of ${\varphi^*}_{e\alpha}(\boldsymbol{r})\varphi_{h\beta}(\boldsymbol{r})$ and ${\varphi^*}_{h\beta}(\boldsymbol{r})\varphi_{e\alpha}(\boldsymbol{r})$ in $\rho_{\alpha\beta\lambda}(\boldsymbol{k})$ and $\rho_{\beta\alpha\lambda}(\boldsymbol{k})$ of (A.8) and (A.9). However, a more detailed estimation of the interaction range is required because $\varphi_{e\alpha}(\boldsymbol{r})$ and $\varphi_{h\beta}(\boldsymbol{r})$ are nothing more than the state functions of the electron and hole, respectively, whose penetration length outside the nanomaterial surface is very short. A detailed discussion of the interaction range will be given in Appendix B, in which the interaction range is shown to be equivalent to the size of the nanomaterial. That is, the effect of the DP spreads throughout a nanometric space whose volume is equivalent to that of the nanomaterial. In the process of this derivation, a physical picture of the virtual photons will be given in relation to the energy conservation law.

By using the DP annihilation and creation operators, the interaction between the two nanomaterials can be represented by the energy transfer, i.e., the annihilation of a DP from the first nanomaterial and its creation on the second nanomaterial, or in other words, emission and absorption of the DP. Here, since the range of interaction mediated by the DP is equivalent to the size of the nanomaterial, emission and absorption of the DP is realized by keeping the separation between the two nanomaterials as short as their sizes. This energy transfer can be regarded as tunneling of the DP.

Annihilation and creation operators $\tilde{b}_{\alpha\beta}$ and $\tilde{b}^{\dagger}_{\alpha\beta}$ in (A.16) are also derived in a similar way and are expressed as

$$\tilde{b}_{\alpha\beta} = \hat{U}^{-1}\hat{b}_{\alpha\beta}\hat{U} = \hat{b}_{\alpha\beta} - i\sum_{\boldsymbol{k}\lambda}\left(\rho_{\alpha\beta\lambda}(\boldsymbol{k})\,\hat{a}_{\boldsymbol{k}\lambda} + \rho^*_{\beta\alpha\lambda}(\boldsymbol{k})\,\hat{a}^{\dagger}_{\boldsymbol{k}\lambda}\right), \tag{A.23a}$$

$$\tilde{b}^{\dagger}_{\alpha\beta} = \hat{U}^{-1}\hat{b}^{\dagger}_{\alpha\beta}\hat{U} = \hat{b}^{\dagger}_{\alpha\beta} - i\sum_{\boldsymbol{k}\lambda}\left(\rho_{\beta\alpha\lambda}(\boldsymbol{k})\,\hat{a}_{\boldsymbol{k}\lambda} + \rho^*_{\alpha\beta\lambda}(\boldsymbol{k})\,\hat{a}^{\dagger}_{\boldsymbol{k}\lambda}\right). \tag{A.23b}$$

By summing with respect to α and β, the operators $\sum_{\alpha>F,\beta<F} \tilde{b}_{\alpha\beta}$ and $\sum_{\alpha>F,\beta<F} \tilde{b}^{\dagger}_{\alpha\beta}$ represent the electron–hole pair dressing the photon energy. However, since the separation between the two nanomaterials is sufficiently long to avoid electron tunneling, the interaction between the two nanomaterials is described by the absorption and emission of the DP, and, thus, the operators $\tilde{a}$ and $\tilde{a}^{\dagger}$ are used in the following discussions.

Unlike an exciton-polariton in a macroscopic material, since the wave-number, momentum, and resulting phase are not conserved in the nanometric space, annihilation ($\tilde{a}$) and creation ($\tilde{a}^{\dagger}$) of the DP do not occur temporally or spatially in an anti-correlated manner to the annihilation and creation of the electron–hole pair ($\sum_{\alpha>F,\beta<F} \tilde{b}_{\alpha\beta}$ and $\sum_{\alpha>F,\beta<F} \tilde{b}^{\dagger}_{\alpha\beta}$). That is, their wave amplitudes in the classical picture are represented not by simple sinusoidal functions but by temporally and spatially modulated function. The angular frequencies $\omega'_{\boldsymbol{k}}$ in the first term of (A.16) are for such a modulation sideband component of the photon. As a dual relation, in the second term, the eigenenergy $E'_{\alpha} - E'_{\beta}$ is also for the modulation sideband of the electron–hole pair.

Reference

1. M. Ohtsu, *Dressed Photons* (Springer, Berlin, 2013), pp. 11–18

Appendix B
Range of Interaction Mediated by Dressed Photons

The end of Appendix A described the sidebands of the eigenenergy, generated as a result of the temporal modulation feature of the DP field. As the next step, this appendix describes the spatial modulation feature. Although, for simplicity, the nanomaterials are assumed to be isolated from the outside in Appendix A, actual nanomaterials are surrounded by, for example, a macroscopic substrate on which they are fixed or a macroscopic host crystal in which they are buried. Furthermore, the incident real photon is also treated as a macroscopic electromagnetic field. In short, since actual nanomaterials are always surrounded by a macroscopic system composed of macroscopic materials and electromagnetic fields, the contribution from the macroscopic system must be considered in analyzing the interaction between the nanomaterials and the resultant energy transfer. This appendix discusses the electromagnetic interaction between such nanomaterials surrounded by a macroscopic system. It should be noted that it is also difficult to define a cavity for quantization because the nanomaterials are in a nanometric system, and, more complicatedly, they couple with the surrounding macroscopic material. This appendix describes in detail the spatial modulation feature of DPs by solving these complicated problems [1].

In order to derive the effective interaction energy between the two nanomaterials surrounded by the macroscopic system, the effects originated from the macroscopic system are renormalized by using the projection operator method. This effective interaction is called a near-field optical interaction [2, 3]. As a result of renormalization, the energy of the near-field optical interaction between the two nanomaterials as a function of their separation r will be given by (B.44); i.e., it is expressed by a Yukawa function

$$V_{eff} = \frac{e^{-r/a}}{r}, \tag{B.1}$$

where a represents the interaction range. This range is equivalent to the size of the nanomaterial and does not depend on the wavelength of the applied incident light. This means that the DP is localized on the surface of the nanomaterial, and therefore, the electromagnetic interaction between the nanomaterials is interpreted as originating from the DP energy transfer between them [4–6]. In the following

M. Ohtsu, *Silicon Light-Emitting Diodes and Lasers*,
Nano-Optics and Nanophotonics, DOI 10.1007/978-3-319-42014-1

sections, an equation representing the near-field optical interaction is derived by using an effective interaction operator $\hat{V}_{eff}$ based on the projection operator method [2, 7].

The light–matter interaction system under consideration here is composed of two subsystems. One is a nanometric subsystem composed of two nanomaterials. The other is a macroscopic subsystem including the incident real photon, whose size is much larger than the wavelength of the incident light. They interact with each other. Here, the nanometric subsystem is called a relevant subsystem n, and the macroscopic subsystem an irrelevant subsystem M. Since the interaction induced in subsystem n is to be analyzed, it is essential to renormalize the effects originating from subsystem M in a consistent and systematic way. The following description reviews a formulation based on the projection operator method.

B.1 Bare Interaction and Effective Interaction

The operator $\hat{V}$ of the interaction between nanomaterials s and p surrounded by subsystem M is expressed in the multipolar formalism under the electric dipole approximation as

$$\hat{V} = -\frac{1}{\varepsilon_0}\left\{\hat{\boldsymbol{p}}_s \cdot \hat{\boldsymbol{D}}^{\perp}(\boldsymbol{r}_s) + \hat{\boldsymbol{p}}_p \cdot \hat{\boldsymbol{D}}^{\perp}(\boldsymbol{r}_p)\right\}, \tag{B.2}$$

Here, $\hat{\boldsymbol{p}}_\alpha$ ($\alpha = s, p$) is an electric dipole operator. The positions of the nanomaterials s and p are denoted by $\boldsymbol{r}_s$ and $\boldsymbol{r}_p$, respectively. The transverse component of the electric displacement operator of the incident real photon is expressed as $\hat{\boldsymbol{D}}^{\perp}(\boldsymbol{r})$, which has been given in (A.6).

Exciton-polariton states are employed as a basis to describe subsystem M because the incident light reaches and excites the nanomaterials s and p after propagating through the macroscopic material. For this purpose, after the annihilation and creation operators in (A.6) are rewritten using the exciton-polariton operators $\hat{\xi}(\boldsymbol{k})$ and $\hat{\xi}^{\dagger}(\boldsymbol{k})$, they are inserted into (B.2). Using the electric dipole operator defined by

$$\hat{\boldsymbol{p}}_\alpha = \left\{\hat{b}(\boldsymbol{r}_\alpha) + \hat{b}^{\dagger}(\boldsymbol{r}_\alpha)\right\}\boldsymbol{p}_\alpha, \tag{B.3}$$

with the annihilation and creation operators $\hat{b}(\boldsymbol{r}_\alpha)$ and $\hat{b}^{\dagger}(\boldsymbol{r}_\alpha)$ of the electron–hole pair (exciton) in subsystem n and the transition dipole moments $\boldsymbol{p}_\alpha$ yields the bare interaction operator in the exciton-polariton picture:

$$\hat{V} = -i\sum_{\alpha=s}^{p}\sum_{\boldsymbol{k}}\sqrt{\frac{\hbar}{2\varepsilon_0 V}}\left(\hat{b}(\boldsymbol{r}_\alpha) + \hat{b}^{\dagger}(\boldsymbol{r}_\alpha)\right)\left(K_\alpha(\boldsymbol{k})\hat{\xi}(\boldsymbol{k}) - K^{*}{}_{\alpha}(\boldsymbol{k})\hat{\xi}^{\dagger}(\boldsymbol{k})\right). \tag{B.4}$$

Here, ε_0 is the dielectric constant in vacuum, and V is the volume of the cavity in subsystem M for describing the exciton-polariton. $K_\alpha(\boldsymbol{k})$ and $K_\alpha^*(\boldsymbol{k})$ are the coupling coefficients between subsystem n and the exciton-polariton in subsystem M, given by

$$K_\alpha(\boldsymbol{k}) = \sum_{\lambda=1}^{2} (\boldsymbol{p}_\alpha \cdot \boldsymbol{e}_\lambda(\boldsymbol{k})) f(\boldsymbol{k}) e^{i\boldsymbol{k}\cdot\boldsymbol{r}_\alpha}, \tag{B.5}$$

where $\boldsymbol{e}_\lambda(\boldsymbol{k})$ is a unit vector along the direction of polarization of light. The wave-number dependence of $f(\boldsymbol{k})$ will be rewritten as (B.38).

In order to derive the effective interaction energy, it is preferable to express the state $|\psi\rangle$ of the total system in terms of a basis whose degree of freedom is as low as possible. For this purpose, the total system is divided into two functional spaces. One is called the relevant P space. The other is the complementary space to the P space, which is called Q space. The next step is to evaluate the energy of the effective interaction exerted in the P space after tracing out the exciton-polariton degree of freedom:

$$V_{eff} = \langle \phi_{Pf} | \hat{V}_{eff} | \phi_{Pi} \rangle . \tag{B.6}$$

The two states $\langle \phi_{Pi}|$ and $|\phi_{Pf}\rangle$ on the right-hand side of this equation are the initial and final states in the P space before and after the interaction, respectively, both of which are eigenstates of the unperturbed Hamiltonian. The effective interaction operator $\hat{V}_{eff}$ on the right-hand side of this equation is expressed by using the bare interaction operator $\hat{V}$ of (B.4):

$$\hat{V}_{eff} = \sum_j \hat{\boldsymbol{p}} \hat{V} \hat{Q} |\phi_{Qj}\rangle\langle\phi_{Qj}| \hat{Q} \hat{V} \hat{P} \left(\frac{1}{E_{Pi}^0 - E_{Qj}^0} + \frac{1}{E_{Pf}^0 - E_{Qj}^0} \right). \tag{B.7}$$

Using this expression, (B.6) is given by

$$V_{eff} = \sum_j \langle \phi_{Pf} | \hat{P} \hat{V} \hat{Q} |\phi_{Qj}\rangle\langle\phi_{Qj}| \hat{Q} \hat{V} \hat{P} |\phi_{Pi}\rangle \left(\frac{1}{E_{Pi}^0 - E_{Qj}^0} + \frac{1}{E_{Pf}^0 - E_{Qj}^0} \right). \tag{B.8}$$

Here, $\hat{P}$ is the projection operator, which is defined by using the basis $\{|\phi_{Pj}\rangle\}$ in the P space as

$$\hat{P} = \sum_j |\phi_{Pj}\rangle\langle\phi_{Pj}|. \tag{B.9}$$

This projection operator transforms the arbitrary state $|\psi\rangle$ into the P space spanned by the basis $\{|\phi_{Pj}\rangle\}$. The complimentary operator $\hat{Q}$ is defined by using the basis $\{|\phi_{Qj}\rangle\}$ in the Q space as

$$\hat{Q} = \sum_j |\phi_{Qj}\rangle\langle\phi_{Qj}|. \tag{B.10}$$

The eigenenergies of the initial and final states in the P space are denoted by E^0_{Pi} and E^0_{Pf}, respectively. The eigenenergy of the intermediate state in the Q space is E^0_{Qj}. On the right-hand side of (B.7), the bare interaction operator $\hat{V}$ is placed between the projection operators $\hat{P}$ and $\hat{Q}$, which represents the screening effect by the P and Q spaces. Furthermore, the right-hand side of (B.8) represents the virtual transition from the initial state $|\phi_{Pi}\rangle$ in the P space to the intermediate state $|\phi_{Qj}\rangle$ in the Q space, and the successive virtual transition from this intermediate state $|\phi_{Qj}\rangle$ to the final state $|\phi_{Pf}\rangle$ in the P space.

B.2 Magnitude of Effective Interaction Energy

As the initial state $|\phi_{Pi}\rangle$ in the P space, it is assumed that the electron–hole pairs (excitons) in the nanomaterials s and p in subsystem n are in their excited and ground states $|s_{ex}\rangle$ and $|p_g\rangle$, respectively. In addition, the exciton-polariton states, which are used as bases to describe subsystem M, are in their vacuum state $|0_{(M)}\rangle$. Therefore, the initial state in the P space is expressed as

$$|\phi_{Pi}\rangle = |s_{ex}\rangle\,|p_g\rangle \otimes |0_{(M)}\rangle, \tag{B.11}$$

where the symbol $\otimes$ represents the direct product. By the energy transfer from the nanomaterial s to nanomaterial p as a result of the interaction, the electron–hole pairs (excitons) in the nanomaterials s and p transition to the ground and excited states $|s_g\rangle$ and $|p_{ex}\rangle$, respectively. The exciton-polariton in subsystem M is also in the vacuum state $|0_{(M)}\rangle$. Therefore, the final state $|\phi_{Pf}\rangle$ in the P space is expressed as

$$|\phi_{Pf}\rangle = |s_g\rangle\,|p_{ex}\rangle \otimes |0_{(M)}\rangle. \tag{B.12}$$

The basis $\{|\phi_{Pj}\rangle\}$ in the P space is spanned by the two states given by (B.11) and (B.12). Other states cannot be employed for the basis because they violate the energy conservation law in subsystem n in the process of interaction.

On the other hand, the complimentary Q space is composed of many states, including states that violate the energy conservation law in subsystem n, and therefore, they are not employed for the basis of the P space. That is, the basis $\{|\phi_{Qj}\rangle\}$ of the Q space is spanned by

$$|\phi_{Q1n}\rangle = |s_g\rangle\,|p_g\rangle \otimes |n_{(M)}\rangle \tag{B.13a}$$

and

$$\left|\phi_{Q2n}\right\rangle = \left|s_{ex}\right\rangle \left|p_{ex}\right\rangle \otimes \left|n_{(M)}\right\rangle. \tag{B.13b}$$

Here, $\left|n_{(M)}\right\rangle$ represents the state in which $n_{(M)}$ quanta of exciton-polaritons exist in subsystem M. However, as will be described immediately after presenting (B.20), since only the state $\left|1_{(M)}\right\rangle$ gives a nonzero value of the effective interaction energy, the states with $\left|1_{(M)}\right\rangle$ are extracted from (B.13a) and (B.13b) and expressed as $\left|\phi_{Q11}\right\rangle$ and $\left|\phi_{Q21}\right\rangle$. Furthermore, for consistency of expression with (B.7), $\left|\phi_{Q11}\right\rangle$ and $\left|\phi_{Q21}\right\rangle$ are written as

$$\left|\phi_{Q1}\right\rangle = \left|s_g\right\rangle \left|p_g\right\rangle \otimes \left|1_{(M)}\right\rangle \tag{B.14a}$$

and

$$\left|\phi_{Q2}\right\rangle = \left|s_{ex}\right\rangle \left|p_{ex}\right\rangle \otimes \left|1_{(M)}\right\rangle. \tag{B.14b}$$

By noting that the relations

$$\hat{P}\left|\phi_{Pj}\right\rangle = \left|\phi_{Pj}\right\rangle \tag{B.15}$$

and

$$\hat{Q}\left|\phi_{Qjn}\right\rangle = \left|\phi_{Qjn}\right\rangle \quad (j = 1, 2) \tag{B.16}$$

hold due to (B.9) and (B.10), one can derive

$$\left\langle\phi_{Qjn}\right| \hat{Q}\hat{V}\hat{P}\left|\phi_{Pi}\right\rangle = \left\langle\phi_{Qjn}\right| \hat{V}\left|\phi_{Pi}\right\rangle \tag{B.17}$$

and

$$\left\langle\phi_{Pf}\right| \hat{P}\hat{V}\hat{Q}\left|\phi_{Qjn}\right\rangle = \left\langle\phi_{Pf}\right| \hat{V}\left|\phi_{Qjn}\right\rangle. \tag{B.18}$$

When the bare interaction operator $\hat{V}$ of (B.4) is inserted into these equations, the annihilation and creation operators $\hat{b}\left(\boldsymbol{r}_\alpha\right)$ and $\hat{b}^\dagger\left(\boldsymbol{r}_\alpha\right)$ of the electron–hole pair (exciton) apply only to $\left|n_{(M)}\right\rangle$ $(n_{(M)} = 0, 1, 2, \ldots)$, and those of the exciton-polariton, $\hat{\xi}\left(\boldsymbol{k}\right)$ and $\hat{\xi}^\dagger\left(\boldsymbol{k}\right)$ apply only to $\left|s_g\right\rangle$, $\left|s_{ex}\right\rangle$, $\left|p_g\right\rangle$, and $\left|p_{ex}\right\rangle$. From (B.11)–(B.14) one can derive

$$\begin{aligned}\left\langle\phi_{Q1n}\right| \hat{V}\left|\phi_{Pi}\right\rangle &= -i\sum_{\alpha=s}^{p}\sum_{\boldsymbol{k}}\sqrt{\frac{\hbar}{2\varepsilon_0 V}}\left\langle s_g\right|\left\langle p_g\right| \otimes \left\langle n_{(M)}\right| \left(\hat{b}\left(\boldsymbol{r}_\alpha\right) + \hat{b}^\dagger\left(\boldsymbol{r}_\alpha\right)\right) \\ &\quad \times \left(K_\alpha\left(\boldsymbol{k}\right)\hat{\xi}\left(\boldsymbol{k}\right) - {K^*}_\alpha\left(\boldsymbol{k}\right)\hat{\xi}^\dagger\left(\boldsymbol{k}\right)\right)\left|s_{ex}\right\rangle \left|p_g\right\rangle \otimes \left|0_{(M)}\right\rangle \\ &= -i\sum_{\boldsymbol{k}}\sqrt{\frac{\hbar}{2\varepsilon_0 V}}K_s\left(\boldsymbol{k}\right)\end{aligned} \tag{B.19}$$

and

$$\begin{aligned}\left\langle \phi_{Pf}\right| \hat{V} \left|\phi_{Q1n}\right\rangle &= -i \sum_{\alpha=s}^{p} \sum_{\boldsymbol{k}} \sqrt{\frac{\hbar}{2\varepsilon_0 V}} \left\langle s_g\right| \left\langle p_{ex}\right| \otimes \left\langle 0_{(M)}\right| \left(\hat{b}\left(\boldsymbol{r}_\alpha\right) + \hat{b}^\dagger\left(\boldsymbol{r}_\alpha\right)\right) \\ &\quad \times \left(K_\alpha\left(\boldsymbol{k}\right) \hat{\xi}\left(\boldsymbol{k}\right) - K^*{}_\alpha\left(\boldsymbol{k}\right) \hat{\xi}^\dagger\left(\boldsymbol{k}\right)\right) \left|s_g\right\rangle \left|p_g\right\rangle \otimes \left|n_{(M)}\right\rangle \\ &= i \sum_{\boldsymbol{k}} \sqrt{\frac{\hbar}{2\varepsilon_0 V}} K_p^*\left(\boldsymbol{k}\right). \end{aligned} \tag{B.20}$$

Here, only the term $n_{(M)} = 1$ gives a nonzero value in the second rows of (B.19) and (B.20) because $\left\langle 0_{(M)}\right| \left(\hat{b}\left(\boldsymbol{r}_\alpha\right) + \hat{b}^\dagger\left(\boldsymbol{r}_\alpha\right)\right) \left|n_{(M)}\right\rangle = 0$ $\left(n_{(M)} \neq 1\right)$, which leads to the third rows. Therefore, the $(j = 1)$th term on the right-hand side of (B.8) is expressed as

$$\begin{aligned}&\left\langle \phi_{Pf}\right| \hat{P}\hat{V}\hat{Q} \left|\phi_{Q1}\right\rangle \left\langle \phi_{Q1}\right| \hat{Q}\hat{V}\hat{P} \left|\phi_{Pi}\right\rangle \left(\frac{1}{E_{Pi}^0 - E_{Q1}^0} + \frac{1}{E_{Pf}^0 - E_{Q1}^0}\right) \\ &= \sum_{\boldsymbol{k}} \frac{\hbar}{2\varepsilon_0 V} K_s\left(\boldsymbol{k}\right) K_p^*\left(\boldsymbol{k}\right) \left(\frac{1}{E_{Pi}^0 - E_{Q1}^0} + \frac{1}{E_{Pf}^0 - E_{Q1}^0}\right). \end{aligned} \tag{B.21}$$

In order to similarly express the $(j = 2)$th term on the right-hand side of (B.8), the relations

$$\begin{aligned}\left\langle \phi_{Q2n}\right| \hat{V} \left|\phi_{Pi}\right\rangle &= -i \sum_{\alpha=s}^{p} \sum_{\boldsymbol{k}} \sqrt{\frac{\hbar}{2\varepsilon_0 V}} \left\langle s_{ex}\right| \left\langle p_{ex}\right| \otimes \left\langle n_{(M)}\right| \left(\hat{b}\left(\boldsymbol{r}_\alpha\right) + \hat{b}^\dagger\left(\boldsymbol{r}_\alpha\right)\right) \\ &\quad \times \left(K_\alpha\left(\boldsymbol{k}\right) \hat{\xi}\left(\boldsymbol{k}\right) - K^*{}_\alpha\left(\boldsymbol{k}\right) \hat{\xi}^\dagger\left(\boldsymbol{k}\right)\right) \left|s_{ex}\right\rangle \left|p_g\right\rangle \otimes \left|0_{(M)}\right\rangle \\ &= i \sum_{\boldsymbol{k}} \sqrt{\frac{\hbar}{2\varepsilon_0 V}} K_p^*\left(\boldsymbol{k}\right) \end{aligned} \tag{B.22}$$

and

$$\begin{aligned}\left\langle \phi_{Pf}\right| \hat{V} \left|\phi_{Q2n}\right\rangle &= -i \sum_{\alpha=s}^{p} \sum_{\boldsymbol{k}} \sqrt{\frac{\hbar}{2\varepsilon_0 V}} \left\langle s_g\right| \left\langle p_{ex}\right| \otimes \left\langle 0_{(M)}\right| \left(\hat{b}\left(\boldsymbol{r}_\alpha\right) + \hat{b}^\dagger\left(\boldsymbol{r}_\alpha\right)\right) \\ &\quad \times \left(K_\alpha\left(\boldsymbol{k}\right) \hat{\xi}\left(\boldsymbol{k}\right) - K^*{}_\alpha\left(\boldsymbol{k}\right) \hat{\xi}^\dagger\left(\boldsymbol{k}\right)\right) \left|s_{ex}\right\rangle \left|p_{ex}\right\rangle \otimes \left|n_{(M)}\right\rangle \\ &= -i \sum_{\boldsymbol{k}} \sqrt{\frac{\hbar}{2\varepsilon_0 V}} K_s\left(\boldsymbol{k}\right) \end{aligned} \tag{B.23}$$

are used, which are similar to (B.19) and (B.20), respectively. Then, the $(j = 2)$th term is expressed as

$$\left\langle \phi_{Pf} \right| \hat{P}\hat{V}\hat{Q} \left| \phi_{Q2} \right\rangle \left\langle \phi_{Q2} \right| \hat{Q}\hat{V}\hat{P} \left| \phi_{Pi} \right\rangle \left(\frac{1}{E_{Pi}^0 - E_{Q2}^0} + \frac{1}{E_{Pf}^0 - E_{Q2}^0} \right)$$
$$= \sum_{\boldsymbol{k}} \frac{\hbar}{2\varepsilon_0 V} K_s(\boldsymbol{k}) K_p^*(\boldsymbol{k}) \left(\frac{1}{E_{Pi}^0 - E_{Q2}^0} + \frac{1}{E_{Pf}^0 - E_{Q2}^0} \right). \tag{B.24}$$

By summing (B.21) and (B.24), (B.8) is rewritten as

$$V_{eff}(s \to p) = \sum_{\boldsymbol{k}} \frac{\hbar}{2\varepsilon_0 V} K_s(\boldsymbol{k}) K_p^*(\boldsymbol{k}) \left(\frac{1}{E_{Pi}^0 - E_{Q1}^0} + \frac{1}{E_{Pf}^0 - E_{Q1}^0} \right.$$
$$\left. + \frac{1}{E_{Pi}^0 - E_{Q2}^0} + \frac{1}{E_{Pf}^0 - E_{Q2}^0} \right). \tag{B.25}$$

Here V_{eff} on the left-hand side of (B.8) was rewritten as $V_{eff}(s \to p)$ in order to represent that energy is transferred from the nanomaterial s to the nanomaterial p. By replacing the sum for the wave-vector $\boldsymbol{k}$ by the integral $\frac{V}{(2\pi)^3} \int_0^\infty d\boldsymbol{k}$, the symbol V is eliminated from this equation, yielding

$$V_{eff}(s \to p) = \frac{\hbar^2}{(2\pi)^3 \varepsilon_0} \int_0^\infty d\boldsymbol{k} K_s(\boldsymbol{k}) K_p^*(\boldsymbol{k}) \left(\frac{1}{E_{Pi}^0 - E_{Q1}^0} + \frac{1}{E_{Pf}^0 - E_{Q1}^0} \right.$$
$$\left. + \frac{1}{E_{Pi}^0 - E_{Q2}^0} + \frac{1}{E_{Pf}^0 - E_{Q2}^0} \right). \tag{B.26}$$

By denoting the eigenenergies of the states $|s_g\rangle$, $|s_{ex}\rangle$, $|p_g\rangle$, and $|p_{ex}\rangle$ in the nanomaterials s and p by $E_{s,g}$, $E_{s,ex}$, $E_{p,g}$, and $E_{p,ex}$, and by denoting the eigenenergy of the state $|1_{(M)}\rangle$ in the exciton-polariton by $E(\boldsymbol{k})$, one obtains

$$E_{Pi}^0 - E_{Q1}^0 = \left(E_{s.ex} + E_{p,g}\right) - \left(E_{s,g} + E_{p,g} + E(\boldsymbol{k})\right)$$
$$= \left(E_{s.ex} - E_{s,g}\right) - E(\boldsymbol{k}) = -\left(E(\boldsymbol{k}) - E_s\right), \tag{B.27a}$$

$$E_{Pi}^0 - E_{Q2}^0 = \left(E_{s.ex} + E_{p,g}\right) - \left(E_{s,ex} + E_{p,ex} + E(\boldsymbol{k})\right)$$
$$= -\left(E_{p.ex} - E_{p,g}\right) - E(\boldsymbol{k}) = -\left(E(\boldsymbol{k}) + E_p\right), \tag{B.27b}$$

$$E_{Pf}^0 - E_{Q1}^0 = \left(E_{s.g} + E_{p,ex}\right) - \left(E_{s,g} + E_{p,g} + E(\boldsymbol{k})\right)$$
$$= \left(E_{p.ex} - E_{p,g}\right) - E(\boldsymbol{k}) = -\left(E(\boldsymbol{k}) - E_p\right), \tag{B.27c}$$

$$E_{Pf}^{0} - E_{Q2}^{0} = \left(E_{s.g} + E_{p,ex}\right) - \left(E_{s,ex} + E_{p,ex} + E\left(\boldsymbol{k}\right)\right)$$
$$= -\left(E_{s.ex} - E_{s,g}\right) - E\left(\boldsymbol{k}\right) = -\left(E\left(\boldsymbol{k}\right) + E_{s}\right). \tag{B.27d}$$

Here, the difference $E_{\alpha,ex} - E_{\alpha,g}$ between the eigenenergies of the excited state ($E_{\alpha,ex}$) and ground state ($E_{\alpha,g}$) was replaced with the transition energy $E_{\alpha}(\alpha = s, p)$. Inserting these into (B.26) yields

$$V_{eff}\left(s \rightarrow p\right) = -\frac{\hbar^{2}}{(2\pi)^{3}\varepsilon_{0}} \int_{0}^{\infty} d\boldsymbol{k} K_{s}\left(\boldsymbol{k}\right) K_{p}^{*}\left(\boldsymbol{k}\right) \left(\frac{1}{E\left(\boldsymbol{k}\right) - E_{s}} + \frac{1}{E\left(\boldsymbol{k}\right) - E_{p}} + \frac{1}{E\left(\boldsymbol{k}\right) + E_{p}} + \frac{1}{E\left(\boldsymbol{k}\right) + E_{s}}\right). \tag{B.28}$$

By exchanging the subscripts of the nanomaterials s and p in order to assume the initial and final states

$$\left|\phi_{Pi}\right\rangle = \left|s_{g}\right\rangle \left|p_{ex}\right\rangle \otimes \left|0_{(M)}\right\rangle \tag{B.29}$$

and

$$\left|\phi_{Pf}\right\rangle = \left|s_{ex}\right\rangle \left|p_{g}\right\rangle \otimes \left|0_{(M)}\right\rangle, \tag{B.30}$$

the energy $V_{eff}\left(p \rightarrow s\right)$ transferred from the nanomaterial p to the nanomaterial s can be derived in the same manner as above, and is given by

$$V_{eff}\left(p \rightarrow s\right) = -\frac{\hbar^{2}}{(2\pi)^{3}\varepsilon_{0}} \int_{0}^{\infty} d\boldsymbol{k} K_{p}\left(\boldsymbol{k}\right) K_{s}^{*}\left(\boldsymbol{k}\right) \left(\frac{1}{E\left(\boldsymbol{k}\right) - E_{p}} + \frac{1}{E\left(\boldsymbol{k}\right) - E_{s}} + \frac{1}{E\left(\boldsymbol{k}\right) + E_{s}} + \frac{1}{E\left(\boldsymbol{k}\right) + E_{p}}\right). \tag{B.31}$$

Furthermore, inserting (B.5) into (B.28) and (B.31) and summing them gives

$$V_{eff}\left(\boldsymbol{r}\right) = -\frac{\hbar^{2}}{(2\pi)^{3}\varepsilon_{0}} \sum_{\lambda=1}^{2} \int_{0}^{\infty} f^{2}\left(\boldsymbol{k}\right) d\boldsymbol{k} \left(\boldsymbol{p}_{s} \cdot \boldsymbol{e}_{\lambda}\left(\boldsymbol{k}\right)\right) e^{i\boldsymbol{k}\cdot\left(\boldsymbol{r}_{s} - \boldsymbol{r}_{p}\right)} \left(\boldsymbol{p}_{p} \cdot \boldsymbol{e}_{\lambda}\left(\boldsymbol{k}\right)\right)$$
$$\times \left(\frac{1}{E\left(\boldsymbol{k}\right) - E_{s}} + \frac{1}{E\left(\boldsymbol{k}\right) - E_{p}} + \frac{1}{E\left(\boldsymbol{k}\right) + E_{p}} + \frac{1}{E\left(\boldsymbol{k}\right) + E_{s}}\right)$$
$$= -\frac{\hbar^{2}}{(2\pi)^{3}\varepsilon_{0}} \sum_{\lambda=1}^{2} \sum_{\alpha=s}^{p} \int_{0}^{\infty} \left(\boldsymbol{p}_{s} \cdot \boldsymbol{e}_{\lambda}\left(\boldsymbol{k}\right)\right) \left(\boldsymbol{p}_{p} \cdot \boldsymbol{e}_{\lambda}\left(\boldsymbol{k}\right)\right) f^{2}\left(\boldsymbol{k}\right)$$
$$\times \left(\frac{1}{E\left(\boldsymbol{k}\right) + E_{\alpha}} + \frac{1}{E\left(\boldsymbol{k}\right) - E_{\alpha}}\right) e^{i\boldsymbol{k}\cdot\boldsymbol{r}} d\boldsymbol{k}, \tag{B.32}$$

where $\boldsymbol{r} = \boldsymbol{r}_{s} - \boldsymbol{r}_{p}$.

B.3 Summation and Integration for Deriving a Yukawa Function

First, as a result of summation with respect to polarization state λ and the integral with respect to the azimuth angles ϑ and ϕ of $\boldsymbol{k}$, the effective interaction energy is expressed as

$$V_{eff}(\boldsymbol{r}) = -\frac{\hbar^2}{(2\pi)^2\varepsilon_0}\int_{-\infty}^{\infty} k^2 dk\, f^2(\boldsymbol{k}) \sum_{\alpha=s}^{p}\left(\frac{1}{E(\boldsymbol{k})+E_\alpha}+\frac{1}{E(\boldsymbol{k})-E_\alpha}\right) \times\left\{\left(\boldsymbol{p}_s\cdot\boldsymbol{p}_p\right)e^{i\boldsymbol{k}\cdot\boldsymbol{r}}\left(\frac{1}{ikr}+\frac{1}{k^2r^2}-\frac{1}{ik^3r^3}\right) -\left(\boldsymbol{p}_s\cdot\boldsymbol{u}_r\right)\left(\boldsymbol{p}_p\cdot\boldsymbol{u}_r\right)e^{i\boldsymbol{k}\cdot\boldsymbol{r}}\left(\frac{1}{ikr}+\frac{3}{k^2r^2}-\frac{3}{ik^3r^3}\right)\right\}, \tag{B.33}$$

where $\boldsymbol{u}_r = \boldsymbol{r}/r$.

Second, as a result of averaging over the azimuth angle of the electric dipole moment, the effective interaction energy is expressed as

$$V_{eff}(\boldsymbol{r}) = -\frac{2\hbar^2 p_s p_p}{3(2\pi)^2\varepsilon_0}\int_{-\infty}^{\infty} k^2 dk\, f^2(\boldsymbol{k}) \times\sum_{\alpha=s}^{p}\left(\frac{1}{E(\boldsymbol{k})+E_\alpha}+\frac{1}{E(\boldsymbol{k})-E_\alpha}\right)\frac{e^{i\boldsymbol{k}\cdot\boldsymbol{r}}}{ikr}. \tag{B.34}$$

The eigenenergy E_α of the nanomaterial $\alpha\,(=s, p)$ is expressed as $E_\alpha = p_\alpha^2/2m_\alpha$, where p_α and m_α are the momentum and effective mass of the exciton, respectively. Inserting $p_\alpha = h/a_\alpha$ into this expression yields

$$E_\alpha = \frac{1}{2m_\alpha}\left(\frac{h}{a_\alpha}\right)^2, \tag{B.35}$$

where a_α is the size of the nanomaterial. On the other hand, the energy $E(\boldsymbol{k})$ is assumed to follow the dispersion relation

$$E(\boldsymbol{k}) = E_m + \frac{(\hbar k)^2}{2m_{pol}}, \tag{B.36}$$

where m_{pol} and E_m are the effective mass of the exciton-polariton and the eigenenergy of the exciton of subsystem M, respectively. In the case of a semiconductor, for example, E_m corresponds to the bandgap energy E_g. The nanomaterials in subsystem n are excited by a real photon whose photon energy is adjusted to be lower than E_m in order to avoid absorption by the macroscopic subsystem M. By adjusting the photon energy in this way, the light propagates through subsystem M without attenuating its power and successfully reaches subsystem n. Under this transparent situation, E_m can be excluded from (B.36), and the energy of the exciton-polariton of subsystem M, contributing the effective interaction energy, is simply expressed as

$$E(\boldsymbol{k}) = \frac{(\hbar k)^2}{2m_{pol}}. \tag{B.37}$$

By using this equation, the term $f(\boldsymbol{k})$ in (B.5) is given by

$$f(\boldsymbol{k}) = \frac{ck\sqrt{\frac{\hbar}{2m_{pol}}}}{\sqrt{\frac{\hbar^2}{2m_{pol}^2}k^2 - c^2}}, \tag{B.38}$$

where c is the speed of light in vacuum. By using (B.37), (B.34) is expressed as

$$\begin{aligned} V_{eff}(\boldsymbol{r}) = &-\frac{2\hbar^2 p_s p_p}{3(2\pi)^2\varepsilon_0}\int_{-\infty}^{\infty} k^2 dk\, f^2(\boldsymbol{k}) \sum_{\alpha=s}^{p} \frac{2m_{pol}}{\hbar^2} \\ &\times \left\{ \frac{1}{(k + i\Delta_{\alpha+})(k - i\Delta_{\alpha+})} \frac{1}{(k + i\Delta_{\alpha-})(k - i\Delta_{\alpha-})} \right\} \frac{e^{i\boldsymbol{k}\cdot\boldsymbol{r}}}{ikr} \\ \equiv &\sum_{\alpha=s}^{p} \left[V_{eff,\alpha+}(\boldsymbol{r}) + V_{eff,\alpha-}(\boldsymbol{r}) \right] \end{aligned} \tag{B.39}$$

where

$$\Delta_{\alpha\pm} \equiv \frac{1}{\hbar}\sqrt{2m_{pol}(\pm E_\alpha)}. \tag{B.40}$$

Finally, after taking the complex integral over k, by noting the pole of the first order $k = i\Delta_{\alpha\pm}$ and by rewriting $f(\boldsymbol{k})$ in (B.39) as $f(i\Delta_{\alpha\pm})$, $V_{eff,\alpha+}(\boldsymbol{r})$ and $V_{eff,\alpha-}(\boldsymbol{r})$ in the third row of (B.39) are expressed as

$$V_{eff,\alpha\pm}(\boldsymbol{r}) = \mp\frac{p_s p_p}{3(2\pi)\varepsilon_0} W_{\alpha\pm}(\Delta_{\alpha\pm})^2 \frac{e^{-\Delta_{\alpha\pm} r}}{r}, \tag{B.41}$$

where

$$W_{\alpha\pm} \equiv \frac{m_{pol}c^2}{\left(m_{pol}c^2 \pm E_\alpha\right)}. \tag{B.42}$$

Inserting (B.41) and (B.42) into (B.39) yields

$$V_{eff}(\boldsymbol{r}) = -\frac{p_s p_p}{3(2\pi)\varepsilon_0}\sum_{\alpha=s}^{p}\left[W_{\alpha+}(\Delta_{\alpha+})^2\frac{e^{-\Delta_{\alpha+}r}}{r} - W_{\alpha-}(\Delta_{\alpha-})^2\frac{e^{-\Delta_{\alpha-}r}}{r}\right], \quad \text{(B.43)}$$

which is the expression for the effective interaction energy, representing the spatial modulation feature of the DP. As a result of this interaction, the exciton in the nanomaterial emits a real photon after time γ_{rad}^{-1}, which is the inverse of the radiative relaxation rate γ_{rad}, depending on the structure and size of the nanomaterial. Then, the emitted real photon, i.e., the scattered light, can be detected in the far field.

Equation (B.43) is composed of two terms. By noting (B.40), it is found that the first term is merely the Yukawa function

$$Y(\Delta_{\alpha+}) = \frac{\exp\left(-2\pi\sqrt{\frac{m_{pol}}{m_\alpha}}\frac{r}{a_\alpha}\right)}{r}, \quad \text{(B.44)}$$

as has been shown in (B.1), which was derived because $\Delta_{\alpha+}$ takes a real number. The value of this function decreases rapidly with increasing r. The interaction range, i.e., a in (B.1), is found to be $(a_\alpha/2\pi)\sqrt{m_\alpha/m_{pol}}$ from this equation, which is proportional to the size a_α of the nanomaterial α. Thus, (B.44) means that the electromagnetic field exists on the surface of the nanomaterial α within a range that depends on the material size. In other words, the nanomaterial α is covered with a localized electromagnetic field cloud. The effective interaction energy mediated by the DP is represented by this function $Y(\Delta\alpha_+)$.

The second term is given by the function

$$Y(\Delta_{\alpha-}) = \frac{\exp\left(-i2\pi\sqrt{\frac{m_{pol}}{m_\alpha}}\frac{r}{a_\alpha}\right)}{r}, \quad \text{(B.45)}$$

which was derived because $\Delta_{\alpha-}$ takes an imaginary number. The numerator of this equation sinusoidally oscillates with period $\lambda_\alpha = a_\alpha\sqrt{m_\alpha/m_{pol}}$ by varying r. This means that (B.45) represents a spherical wave with wavelength λ_α. However, this is not the real photon to be detected in the far field, and furthermore, the wavelength λ_α is not correlated with the wavelength of the real photon incident on the nanomaterial α. Equation (B.45) originates from the fact that no boundary conditions are set on the nanomaterial. That is, the spatial distribution of the electromagnetic field is, in general, determined by the boundary conditions if the wavelength is sufficiently short. However, because no boundary conditions are set in the present case, (B.45) means that an oscillatory electromagnetic field leaks out from the surface of the nanomaterial. It is expected that this leaking field can be eliminated by using a more detailed theoretical model with accurate boundary conditions in the future.

Now, (B.44) and (B.45) are compared from the viewpoint of the energy transfer between the subsystems n and M. Equation (B.28) means that (B.44) originates from the transition from the initial state $|\phi_{Pi}\rangle$ of (B.11) to the final state $\left|\phi_{Pf}\right\rangle$ of (B.12) via the intermediate state $\left|\phi_{Q2}\right\rangle$ of (B.14b). Here, in the initial state $|\phi_{Pi}\rangle$, the nanomaterial p is in the ground state $\left|p_g\right\rangle$, and the exciton-polariton in subsystem M is in the vacuum state $\left|0_{(M)}\right\rangle$. First, by the transition from the initial state $|\phi_{Pi}\rangle$ to the intermediate state $\left|\phi_{Q2}\right\rangle$, the nanomaterial p is excited to the excited state $|p_{ex}\rangle$, and one exciton-polariton is generated in subsystem M; i.e., it is excited to the state $\left|1_{(M)}\right\rangle$. Therefore, this transition violates the energy conservation law because the two subsystems increase their energies simultaneously. Next, by the transition from the intermediate state $\left|\phi_{Q2}\right\rangle$ to the final state $\left|\phi_{Pf}\right\rangle$, the nanomaterial s is de-excited from the excited state $|s_{ex}\rangle$ to the ground state $\left|s_g\right\rangle$, and the exciton-polariton in subsystem M is also de-excited from the state $\left|1_{(M)}\right\rangle$ to the vacuum state $\left|0_{(M)}\right\rangle$. Therefore, this transition also violates the energy conservation law because the two subsystems decrease their energies simultaneously.

On the other hand, (B.28) also means that (B.45) originates from the transition from the initial state $|\phi_{Pi}\rangle$ of (B.11) to the final state $\left|\phi_{Pf}\right\rangle$ of (B.12) via the intermediate state $\left|\phi_{Q1}\right\rangle$ of (B.14a). Here, in the initial state $|\phi_{Pi}\rangle$, the nanomaterial s is in the excited state $|s_{ex}\rangle$, and the exciton-polariton in subsystem M is in the vacuum state $\left|0_{(M)}\right\rangle$. First, by the transition from the initial state $|\phi_{Pi}\rangle$ to the intermediate state $\left|\phi_{Q1}\right\rangle$, the nanomaterial s is de-excited to the ground state $\left|s_g\right\rangle$. Since the single exciton-polariton is simultaneously generated in subsystem M, i.e., is excited to the state $\left|1_{(M)}\right\rangle$, this transition follows the energy conservation law. Next, by the transition from the intermediate state $\left|\phi_{Q1}\right\rangle$ to the final state $\left|\phi_{Pf}\right\rangle$, the nanomaterial p is excited from the ground state $\left|p_g\right\rangle$ to the excited state $|p_{ex}\rangle$, and the exciton-polariton in subsystem M is de-excited from the state $\left|1_{(M)}\right\rangle$ to the vacuum state $\left|0_{(M)}\right\rangle$. Therefore, this transition also follows the energy conservation law.

Because the two successive transitions of (B.44) violate the energy conservation law, these transition processes are called virtual processes. This violation is allowed within a very short duration Δt. In other words, the Heisenberg uncertainty principle $\Delta E \Delta t \geq \hbar$ allows a large energy uncertainty ΔE if Δt is small. Therefore, within a sufficiently short duration, the vacuum fluctuations can trigger the successive transitions from the initial state to the intermediate state, and then to the final state, even though they violate the energy conservation law. Since the DP energy is transferred by these transitions, the DP is also called a virtual photon.

The second term in the third row in (B.32) corresponds to (B.45). It is easily found that it becomes infinity if $E(\boldsymbol{k}) = E_\alpha$ because its denominator is $E(\boldsymbol{k}) - E_\alpha$. The transition process represented by this term is called a resonant process. On the other hand, the first term corresponds to (B.44). The relevant transition process is called a non-resonant process because the denominator of this term is $E(\boldsymbol{k}) + E_\alpha$, which takes a finite value at $E(\boldsymbol{k}) = E_\alpha$.

B.4 Size-Dependent Resonance and Hierarchy

The terms $Y\left(\Delta_{s+}\right)$ and $Y\left(\Delta_{p+}\right)$ are picked up from (B.43) and used in order to discuss the spatial properties of DPs. In the future, it is expected that a more-detailed theoretical model will be able to eliminate the leaking electromagnetic field of (B.45), and therefore, the terms $Y\left(\Delta_{s-}\right)$ and $Y\left(\Delta_{p-}\right)$ are excluded in the discussion. The effective interaction energy is thus expressed as

$$V_{eff}(\boldsymbol{r}) = -\frac{p_s p_p}{3(2\pi)\varepsilon_0} W_+ \left\{ \frac{\exp\left(-\frac{r}{a_s'}\right)}{a_s'^2 r} + \frac{\exp\left(-\frac{r}{a_p'}\right)}{a_p'^2 r} \right\}, \tag{B.46a}$$

where

$$a_\alpha' = \frac{a_\alpha}{2\pi\sqrt{m_{pol}/m_\alpha}} \qquad (\alpha = s,\ p). \tag{B.46b}$$

Here, $W_{+\alpha}$ in (B.43) was rewritten as W_+ by removing the subscript α because it does not strongly depend on the size of the nanomaterial a_α. Furthermore, the relation $\Delta_{\alpha+} = 1/a_\alpha'$ was used based on (B.35) and (B.40). In the case where the center-to-center separation between the nanomaterials s and p is $\boldsymbol{r}_{sp}$, the magnitude of the detectable real photon energy, generated as a result of the interaction, is given by the volume integral of the spatial derivative $\nabla_r V_{eff}\left(\boldsymbol{r}_p - \boldsymbol{r}_s\right)$ of (B.46a), which is given by

$$\begin{aligned} I\left(\boldsymbol{r}_{sp}\right) &= \left| \iint \nabla_{\boldsymbol{r}_p} V_{eff}\left(\boldsymbol{r}_p - \boldsymbol{r}_s\right) d^3 r_s d^3 r_p \right|^2 \\ &= \left(\frac{p_s p_p}{3(2\pi)\varepsilon_0} W_+ \right)^2 \left[8\pi \sum_{\alpha=s}^{p} a_\alpha'^2 \left\{ \frac{a_s}{a_\alpha'} \cosh\left(\frac{a_s}{a_\alpha'}\right) - \sinh\left(\frac{a_s}{a_\alpha'}\right) \right\} \right. \\ &\quad \left. \times \left\{ \frac{a_p}{a_\alpha'} \cosh\left(\frac{a_p}{a_\alpha'}\right) - \sinh\left(\frac{a_p}{a_\alpha'}\right) \right\} \left(\frac{a_\alpha'}{r_{sp}} + \frac{a_\alpha'^2}{r_{sp}^2} \right) \exp\left(-\frac{r_{sp}}{a_\alpha'}\right) \right]^2. \end{aligned} \tag{B.47}$$

In order to convert this to the real photon intensity, the right-hand side is divided by $\left(a_s^3 + a_p^3\right)^2$ so that the resultant quantity has dimensions of optical power per unit area and is expressed a

$$\begin{aligned} I_d\left(\boldsymbol{r}_{sp}\right) &= \frac{1}{\left(a_s^3 + a_p^3\right)^2} \left[\sum_{\alpha=s}^{p} a_\alpha'^2 \left\{ \frac{a_s}{a_\alpha'} \cosh\left(\frac{a_s}{a_\alpha'}\right) - \sinh\left(\frac{a_s}{a_\alpha'}\right) \right\} \right. \\ &\quad \left. \times \left\{ \frac{a_p}{a_\alpha'} \cosh\left(\frac{a_p}{a_\alpha'}\right) - \sinh\left(\frac{a_p}{a_\alpha'}\right) \right\} \left(\frac{a_\alpha'}{r_{sp}} + \frac{a_\alpha'^2}{r_{sp}^2} \right) \exp\left(-\frac{r_{sp}}{a_\alpha'}\right) \right]^2, \end{aligned} \tag{B.48}$$

where, for simplicity, all the constants appearing on the left of the symbol $\sum_{\alpha=s}^{p}$ in (B.47) have been removed.

Now, the value of $2\pi\sqrt{m_{pol}/m_{\alpha}}$ in the denominator of (B.46b) must be estimated. The effective mass m_{α} of the exciton in the nanomaterial α can be assumed to be $0.5m_0$ in the case of a semiconductor [8], where m_0 is the mass of the electron in vacuum. On the other hand, the effective mass m_{pol} of the exciton-polariton in subsystem M can be assumed to be $(0.004–0.03)m_0$ based on experimental and theoretical considerations by taking polariton–polariton scattering into account [9, 10]. Using the values of m_{α} and m_{pol} assumed above, the value of $2\pi\sqrt{m_{pol}/m_{\alpha}}$ can be estimated to be 0.56–1.54, which is close to unity. Based on this estimation, (B.48) represents that the light intensity takes the maximum if a_p is close to a_s, a feature called size-dependent resonance, which means that the interaction energy takes the maximum when the sizes of the nanomaterials s and p are equal.

Size-dependent resonance means that the magnitude of the energy transfer mediated by the DP takes the maximum when the sizes of the nanomaterials s and p are equal. On the other hand, it has been pointed out that the separation between the nanomaterials s and p must be as short as their sizes because the interaction range mediated by the DP is equivalent to the sizes of the nanomaterials. For these reasons, one finds that the energy transfer mediated by a DP gains a unique feature, named hierarchy.

That is to say, if there is a material s with a complicated shape (its size may not necessarily be nanometric) in the proximity of the nanomaterial p of size a_p, and if their separation is as short as a_p, the energy is preferably transferred from the nanomaterial p to the part of the material s whose size is equal to a_p. On the other hand, if there exists another nanomaterial p' of size $a_p^{'}$ in proximity to the material s, and if their separation is as short as $a_p^{'}$, the energy is preferably transferred to the other part of the material s whose size is equal to $a_p^{'}$. Furthermore, these two channels of the preferable energy transfers do not interfere with each other. Thus, it is found that the energy transfer between small materials located in close proximity is independent of the energy transfer between larger materials located farther away. This feature is called the hierarchy, which means that different energy transfer occurs independently for different material sizes and separations.

References

1. M. Ohtsu, K. Kobayashi, T. Kawazoe, T. Yatsui, M. Naruse, *Prinicples of Nanophotonics* (CRC Press, Boca Raton, 2007), pp.19–29
2. K. Kobayashi, M. Ohtsu, J. Microsc. **194**, 249 (1999)
3. S. Sangu, K. Kobayashi, M. Ohtsu, J. Microsc. **202**, 279 (2001)
4. S. John, T. Quang, Phys. Rev. A **52**, 4083 (1995)
5. H. Suzuura, T. Tsujikawa, T. Tokihiro, Phys. Rev. B **53**, 1294 (1996)
6. A. Shojiguchi, K. Kobayashi, S. Sangu, K. Kitahara, M. Ohtsu, J. Phys. Soc. Jpn. **72**, 2984 (2003)

7. K. Kobayashi, S. Sangu, H. Ito, M. Ohtsu, Phys. Rev. A **763**, 013806 (2001)
8. Y. Liu, T. Morishima, T. Yatsui, T. Kawazoe, M. Ohtsu, Nanotechnology **22**, 15605 (2011)
9. T. Itoh, T. Suzuki, M. Ueta, J. Phys. Soc. Jpn. **42**, 1069 (1977)
10. T. Itoh, T. Suzuki, J. Phys. Soc. Jpn. **45**, 1939 (1978)

Appendix C
Coupling Dressed Photons and Phonons

C.1 Novel Molecular Dissociation and the Need for a Theoretical Model

It has been pointed out that a novel molecular dissociation is possible when the molecules are excited by DPs. When DPs are created at the apex of a tapered glass fiber probe by injecting light from the tail of the probe, gaseous molecules jumping into the DP field are dissociated even though the photon energy of the injected light is lower than both the excitation energy E_{ex} and the dissociation energy E_{dis}.

Although the molecule is not dissociated by propagating light with a photon energy lower than E_{dis}, it will be found from the theoretical model described below that the molecule, when jumping into the DP field at the probe apex, absorbs not only the DP energy but also phonon energy [1, 2]. That is, the molecule can receive energy from phonons, exciting molecular vibrations, while the electrons remain in the ground state. As a result, the molecule gains vibrational energy by phonon absorption, and the excitation exceeds the potential barrier even though low-photon-energy light is injected into the tail of the probe.

However, it should be noted that the phonon energy is several tens of meV, which is about 1/100th of E_{dis}. Accordingly, multiple phonons need to be absorbed for dissociating the molecule. Here, if only one phonon is exchanged per interaction between the molecule and the probe apex, the probability of absorbing multiple phonons is very low because it is a multi-step process. Therefore, for theoretically explaining the unique experimental results based on the absorption of multiple phonons, it should be assumed that multiple phonons cohere with each other, and thus, multiple phonons are exchanged per interaction between the molecule and the probe apex.

Based on the assumptions above, it can be considered that the molecule interacts not only with the DP but also with phonons. This means that a quasi-particle, that is, a coupled state of the DP and phonons, is created at the probe apex, and the energy of this quasi-particle is exchanged between the molecule and the probe apex. This appendix gives theoretical formulations for describing this quasi-particle.

M. Ohtsu, *Silicon Light-Emitting Diodes and Lasers*,
Nano-Optics and Nanophotonics, DOI 10.1007/978-3-319-42014-1

In order to study the interaction between the molecule and the probe apex, the probe apex is approximated as a one-dimensional material, and its one-dimensional lattice vibration is analyzed. Here, it should be noted that the size of this material is finite because this approximation is applied only to the probe apex. Since the representative size of the probe is the radius of curvature a of the apex (corresponding to the constant a in the Yukawa function of (B.1) in Appendix B), the probe is coarse-grained with this size.

Constituent elements of the probe apex, assumed as a result of coarse-graining, are called "atoms" for convenience, and they are connected by springs. The number of atoms is finite and is denoted by N. The mechanical motions of these atoms correspond to the lattice vibrations, whose system Hamiltonian is expressed as

$$H = \sum_{i=1}^{N} \frac{\boldsymbol{p}_i^2}{2m_i} + \sum_{i=1}^{N-1} \frac{k}{2}(\boldsymbol{x}_{i+1} - \boldsymbol{x}_i)^2 + \sum_{i=1,N} \frac{k}{2}\boldsymbol{x}_i^2, \tag{C.1}$$

where $\boldsymbol{x}_i$, $\boldsymbol{p}_i$, and m_i are the displacement from an equilibrium point, its conjugate momentum, and the mass of an atom at site i, respectively, and k is the spring constant. Both ends ($i = 1$ and $i = N$) of the spring are assumed to be fixed, and one-dimensional longitudinal motions are considered in the following. Therefore, these lattice vibrations correspond to longitudinal acoustic and optical phonons. In the case of a three-dimensional material, two transverse acoustic phonons and two transverse optical phonons have to be also taken into account.

By rewriting the Hamiltonian in terms of the normal coordinate $\boldsymbol{y}_p$, which is given by

$$\boldsymbol{x}_i = \frac{1}{\sqrt{m_i}} \sum_{p=1}^{N} P_{ip} \boldsymbol{y}_p, \tag{C.2}$$

and the conjugate momentum $\boldsymbol{\pi}_p = (d/dt)\, \boldsymbol{y}_p$, and moreover, by replacing them with the corresponding operators $\hat{\boldsymbol{y}}_p$ and $\hat{\boldsymbol{\pi}}_p$ for quantization, one has

$$\hat{H}\left(\hat{\boldsymbol{y}}, \hat{\boldsymbol{\pi}}\right) = \sum_{p=1}^{N} \frac{\hat{\boldsymbol{\pi}}_p^2}{2} + \sum_{p=1}^{N} \Omega_p^2 \frac{\hat{\boldsymbol{y}}_p^2}{2}. \tag{C.3}$$

Here, the commutation relation

$$\left[\hat{\boldsymbol{y}}_p, \hat{\boldsymbol{\pi}}_q\right] = \hat{\boldsymbol{y}}_p \hat{\boldsymbol{\pi}}_q - \hat{\boldsymbol{\pi}}_q \hat{\boldsymbol{y}}_p = i\hbar\delta_{pq} \tag{C.4}$$

is imposed. When the operators $\hat{c}_p$ and $\hat{c}_p^\dagger$ are defined as

$$\hat{c}_p = \frac{1}{\sqrt{2\hbar\Omega_p}} \left(\Omega_p \hat{\boldsymbol{y}}_p + i\hat{\boldsymbol{\pi}}_p\right), \tag{C.5}$$

$$\hat{c}_p^\dagger = \frac{1}{\sqrt{2\hbar\Omega_p}} \left(\Omega_p \hat{y}_p - i\hat{\pi}_p \right), \tag{C.6}$$

they satisfy the boson commutation relation

$$\left[\hat{c}_p, \hat{c}_q^\dagger \right] \equiv \hat{c}_p \hat{c}_q^\dagger - \hat{c}_q^\dagger \hat{c}_p = \delta_{pq}. \tag{C.7}$$

The operators $\hat{c}_p$ and $\hat{c}_p^\dagger$ respectively represent annihilation and creation operators for a phonon with eigenenergy $\hbar\Omega_p$. By using them, (C.3) is rewritten as

$$\hat{H}_{phonon} = \sum_{p=1}^{N} \hbar\Omega_p \left(\hat{c}_p^\dagger \hat{c}_p + \frac{1}{2} \right). \tag{C.8}$$

When all the atoms are identical, that is, $m_i = m$, the Hamiltonian of (C.1) is diagonalized by the orthonormal matrix P with elements

$$P_{ip} = \sqrt{\frac{2}{N+1}} \sin\left(\frac{ip}{N+1}\pi \right) \quad (1 \le i, p \le N), \tag{C.9}$$

yielding the eigen angular frequency

$$\Omega_p = 2\sqrt{\frac{k}{m}} \sin\left[\frac{p}{2(N+1)}\pi \right]. \tag{C.10}$$

In this case, all the vibration modes are delocalized; that is, they spread over the whole probe apex. In contrast, if there are some doped impurity atoms or defects in the probe apex, the modes cannot be simply expressed by using the sinusoidal functions of (C.9) and (C.10). If the masses of the impurity atoms are assumed to be different from the other atoms, and the spring constant remains unchanged, the behaviors of the vibration modes strongly depend on the positions of the impurity atoms and their masses.

In particular, if the masses of the impurity atoms are smaller than those of other atoms, special vibration modes, called localized modes, manifest themselves [3–6]. Figure C.1 shows the vibration amplitude as a function of the site number of atoms, where the total number of sites is 30. Squares and circles represent two localized modes with the highest and the second-highest energies of phonons, respectively, while the triangles are for the delocalized mode with the lowest energy. In the localized modes, the vibration amplitudes are large around the sites of impurity atoms, whereas that of the delocalized mode spreads over the whole probe apex. When the mass of the impurity atom is smaller than that of the other atoms, the phonon energies of the localized modes are higher than those of the delocalized modes.

Since the glass fiber typically used for an actual probe is not a perfect crystal but an amorphous material, it always contains lattice defects, as well as doped impurity atoms. In addition, since the probe apex has a tapered profile, the effective masses of

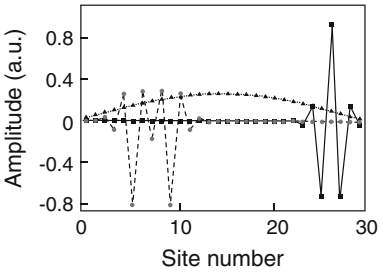

Fig. C.1 Vibration amplitudes of vibration modes. The number N of the mode is 30. The impurity atoms are at the sites 5, 9, 18, 25, 26, and 27. Their masses are 0.5 times that of the other atoms. $\hbar\sqrt{k/m} = 22.4\,\mathrm{meV}$. *Squares* and *circles* represent the first and second localized modes, respectively. *Triangles* represent the delocalized mode

the atoms depend on the position in the probe apex. Therefore, high-energy localized modes whose vibration amplitudes are spatially inhomogeneous can be created in the probe.

C.2 Transformation of the Hamiltonian

This section discusses the interaction between the DP and phonons. That is, as a result of the interaction with the DP, many phonons can cohere with each other, thus enabling a unique interaction that is different from the interaction between photons and phonons in a macroscopic material. This originates from the fact that the probe apex is a finite system and nanometric in size.

On the other hand, the DP localizes at one site of the lattice in the probe apex, where the extent of localization corresponds to the size of the atoms. The Hamiltonian for this model is given by

$$\hat{H} = \sum_{i=1}^{N} \hbar\omega \tilde{a}_i^{\dagger}\tilde{a}_i + \left\{ \sum_{i=1}^{N} \frac{\hat{\boldsymbol{p}}_i^2}{2m_i} + \sum_{i=1}^{N-1} \frac{k}{2}\left(\hat{\boldsymbol{x}}_{i+1} - \hat{\boldsymbol{x}}_i\right)^2 + \sum_{i=1,N} \frac{k}{2}\hat{\boldsymbol{x}}_i^2 \right\} + \sum_{i=1}^{N} \hbar\chi \tilde{a}_i^{\dagger}\tilde{a}_i \hat{\boldsymbol{x}}_i + \sum_{i=1}^{N-1} \hbar J \left(\tilde{a}_i^{\dagger}\tilde{a}_{i+1} + \tilde{a}_{i+1}^{\dagger}\tilde{a}_i \right), \tag{C.11}$$

where $\tilde{a}_i$ and $\tilde{a}_i^{\dagger}$ respectively denote the annihilation and creation operators of a DP with energy $\hbar\omega$ at site i in the lattice, and $\hat{\boldsymbol{x}}_i$ and $\hat{\boldsymbol{p}}_i$ respectively represent the displacement and conjugate momentum operators of the vibration. The mass of the atom at the site i is designated by m_i, and the atoms are assumed to be connected by springs with a spring constant k. The third and fourth terms stand for the DP–vibration interaction with the interaction energy $\hbar\chi$ and DP hopping with hopping

energy $\hbar J$, respectively. The quantities χ and J are called the coupling constant and hopping constant, respectively.

After the vibration field is quantized in terms of phonon operators of mode p and eigenenergy $(\hat{c}_p^\dagger, \hat{c}_p, \hbar\Omega_p)$, (C.11) can be rewritten as

$$\hat{H} = \sum_{i=1}^{N} \hbar\omega \tilde{a}_i^\dagger \tilde{a}_i + \sum_{p=1}^{N} \hbar\Omega_p \hat{c}_p^\dagger \hat{c}_p + \sum_{i=1}^{N}\sum_{p=1}^{N} \hbar\chi_{ip} \tilde{a}_i^\dagger \tilde{a}_i \left(\hat{c}_p^\dagger + \hat{c}_p\right) + \sum_{i=1}^{N-1} \hbar J \left(\tilde{a}_i^\dagger \tilde{a}_{i+1} + \tilde{a}_{i+1}^\dagger \tilde{a}_i\right), \tag{C.12}$$

with the coupling constant χ_{ip} at the site i for the phonon of mode p. The site-dependent coupling constant χ_{ip} is expressed by the original coupling constant χ of (C.11):

$$\chi_{ip} = \chi P_{ip} \sqrt{\frac{\hbar}{2m_i\Omega_p}}. \tag{C.13}$$

In addition to (C.7), annihilation and creation operators for a DP and a phonon satisfy the boson commutation relations as follows:

$$\begin{aligned} &\left[\tilde{a}_i, \tilde{a}_j^\dagger\right] = \delta_{ij}, \\ &\left[\tilde{a}_i, \hat{c}_p\right] = \left[\tilde{a}_i, \hat{c}_p^\dagger\right] = \left[\tilde{a}_i^\dagger, \hat{c}_p\right] = \left[\tilde{a}_i^\dagger, \hat{c}_q^\dagger\right] = 0, \\ &\left[\tilde{a}_i, \tilde{a}_j\right] = \left[\tilde{a}_i^\dagger, \tilde{a}_j^\dagger\right] = \left[\hat{c}_p, \hat{c}_q\right] = \left[\hat{c}_p^\dagger, \hat{c}_q^\dagger\right] = 0. \end{aligned} \tag{C.14}$$

Based on the discussions in Sect. C.1, in the probe apex, there are localized phonons, which govern the spatial features of the DP. However, (C.12) is not easily handled because of the third power of the operators in the third term. To overcome this difficulty, this term will be eliminated by diagonalizing a part of the Hamiltonian using a unitary transformation [7–9].

For this diagonalization, an anti-Hermitian operator $\hat{S}$ is used which is defined as

$$\hat{S} = \sum_{i=1}^{N}\sum_{p=1}^{N} \frac{\chi_{ip}}{\Omega_p} \tilde{a}_i^\dagger \tilde{a}_i \left(\hat{c}_p^\dagger - \hat{c}_p\right) \tag{C.15}$$

Unitary operators $\hat{U}$ for the unitary transformation are given by

$$\hat{U} = e^{\hat{S}}. \tag{C.16}$$

These operators lead us to the exact transformation of the annihilation and creation operators for the DP and phonons:

$$\hat{\alpha}_i^\dagger \equiv \hat{U}^\dagger \tilde{a}_i^\dagger \hat{U} = \tilde{a}_i^\dagger \exp\left\{ -\sum_{p=1}^{N} \frac{\chi_{ip}}{\Omega_p} \left(\hat{c}_p^\dagger - \hat{c}_p \right) \right\}, \tag{C.17a}$$

$$\hat{\alpha}_i \equiv \hat{U}^\dagger \tilde{a}_i \hat{U} = \tilde{a}_i \exp\left\{ \sum_{p=1}^{N} \frac{\chi_{ip}}{\Omega_p} \left(\hat{c}_p^\dagger - \hat{c}_p \right) \right\}, \tag{C.17b}$$

$$\hat{\beta}_p^\dagger \equiv \hat{U}^\dagger \hat{c}_p^\dagger \hat{U} = \hat{c}_p^\dagger + \sum_{p=1}^{N} \frac{\chi_{ip}}{\Omega_p} \tilde{a}_i^\dagger \tilde{a}_i, \tag{C.18a}$$

$$\hat{\beta}_p \equiv \hat{U}^\dagger \hat{c}_p \hat{U} = \hat{c}_p + \sum_{p=1}^{N} \frac{\chi_{ip}}{\Omega_p} \tilde{a}_i^\dagger \tilde{a}_i. \tag{C.18b}$$

These transformed operators can be regarded as the creation and annihilation operators of a new quasi-particle, which represents the coupled state of the DP and phonons. Since they are derived by a unitary transformation, they satisfy the same boson commutation relations as those of the DP and phonons:

$$\left[\hat{\alpha}_i, \hat{\alpha}_j^\dagger \right] = \hat{U}^\dagger \tilde{a}_i \hat{U} \hat{U}^\dagger \tilde{a}_j^\dagger \hat{U} - \hat{U}^\dagger \tilde{a}_j^\dagger \hat{U} \hat{U}^\dagger \tilde{a}_i \hat{U} = \hat{U}^\dagger \left[\tilde{a}_i, \tilde{a}_j^\dagger \right] \hat{U} = \delta_{ij}, \tag{C.19}$$

$$\left[\hat{\beta}_p, \hat{\beta}_q^\dagger \right] = \delta_{pq}, \tag{C.20}$$

$$\left[\tilde{\alpha}_i, \tilde{\beta}_p \right] = \left[\tilde{\alpha}_i, \tilde{\beta}_p^\dagger \right] = \left[\tilde{\alpha}_i^\dagger, \tilde{\beta}_p \right] = \left[\tilde{\alpha}_i^\dagger, \tilde{\beta}_p^\dagger \right] = 0, \tag{C.21a}$$

$$\left[\tilde{\alpha}_i, \tilde{\alpha}_j \right] = \left[\tilde{\alpha}_i^\dagger, \tilde{\alpha}_j^\dagger \right] = \left[\tilde{\beta}_p, \tilde{\beta}_q \right] = \left[\tilde{\beta}_p^\dagger, \tilde{\beta}_q^\dagger \right] = 0. \tag{C.21b}$$

Using these creation and annihilation operators, the Hamiltonian of (C.12) can be rewritten as

$$\begin{aligned} \hat{H} = & \sum_{i=1}^{N} \hbar\omega \hat{\alpha}_i^\dagger \hat{\alpha}_i + \sum_{p=1}^{N} \hbar\Omega_p \hat{\beta}_p^\dagger \hat{\beta}_p - \sum_{i=1}^{N} \sum_{j=1}^{N} \sum_{p=1}^{N} \frac{\hbar\chi_{ip}\chi_{jp}}{\Omega_p} \hat{\alpha}_i^\dagger \hat{\alpha}_i \hat{\alpha}_j^\dagger \hat{\alpha}_j \\ & + \sum_{i=1}^{N-1} \hbar \left(\hat{J}_i \hat{\alpha}_i^\dagger \hat{\alpha}_{i+1} + \hat{J}_i^\dagger \hat{\alpha}_{i+1}^\dagger \hat{\alpha}_i \right), \end{aligned} \tag{C.22}$$

with

$$\hat{J}_i = J \exp\left\{\sum_{p=1}^{N} \frac{(\chi_{ip} - \chi_{i+1p})}{\Omega_p}\left(\hat{\beta}_p^\dagger - \hat{\beta}_p\right)\right\}. \tag{C.23}$$

In order to create a physical picture of the new quasi-particle, the creation operator $\hat{\alpha}_i^\dagger$ is applied to the vacuum state $|0\rangle$. Then, from (C.17a) one derives

$$\begin{aligned}\hat{\alpha}_i^\dagger |0\rangle &= \tilde{a}_i^\dagger \exp\left\{-\sum_{p=1}^{N} \frac{\chi_{ip}}{\Omega_p}\left(\hat{c}_p^\dagger - \hat{c}_p\right)\right\}|0\rangle \\ &= \tilde{a}_i^\dagger \prod_{p=1}^{N} \exp\left\{-\frac{\chi_{ip}}{\Omega_p}\left(\hat{c}_p^\dagger - \hat{c}_p\right)\right\}|0\rangle \\ &= \tilde{a}_i^\dagger \prod_{p=1}^{N} \exp\left\{-\frac{1}{2}\left(\frac{\chi_{ip}}{\Omega_p}\right)^2\right\} \exp\left(-\frac{\chi_{ip}}{\Omega_p}\hat{c}_p^\dagger\right)|0\rangle\,. \end{aligned} \tag{C.24}$$

The third row of this equation represents that the state of the DP at site i is associated with multimode coherent phonons. In other words, it means that the DP is dressed by the energies of an infinite number of phonons. When $\hat{\beta}_p^\dagger$ is applied to the vacuum state $|0\rangle$, one has

$$\hat{\beta}_p^\dagger |0\rangle = \hat{c}_p^\dagger |0\rangle \tag{C.25}$$

which is expressed only by the bare phonon operator $\hat{c}_p^\dagger$ (before the transformation) of the same mode p. That is, the phonon is not affected by the DP. Therefore, in the following discussions, it is possible to focus on the quasi-particle expressed by $\hat{\alpha}_i^\dagger$ and $\hat{\alpha}_i$.

The coherent state means that an infinite number of quasi-particles cohere with each other. Since it is not an eigenstate of the Hamiltonian, the number of quasi-particles fluctuates. When the light is injected into the probe apex, the phonons are excited by this fluctuation. If the phonons are in the vacuum state and the DP is created at site i in the one-dimensional lattice by the injected light, the initial condition of the system at time $t = 0$ is expressed as $|\psi\rangle = \tilde{a}_i^\dagger |0\rangle \equiv \hat{\alpha}_i^\dagger |\gamma\rangle$. Under this condition, the probability that the phonons still stay in the vacuum state at time t is given by

$$P'(t) = \left|\langle\psi| \exp\left(-\frac{iH't}{\hbar}\right)|\psi\rangle\right|^2, \tag{C.26a}$$

from which the probability of exciting the phonons of the mode p is given by $P(t) = 1 - P'(t)$, i.e.,

$$P(t) = 1 - \exp\left\{2\left(\frac{\chi_{ip}}{\Omega_p}\right)^2 \left[\cos\left(\Omega_p t\right) - 1\right]\right\}. \tag{C.26b}$$

Here, the hopping term was neglected for simplicity. This means that the $\hat{H}'$ in (C.26a) corresponds to the Hamiltonian of (C.22), from which the fourth term was excluded.

The probability expressed by (C.26b) oscillates with the period $2\pi/\Omega_p$ and takes the maximum at time $t = \pi/\Omega_p$. Since the frequencies of the localized modes are larger than those of the delocalized modes, the delocalized modes are excited after the excitation probability of the localized modes reaches the maximum. The excitation probability $\boldsymbol{p}_{\boldsymbol{p}_0}(t)$ for the localized and delocalized modes, respectively, is calculated from

$$\begin{aligned}
\boldsymbol{p}_{\boldsymbol{p}_0}(t) &= P\left(t : p = \boldsymbol{p}_0\right) P'\left(t : p \neq \boldsymbol{p}_0\right) \\
&= \left[1 - \exp\left\{2\left(\frac{\chi_{i\boldsymbol{p}_0}}{\Omega_{\boldsymbol{p}_0}}\right)^2 \left[\cos\left(\Omega_{\boldsymbol{p}_0} t\right) - 1\right]\right\}\right] \\
&\quad \times \exp\left\{\sum_{p \neq \boldsymbol{p}_0} 2\left(\frac{\chi_{ip}}{\Omega_p}\right)^2 \left[\cos\left(\Omega_p t\right) - 1\right]\right\},
\end{aligned} \tag{C.27}$$

where a specific phonon mode p_0 is excited, and other modes remain in the vacuum state. It is found that the localized mode is excited soon after the light is injected, and then the excitation probability of the delocalized mode gradually increases. Furthermore, the localized mode is not excited if the DP is not created at the localized site, i.e., at the impurity site. The excitation probabilities of other modes gradually increase triggered by the fluctuations. In summary, the localized modes can be excited by the fluctuations in the number of phonons if the phonons are in the coherent state.

C.3 Localization Mechanism of Dressed Photons

The expectation value $\left\langle \hat{\boldsymbol{x}}_j \right\rangle_i$ of the displacement $\hat{\boldsymbol{x}}_j$ of site j is derived when the DP is localized at site i (state $\hat{\alpha}_i^\dagger |0\rangle$). Here, the state $\hat{\alpha}_i^\dagger |0\rangle$ is expressed, using (C.24), as

$$\hat{\alpha}_i^\dagger |0\rangle = \tilde{a}_i^\dagger A \exp\left(\sum_{p=1}^{N} \gamma_{ip} \hat{c}_p^\dagger\right) |0\rangle \tag{C.28}$$

with

$$\gamma_{ip} = -\frac{\chi_{ip}}{\Omega_p}, \tag{C.29a}$$

$$A = \exp\left\{-\frac{1}{2}\sum_{p=1}^{N}\gamma_{ip}^2\right\}. \tag{C.29b}$$

By noting that the coherent state is the eigenstate of the annihilation operator and is normalized, the expectation value $\langle\hat{\boldsymbol{x}}_j\rangle_i$ is

$$\begin{aligned}\langle\hat{\boldsymbol{x}}_j\rangle_i &= \langle 0|\,\hat{\alpha}_i\hat{\boldsymbol{x}}_j\hat{\alpha}_i^\dagger\,|0\rangle \\ &= \langle 0|\,\tilde{a}_i A\exp\left(\sum_{p'=1}^{N}\gamma_{ip'}\hat{c}_{p'}\right)\sum_{p=1}^{N}P_{jp}\frac{\hbar}{2m_j\Omega_p} \\ &\quad\times\left(\hat{c}_p^\dagger+\hat{c}_p\right)A\exp\left(\sum_{p''=1}^{N}\gamma_{ip''}\hat{c}_{p''}^\dagger\right)\tilde{a}_i^\dagger\,|0\rangle \\ &= \sum_{p=1}^{N}2\gamma_{ip}P_{ip}\frac{\hbar}{2m_j\Omega_p} = -\sum_{p=1}^{N}\frac{\hbar\chi P_{ip}P_{jp}}{\sqrt{m_i m_j}\Omega_p^2} \\ &= -\frac{2}{\chi}\sum_{p=1}^{N}\frac{\chi_{ip}\chi_{jp}}{\Omega_p}.\end{aligned} \tag{C.30}$$

By inserting this into the third term of (C.22), the Hamiltonian is rewritten as

$$\begin{aligned}\hat{H} = &\sum_{i=1}^{N}\hbar\omega\hat{\alpha}_i^\dagger\hat{\alpha}_i + \sum_{p=1}^{N}\hbar\Omega_p\hat{\beta}_p^\dagger\hat{\beta}_p + \sum_{i=1}^{N}\sum_{j=1}^{N}\frac{\hbar\chi}{2}\langle\boldsymbol{x}_j\rangle_i\hat{\alpha}_i^\dagger\hat{\alpha}_i\hat{\alpha}_j^\dagger\hat{\alpha}_j \\ &+\sum_{i=1}^{N-1}\hbar\left(\hat{J}_i\hat{\alpha}_i^\dagger\hat{\alpha}_{i+1}+\hat{J}_i^\dagger\hat{\alpha}_{i+1}^\dagger\hat{\alpha}_i\right).\end{aligned} \tag{C.31}$$

The third term of this equation represents the DP–phonon interaction.

By the DP-phonon interaction, the spatial behavior of the DP is drastically modified due to the localized modes of phonons. This behavior can be analyzed by diagonalizing the first, third, and fourth terms of (C.31), which contain the operators for the DP. For this diagonalization, the mean field approximation is employed for the third term. That is, the average value of the number of DPs is inserted into the operator $\hat{N}_i\left(=\hat{\alpha}_i^\dagger\hat{\alpha}_i\right)$ or $\hat{N}_j\left(=\hat{\alpha}_j^\dagger\hat{\alpha}_j\right)$ in this term. This average value can be assumed to be $1/N$ in the case when the number of DPs is unity and its field is homogeneously distributed over the whole one-dimensional lattice. Thus, the third term is approximated as

$$\sum_{i=1}^{N}\sum_{j=1}^{N}\frac{\hbar\chi}{2}\langle\boldsymbol{x}_j\rangle_i\hat{\alpha}_i^\dagger\hat{\alpha}_i\hat{\alpha}_j^\dagger\hat{\alpha}_j \simeq \sum_{i=1}^{N}\sum_{j=1}^{N}\frac{\hbar\chi}{2}\langle\boldsymbol{x}_j\rangle_i\frac{1}{N}\hat{\alpha}_i^\dagger\hat{\alpha}_i \equiv -\sum_{i=1}^{N}\hbar\omega_i\hat{\alpha}_i^\dagger\hat{\alpha}_i. \tag{C.32}$$

The angular frequency ω_i on the right-hand side is expressed as

$$\omega_i = -\sum_{j=1}^{N} \frac{\chi \langle \boldsymbol{x}_j \rangle_i}{2N} \equiv \sum_{j=1}^{N}\sum_{p=1}^{N} \frac{\hbar\chi^2 P_{ip} P_{jp}}{2N\sqrt{m_i m_j}\Omega_p^2}, \tag{C.33}$$

where (C.30) was used to replace the middle part with the right-hand side.

Furthermore, for simplicity, by replacing the operator $\hat{J}_i$ of (C.23) with the hopping constant J

$$\hat{J}_i = J, \tag{C.34}$$

i.e., neglecting the site-dependence of the hopping, the first, third, and fourth terms of (C.31) are expressed in a quadratic form

$$\hat{H}_{DP} = \sum_{i=1}^{N} \hbar(\omega - \omega_i)\hat{\alpha}_i^\dagger \hat{\alpha}_i + \sum_{i=1}^{N-1} \hbar J \left(\hat{\alpha}_i^\dagger \hat{\alpha}_{i+1} + \hat{\alpha}_{i+1}^\dagger \hat{\alpha}_i\right), \tag{C.35}$$

or in the matrix form

$$\hat{H}_{DP} = \hbar\hat{\alpha}^\dagger \begin{pmatrix} \omega-\omega_1 & J & \cdot & 0 \\ J & \omega-\omega_2 & \cdot & \cdot \\ \cdot & \cdot & \cdot & J \\ 0 & \cdot & J & \omega-\omega_N \end{pmatrix} \hat{\alpha}, \tag{C.36a}$$

where

$$\hat{\alpha} = \begin{pmatrix} \hat{\alpha}_1 \\ \hat{\alpha}_2 \\ \cdot \\ \hat{\alpha}_N \end{pmatrix}. \tag{C.36b}$$

The effect from the phonons is involved in ω_i in the diagonal elements of this matrix.

Denoting an orthonormal matrix to diagonalize the Hamiltonian of (C.36) by Q, one has

$$\hat{H}_{DP} = \sum_{r=1}^{N} \hbar\Omega_r \hat{A}_r^\dagger \hat{A}_r, \tag{C.37}$$

where $\hbar\Omega_r$ is the rth eigenvalue, and the relations

$$\hat{A}_r = \sum_{i=1}^{N} \left(Q^{-1}\right)_{ri} \hat{\alpha}_i = \sum_{i=1}^{N} Q_{ir}\hat{\alpha}_i, \tag{C.38}$$

$$\left[\hat{A}_r, \hat{A}_s^\dagger\right] \equiv \hat{A}_r\hat{A}_s^\dagger - \hat{A}_s^\dagger\hat{A}_r = \delta_{rs} \tag{C.39}$$

hold. Using these relations, the time evolution of the number operator for the DP at site i is derived by using

$$\hat{N}_i = \hat{\alpha}_i^\dagger \hat{\alpha}_i = \left(\sum_{r=1}^{N} Q_{ir} \hat{A}_r^\dagger \right) \left(\sum_{s=1}^{N} Q_{is} \hat{A}_s \right) \tag{C.40}$$

and (C.39). The result is expressed in the Heisenberg representation as

$$\begin{aligned} \hat{N}_i(t) &= \exp\left(i \frac{\hat{H}_{DP}}{\hbar} t \right) \hat{N}_i \exp\left(-i \frac{\hat{H}_{DP}}{\hbar} t \right) \\ &= \sum_{r=1}^{N} \sum_{s=1}^{N} Q_{ir} Q_{is} \hat{A}_r^\dagger \hat{A}_s \exp\{ i (\Omega_r - \Omega_s) t \} \\ &= \sum_{r=1}^{N} \sum_{s=1}^{N} Q_{ir} Q_{is} \hat{A}_r^\dagger \hat{A}_s \cos\{ (\Omega_r - \Omega_s) t \} . \end{aligned} \tag{C.41}$$

Since $\hat{N}_i(t)$ is a Hermitian operator, the exponential function in the second row was replaced with the cosinusoidal function in the third row. Since one can express the state $|\psi_j\rangle$ of the DP localized at site j at time $t = 0$ as

$$|\psi_j\rangle = \hat{\alpha}_j^\dagger |0\rangle = \sum_{r=1}^{N} Q_{jr} \hat{A}_r^\dagger |0\rangle, \tag{C.42}$$

the expectation value of the number of DPs at site i at time t under the initial condition of (C.42) is given by

$$\langle N_i(t) \rangle_j = \langle \psi_j | \hat{N}_i(t) | \psi_j \rangle = \sum_{r=1}^{N} \sum_{s=1}^{N} Q_{ir} Q_{jr} Q_{is} Q_{js} \cos\{ (\Omega_r - \Omega_s) t \} , \tag{C.43}$$

The value of $\langle N_i(t) \rangle_j$ given by this equation can be regarded as the observation probability of a DP at an arbitrary site i and time t, initially located at site j. In the case of no DP–phonon interaction ($\omega_i = 0$) and an infinite number of sites ($N \to \infty$), this function is analytically expressed in terms of a Bessel function $J_n(x)$ of the first kind as

$$\langle N_i(t)\rangle_j = \left\{J_{j-i}(2Jt) - (-1)^i J_{j+i}(2Jt)\right\}^2. \tag{C.44}$$

Here, the argument J in the Bessel function is the hopping constant. Equation (C.44) means that the expectation value is small at sites distant from the site j at which the DP is generated at time $t = 0$, and furthermore, it decreases with time. This decrease suggests diffusion of the DP from the initial site j.

The temporal evolution of the observation probability $\langle N_i(t)\rangle_j$ of a DP at each site can be derived by summing up only the localized modes. Without the DP–phonon coupling ($\chi = 0$), the DP spreads over the whole lattice as a result of hopping, which can be approximated by (C.44). That is, the DP is reflected at the end of the finite lattice, and freely hops, meaning that the DP is not localized at any site. On the other hand, with DP–phonon coupling ($\chi = 1.4 \times 10^3$ fs^{-1} nm^{-1}), the DP slowly moves from one impurity site to the other instead of freely hopping.

Since the effect of localization represented by χ is contained in the diagonal elements in the Hamiltonian, whereas the hopping constant J is contained in the off-diagonal elements, localization or hopping can be judged by comparing the values of these constants. Since the DP is localized when $\omega_i > J$, one can derive

$$\chi > N\sqrt{\frac{kJ}{\hbar}}, \tag{C.45}$$

which is the criterion for localization. Here, the relations $\omega_i \simeq \hbar\chi^2 P_{ip}^2/Nm_i\Omega_p^2$ (obtained from (C.33)) and $\boldsymbol{p}_{ip}/\Omega_p \simeq \sqrt{m_i/Nk}$ (obtained from (C.9) and (C.10)) were inserted into $\omega_i > J$. It is found that the DP localizes only at the impurity sites and its extent of localization is narrow.

Equation (C.45) represents the criterion for DP localization at a specific site by analyzing the diagonal elements of the Hamiltonian. The following part of this section analyzes the off-diagonal elements, which are represented by the fourth term of (C.22) with the site-dependent hopping operator as a result of the unitary transformation. Since the site-dependence, represented by (C.23), contains the phonon operators and thus cannot be readily treated, the mean field approximation is employed again. That is, since the phonons are in the coherent state $|\gamma\rangle$, which is represented by the third row of (C.24), the expectation value $J_i\left(=\langle\gamma|\,\hat{J}_i\,|\gamma\rangle\right)$ of the hopping operator $\hat{J}_i$ of (C.23) is derived and inserted into the fourth-term of (C.22).

Since the coherent state $|\gamma\rangle$ of the phonons is the eigenstate of the annihilation operator $\hat{c}_p$, it satisfies the relation

$$\hat{c}_p\,|\gamma\rangle = \gamma_p\,|\gamma\rangle\,, \tag{C.46}$$

where γ_p is an eigenvalue. Thus, the relation

$$\exp\left(-\sum_p \kappa_p \hat{c}_p\right)|\gamma\rangle = \exp\left(-\sum_p \kappa_p\gamma_p\right)|\gamma\rangle\,, \tag{C.47}$$

holds, where κ_p is a real number constant. Equations (C.46) and (C.47) lead us to derive the expectation value J_i, which is expressed as

$$J_i = \langle\gamma|\,\hat{J}_i\,|\gamma\rangle = J\exp\left(-\frac{1}{2}\sum_{p=1}^{N} C_{ip}^2\right). \tag{C.48a}$$

The constant C_{ip} is defined by

$$C_{ip} \equiv \frac{\chi_{ip} - \chi_{i+1p}}{\Omega_p}. \tag{C.48b}$$

Since (C.48a) does not contain the eigenvalue γ_p, it is found that the result of the mean field approximation is independent of γ_p as long as the phonons are in the coherent state. On the other hand, the argument in the exponential function represents the summation of C_{ip}^2 over all the modes ($p = 1 - N$) of the phonons, including the localized modes. Therefore, all of the phonon modes will be summed up in the following calculations. In this case, the expectation value J_i of (C.48a) corresponds to the off-diagonal elements in the Hamiltonian of (C.36) and represents the effect of the localized modes, i.e., the inhomogeneity of the phonon field. It is found that the hopping constants are highly modified around the impurity sites.

It is not straightforward to grasp the possibility of localization at each site from the time dependence of the spatial profile of the DP, and therefore, eigenstates of the DP energy have to be investigated. The eigenstate $|r\rangle$ of the Hamiltonian with the eigenvalue $\hbar\Omega_r$ is given by the superposition of the states $\hat{\alpha}_i^\dagger\,|0\rangle$ of the DP localized at all sites i and expressed as

$$|r\rangle = \sum_{i=1}^{N} Q_{ir}\hat{\alpha}_i^\dagger\,|0\rangle. \tag{C.49}$$

Here, the coefficient Q_{ir} is the (i, r)th element of the orthonormal matrix Q used for diagonalizing the Hamiltonian of (C.36); i.e., this coefficient can be regarded as the spatial coordinate representation of the eigenstate of the DP energy. Thus, by considering the column vector of the matrix Q for representing the eigenstate of the maximum energy, as an example, the values of the squares of this vector's elements, $|Q_{ir}|^2$, are calculated and displayed in Fig. C.2. These values represent the occupation probabilities of the DP at each site. In the absence of DP–phonon coupling (curve A: $\chi = 0$), the DP hops and, thus, its field is distributed over the whole probe apex. In the case of the DP–phonon coupling (curve B: $\chi = 40.0$ fs^{-1} nm^{-1}), the DP can localize at an impurity site. Although this figure represents the results for one mode only, there exist other modes in which the DP localizes at the

other impurity sites. By increasing the coupling constant (curve C: $\chi = 54.0\ \mathrm{fs}^{-1}\ \mathrm{nm}^{-1}$), the DP can localize at the end of the lattice (see the right end of the curve C). This originates from the finite size of the lattice and is called the "finite-size effect" [7–10]. In this case, besides the modes shown by the curve C, there exist several other modes that localize at the left end or at the impurity sites. Further increases in the coupling constant decrease the value of J_i, as is understood from (C.48a), which suppresses the DP hopping. However, since the angular frequency $\omega - \omega_i$ of the DP becomes negative if the value of χ becomes larger than a certain value, the present theoretical model becomes invalid. The above discussions enable us to find the site of the DP localization by analyzing the off-diagonal elements. It is found that the curves B and C in Fig. C.2 have peaks at the impurity sites and the tails of the curves extend to the sites that are adjacent to the relevant impurity sites. That is, the extent of this localization is broader. Since the extent of localization is determined by the competition between the effects of localization (χ) and hopping (J), a larger value of χ decreases this extent.

The "atoms" in the theoretical model described above correspond to nanomaterials whose sizes are equivalent to the radius of curvature of the probe apex, and Fig. C.2 shows that the DP field is as broad as several atomic sizes due to the coupling with the localized modes of the phonons. The quasi-particle created by this coupling is called a dressed-photon–phonon (DPP). When the DP is localized at the end of the lattice, the DPP field penetrates the probe surface, and the penetration length is equivalent to the radius of curvature at the top of the probe apex. If a gas molecule comes flying into this penetration area, the DPP energy is transferred to the molecule and, as a result, the molecule is excited to a vibrational excited state by multiple phonons in the DPP and, successively, to a higher electronic state. By these successive excitations,

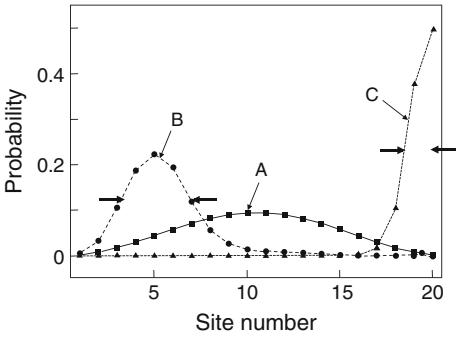

Fig. C.2 Occupation probability of the dressed photon at each site. *Curves* A, B, and C represent the results for $\chi = 0$, 40.0, and $54.0\,\mathrm{fs}^{-1}\,\mathrm{nm}^{-1}$, respectively. The number of modes, N, is 20. The impurity atoms are at the sites, 4, 6, 13, and 19. Their masses are 0.2-times that of the other atoms. $\hbar\omega = 1.81\,\mathrm{eV}$, $\hbar J = 0.5\,\mathrm{eV}$

the molecule can be dissociated even though the photon energy of the light injected into the probe is lower than the dissociation energy of the molecule. These energy transfer and excitations are the origin of the novel dissociation phenomenon reviewed in Sect. C.1.

References

1. Y. Tanaka, K. Kobayashi, Physica E **40**, 297 (2007)
2. Y. Tanaka, K. Kobayashi, J. Microsc. **229**, 228 (2008)
3. D.N. Payton, W.M. Visscher, Phys. Rev. **154**, 802 (1967)
4. A.J. Sievers, A.A. Maradudin, S.S. Jaswal, Phys. Rev. **138**, A272 (1965)
5. S. Mizuno, Phys. Rev. B **65**, 193302 (2002)
6. T. Yamamoto, K. Watanabe, Phys. Rev. Lett. **96**, 255503 (2006)
7. C. Falvo, V. Pouthier, J. Chem. Phys. **122**, 014701 (2005)
8. A.S. Davydov, G.M. Pestryakov, Phys. Stat. Sol. (b) **9**(4), 505 (1972)
9. L. Jacak, P. Machnikowski, J. Krasynj, P. Zoller, Eur. Phys. J. **D22**, 319 (2003)
10. V. Pouthier, C. Girardet, J. Chem. Phys. **112**, 5100 (2000)

Appendix D
Photon Absorption and Emission Via Dressed Photon–Phonons

Since the DP is a photon that is dressed by the energy of the electron–hole pair, its eigenenergy has a large number of modulation sidebands. Among them, the eigenenergy $\hbar\omega_k^{'}$ of the upper sideband is larger than the photon energy $\hbar\omega_0$ of the incident real photon. Furthermore, since the DPP described in Appendix C is a photon that is dressed not only by the energy of the electron–hole pair but also by the energies of the multiple coherent phonons, it also has modulation sidebands whose number is larger than that of the DP. Among these sidebands, the eigenenergy of the upper sideband is larger than $\hbar\omega_0$. Therefore, if the DPP energy is transferred from nanomaterial s to nanomaterial p and if the electron–hole pair in nanomaterial p is resonant with one of the upper sidebands of the DPP, the electron–hole pair is excited by absorbing the eigenenergy. $\hbar\omega_k^{''}$ of this sideband. Since $\hbar\omega_k^{''}$ is larger than the photon energy $\hbar\omega_o$ of the incident light, this excitation process can be regarded as energy up-conversion. This appendix describes the fundamental processes of light absorption and emission for this conversion. Since not only the electronic states but also the phonon states are involved in the energy states of the nanomaterial, for simplicity, only one specific sideband component that is resonant with the phonon states is considered from among the large number of sidebands in the following discussions.

In the operators for the DPP given by (C.17a) and (C.17b), the annihilation ($\tilde{a}_i$) and creation ($\tilde{a}_i^{\dagger}$) operators for the DP are involved in the transition of the electron between the ground state $\left|E_g; el\right\rangle$ and the excited state $|E_{ex}; el\rangle$. Furthermore, the phonon operators ($\hat{c}_p$, $\hat{c}_p^{\dagger}$) in the exponential functions of (C.17a) and (C.17b) are involved in the transition of the phonons between the thermal equilibrium state (ground state) $|E_{thermal}; phonon\rangle$ and the excited state $|E_{ex}; phonon\rangle$. Therefore, in order to analyze the DPP-mediated interaction between nanomaterials, one has to consider the states represented by the direct product $\otimes$ of the electronic state and phonon state of the nanomaterials, e.g., $\left|E_g; el\right\rangle \otimes |E_{thermal}; phonon\rangle$, $\left|E_g; el\right\rangle \otimes |E_{ex}; phonon\rangle$, $|E_{ex}; el\rangle \otimes |E_{thermal}; phonon\rangle$, and $|E_{ex}; el\rangle \otimes |E_{ex}; phonon\rangle$. The origins of the energy up-conversion can be analyzed in terms of these states.

For energy conversion, it is essential to excite or de-excite electrons or electron–hole pairs. If the DPP is involved in this excitation or de-excitation, energy up-

M. Ohtsu, *Silicon Light-Emitting Diodes and Lasers*,
Nano-Optics and Nanophotonics, DOI 10.1007/978-3-319-42014-1

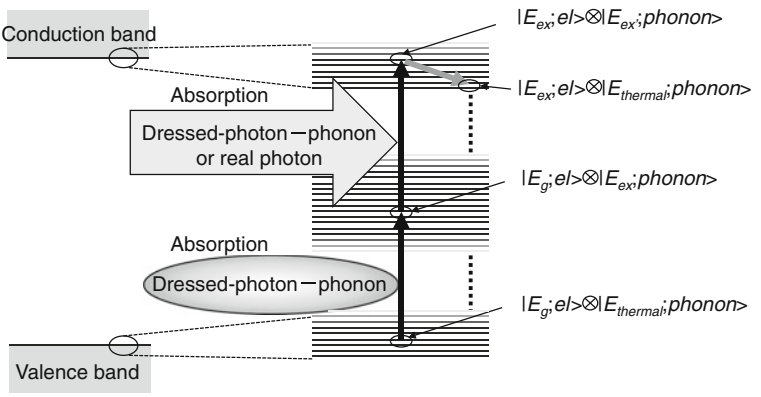

Fig. D.1 Energy band structure of Si. *Horizontal lines* represent the phonon-coupled electronic states

conversion becomes possible. This appendix discusses the two-step excitation and de-excitation, i.e., the relation between DPPs and absorption, spontaneous emission, and stimulated emission, in more detail than those reviewed in Sect. 1.3.2. In the case of a semiconductor, for example, absorption or emission of a real photon is not possible if its photon energy is lower than the bandgap energy E_g of the semiconductor material, i.e., if its wavelength is longer than the cut-off wavelength $\lambda_c = E_g/hc$. However, absorption or emission becomes possible if a DPP is involved, and as a result, energy up-conversion is realized. In this case, since the real photon incident on the material has a lower photon energy than E_g, excitation or de-excitation of the electrons or electron–hole pairs takes place in multiple steps. Here, a two-step process is considered for simplicity.

First, the photon absorption process is described. Since the energies of the incident real photon and DP are lower than the bandgap energy E_g, the two-step process is required for exciting an electron from the valence band to the conduction band, as is shown in Fig. D.1. The steps are:

First step The initial state of the electron is the ground state $\left|E_g;\, el\right\rangle$, which corresponds to the valence band in the semiconductor. On the other hand, the phonon is in the thermal equilibrium state $|E_{thermal};\, phonon\rangle$, which depends on the crystal lattice temperature. Therefore, the initial state is expressed by the direct product of these two states: $\left|E_g;\, el\right\rangle \otimes |E_{thermal};\, phonon\rangle$. In the excitation by absorbing the DPP, the electron is not excited to the conduction band but remains in the ground state $\left|E_g;\, el\right\rangle$ because the energies of the incident real photon and the DP are lower than the bandgap energy E_g of the material. However, the phonon is excited to one of the excited states $|E_{ex};\, phonon\rangle$ depending on the DP energy, and thus, the final state of the transition is expressed as $\left|E_g;\, el\right\rangle \otimes |E_{ex};\, phonon\rangle$. It should be noted that this transition is electric dipole-forbidden because the electron stays in the ground state even after the transition. This state, $\left|E_g;\, el\right\rangle \otimes |E_{ex};\, phonon\rangle$, is the intermediate state of the two-step excitation.

Second step In the excitation from the above intermediate state to the final state, the electron is excited to the excited state $|E_{ex}; el\rangle$, i.e., the conduction band. This transition is electric dipole-allowed because it is a transition from the ground state $\left|E_g; el\right\rangle$ to the excited state $|E_{ex}; el\rangle$ of the electron. Therefore, this transition is possible not only due to the DPP but also the real photon. As a result of this transition, the system reaches the state $|E_{ex}; el\rangle \otimes |E_{ex'}; phonon\rangle$, which is represented by the direct product of the excited state $|E_{ex}; el\rangle$ of the electron and the excited state $|E_{ex'}; phonon\rangle$ of the phonon. Since the phonon promptly relaxes to the thermal equilibrium state $|E_{thermal}; phonon\rangle$ after this excitation, the final state of this two-step excitation is expressed by the direct product of the excited state of the electron and the thermal equilibrium state of the phonon: $|E_{ex}; el\rangle \otimes |E_{thermal}; phonon\rangle$. Table D.1 summarizes the two-step absorption process.

Second, the photon emission process is described. The two-step process is also required in this case for the same reason as described above. Spontaneous emission occurs by the following two steps, as is schematically explained by Fig. 1.3a and summarized in Table D.2.

Table D.1 Two-step absorption

First step	Initial state: $\|E_g; el\rangle \otimes \|E_{thermal}; phonon\rangle$ ⇓Electric dipole-forbidden transition Intermediate state: $\|E_g; el\rangle \otimes \|E_{ex}; phonon\rangle$
Second step	Route 1 (by DPP) | Route 2 (by real photon) ⇓Electric dipole-allowed transition⇓ $\|E_{ex}; el\rangle \otimes \|E_{ex'}; phonon\rangle$ ⇓Relaxation Final state: $\|E_{ex}; el\rangle \otimes \|E_{thermal}; phonon\rangle$

Table D.2 Two-step spontaneous emission

First step	Initial state: $\|E_{ex}; el\rangle \otimes \|E_{ex}, phonon\rangle$ ⇓Electric dipole-allowed transition⇓	
	Route 1 (Spontaneous emission: DPP creation) Intermediate state: $\|E_g; el\rangle \otimes \|E_{ex'}; phonon\rangle$	Route 2 (Spontaneous emission: Real photon creation) Intermediate state: $\|E_g; el\rangle \otimes \|E_{ex'}; phonon\rangle$
Second step	⇓Electric dipole-forbidden transition⇓ (Spontaneous emission: DPP creation) $\|E_g; el\rangle \otimes \|E_{ex''}; phonon\rangle$	
	⇓Relaxation Final state: $\|E_g; el\rangle \otimes \|E_{thermal}; phonon\rangle$	

First step The initial state is expressed by the direct product of the excited state of the electron in the conduction band and the excited state of the phonon: $|E_{ex}; el\rangle \otimes |E_{ex}; phonon\rangle$. De-excitation to the ground state $\left|E_g; el\right\rangle$ of the electron, i.e., to the valence band, is an electric dipole-allowed transition because it corresponds to the opposite process of the second step of absorption described above. Therefore, this emission process create not only a DPP but also a real photon. As a result, the system reaches the intermediate state $\left|E_g; el\right\rangle \otimes |E_{ex'}; phonon\rangle$. Here, the excited state $|E_{ex'}; phonon\rangle$ of the phonon after DPP emission (route 1 in Table D.2) has a much higher eigenenergy than that of the thermal equilibrium state $|E_{thermal} : phonon\rangle$. This is because the DP couples with the phonon, resulting in phonon excitation. On the other hand, the excited state $|E_{ex'}; phonon\rangle$ of the phonon after the real photon emission (route 2 in Table D.2) has an eigenenergy as low as that of $|E_{thermal} : phonon\rangle$. This is because the real photon does not couple with the phonon.

Second step This step is an electric dipole-forbidden transition because it corresponds to the opposite process of the first step of absorption described above. Thus, only the DPP is created by this emission process. As a result, the electron is de-excited to the ground state $\left|E_g; el\right\rangle$, i.e., to the valence band, and the system is expressed as $\left|E_g; el\right\rangle \otimes |E_{ex''}; phonon\rangle$. After this transition, the phonon promptly relaxes to the thermal equilibrium state, and thus, the final state is expressed as $\left|E_g; el\right\rangle \otimes |E_{thermal}; phonon\rangle$.

Finally, the stimulated emission process is explained by Fig. 1.3b and summarized in Table D.3, which are similar to Fig. 1.3a and Table D.2, respectively. The only difference is that the DPP is incident on the electron in the conduction band to trigger the stimulated emission for the transition from the initial state to the intermediate state in the first step.

Table D.3 Two-step stimulated emission

First step	DP incident on the electron in the conduction band ⇓ Initial state: $\|E_{ex}; el\rangle \otimes \|E_{ex}; phonon\rangle$ ⇓Electric dipole-allowed transition⇓	
	Route 1(Stimulated emission: DPP creation) Intermediate state: $\|E_g; el\rangle \otimes \|E_{ex'}; phonon\rangle$	Route 2 (Stimulated emission: Real photon creation) Intermediate state: $\|E_g; el\rangle \otimes \|E_{ex'}; phonon\rangle$
Second step	⇓Electric dipole-forbidden transition⇓ (Stimulated emission: DPP creation) $\|E_g; el\rangle \otimes \|E_{ex''}; phonon\rangle$ ⇓Relaxation Final state: $\|E_g; el\rangle \otimes \|E_{thermal}; phonon\rangle$	

Appendix E
Two-Level System Model

A two-level system model theoretically describes the transition between two states in a complex material system, and has been popularly applied to analyze a variety of phenomena, such as persistent hole burning (PHB) in organic glasses [1]. This model is reviewed here and is used to describe temporal variation of the light intensity emitted from a device fabricated by DPP–assisted annealing.

Figure E.1 shows the energy level diagram of the two-level system model used for describing the DPP–assisted annealing process. The horizontal axis does not represent any specific physical quantity, in contrast to that used in the PHB, which is the configuration coordinate of the material [2]. The vertical axis represents the electron energy. States A and B represent the electron state before and after the DPP–assisted annealing, respectively. They are composed of two energy levels, i.e., the ground state ($|E_{gA}\rangle$, $|E_{gB}\rangle$) and excited state ($|E_{exA}\rangle$, $|E_{exB}\rangle$), which respectively correspond to the valence and conduction bands in a semiconductor. The DPP–assisted annealing forces a transition from state A to state B. The initial $|I\rangle$ and final $|F\rangle$ states of this transition are $|E_{gA}\rangle$ and $|E_{gB}\rangle$, respectively. The heights of the potential barriers in the ground and excited states are represented by V_g and V_{ex}, respectively.

As an example, the values of V_g and V_{ex} for the SiC-LED in Sect. 6.3, have been experimentally evaluated to be 0.53–0.63 eV and 0.10–0.11 eV, respectively [3]. Since the potential barrier V_g is generally higher than V_{ex}, as is represented by this example, the transition takes place efficiently not through V_g but through the lower potential barrier V_{ex} after the excitation from $|I\rangle$ $(= |E_{gA}\rangle)$ to $|E_{exA}\rangle$. The de-excitation from $|E_{exB}\rangle$ to $|F\rangle$ $(= |E_{gA}\rangle)$ takes place after the transition.

By this transition, the electron number $N_I(t)$ in $|I\rangle$ decreases, as is expressed by

$$N_I(t) = N_I(t_0) \exp[-k_t(t - t_0)], \tag{E.1}$$

where t_0 and k_t are the initial time of transition and the transition rate, respectively. The transition rate k_t is expressed as

$$k_t = k_t^0 \exp(-\gamma). \tag{E.2}$$

M. Ohtsu, *Silicon Light-Emitting Diodes and Lasers*,
Nano-Optics and Nanophotonics, DOI 10.1007/978-3-319-42014-1

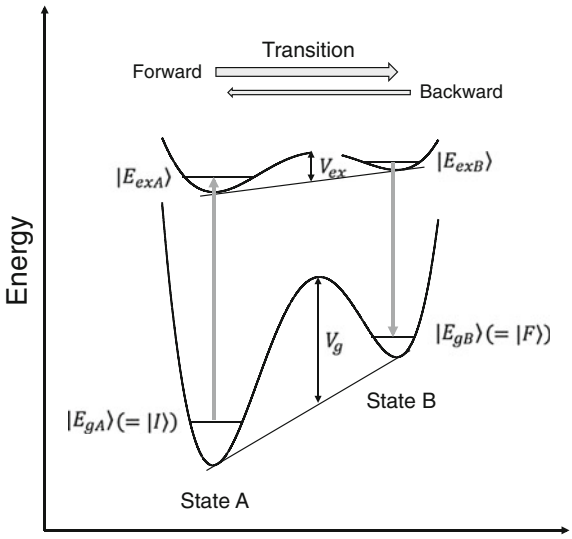

Fig. E.1 Energy level diagram of the two-level system model

In this expression, the rate-controlling parameter, γ, takes a range of values, depending on the inhomogeneous spatial distribution of the DPPs in the host crystal. This dependency is represented by a Gaussian distribution function [1]:

$$P(\gamma) = \frac{1}{\sqrt{2\pi}\sigma} \exp\left(-\frac{(\gamma - \gamma_0)^2}{2\sigma^2}\right), \tag{E.3}$$

where γ_0 and σ represent the center and width of the distribution, respectively. From (E.2) and (E.3), the total electron number $N_{I,total}(t)$ in $|I\rangle$, normalized to that at the initial time t_0, is expressed as

$$N_{I,total}(t)/N_{I,total}(t_0) = \frac{1}{\sqrt{2\pi}\sigma} \int_{-\infty}^{\infty} \exp\left(-\frac{(\gamma - \gamma_0)^2}{2\sigma^2}\right) \exp\left[-\left\{k_t^0 \exp(-\gamma)\right\}(t - t_0)\right] d\gamma. \tag{E.4}$$

Since the temporal decrease in the electron number given by this equation is proportional to the temporal increase in the light intensity emitted as a result of the DPP–assisted annealing, the normalized light intensity is expressed as

$$I(t)/I(t_0) = 1 - \frac{1}{\sqrt{2\pi}\sigma} \int_{-\infty}^{\infty} \exp\left(-\frac{(\gamma - \gamma_0)^2}{2\sigma^2}\right) \exp\left[-\left\{k_t^0 \exp(-\gamma)\right\}(t - t_0)\right] d\gamma. \tag{E.5}$$

In the case where the width σ is sufficiently large, (E.4) is approximated as

$$N_{I,total}\,(t)\,/N_{I,total}\,(t_0) = 1 - a\ln\left(t/t_0\right), \tag{E.6}$$

where a is a constant.

References

1 R. Jankowiak, R. Richert, H. Baessler, J. Phys. Chem. **89**, 4569 (1985)
2 W. Kohler, J. Meiler, J. Friedrich, Phys. Rev. B **35**, 4031 (1987)
3 T. Kawazoe, M. Ohtsu, J.-H. Kim, Abstract of the 76th JSAP Autumn Meeting, September 1025, Nagoya, Japan, paper number 16p-2G-6

Index

M. Ohtsu, *Silicon Light-Emitting Diodes and Lasers*,
Nano-Optics and Nanophotonics, DOI 10.1007/978-3-319-42014-1